High-Flux Experiments and Simulations of Pulse-Mode Position-Sensitive CdZnTe Pixelated Detectors

by

Miesher Lage Rodrigues

A dissertation submitted in partial fulfillment
of the requirements for the degree of
Doctor of Philosophy
(Nuclear Engineering and Radiological Sciences)
in The University of Michigan
2012

Doctoral Committee:

Professor Zhong He, Chair
Professor Frederick Becchetti Jr
Emeritus Professor Ronald Fenton Fleming
Professor James Paul Holloway
Assistant Research Scientist Feng Zhang

Believe in your dreams and they *may* come true.

Believe in yourself and they *will* come true.

Believe!!!

ACKNOWLEDGEMENTS

I am thankful for my wife Monick. She has been my greatest supporter over more than 15 years of what I consider to be a very happy marriage. Without her unconditional love and acceptance I would not be here. I am thankful for my parents Irineu and Bete. They provided me the best education they possibly could afford and for that I am very thankful. More than that, through their own experiences and good example, they are responsible for whom I am. I am thankful for my kids João Victor, Zion and Nicole. They provide me with joy and new experiences every day. I am very happy to be their father and to be able to see them growing every day. I am thankful for my brother and sister Hugo and Fabiani, my grandparents Daphnis, Ilze, Silvio and Maria, my cousin Marcelo, my aunt Edna and uncle Silvio and all my other cousins, aunts and uncles who both directly and indirectly contributed to this great moment in my life. I am thankful for my friends both in Brazil and in the United States. I truly value my friends and I respect each one of them. I am thankful for the opportunity to be here surrounded by a great group of staff and faculty friends who have helped to make this dissertation possible, and to them I am grateful. I am specially thankful to my adviser, Prof. Zhong He, who supported and trusted me throughout all these years. I feel very lucky to be part of his group where I have learned so much from him and all his graduate students, post-docs, staff, research scientist and visitor students that have been part of this group since 2006, when I was fortunate to became a member: Dan Xu, Dr. Meng, Scott Kiff, Ben Sturm, Weiyi Wang, Dan Lingenfelter, Jason Jaworski, Sonal Joshi, Crystal

Thrall, Jim Berry, Dr. Feng Zhang, Yuefeng Zhu, Willy Kaye, Cedric Herman, Hao Yang, and Andy Boucher, Steve Anderson, Dr. JaeCheon Kim, Dr. Burcin Donmez, Suzanne Nowicki, and many others. I am thankful for Prof. Glenn Knoll. He is truly an amazing man and an excellent example to be followed. I can't wait to read his 5th edition in portuguese. Thank Dr. Knoll for your support in Rio during the INAC 2009 conference. With all his knowledge and wisdom, he is greatly responsible for this happy ending story. I am thankful to Peggy Gramer, who is a great friend. I am thankful for my old friends Greg Davidson, Troy Becker, Jeremy Conlin, and Tiberious, Jessie and many others. I am grateful for the gift of many friends during my time as a graduate student in Michigan − too many to list here − who welcomed me, trusted me, listened to me, included me, encouraged me, strengthened me, grew me, and put up with me. I also thankful for Dr. Martin and Dr. Gilgenbach, my Chairs when I was accepted and welcomed in Michigan. Finally, I am thankful for the support received from the Department of Energy under office NA-22 office, which provided me and family with the proper resources which enabled the conclusion of my Ph.D. and the beginning of a new chapter in my life. Also, many thanks to the people who made this dissertation possible, especially those who put together a nice LaTeX template for me to use. Thank you to you all.

TABLE OF CONTENTS

LIST OF FIGURES

Figure

LIST OF TABLES

Table

LIST OF APPENDICES

Appendix

ABSTRACT

High-Flux Experiments and Simulations of Pulse-Mode Position-Sensitive CdZnTe Pixelated Detectors

by

Miesher Lage Rodrigues

Chair: Zhong He

In recent years, operation of wide band-gap semiconductor detectors under high-flux irradiation for medical and security applications has been pursued by many research groups. However, the operation of these devices under high-flux scenarios is limited by poor hole transport properties and other factors, causing the build-up of positive space charge as a function of irradiation time, the so-called *polarization effect*. In order to study this problem, high-flux experiments and simulations have been conducted at the University of Michigan. At first, charge transport properties of the CdZnTe detectors used in high-flux experiments were measured using γ-rays, α-particles and K_α X-rays, by direct comparison between cathode measured and simulated induced signals from cathode-side and lateral-side irradiations at normal and reverse cathode bias voltages. In these simulations, a Monte-Carlo model of the experimental apparatus was implemented using Geant4 to generate initial interaction positions. Using this model, 3D interaction positions and energies were generated and stored in list-mode. These simulated interactions were used as electron and hole source terms in the high-flux simulations, by injecting each simulated event at fixed time intervals.

This time was calculated as the average time between real interactions in the high-flux experiments, simulating different irradiation fluxes. Each simulated event consisted of single, double or multiple interactions, and the final distribution of charges in the simulated volume was determined by the superposition of each injected charge cloud. Each interaction assumed a homogeneous and spherical cloud of electrons and holes. The diameter of each charge cloud was pre-calculated using *Geant*4 as a function of the deposited energy. Charge drift calculations were carried out by numerically solving the charge continuity equations coupled with Poisson's equation, assuming multiple electron and hole defect levels. In contrast to previous reported work, a numerical approach was used to solve in 3D system of charge transport equations coupled with Poisson's equation. One defect level for electrons and two for holes were considered in this modeling. In order to reduce computational time, a simplified 3D axisymmetric model was used to study the polarization effect. This approach significantly reduced the amount of time needed to numerically solve the proposed system of equations and enabled the implementation of more advanced physical models to describe the detector behavior under high-flux irradiation. Look-up tables containing values of the operating and space charge electric fields, weighting potential, and distribution of charges as a function of cloud diameter and position were pre-computed and used during simulations. These pre-calculated values were readout once and stored in the computer memory in the beginning of each simulation execution. Applied electric field E and operating and weighting potentials, Φ and Φ_{wp}, were calculated using the Finite Element Method using the software Maxwell 3D. Space-charge electric field was calculated using the mirror charge method, while the number of mirror charges used was determined using a 0.5% precision criterion near the electrodes. Signals induced on each electrode were calculated by applying the Shockley-Ramo theorem and the principle of superposition. Compensation techniques applied by detector manufactures to increase the resistivity of CdZnTe detectors, which are known to be plagued

by shallow defect levels, introduce deep defect levels in the material. These defects act as trapping centers, trapping free charge carriers for longer times, degrading the performance of these devices when operated under high-flux scenarios. Characterization of shallow and deep trapping centers was required to understand the causes of the polarization effect. Since holes limit the performance of these devices under high-flux irradiation, more emphasis was given to measuring this charge polarity electrical transport properties. A systematic approach was used to measure these properties, i.e. electron and hole average trapping ($\tau_{e,h}$) and detrapping ($\tau_{eD,hD}$) times. In this work one-electron defect level and two-hole defect levels were considered. This was accomplished by detailed analysis of measured induced signals irradiating the detectors with γ-rays, α-particles and K_α X-rays on the sides, through the protective paint, and on the cathode surface. Then, holes-only induced signals were obtained by removing the electron contribution in the measured signals and charge transport properties were calculated. High-flux experiments using a JL Shepherd & Associates 3 Ci (09-20-2001) Cs-137 γ-ray irradiator and a custom-built experimental apparatus were conducted in the Ford Nuclear Reactor (FNR) building at the University of Michigan. The main objective of these experiments was to understand charge polarization effects caused by positive space charge build up as a function of irradiation flux and time, i.e., the polarization effect. The framework developed in this work used a Cs-137 γ-source rather than conventional X-ray sources. In future work, the same methodology should be applied to other types of radiation, such as X-rays, different detector materials, geometries, electrode configurations and different incident fluxes. The hardware used to acquire data in the high-flux experiments as well as details of the collimator and detectors used are described in this work. High photon fluxes were produced in these experiments by changing the distance between the source and detector. In these experiments, signals induced on electrodes were digitized in continuous mode using commercially available digitizers. These signals were post-

processed using a 1D edge detection algorithm. Initial experiments using the 3 Ci Cs-137 irradiator showed that the detectors polarized before reaching the maximum achievable flux, which corresponded to the minimum possible distance between source and detector. In order to understand the polarization effect, temporal evolution of the detector's response as a function of incident radiation flux was measured from $t = 0 \ldots 25.6$ s and $\Phi = 0 \ldots 219\ 000$ photons/pixel/s. These experiments showed photopeak shifts towards lower energy bins and spectral degradation as a function of increasing radiation flux. A series of experiments were conducted, where the design of the experiemental apparatus evolved over time in multiple iteration cycles. The main objective of these experiments was to polarize these detectors in order to provide information to study the causes of this phenomenon. Measured and simulated spectra as a function of increasing flux showed photopeaks shifting towards lower energy bins followed by complete absence of spectral information, which was found to be caused by positive space charge build up distorting and completely breaking down the operating electric field as flux increased. More importantly, in this work we have developed a complete 3D framework that can be extended to other semiconductor detector materials to study and predict their performance under high-flux scenarios.

CHAPTER I

Introduction

Over the past several years, the prospect of a terrorist group armed with a nuclear weapon has frequently been cited as a genuine and overriding threat to the security of the United States, *Shanker and Scmitt* (2009), *Montgomery* (2009), *Blair* (2010), *McConnell* (2008) and alq (2010). Independent of the special nuclear material (SNM) chosen, highly-enriched uranium (HEU) or weapons-grade plutonium (WGPu), both have in common high atomic numbers (Z=92 and 94, respectively) which are distinct from other ordinary materials. This intrinsic characteristic can be used selectively in either an energy binned or full spectral X-ray computer tomography (CT) cargo inspection system operated standalone or integrated with other detection technologies. If a terrorist group tries to slowly smuggle small quantities of SNM hidden inside small packages using conventional routes - by air, sea or land, into or within the United States, the proposed technology can be used as a cargo inspection system adding to conventional scanners the capability of making images as a function of atomic numbers. This would enable the identification of the presence of SNM without relying on their naturally emitted radiation, which could potentially make a significant impact in future inspection systems. This is particularly important if small quantities of shielded or masked SNM are intentionally placed inside luggage size objects either by passengers or sent unattended using the United States Postal Service (USPS) or

similar carrier services.

It is well known that detecting small quantities of shielded SNM is a difficult task, *Slaughter et al.* (2003), *Dougan et al.* (2004) and *Medalia* (2010). In general, current detection systems detect the presence of SNM by either measuring its naturally occurring radiation (passive systems) or its artificially induced radiation (active interrogation systems). Both approaches have been extensively studied in the past years, *Yang* (2009). The limitations of any detection or inspection techniques currently been studied and used are inherent to the requirements imposed by the environment where they need to be deployed. Usually, scanning/screening technologies for cargo inspection systems are required to be *affordable*, *unattended*, *agile*, *mobile*, *re-locatable*, *high-capacity* and *low dose to the environment*. Current small-size inspection systems being used at checkpoints that operate with X-ray sources are unable to distinguish between two different materials having high densities and high atomic numbers, *Lanza* (2009). For instance, a small object made of relative high-Z material could be intentionally built as a shielding material to absorb low energy photons (< 200 keV) emitted by small amounts of either HEU or WGPu. Current passive and X-ray scanning systems provide relative low probability of detection of this masked materials. Depending on the scenario, this is true even if the object in question is visually inspected by Homeland Security agents at security checkpoints.

Cargo inspection systems providing targeted-material specific imaging and identification capabilities, measuring full spectral information of attenuated X-rays, can potentially provide improved imaging and identification performance. X-ray detectors need to operate at intense radiation fluxes ($\sim 1 \times 10^8$ photons/cm^2/s) for this application due to scanning time requirements, in order to determine material specific compositions, identifying atomic numbers of targeted materials in the absorbing medium. Good spectral energy resolution of attenuated X-ray beam is required in the X-ray energy range of interest, *Schlomka et al.* (2008). The main mechanisms of

absorption of the incident photons in the energy range of interest are either photoelectric absorption or Compton scatter. A simple realization of this technique, known as dual-energy imaging, was initially proposed in the mid-1970's, *Alvarez and Macovski* (1976). This technique uses the well known dependence of the attenuation coefficient with energy for different materials. K-edge imaging can be realized using multi-bin energy-discrimination counting detectors. New developments in direct-conversion radiation detectors, e.g. CdZnTe detectors, provide the required detection capabilities necessary for this technique in medical imaging as well as security applications, *Butler et al.* (2008), *Halpern et al.* (2009), *Persson and Cederwall* (2011) and *Kalender et al.* (2008). Also, multi-energy CT for small animals using CdZnTe is being developed by many groups, *Masetti et al.* (2009b), *Kim et al.* (2006) and *Masetti et al.* (2009a). The K absorption edge corresponds to a sudden increase in the attenuation coefficient of photons occurring at a photon energy just above the binding energy of the K shell electron of the atoms interacting with the photons, which corresponds to a sudden decrease in the number of counted events at the same corresponding energy. The sudden increase in attenuation is due to photoelectric absorption of the photons. The challenge is to measure these absorption jumps caused by the K-edges of different materials at significantly high-fluxes using semiconductor detectors, *Veigele* (1973). In some applications, e.g. Spectral CT, measuring these features using CdZnTe pixelated detectors operated in pulse mode at room-temperature is advantageous, *Soldner et al.* (2007), *Bale et al.* (2008) and *Bale and Szeles* (2008).

The problem becomes more challenging as incident photon flux increases, since it is observed at room-temperature through experiments and simulations that build-up of positive space charge in the bulk of these devices causes signal degradation. In this work, it is shown that positive space charge build-up causes distortions in the operating electric field E mainly due to holes getting trapped in deep trapping centers in CdZnTe. At higher fluxes, positive space charge build-up completely breaks down

the operating electric field causing the detector to stop working. Then, in order to minimize this undesirable effect it is necessary to understand which material properties and operating parameters limit the performance of these devices under high-flux operating conditions. Also, the optimization of algorithms used to reconstruct images as a function of atomic numbers using spectral information provided by these detectors is an important topic suggested for future work.

A spiral model described in Figure 1.1 is used to represent the main topics addressed in this work.

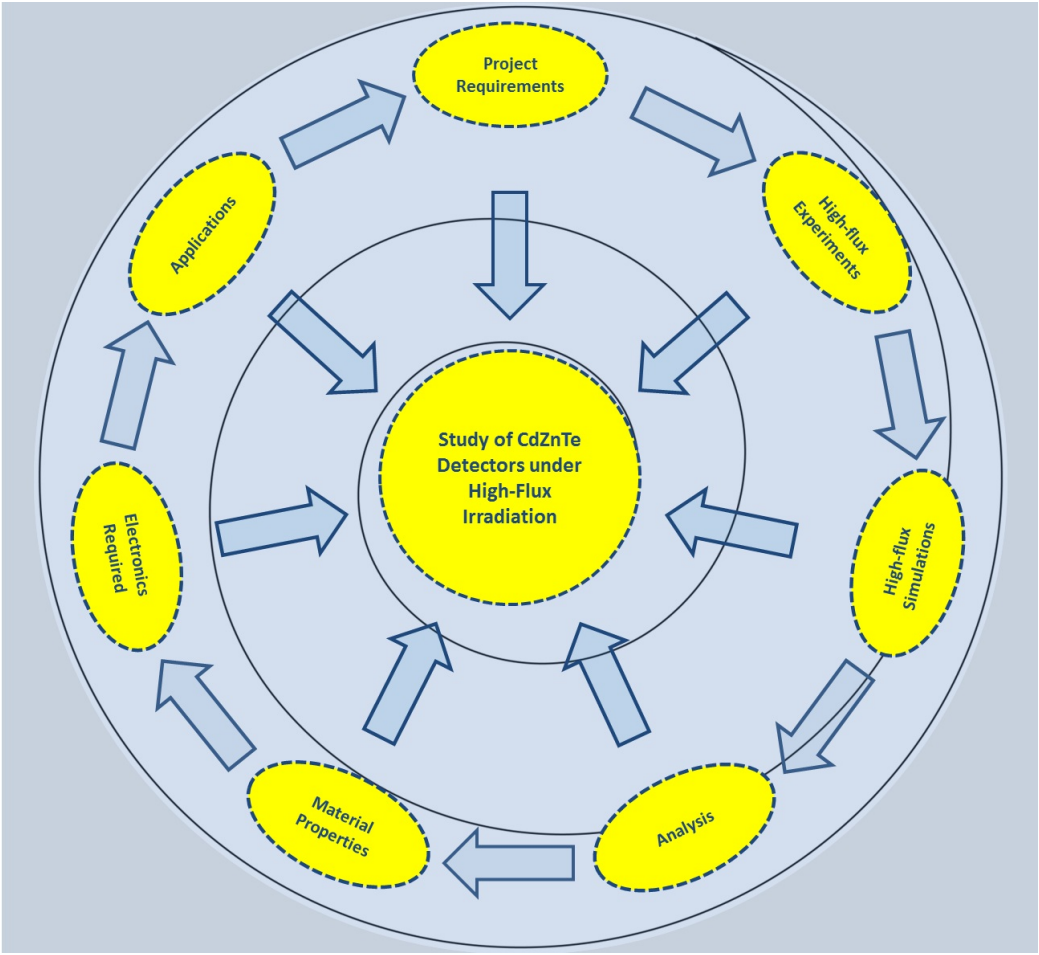

Figure 1.1: A spiral model showing the seven main topics which were addressed during this Ph.D. research.

It shows in a simplified way seven main topics, which were investigated at different phases during the life cycle of this Ph.D. research:

a) Project requirements

b) High-flux experiments

c) High-flux simulations

d) Analysis

e) Material properties

f) Electronics requirements

g) Applications

Figure 1.1 illustrates that very little was known in the beginning of this research. This is represented by drawing further from the center of the figure, the state-of-the-art in this research, what was known in the beginning of this research. All of these seven topics were not thoroughly investigated in this research. More attention was given to the high-flux experiments and simulations, data analysis and measuring the electrical transport properties of CdZnTe while less attention was given to the electronics required, the applications and the project requirements. In future studies, more effort should be spent on these other topics. In particular, the requirements for the operation of these detectors were not clearly defined in the beginning of this study and there was no clear definition of the meaning of the term *high-flux*. Different researchers reported different flux levels, *Soldner et al.* (2007), *Bale et al.* (2008) and *Du et al.* (2003). Also, initial studies published by these and other researchers concluded that the incident flux Φ was the only factor limiting the operation of CdZnTe detectors in high-flux scenarios. In these early studies, important parameters such as the energy of the source, the operating conditions (i.e. temperature T and applied voltage V) and the dimension of the detector as well as electrode configuration were not fully explored in previous work.

In order to make significant contributions to the scientific community, this research focused on understanding the main causes of the so-called *polarization effect*. Here, the *polarization effect* was considered to be the build up of positive space charge

as a function of irradiation time when operating these semiconductor detectors at high-flux ($\sim 1 \times 10^8$ photons/cm^2/s) scenarios.

CHAPTER II

Current Technologies and Applications

Current technologies that have been used to inspect cargo or can potentially be applied for this application are briefly discussed here. In this chapter, an introduction to conventional, dual-energy and multiple energy CT systems is presented. Some of the techniques presented here are still not commercially available in cargo inspection systems, such as multiple energy CT. On the contrary, some applications of this technique in medical systems are being used to describe the benefits of multiple energy CT over conventional and dual energy CT systems, *Roessl and Proksa* (2007), *Shikhaliev and Fritz* (2011) and *Feuerlein et al.* (2008). This is necessary to understand the advantages of having full spectral CT functionality, as proposed here, in future inspection systems. A brief and overall discussion on the limitations in detecting small quantities of shielded or masked SNM is also presented here. In general, imaging systems using X-rays as incident radiation source have been vastly used in both cargo inspection and medical applications as digital X-ray systems. Then, only systems that use X-ray sources in scanning mode of operation, i.e. CT scanners, either conventional or dual-energy, are considered in this analysis. They enable attended or unattended operation through the use of specialized algorithms, i.e., pattern recognition, artificial intelligence, and other more advanced techniques that in some applications can be applied in real time.

3D images of scanned objects are formed by counting the X-rays incident at the detector, usually operating the system in current mode, integrating the signal over all energies. These detectors are usually 2D sensitive, e.g., x-ray films, digital CsI sensors, scintillators with PMT, and sometimes in recent systems can have limited depth sensing capability, e.g., layers of scintillators in dual-energy CT, *Schlomka et al.* (2008). These techniques usually generate large volumes of data that after acquisition, using fast detectors and specialized readout electronics, are post-processed in order to demonstrate various structures based on their ability to attenuate the incident X-ray beam. It is well understood that attenuation of photons by matter due to photoelectric absorption and Compton scatter are dependent on the energy of the incident photon. X-ray sources are characterized by a broad energy spectrum and current systems operate with X-rays energies peaking around 100 keV. Therefore, different spectral components are attenuated with different strengths, a process called *beam hardening*, *deCasteele et al.* (2002). The main difference between conventional and dual-energy CT scanners is that conventional CT scanners do not use the energy information of the X-ray beam while dual-energy CT scanners either use two energy X-ray beams or have layers of detectors with different efficiencies to discriminate regions of predominance of photoelectric absorption from regions of predominance of Compton scattering. The later separates effects of photoelectric absorptions from Compton scattering sometimes using two incident X-ray beams for each scanned position, having each beam at distinct energies (low for mostly photoelectric absorption and high for mostly Compton scatterings). This is the so called *dual-energy approach*, *Ying et al.* (2006) and *Xing et al.* (2011). More recent scanners apply this same technique using a single X-ray beam and two layers of detectors, the first for Compton scatter interactions and the second for photoelectric absorption, still operating both layers in current mode, *Kang et al.* (2010). For scanning materials with low atomic number Z, the dual energy method works well while energy binned or full spectral

CT may not be advantageous, *Xing et al.* (2011). Since these systems integrate the induced signals over all energies, or in the particular case of dual-energy systems over two large energy ranges, they cannot use the additional information contained in the photoelectric absorption of high-Z materials (Z$>$ 25).

Dual-energy attempts for a correct treatment of the energy dependence of attenuation in matter considers the photoelectric absorption and Compton scatter as distinct effects. In these systems detectors are used in current mode and attenuation is considered as an average value over the entire X-ray energy. This decomposition is beneficial within the regime of diagnostic X-ray energies for elements with low-Z, i.e. those elements where the K-edge discontinuities in the attenuation coefficient lie below the energy regime of operation of current detectors ($<$ 10 keV). When assessing high-Z materials, the previously described technique is inefficient either if one tries to change the energy of the source or if different layers of detectors are used. Using a linear accelerator to generate monoenergetic X-rays makes this task possible without relying on the energy information of the incoming photon, although this is not practical since it would be extremely time consuming. More recently, several groups are investigating multiple energy CT systems using large band-gap semiconductor detectors, e.g., CdZnTe, by selecting a small number of energy bins (around six energy bins are realizable in some systems, *Mikkelsen et al.* (2008b)) and counting photons at specific energy windows. These systems enable a rough estimation of the spectrum, which can be used to assemble a small and finite basis of images which, if correctly chosen, can be used to determine material specific compositions. The major drawback of this system is the impossibility of using the additional 3D-position-sensing information provided by pixelated CdZnTe detectors, which would improve the energy resolution by applying depth or time-of-flight corrections to the recorded signals, e.g., charge trapping, *Li et al.* (1999c), *Li et al.* (1999a), *Li et al.* (1999b), *Zhang et al.* (2004), *Zhang et al.* (2005) and *Zhang* (2005). This additional

feature enables correct identification and assessment of measured spectral jumps due to L,M,N and K-edges. The main problem encountered is the limitation imposed by the inherent charge transport characteristic of current semiconductor detector materials, e.g., CdZnTe, CdTe and HgI_2, mostly related to low hole mobility compared with electron mobility, *Rodrigues and He* (2010) and *Rodrigues and He* (2011).

During the last two decades, CdZnTe has been explored as an alternative and future material for nuclear imaging applications, *Scheiber* (1996), *Heanue et al.* (1996), *Iwata et al.* (1999), *Barber et al.* (2003) and *Barber et al.* (2005). This has led to improved semiconductor detector's performance under low- and high-flux scenarios and the development of new theories that take advantage of these devices and enable their use in new applications, e.g., spectral CT. Spectral CT systems using CdZnTe detectors have been proposed by many researchers due to the ideal characteristics of these devices. Compared to dual-energy and conventional CT systems, spectral CT has the advantage not only to distinguish and identify contrast agents from other highly absorbing materials but also gain quantitative information on the specific material itself. Preliminary results showed that both dose to the patient as well as overall image quality improved using multi-energy CT approach with monochromatic X-ray beams, *Masetti et al.* (2009a). This technique can be used to selectively remove unwanted background from the image - resulting in an image of a single element for instance (single Z), since spectral CT can be much more selective than current systems. The desired characteristics of semiconductor detectors to be used in spectral CT systems include:

a) Detector Response

- High response speed to minimize pile-up and dead time.
- High count rate limitation to enable high-flux operation (photon flux $\Phi > 1 \times 10^8$ counts/cm^2/s).
- Good response uniformity: count rate, gain and energy resolution uniformities.

b) Device Fabrication

- High crystal quality: uniform and optimized charge transport properties for high-flux applications without device polarization.
- Low noise: good device fabrication, since most sources of noise are originated from surface, interface and subsurface defects.
- High breakdown voltage: high response speed of detector arrays due to short transit time of the photon induced carriers.

c) Device Testing

- Fast screening techniques: fast selection of regions with desirable properties, reducing fabrication costs.

d) Hybridization

- Improving bonding technology: lowering the ASIC bonding temperature, reducing introduction of additional defects.

e) Readout Integrated Circuit

- High speed signal processing: enabling high count rate, high dynamic range, good linearity operation without serious pile-up and reduced electronics dead time.
- Multi-channel parallel readout: efficient processing signals from multiple pixels in parallel.

In the 1990's, researchers were looking at CdZnTe and other semiconductor detectors as *possible* radiation detectors in Nuclear Medical Imaging (NMI). During this time, the operation of these devices in current as well as pulse mode were investigated by many research groups. Results for pulse mode were less encouraging due to poor detector's performance observed under high-flux irradiation. The detectors could not achieve the required flux for CT systems and were limited to PET applications. By 1991, researchers recognized the need to invest more heavily on computer simulations as a need to better understand the physics involved in semiconductors, *Gustafson* (1991). By 1992, the use of CdZnTe in spectral CT applications were still

at the experimental stage in most companies and R&D laboratories. During this time, CdTe was limited by the *rather long afterglow*, *Scheiber* (1996). This problem was solved around 1996, when significant progress was accomplished in shortening the photodecay in CdTe X-ray detectors by modifying their structure and contacts. By 1996, hybrid spectral CT and SPECT systems had been developed using either Ge or CdTe detectors. During this time, applications using CdZnTe and other semiconductor detectors operated under high-flux scenarios were being envisioned in current mode, as a solution to pile-up and other problems which were known at that time, *Scheiber* (1996) and *Heanue et al.* (1996). By 1999, it was recognized that although CdTe and CdZnTe were attractive detector materials in many aspects, there was still much work to be done before they could be used in a flexible medical imaging system such as the PET/CT system. During this time, researchers started to develop simulations of semiconductor detectors coupling the charge continuity equations with Poisson's equation. At that time, complex electrode geometries like *coplanar grid* and *pixelated anodes* were considered as a prohibited approach, leading to simpler simulations, decoupling those equations when those geometries were considered. For low-flux applications, this assumption was sufficient since the excess of charges produced by radiation interactions does not significantly perturb the field within the detector, *Prettyman* (1998) and *Eskin et al.* (1999). On the contrary, this assumption is not true for high-flux applications.

In the 2000's, many researchers became more interested in using CdZnTe or CdTe for Nuclear Medicine Imaging NMI applications, while some were investigating other detector materials, e.g., GaAs. In Europe, read-out electronics capable of reading a large number of multiple channels simultaneously were being developed, such as the Medipix and XPAD collaborations, *Llopart et al.* (2002)and *Franchi et al.* (2006). During this time, advances in dual-energy CT systems achieved by the General Electric Co. (GE), Siemens and other companies and research laboratories around the

world, called the attention of the scientific community. CdZnTe, CdTe and other semiconductors were being quoted as future materials to substitute current CT technologies with many added advantages. By 2008, researchers were looking for theories that could explain the nature of polarization in materials like CdZnTe under high-flux irradiations, *Bale and Szeles* (2008). By 2009, they were showing preliminary results obtained for a multi-energy CT system for small animals. In these experiments, the X-ray energy used was tunable to be either 26 or 72 keV. These results showed that both dose to the patient as well as overall image quality could improve using the multi-energy CT approach, *Masetti et al.* (2009b). It was demonstrated that this technique could be used to selectively remove unwanted background from images, resulting in an image of a single element. Multi-energy CT was proved to be more selective than dual-energy CT systems. By 2009, researchers were able to simulate charge transport processes in CdZnTe including electrostatic repulsion of space charge, *Benoit and Hamel* (2009). Also, during the same period of time, researchers were able to solve the 1D system of equations that describe the problem using Multiple-Scale techniques, *Bale and Szeles* (2009).

2.1 The problem: A spectral CT system for Cargo Inspection

In order to reduce scanning time, the application described in Chapter I requires high incident photon flux $\sim 1 \times 10^8$ photons/cm^2/s. Poor hole mobility causes positive space charge build up in the detector volume, at first distorting the electric field, then at higher fluxes, the operating field completely breaks down causing the detector to stop working. While pioneer studies considered the operation of these devices mostly in current mode, more recent studies concentrated in operating these detectors in pulse mode, taking advantage of the energy information. When operating at high-flux, it becomes challenging to measure the energy of each photon. Positive space charge builds up, reducing the internal field, causing signal degradation and

incomplete charge collection. In this research, it was concluded that this problem is mostly due to incomplete signal integration (ballistic deficit), when analog filters with a fixed shaping time are used to calculate signal amplitudes. In order to design instruments to take advantage of 3D-position-sensitive CdZnTe detectors operating under high-flux, this problem needs to be correctly understood both through simulations and experiments. Much of the progress achieved over the last two decades is in better understanding the physics in semiconductor devices through experiments and simulations. This approach is responsible for the improvement of performance of these devices over the years under low and high-fluxes. Development of new detectors capable of operating at high-flux for spectral CT and PET applications with 3D-position-sensing capability is challenging.

2.1.1 The Challenge

For security applications higher X-ray source energies peaking around 300 keV are needed due to two main reasons: firstly the detection system has to be able to correctly distinguish photoelectric absorption jumps due to L, M, N and K-edges of targeted high Z materials (which for lead is around 88 keV and for uranium and plutonium is around 115 keV and 118 keV respectively), as seen in Figure 2.1, and secondly to reduce scanning time one needs to increase the number of incident photons at these energies. Bremsstrahlung sources are broad energy sources (X-ray bremsstrahlung spectra peaks around 1/3 of maximum energy). Full spectral CT seems to be the only realizable solution and CdZnTe seems to be a promising detector material for this application. The principle of full spectral CT is simple and uses the jumps in the photoelectric absorption coefficient due to L, M, N and K-edges, specially for high Z materials of interest. Combined with conventional and dual-energy techniques that are already being used for detection/imaging of low Z materials, this technique would enable detection/imaging of the entire range of existing materials. In the medical

field there have been extensive research activities to improve detection of target-specific and conventional contrast agents and drugs for this and also a multitude of other medical imaging modalities such as, e.g., magnetic resonance imaging, positron-emission-tomography and optical imaging. In order to be more specific, in both security and medical applications there is a need to implement systems with material identification capabilities and CdZnTe is a promising radiation detection material.

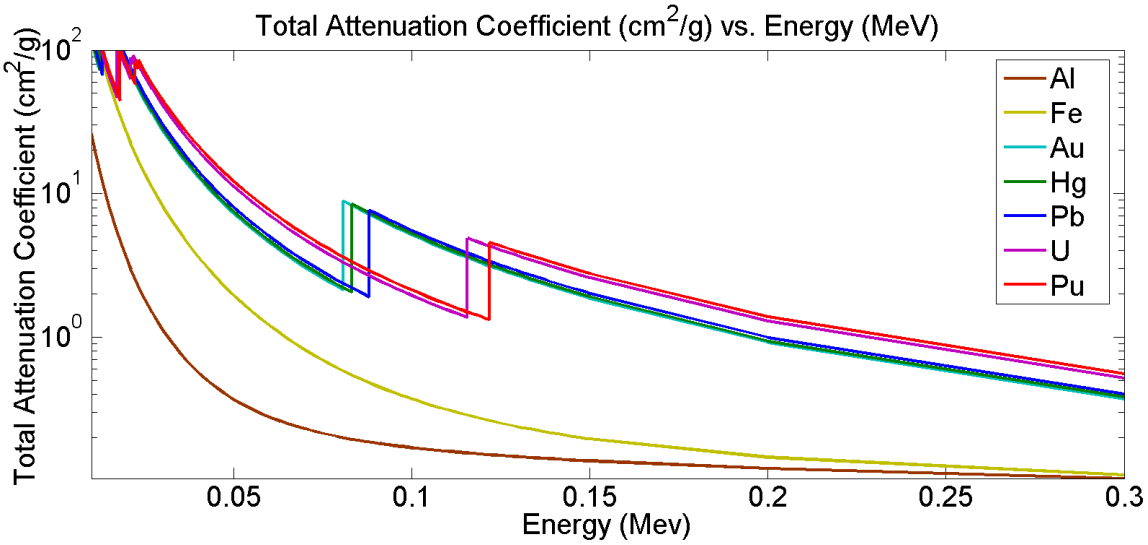

Figure 2.1: Total attenuation coefficient (cm^2/g) as a function of photon energy (MeV) for seven different materials: Aluminum (Al), Iron (Fe), Gold (Au), Mercury (Hg), Lead (Pb), Uranium(U) and Plutonium (Pu).

Security applications need to target materials that have higher atomic numbers compared with contrast agents used in the medical field. Large band-gap semiconductor detectors, e.g., CdZnTe(E_g=1.4 to 2.2 eV), HgI_2(E_g=2.1 eV) and CdTe(E_g=1.5 eV), have the required energy resolution to resolve features measured in the spectrum at this energy range and can be operated at room-temperature with the advantage of giving 3D-position-sensing information. There has been extensive study on the use of CdZnTe pixelated detectors mostly targeting medical applications. Currently there is no commercial system capable of operating these semiconductor detectors in high-flux and pulse mode acquiring full spectroscopic information and also enabling

3D-position-sensing. This system, in theory, would enable the user to quantify and make nondestructive assessment of objects through images and specialized algorithms for every element.

2.1.2 Preliminary Simulations Targeting SNM

A simplified simulation is used to demonstrate this idea. The theory related with the results shown in this section has been described elsewhere by *Firsching et al.* (2004), *Sidky et al.* (2005b), *Faridani* (2003) and *Firsching et al.* (2006). It is assumed a X-ray beam with a flat incident spectrum in the energy range between 30 keV and 150 keV passing through an ideal object, a phantom described in Figure 2.2.

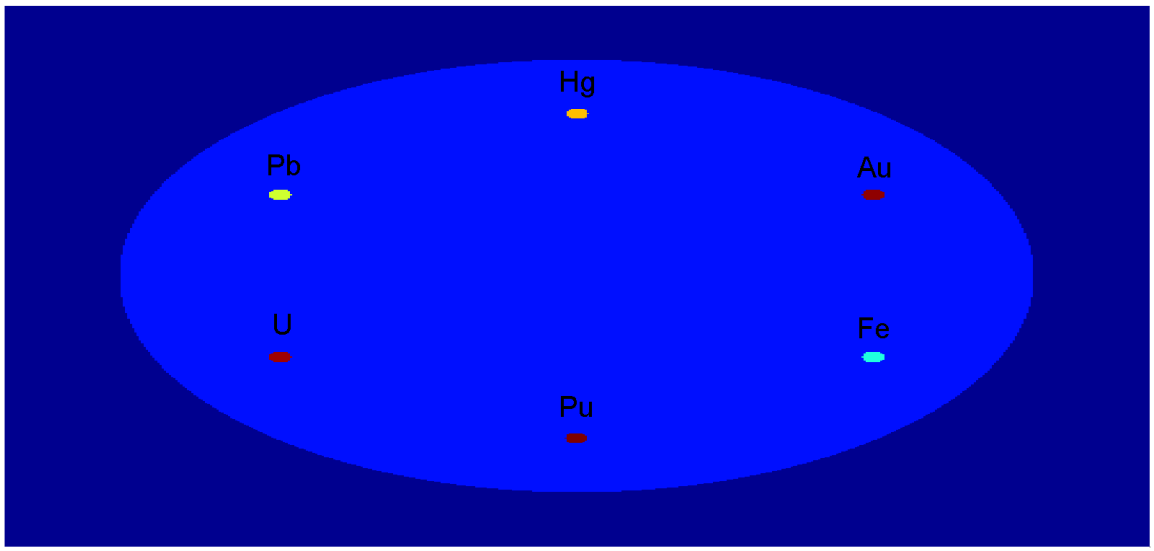

Figure 2.2: Phantom simulated as a sphere made of element Al (Z=13) with density $\rho = 2.7$ g/cm^3 with radius of 2 cm (each mesh corresponds to .01 cm), having six different elements: Fe (Z=26, $\rho = 7.874$ g/cm^3), Au (Z=79, $\rho = 19.3$ g/cm^3), Hg (Z=80, $\rho = 13.534$ g/cm^3), Pb (Z=82, $\rho = 11.34$ g/cm^3), U (Z=92, $\rho = 19.1$ g/cm^3)and Pu (Z=94, $\rho = 19.816$ g/cm^3).

The phantom is made of solid aluminum (Al, Z=13, $\rho = 2.7$ g/cm^3), having small spheres of different elements embedded on it: Iron (Fe, Z=26, $\rho = 7.874$ g/cm^3), Gold (Au, Z=79, $\rho = 19.3$ g/cm^3), Mercury (Hg, Z=80, $\rho = 13.534$ g/cm^3), Lead

(Pb, Z=82, $\rho = 11.34$ g/cm^3), Uranium (U, Z=92, $\rho = 19.1$ g/cm^3) and Plutonium (Pu, Z=94, $\rho = 19.816$ g/cm^3). The simulated geometry is modeled as a 500×500 mesh corresponding to a 5×5 cm^2 area, having a spherical solid aluminum block 2 cm radius centered at the geometric center of the mesh and six small spheres 1 mm diameter positioned 60^o apart from each other, as shown in Figure 2.2.

Figure 2.3 shows reconstructed images at six different measured energies: a) $30 < E < 80$ keV, b) $80 < E < 83$ keV, c) $83 < E < 88$ keV, d) $88 < E < 116$ keV, e) $116 < E < 122$ keV and f) $122 < E < 150$ keV.

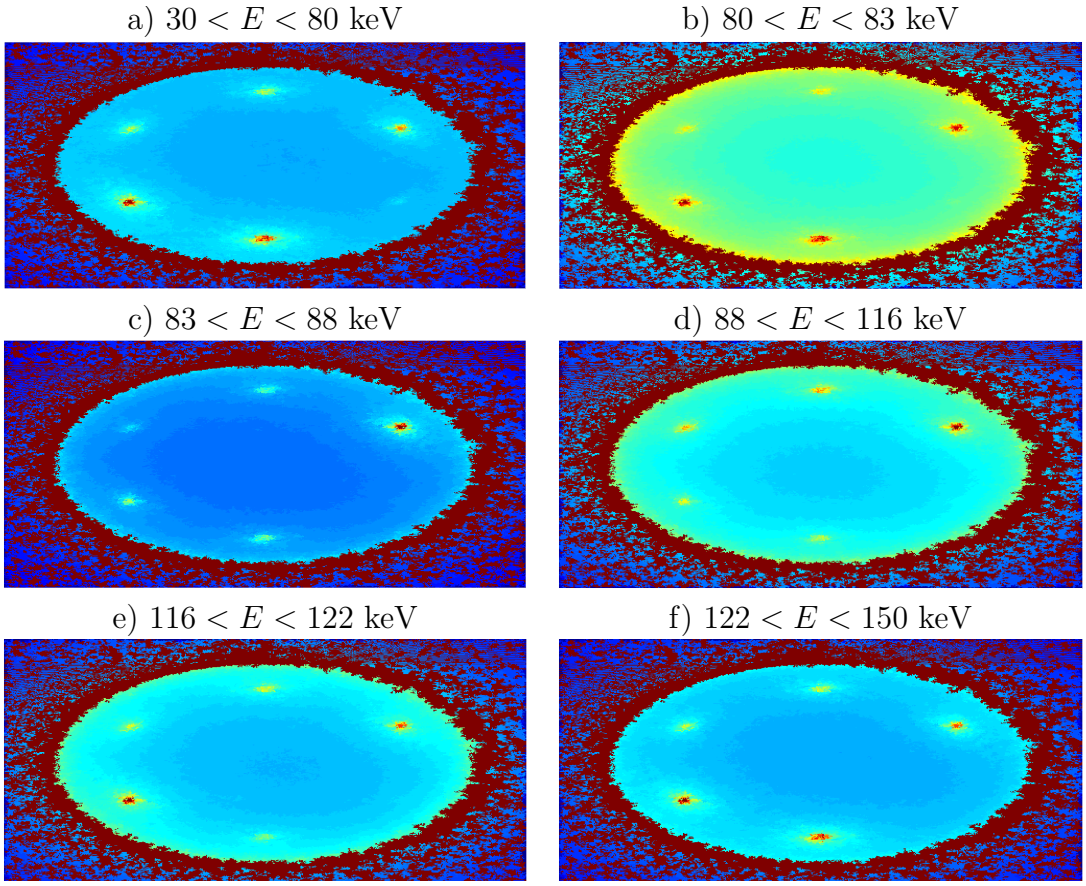

Figure 2.3: Reconstructed images integrated over a) $30 < E < 80$, b) $80 < E < 83$, c) $83 < E < 88$, d) $88 < E < 116$, e) $116 < E < 122$ and f) $122 < E < 150$ keV energy windows.

This simulation considered a parallel beam of X-rays incident on the phantom and

did not take into account the effect of change in the trajectory of the incident X-ray photon caused by Compton scatters in the material. Also, it was considered that the broad X-ray Bremsstrahlung incident spectrum is constant in the ranges of energies simulated. The phantom rotates every degree in a full 360^o rotation. For each angle of rotation, attenuation coefficients are calculated and incident spectra at the surface of the detector are measured. The estimated X-ray flux takes into account the distance between the source and detector and the counts necessary to have enough statistics to measure features in the spectrum. Images shown in Figure 2.3 form a basis, where it is possible to create new images by adding and subtracting the images that form this basis.

Figure 2.4 shows two images made using the basis defined on Figure 2.3.

a) Uranium-Only: by subtracting Figure $116 < E < 122$ keV from Figure $88 < E < 116$ keV

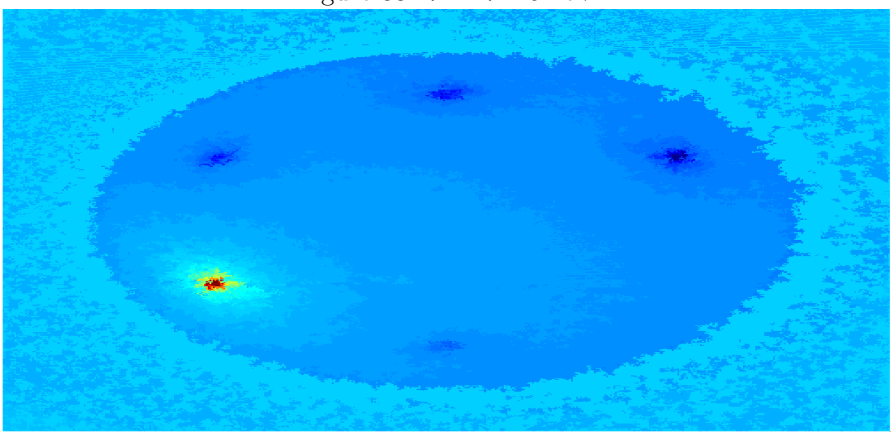

b) Plutonium-Only: by subtracting Figure $122 < E < 150$ keV from Figure $116 < E < 122$ keV

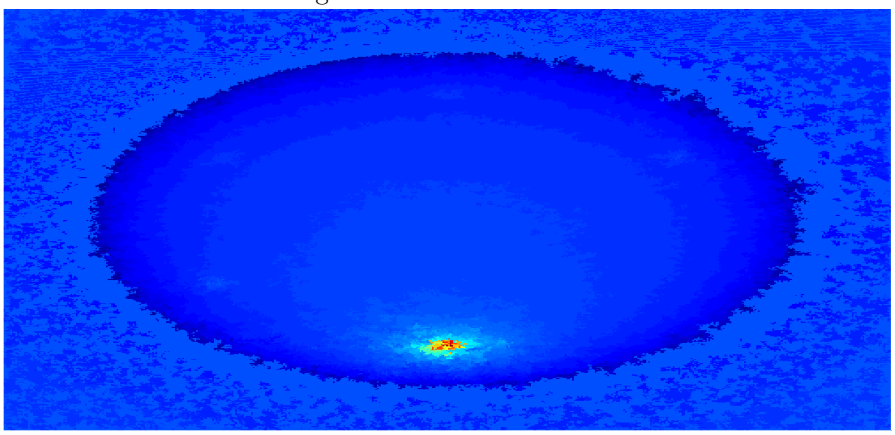

Figure 2.4: Reconstructed image using a simple subtraction operation to obtain images of Uranium-Only and Plutonium-Only. In a), Figure 2.3e) was subtracted from Figure 2.3d), and in b) Figure 2.3f) was subtracted from Figure 2.3e).

In the images shown in Figure 2.4, the high contrast between SNM with respect to other materials is obtained by subtracting Figures 2.3e from 2.3d and 2.3f from 2.3e.

2.2 ASIC Development

Since late 1990's and early 2000's, different groups have been developing application-specific integrated circuit ASIC specific for high count rate to be used in CT and PET

applications, *Blanquart et al.* (2000), *Pangaud et al.* (2010), *Ricq et al.* (2001) and *Llopart et al.* (2002). By 2007, these ASIC started to show promising results in the medical field, *Pangaud et al.* (2007), *Franchi et al.* (2006), *Michel et al.* (2006), *Bohnel et al.* (2007) and *Firsching et al.* (2007). At the same time, other groups started to show results using their own ASIC development, *Szeles et al.* (2007) and *Mikkelsen et al.* (2008b). By 2010, development in ASIC design has enabled researchers to envision new applications for position-sensitive CdZnTe detectors in the future, *Talla et al.* (2008), *Basolo et al.* (2008), *Durst et al.* (2008), *Nachtrab et al.* (2009), *Steadman et al.* (2011), *Tlustos* (2010) and *Aslund et al.* (2010).

Modern ASIC technology available today has been optimized for good performance with CdTe and CdZnTe for single photon energy spectroscopy and imaging, *Mikkelsen et al.* (2008a). These ASIC have been tested at 2.0×10^4 counts/channel/s with the desired characteristics to operate with 3D-position-sensitive CdZnTe detectors under high radiation fluxes, *Mikkelsen et al.* (2008b). ASIC manufacturer simulations predict that signal acquisition at frequencies of 0.1 MHz can be achieved per ASIC channel using this design. Then, the equivalent maximum count rate per unit are depends on the size of the electrode considered.

High-flux experiments in our initial studies using the currently available CdZnTe detectors have measured polarization effects caused by positive space charge build-up at fluxes $\sim 2.0 \times 10^5$ counts/pixels/s ($\sim$3 mm^2 pixel area), which represents the same acquisition rate predicted by ASIC manufacturers. Precise limits of operation, detector geometry, beam geometry and all other parameters can only be really determined after more detailed study of this technology and depends on advances on new ASIC and detector material fabrication.

2.3 Remarks

Full spectral computed tomography CT systems using CdZnTe detectors have been proposed by many researchers due to ideal characteristics of these devices. Compared to conventional and dual-energy CT systems, spectral CT has the advantage to distinguish and identify highly absorbing materials gaining quantitative information on specific materials since the signal can be easily corrected by determining the change in photopeak position as a function of incident flux. Some requirements for systems that use CdZnTe detectors for spectroscopic X-ray imaging are:

a) room-temperature or near-room temperature operation to avoid bulky, power hungry and maintenance of large refrigeration systems

b) short transit time of the X-ray induced charge carriers through the detector crystal to minimize pile-up and maximize count-rate

c) negligible charge trapping to minimize space-charge formation and polarization of the device

d) sufficiently fast and accurate readout electronics to enable the processing of the large number of signals without significant count-rate degradation

Spectral CT systems using CdZnTe pixelated detectors require small pixel-pitch, i.e., $\sim$ 300 μm, to allow high count rate per channel without severely deteriorating energy resolution caused by charge sharing effects, taking advantage of the small pixel effect. Considering this required pixel pitch, charge sharing can severely degrade the performance of the system if not correctly considered in the system. Also, a large number of pixels is needed which imposes a challenge on the readout hardware and software. The reason why CdZnTe has not yet been fully implemented in this application is believed to be related to its material properties and limited performance of fast readout electronics. Current ASIC developed by different manufacturers are becoming more feasible. In the future, it should be possible to use 3D-position-sensitive detectors in pulse mode at reasonably high count rates ($\sim$ 100 kHz per

channel). CdZnTe crystal growth technology is more mature and crystal quality has improved. There has been little agreement between researchers on the fundamental issues related to the properties of materials needed for this specific application. It is known that CdZnTe can be manufactured with different material properties. It is necessary, for this application, to determine the impact of each material parameter in the overall performance of the system. Positive space charge builds-up quickly, in high-flux situations, due to slow drift of holes. This significantly perturb the electric field. In order to completely understand this problem, we have been building over the past years a full 3D simulation tool kit of pulse waveforms induced on pixelated CdZnTe detectors under high irradiation fluxes.

CHAPTER III

Simulation Modeling

A Monte-Carlo model of the experimental apparatus was implemented in *Geant*4, as described in *Sec.3.1.* Using this model, 3D interaction positions and energies were generated and stored in list-mode, as described in Section 3.1.1. These simulated interactions were used as electron and hole source terms in the high-flux simulations, by injecting each simulated event at fixed time intervals. This time was calculated to be equivalent to the average time between real interactions in high-flux experiments, simulating different irradiation fluxes, as described in Section 3.1.2. Each simulated event consisted of single, double or multiple interactions, $i = 1, 2, ..., n$, and the final distribution of charges in the simulated volume was determined by the superposition of each injected charge cloud centered at position (x_i, y_i, z_i) with energy E_i. These interactions were assumed to create homogeneous and spherical clouds of electrons and holes. The diameter of each charge cloud was calculated as a function of deposited energy using *Geant*4, as described in Section 3.1.3.

Charge drift calculations were carried out by numerically solving the charge continuity equations coupled with Poisson's equation, assuming multiple electron and hole defect levels, as described in Section 3.2. In contrast to previously reported work, a numerical approach was used to solve in 3D the system of charge transport equations coupled with Poisson's equation, *Bale and Szeles* (2009), *Bale and Szeles*

(2010), *Kozorezov et al.* (2005), *Barrett et al.* (1995) and *Gatti et al.* (1987). One defect level for electrons and two for holes were considered in this model. Initially, a 3D point-cloud model was used to solve the system of coupled equations in high-flux conditions. Then, changes in the experimental apparatus, described in Section 3.2.1, resulted in a simplified 3D axisymmetric model. This new approach significantly reduced the amount of time needed to numerically solve the proposed system of equations. Additionally, future implementations of more advanced physical models not included in this simulation, such as charge recombination and the effect of the contacts, can be investigated using this approach.

In order to consider the effect of the cathode and anode electrodes, space charge electric field was calculated using the mirror charges method, as described in Section 3.2.2. Look-up tables containing values of operating and space charge electric fields, weighting potential, and distribution of charges as a function of cloud diameter and distance from the axis of symmetry were pre-calculated. Time, precision and computational constraints determined the size of the square mesh used in the simulations, as described in Section 3.3.1. These values were readout once and stored in memory as look-up tables in the beginning of each simulation execution. Applied electric field $\vec{E}$ and operating and weighting potentials, Φ and Φ_{wp}, were calculated using the Finite Element Method using the software Maxwell 3D, as described in Section 3.3.2. Space charge electric field was calculated using the mirror charges method, while the number of mirror charges was determined by considering a 0.5% precision of the space charge electric field near the electrode region, as described in Section 3.3.3. Signals induced on each electrode were calculated by applying the Shockley-Ramo theorem and the principle of superposition, as described in Section 3.3.4.

Finally, validation of the developed simulation tool is presented in Section 3.4, while a critical analysis of the approach chosen to study problems caused by the operation of semiconductor detectors in high-flux irradiation environments, such as

the so-called *polarization effect*, is presented in Section 3.5.

3.1 Monte Carlo Model of The Experimental Apparatus

A Monte-Carlo model of the experimental apparatus consisting of eight objects, as described in Figure 3.1, was implemented using *Geant*4 in order to generate interaction positions (x_i, y_i, z_i) and energies E_i, which were used in the high-flux simulations, *Agostinelli et al.* (2003) and *Rodrigues and He* (2010). Table3.1 lists the names, the materials, the construction methods and the main dimensions of the objects used in these simulations.

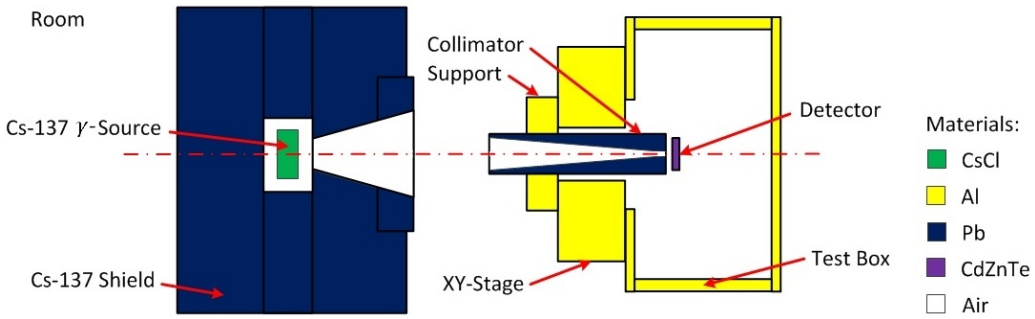

Figure 3.1: Objects modeled in *Geant*4 to simulate the experimental apparatus used in the high-flux experiment (E_γ=662 keV).

Object	Material	Construction in *Geant*4	Main Dimensions
Detector	CdZnTe	G4Box	$20 \times 20 \times 5$ mm^3
Test Box	Al	G4Box-G4Box-G4Tubs	$17.7 \times 17.7 \times 10$ cm^3
XY-Stage	Al	G4Box-G4Tubs	$13.9 \times 13.9 \times 4.35$ cm^3
Support	Al	G4Box-G4Tubs	$7.15 \times 7.15 \times 2.2$ cm^3
Collimator	Pb	G4Tubs-G4Cons	$\phi = 2.54$ cm, $L = 7.5$ cm
Cs-137 Shield	Pb	G4Tubs-G4Tubs-G4Cons	$\phi = 15$ cm, $L = 9.5016$ cm
Cs-137 Source	CsCl	G4Tubs	$\phi = 13.2$ mm, $L = 12.7$ mm
Room	Air	G4Box	$3 \times 3 \times 3$ m^3

Table 3.1: Main dimensions and construction properties of elements included in the Monte-Carlo model of the experimental apparatus created using *Geant*4.

Note that the column labeled *Construction in Geant*4 shows the sequence of operations used to create each object, while the column labeled *Main Dimensions* shows

the overall dimensions of each object.

3.1.1 *Geant4* Interaction Positions and Energies

Initial γ-ray and the secondary particle interactions are created in the detector by *Geant4*. The physical processes considered in the model include pair production, Compton scattering, and photoelectric effect for γ-rays and multiple scattering and ionization for electrons. An energy cutoff was used to improve the code performance, not tracking particles with a kinetic energy lower than this limit, assuming they deposited their energy locally. Interaction positions (x_i, y_i, z_i) and energies E_i were generated using the Monte-Carlo model of the experimental apparatus described in Sec.*3.1*. These were stored in files in list mode, which were then used as an input parameter to the charge transport code. Additionally, using the *GetTrackID()* function provided in *Geant4*, when an event interacted in the detector volume by Compton or photoelectric effects, primary tracks were recorded having $ID = 1$, while secondary tracks were recorded having $ID > 1$. The variable ID was used as a *flag* to track secondary electron ramifications originating from the same primary event, thus identifying events originating from the same charge cloud. The use of a Monte-Carlo code to generate initial interaction positions has been reported by other researchers, *Benoit and Hamel* (2009), *Picone et al.* (2003), *Alirol et al.* (2009) and *Sempau et al.* (1997).

3.1.2 Simulated Average Time Between Events vs. Irradiation Flux

Interactions described in *Sec.3.1.1* were injected into the simulated detector volume at different rates, in order to simulate different photon radiation fluxes. Then, it was required to calculate the relationship between the average time between interactions and the incident flux at the surface of the detector. During high-flux irradiation, it is possible that multiple interactions occur in the detector volume within

a time frame shorter than the time required to drift these charges to their respective collecting electrodes. Simulated and measured spectra were used to calculate the relationship between the average time between interactions and the irradiation flux. The incident flux Φ at the surface of the detector was considered to be inversely proportional to the average time between interactions, as described by Equation 3.1,

$$\Phi = \frac{C}{\bar{t}} \tag{3.1}$$

then, reducing by half the average time between interactions increases by a factor of two the incident flux Φ.

Measurement of the constant of proportionality C was hindered by factors such as multiple scatters from all materials surrounding the detector not being included in the Monte-Carlo model, imperfect alignment between source and detector, unknown source geometry and other factors. Table 3.2 summarizes results used to calculate the value of the constant of proportionality C. The column labeled *Incident Flux* Φ was simulated considering the geometry described in *Sec.3.1* and the known source activity, while the column labeled *Total Count Rate* r was measured in the high-flux experiments operating the detector at -1000 V cathode bias. It can be observed that non-proportional values of C were calculated for incident fluxes Φ higher than $\sim$ 45 570 photons/pixel/s. Then, considering the first four results presented in Table

Simulated Flux (photons/pixel/s)	Measured Total Count Rate (photons/s)	T_{avg} (ns)	C (photons/pixel)
22 125	3580	279 280	6.18
27 315	4510	221 880	6.06
34 810	5850	170 940	5.95
45 570	7700	129 870	5.92
62 950	12610	79 310	4.99
92 495	20160	49 600	4.59
144 990	43730	22 870	3.32

Table 3.2: Average time between interactions as a function of incident photon flux Φ at the surface of the detector.

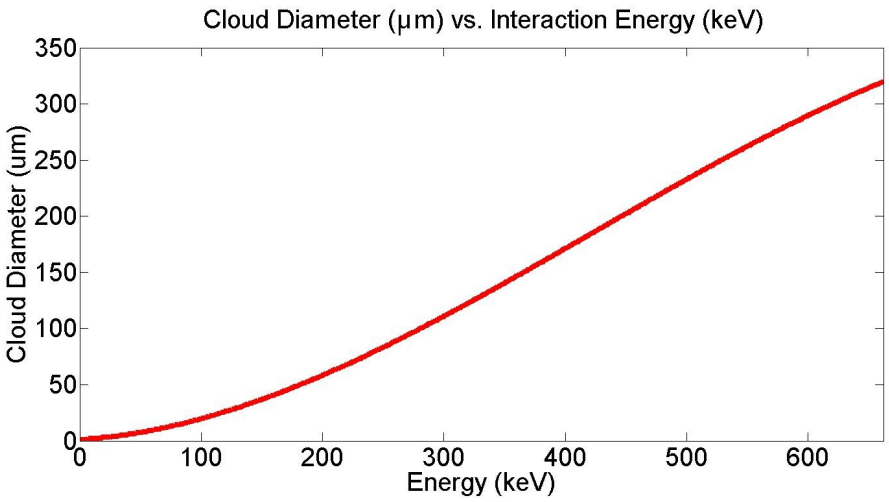

Figure 3.2: Simulated cloud diameters using *Geant*4, showing the averaged maximum distances between electrons in μm as a function of energy in keV.

3.2, the estimated value of the constant of proportionality C was 6.0. For example, injecting events in simulations every 100, 200 and 300 ns corresponds to incident photon fluxes $\Phi = 6 \times 10^7$, 3×10^7, 2×10^7 photons/pixel/s, respectively.

3.1.3 Charge Cloud Diameter vs. Photon Energy

Interactions positions (x_i, y_i, z_i) and energies E_i generated using the Monte-Carlo method described in Sec.3.1.1 are injected into the simulation assuming that each interaction creates a homogeneous and spherical charge cloud. In CdZnTe, the number of electrons and holes created is calculated assuming the average value for the radiation-ionization energy $\epsilon = 4.64$ eV, *Endicott* (2011). Distribution of electrons in a cloud as a function of interaction energy was simulated in *Geant*4 for all energies of interest using the *GetTrackID* function described in *Sec.3.1.1.* For every interaction, the maximum distance between electrons was calculated and recorded within 1 keV energy bin separation. Then, the average value of the distances was calculated considering all events simulated. Results shown in Figure 3.2 were calculated using a total of $\sim$ 820 000 interactions. The relationship between electron cloud diameter $\emptyset$ and energy of interaction E was approximated by a third order degree polynomial

having coefficients $\alpha = -1.042 \times 10^{-9}$ keV^{-3}, $\beta = 1.32 \times 10^{-6}$ keV^{-2}, $\gamma = 6.416 \times 10^{-5}$ keV^{-1}, and constant term $C = 5.118 \times 10^{-4}$, thus $\emptyset(E) = \alpha \cdot E^3 + \beta \cdot E^2 + \gamma \cdot E + C$, with energy E given in keV units and $\emptyset$ in mm.

Initially, electrons are injected as free charge in excess of equilibrium in the conduction band (into *mape*), while holes are injected as free charge in excess of equilibrium in the valence band (into *maph*). These two clouds are assumed to be identical in shape and density of charges when they are created. In current simulations no charge recombination is considered. In each interaction, charges are uniformly distributed inside the cloud. Since the 3D axisymmetric model described in *Sec.3.2.1* requires a 2D rather than a 3D mesh, this idealized cloud needs to be transformed from its original 3D shape, having uniform charge distribution, into a 2D shape with non-uniform charge distribution. The shape of these 2D clouds and their respective charge distribution varies as a function of cloud size and radial distance from the axis of symmetry. In order to illustrate this idea, the projection of a 3D spherical cloud of a 662 keV interaction at 350 μm from the axis of symmetry is shown in Figure 3.3. Results shown in Figures 3.3 and 3.4 are normalized.

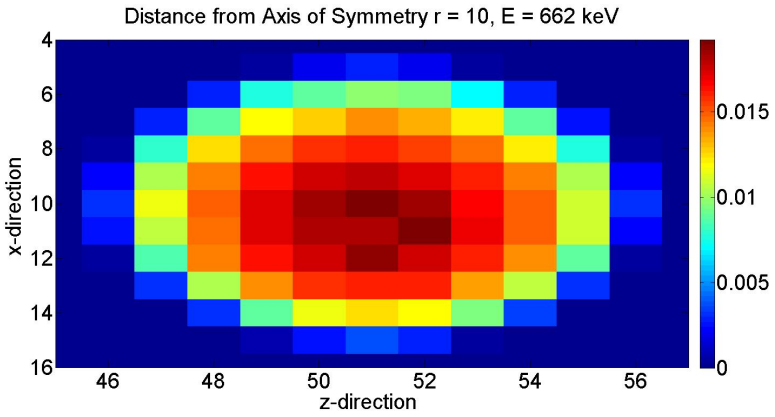

Figure 3.3: Normalized cloud distribution considering an interaction of 662 keV at 350 μm from the axis of symmetry.

Then, knowing the interaction positions (x_i, y_i, z_i) and energies E_i, the shape of the charge cloud is determined using the superposition of the smaller clouds, each

determined by its relative position with respect to the axis of symmetry and deposited energy. An event having multiple interactions, such as the example shown in Figure 3.4, which has two interactions, with 277 and 200 keV at ~ 1.7 mm from the axis of symmetry can be easily added to the simulation.

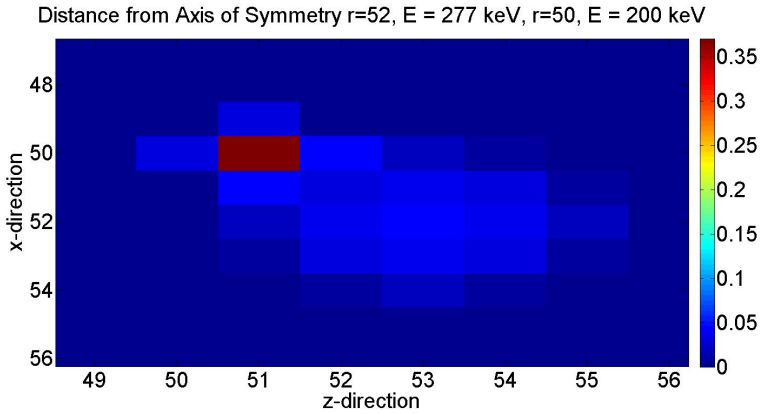

Figure 3.4: Normalized cloud distribution considering two interaction close to each other with of 277 and 200 keV at ~ 1.7 mm from the axis of symmetry.

3.2 Charge Continuity Coupled with Poisson's Equations

Results presented in *Sec.3.1* briefly described the Monte-Carlo methods used to generate initial interaction positions and energies. Also, using Monte-Carlo methods combined with experimental results, the relationship between the average time between interactions and the incident flux at the surface of the detector was calculated. The size and distribution of charges in a cloud as a function of interaction energy and distance from the axis of symmetry were also calculated.

Now, we need to describe the model used to simulate the transport of charges under high-flux irradiation. Charge drift calculations were carried out by numerically solving the charge continuity equations with multiple electron and hole defect levels coupled with Poisson's equation, Equations 3.2-3.9, *Prettyman* (1998), *Durst et al.* (2008), *Ruat et al.* (2007), *Picone et al.* (2003), *Kolobov* (2003) and *Sze* (1981). This model considered one defect level for electrons and two for holes based on measure-

ments of electrons-only and holes-only induced signals, which will be described in more detail in Chapter IV.

$$\frac{\partial n_e}{\partial t} + \nabla \cdot (n_e \mu_e \nabla \phi) - \nabla \cdot (D_e \nabla n_e) = -\frac{1}{\tau_{eT}} n_e + \frac{1}{\tau_{eD}} \tilde{n}_{e1} + \delta_e \tag{3.2}$$

$$\frac{\partial \tilde{n}_{e1}}{\partial t} = \frac{1}{\tau_{eT}} n_e - \frac{1}{\tau_{eD}} \tilde{n}_{e1} \tag{3.3}$$

$$\frac{\partial n_h}{\partial t} + \nabla \cdot (n_h \mu_h \nabla \phi) - \nabla \cdot (D_h \nabla n_h) = -\frac{1}{\tau_{hT1}} n_h - \frac{1}{\tau_{hT2}} n_h + \frac{1}{\tau_{hD1}} \tilde{n}_{h1} + \frac{1}{\tau_{hD2}} \tilde{n}_{h2} + \delta_h \tag{3.4}$$

$$\frac{\partial \tilde{n}_{h1}}{\partial t} = \frac{1}{\tau_{hT1}} n_h - \frac{1}{\tau_{hD1}} \tilde{n}_{h1} \tag{3.5}$$

$$\frac{\partial \tilde{n}_{h2}}{\partial t} = \frac{1}{\tau_{hT2}} n_h - \frac{1}{\tau_{hD2}} \tilde{n}_{h2} \tag{3.6}$$

$$\nabla^2 \phi = -k \frac{q}{\epsilon_0} (n_e + \tilde{n}_{e1} + n_h + \tilde{n}_{h1} + \tilde{n}_{h2}) \tag{3.7}$$

$$E = -\nabla \phi \tag{3.8}$$

$$D_{e,h} = \mu_{e,h} \frac{kT}{e} \tag{3.9}$$

where,

e, h: electrons and holes

$n_{e,h}$: free e-h concentration in excess of equilibrium

$\tilde{n}_{e1}$: trapped e concentration in excess of equilibrium (shallow defect level)

$\tilde{n}_{h1,2}$: trapped h concentration in excess of equilibrium (shallow/deep defect level)

τ_{eT}: e trapping lifetime (shallow defect level)

τ_{eD}: e detrapping lifetime (shallow defect level)

$\tau_{hT1,2}$: h trapping lifetime (shallow/deep defect level)

$\tau_{hD1,2}$: h detrapping lifetime (shallow/deep defect level)

$\mu_{e,h}$: free e-h mobilities

$D_{e,h}$: e-h diffusion coefficients

$\delta_{e,h}$: e-h source terms

Equations 3.2−3.6 represent electron and hole charge continuity equations, considering the defect energy level diagram shown in Figure 3.5, while Equations 3.7 and 3.8 represent the Poisson's equation including space charge and Equation 3.9 represents the diffusion coefficient.

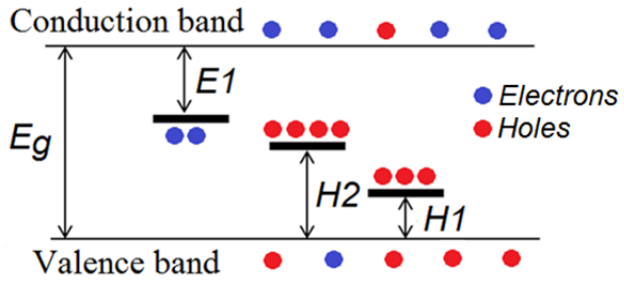

Figure 3.5: Defect energy level diagram in CdZnTe (E_g ∼1.6 eV), showing one-electron trapping center E_1 and two-hole trapping centers H_1 and H_2, where H_1 represents a shallow defect level and H_2 a deep defect level.

The system described by Equations 3.2-3.9 is numerically solved by discretizing the detector into finite regions (meshes) while drifting free charges in finite steps, linearizing the solution in each step. Charges are tracked in each finite region in all maps of charges, one for each type of charge modeled: $n_e, \tilde{n}_{e1}, n_h, \tilde{n}_{h1}$ and $\tilde{n}_{h2}$. Free charges n_e and n_h move in each step, while at the same time the balance between free and trapped charges is calculated in every position of the mesh: between free and trapped electrons (n_e and $\tilde{n}_{e1}$) and free and trapped holes (n_h and $\tilde{n}_{h1}, \tilde{n}_{h2}$).

3.2.1 3D Axisymmetric Model

Initially, a complete 3D simulation was developed considering each interaction cloud as a point, reason why it was referred to as *Point-Cloud Model*. In this model initial interaction positions were generated by *Geant*4 using the Monte-Carlo method. The operating electric field and potentials used in this simulation were calculated using the Finite Element Method (FEM), while electric field perturbations due to space charge were calculated using the method of images (or mirror images). The entire calculation was carried out for a large number of interaction positions in the detector volume in each simulation step, depending on the number of clouds considered in each time step, considering the net field due to both space charge and external applied voltages. A large number of finite volumes (136 803 300 cubes) were used to simulate the detector in these simulations. The size of the problem limited the performance of the simulation, which degraded significantly as the number of accumulated space charge increased as a function of irradiation time. The complete 3D simulation approach was limited in terms of equivalent real-time simulation, since it was only able to simulate the problem on a μs time scale. Also, using this approach it was difficult (or even impossible) to implement important physical processes in the simulation code, such as charge diffusion, charge trapping and detrapping. An improvement in the performance of the simulation of at least two orders of magnitude was required to study the transient behavior of the polarization effect on a longer time scale, which was $\sim$ms time scale. In order to achieve this goal, the complete 3D model was converted into a 3D axisymmetric model. The same approach is commonly used to solve other problems, such as using the Finite Element method to reduce the size of the problem in structural, heat and fluid dynamics problems, *Takekida and Nanbu* (2004).

In order to use the 3D axisymmetric model, high-flux experiments required an additional collimator, described in more detail in Chapter V. Monte-Carlo generated

3D interaction positions (x_i, y_i, z_i) were converted into equivalent 3D axisymmetric interaction positions (r_i, z_i), where the electric field due to the original charge Q_i with energy E_i was calculated assuming that this new interaction had equal probability of occurring at any point at a fixed distance r_i from the axis of symmetry, *the center of the photon beam*. This new charge Q_i was considered to be uniformly distributed around the axis of symmetry, forming a ring of charges, as shown in Figure 3.6,

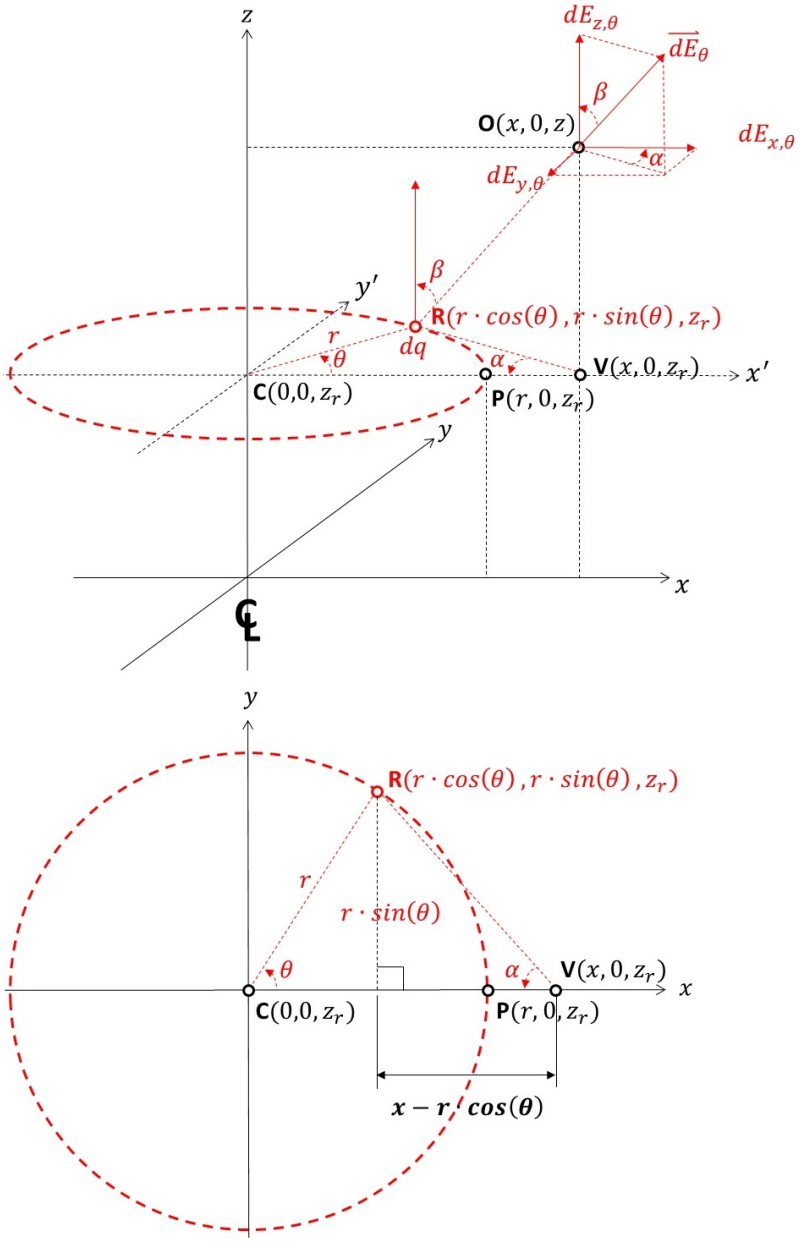

Figure 3.6: Space-charge model, considering equal probabilities of having an interaction around the axis of symmetry.

where,

r: distance from the center of the photon beam (z-axis) measured in the xy-plane, where $r = \sqrt{x^2 + y^2}$

θ: angle around the axis of symmetry, angle of integration, covering all infinitesimal charges $dq = \rho \cdot r d\theta$ lying in the uniform ring of charges

$R(r \cdot cos(\theta), r \cdot sin(\theta), z_r)$: position of an infinitesimal charge dq as a function of θ

$P(r, 0, z_r)$: point of intersection between the uniform unitary ring of charges and the xz-plane

$O(x, 0, z)$: point where the electric field due to an uniform unitary ring of charges is calculated in the xz-plane (the component in the y-direction is not computed, due to the symmetry)

$V(x, 0, z_r)$: point determined by the projection of point O on vector $\overrightarrow{CP}$

α: angle determined by the intersection between vectors $\overrightarrow{CP}$ and $\overrightarrow{VR}$

β: angle between vector $\overrightarrow{RO}$ and the z-axis

$\overrightarrow{dE_\theta} = (dE_{x,\theta}, dE_{y,\theta}, dE_{z,\theta})$: electric field evaluated at position O due to an infinitesimal charge dq at position R

Using the notation described in Figure 3.6, the magnitude of the electric field vector $\overrightarrow{dE_\theta}$ and its components in all xyz-directions were calculated, assuming given positions $P(r, 0, z_r)$ and $O(x, 0, z)$, since

$$|\overrightarrow{dE_\theta}| = \frac{1}{4\pi\varepsilon} \cdot \frac{\rho \cdot r d\theta}{|\overrightarrow{RO}|^2} \tag{3.10}$$

where,

$\varepsilon = \varepsilon_r \varepsilon_0$: linear permittivity of CdZnTe, considering it as a homogeneous material, relative to that of free space, and $\varepsilon_r \sim 10$ and $\varepsilon_r = 8.854 \times 10^{-12}$ F·m^{-1}

Then, using Equation 3.10 and Figure 3.6,

$$\begin{aligned} dE_{x,\theta} = |\overrightarrow{dE_\theta}| \cdot sin(\beta) \cdot cos(\alpha) = \\ \frac{1}{4\pi\varepsilon} \cdot \frac{\rho \cdot r d\theta}{|\overrightarrow{RO}|^2} \cdot sin(\beta) \cdot cos(\alpha) \end{aligned} \tag{3.11}$$

$$dE_{y,\theta} = |\overrightarrow{dE_\theta}| \cdot sin(\beta) \cdot sin(\alpha) = \frac{1}{4\pi\varepsilon} \cdot \frac{\rho \cdot r d\theta}{|\overrightarrow{RO}|^2} \cdot sin(\beta) \cdot sin(\alpha) \tag{3.12}$$

$$dE_{z,\theta} = |\overrightarrow{dE_\theta}| \cdot cos(\beta) = \frac{1}{4\pi\varepsilon} \cdot \frac{\rho \cdot r d\theta}{|\overrightarrow{RO}|^2} \cdot cos(\beta) \tag{3.13}$$

Then, knowing that the E_y component must be zero, the solution to Equations 3.11-3.13 is given by Equations 3.14-3.16,

$$dE_{x,\theta} = \frac{\rho r}{4\pi\varepsilon} \cdot \frac{a \cdot d\theta}{(a^2 + b^2 + c^2)^{\frac{3}{2}}} \tag{3.14}$$

$$dE_y y, \theta = dE_{y,-\theta} \tag{3.15}$$

$$dE_{z,\theta} = \frac{\rho r}{4\pi\varepsilon} \cdot \frac{c \cdot d\theta}{(a^2 + b^2 + c^2)^{\frac{3}{2}}} \tag{3.16}$$

where, the relations described by Equations 3.17-3.24 from Figure 3.6 were used:

$$\overrightarrow{RO} = \overrightarrow{O} - \overrightarrow{R} = (x - r \cdot cos(\theta), -r \cdot sin(\theta), z - z_r) \tag{3.17}$$

$$a = x - r \cdot cos(\theta) \tag{3.18}$$

$$b = -r \cdot sin(\theta) \tag{3.19}$$

$$c = z - z_r \tag{3.20}$$

$$|\overrightarrow{RO}|^2 = a^2 + b^2 + c^2 \tag{3.21}$$

$$cos(\beta) = \frac{z - z_r}{|\overrightarrow{RO}|} = \frac{c}{\sqrt{a^2 + b^2 + c^2}} \tag{3.22}$$

$$sin(\beta) = \frac{\sqrt{a^2 + b^2}}{\sqrt{a^2 + b^2 + c^2}} \tag{3.23}$$

$$cos(\alpha) = \frac{a}{\sqrt{a^2 + b^2}} \tag{3.24}$$

The values of E_x and E_z were evaluated integrating $dE_{x,\theta}$ and $dE_{z,\theta}$ from $\theta = 0 \ldots 2\pi$ and pre-calculated for every position of the ring and all positions in the axisymmetric plane.

3.2.2 The Mirror-Charge Method

Since the field due to a ring of space charges uniformly distributed needed to be evaluated in a finite detector volume having cathode and anode electrodes rather than in an infinite medium, as predicted by the above equations, the method of mirror images was used to include the effect of the boundary electrodes, *Pumplin* (1969). Using this method, the detector was assumed to be finite in the Z-direction, constrained by the cathode and anode planes, although it was assumed to be infinite in the XY-plane directions. This was not a bad assumption, considering that in high-flux experiments the beam was collimated around a central pixel and the diameter of beam was kept much smaller than the detector's dimensions in the XY-plane.

The method of mirror charges requires a large number of mirror charges to calculate the electric field with low uncertainty near the electrode surfaces. Then, the number of mirror charges used was determined by establishing a compromise between precision and required time to compute all fields in all positions. In our calculations, a 0.5 % uncertainty in the value of the calculated electric field near the electrodes was considered. This level of precision required the use of 20 mirror charges in each direction. Figure 3.7 shows the first two mirror charges (or rings of charges, in this case) relative to both electrodes.

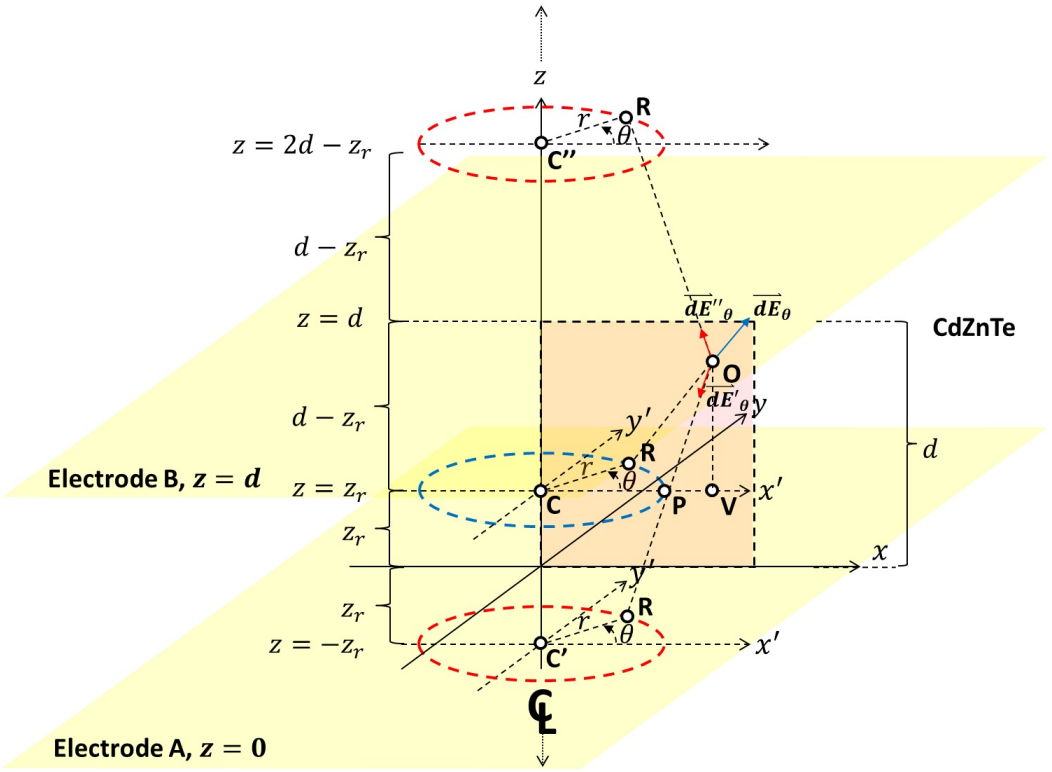

Figure 3.7: Mirror-charge method applied to the unitary ring of charges, showing the first two mirror charges relative to the electrodes.

3.3 3D Axisymmetric Model Implementation Process

A simplified fluxogram of the simulation process is presented in Figure 3.8, where the different colors represent similar functionalities within the simulation code. The solution implemented to speed-up the computational process was to store in memory values that are used multiple times during the simulation and execute independent processes in parallel using the Qt C++ environment. The simulation starts by reading all pre-calculated parameters originally stored in files, i.e. space charge electric field used in the 3D axisymmetric model, as well as other variables, and storing them in memory.

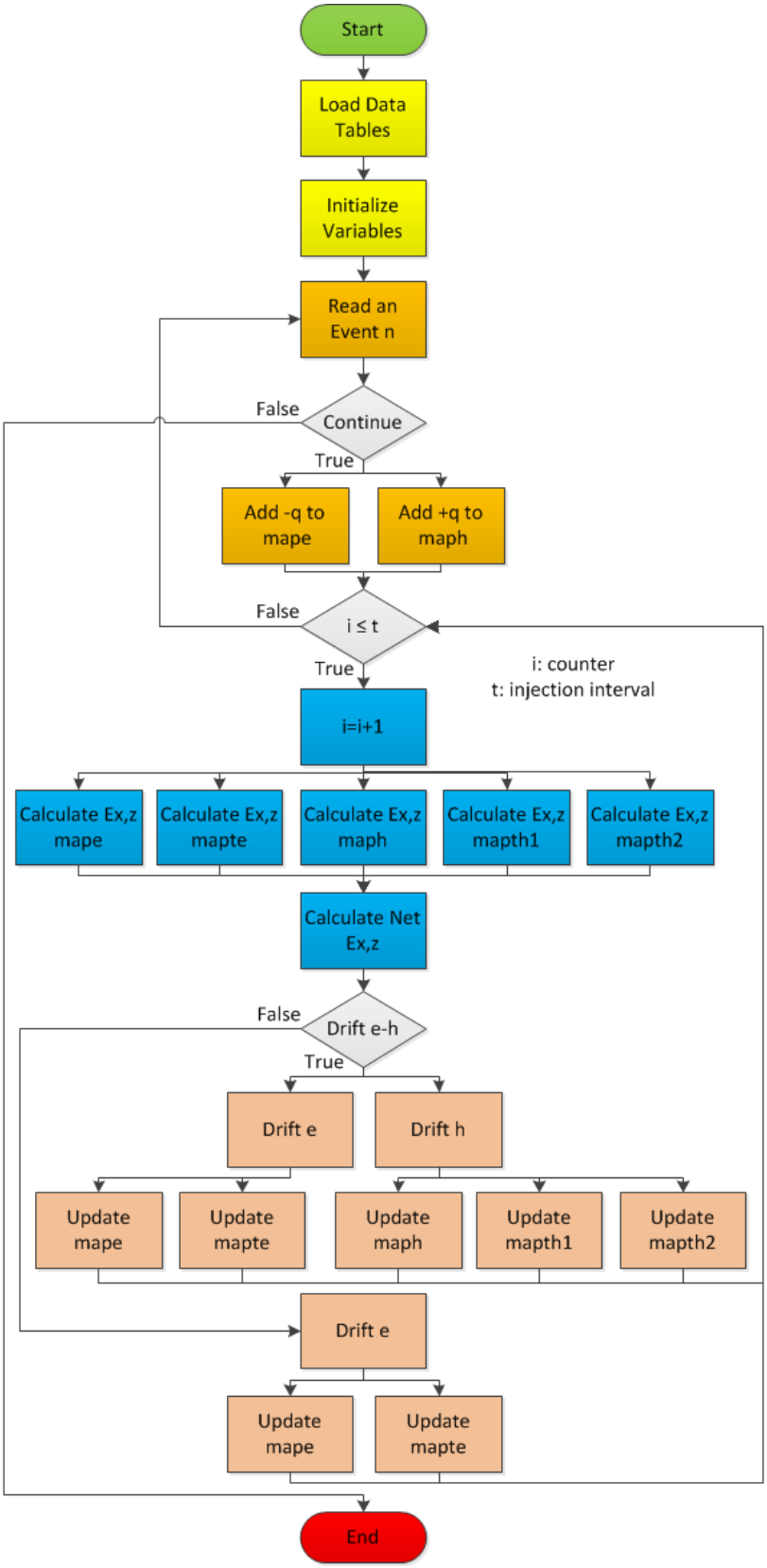

Figure 3.8: Simulation fluxogram, showing with same color parts of the code with similar functionalities.

Since the space charge electric field changes dynamically, depending on the spatial distribution of charges in the simulated region after each time step, pre-computing these field values and storing them in memory considerably reduced the required computational time. Densities of electrons and holes were modeled according to the energy level diagram shown in Figure 3.5. Then, five maps of charges were used to keep track of free and trapped electrons and holes in all different trapping centers in all simulated volume:

mape: map of free electrons in excess of equilibrium in the conduction band

mapte: map of trapped electrons in defect level E_1

maph: map of free holes in excess of equilibrium in the valence band

*mapth*1: map of trapped holes in defect level H_1

*mapth*2: map of trapped holes in defect level H_2

In the beginning of each simulation, all charge maps are initialized having with no space charge. During the simulation, these maps are continuously populated and depopulated with charges according to the physical processes described by Equations 3.2-3.9. Additionally, as described in Figure 3.8, changing the value of t enables the injection of charges at different rates, thus simulating different irradiation fluxes. Also, in order to speed up the simulation, electrons drift in every simulation step while holes drift in every multiple number of steps.

3.3.1 The Size of the Mesh

The size of the mesh was chosen based on a compromise between precision, required memory to store pre-calculated values, current computers processing speed, and available time to calculate pre-calculate electric field values due to space charge. Considering the time required to compute all pre-calculated electric field values, memory size available and precision, the size of the mesh was chosen to be 34.6×34.6 μm^2, which is equivalent to $\sim 1/10^{th}$ of the size of a charge cloud generated by a

662 keV gamma-ray in CdZnTe. Using the selected mesh size, a 100×144 grid was used to discretize the region around the axis of symmetry in the X- and Z-directions, covering a central pixel and a neighbor pixel, as shown in Figure3.9.

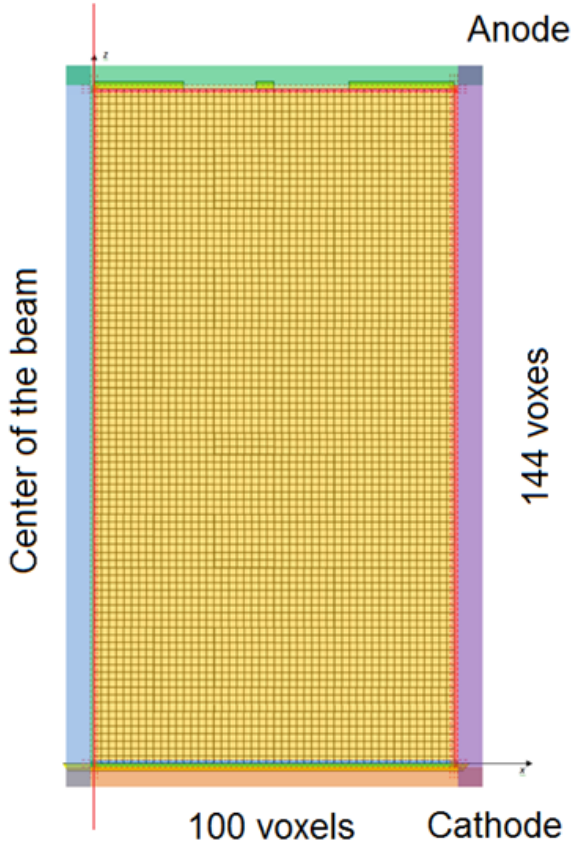

Figure 3.9: Simulated axisymmetric region, showing the central bulk region and boundary regions in different colors.

The simulated region was represented by 14400 voxels, which required $\sim 207 \times 10^6$ electric field values in the X-direction and $\sim 207 \times 10^6$ electric field values in the Z-direction to be pre-calculated and stored in memory. Using this mesh size and considering each value as a float number (4 bytes each), $\sim$ 3 GB of memory space was required. In fact, only $\sim$ 1.5 GB of memory space was needed, since using the axisymmetric model combined with the method of mirror charges, only 1/2 of the total region, i.e., either below or above the mid-plane between cathode and anode, needed to be pre-calculated to represent the entire region.

3.3.2 Operating Field and Weighting Potential

Operating electric field and weighting potential for the two anode electrodes and the cathode were calculated using the software Maxwell 3D, using the Finite Element electromagnetic simulation package. Results for the calculated electric field are shown in Figure 3.10.

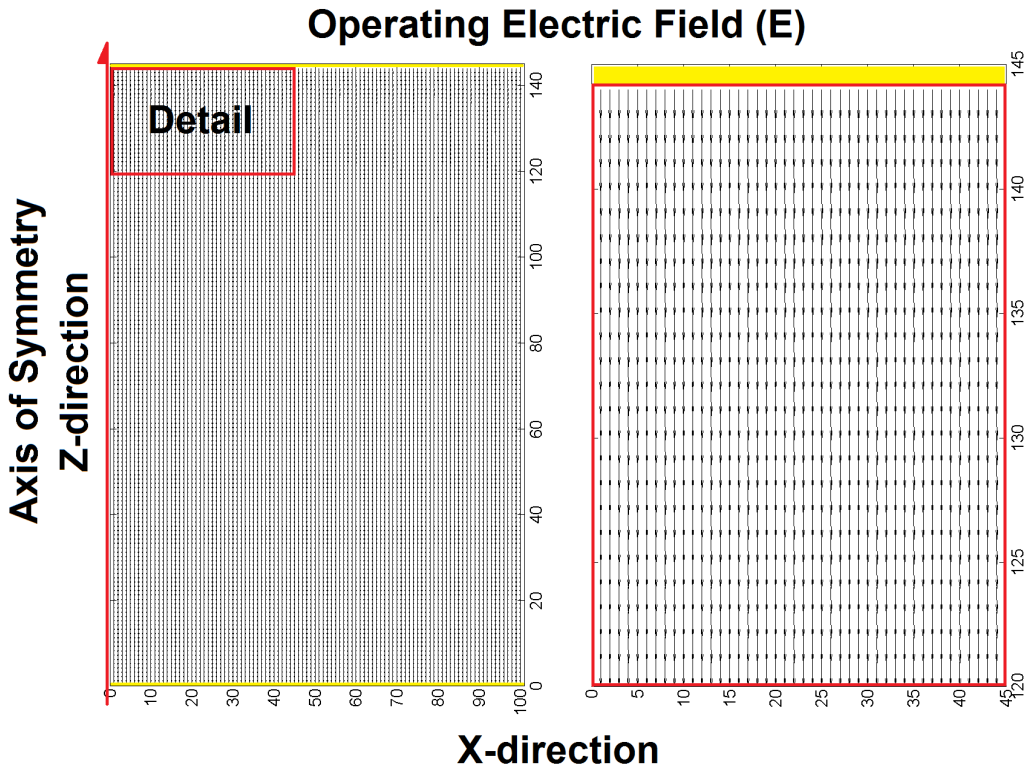

Figure 3.10: Simulated operating electric field using the Maxwell 3D software.

In all simulation, it was considered that -1000 V bias voltage was applied to the cathode electrode. Results showing the weighting potentials for the three electrodes considered in this simulation are shown in Figure 3.11. These values were saved in files and stored in the computer memory in the beginning of each simulation execution. These values were needed to calculate the drift of charges and signals induced on electrodes, *He* (2001), *Ramo* (1939), *Rodrigues et al.* (2009), *Rodrigues and He* (2010), *Kurokawa et al.* (2003), *Moon et al.* (2004), *Samedov* (2007), *Hamel and Julien* (2008),

Kreisler et al. (2008) and *Ettenauer* (2008). Due to the complexity of the pixelated electrode design, no closed-form analytical solution can be found to the 3D system of Equations 3.2-3.9, *Kavadias et al.* (1994), *He* (1995), *Castoldi and Gatti* (1996), *Castoldi et al.* (1996), *Valero et al.* (1999), *Bale et al.* (2002) and *Bale and Szeles* (2009).

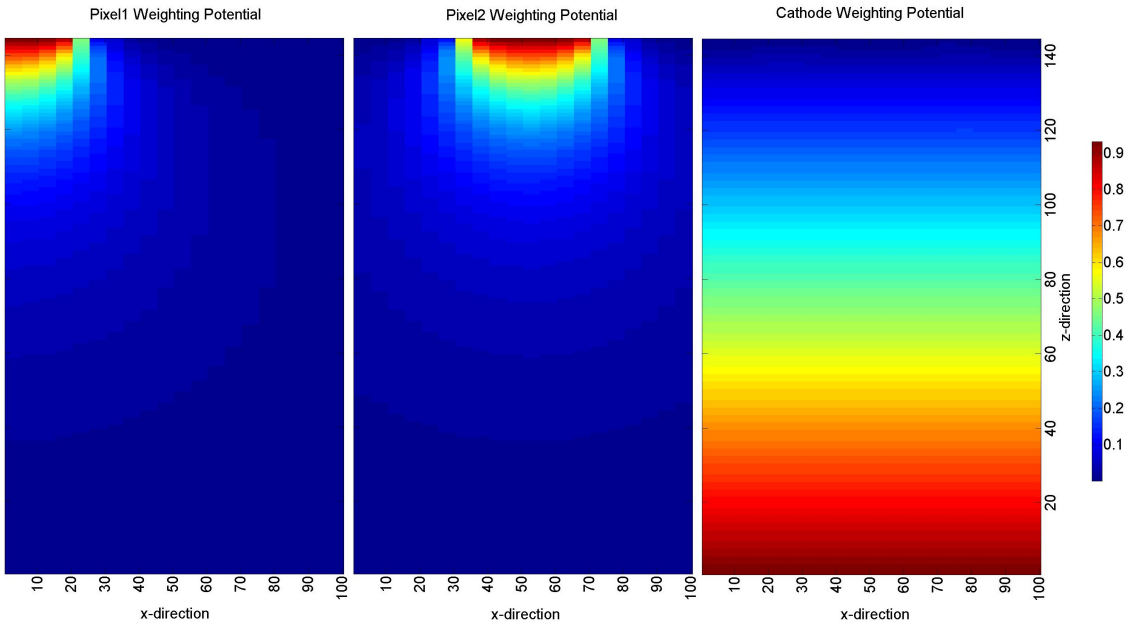

Figure 3.11: Simulated weighting potential for three electrodes: pixel1, pixel2 and cathode.

3.3.3 Space-Charge Field

Electric field due to a ring of charges around the axis of symmetry intercepting the plane of symmetry at any position (i, j), for $i = 1 \ldots 100 and j = 1 \ldots 144$, was pre-calculated at every position (l, m), for $l = 1 \ldots 100 and m = 1 \ldots 144$. Then, for each position (i, j), the electric field in the X- and Z-directions were calculated for all other positions (l, m). Figure 3.12 shows, as an example, results calculated for two positions of the ring of charges, (i, j)=$(10, 10)$ and $(50, 72)$. In total, the values of the electric field in the X- and Z-directions were calculated 14 400 times for 14

400 different positions. This bigger task was sub-divided into smaller tasks due to the excessive time needed to pre-calculate these field values. The smaller tasks, or jobs, were submitted to several computers using the Center for Advanced Computing (CAC) cluster Flux in the College of Engineering at the University of Michigan.

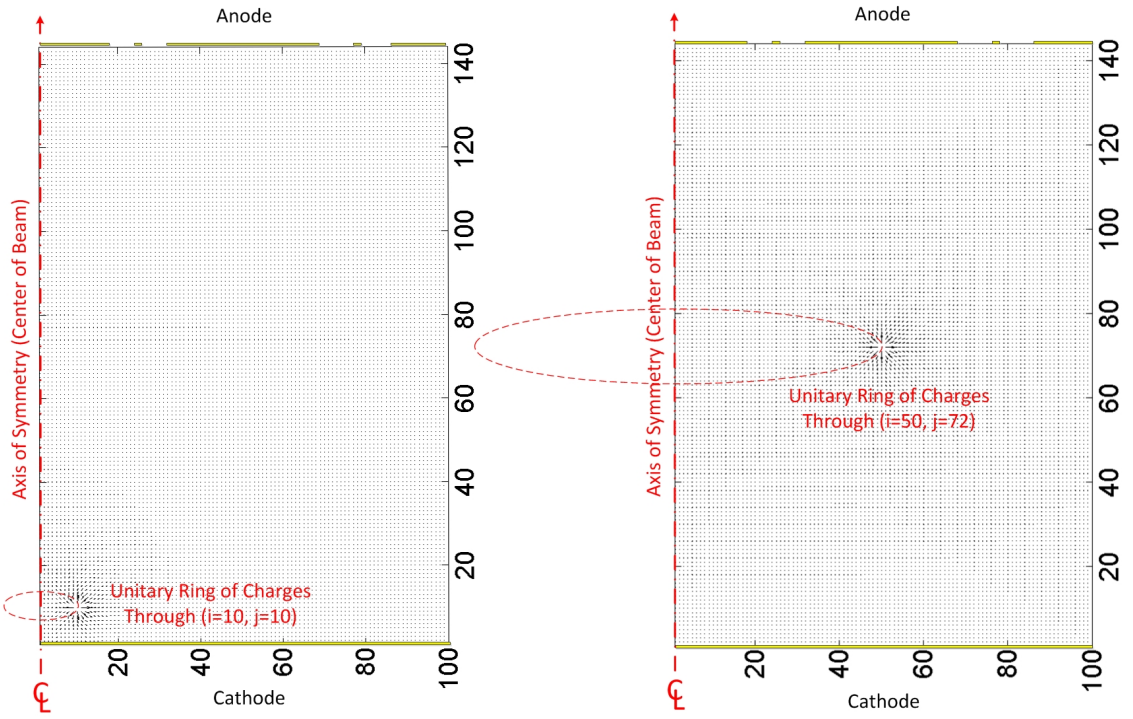

Figure 3.12: Space-charge electric field calculated in two distinct ring positions, (i, j)=$(10, 10)$ and $(50, 72)$.

3.3.4 Charge Drift, Boundary Conditions and Signal Induction

Although a cross-section of the detector surface with 100×144 meshes was modeled, the actual simulated region of the detector considered a surface with $\sim 200 \times 144$ meshes. This was required to take into account all possible cases, for example when a charge contained inside the 100×144 region drifts across the axis of symmetry. The reason why it is necessary to consider both planes (with positive and negative i indexes), is related with the fact that any charge Q in the 100×144 region can potentially move to any other position in the positive and negative planes in a single

step. Then, each mesh position (i, j) initially contained a charge $Q_{i,j}$ at time t, that after a small step Δ_t is drifted to another position according to the *net electric field*. In this simulation, it is assumed that all the charge $Q_{i,j}$ contained in the original mesh position drift according to the net electric field evaluated at the center of the original mesh. It is assumed that the original charge $Q_{i,j}$ does not rotate while moving from one position to the next. The step size Δ_t used in these simulations was 5 ns. Smaller step sizes required longer simulation time while larger steps were not sufficient to describe the physics of the problem due to lack of sampling points. In experiments, the sampling rate used was 25 MHz, which corresponded to digitizing the signals induced at every 40 ns. In order to speed up calculations, a sub-routine was implemented to skip meshes that contained less charge $Q_{i,j}$ than a threshold value $Q_{min} \equiv 1$ eV.

The amount of charges trapped and detrapped in each step was calculated using Equations 3.25-3.27,

$$Q'_{ehT} = Q_{ehT} \tag{3.25}$$

$$Q_{ehT} = Q'_{ehT} + Q_{eh} \cdot (1 - P_{(eh,T)}) - Q'_{ehT} \cdot (1 - P_{(eh,D)}) \tag{3.26}$$

$$Q_{eh} = Q_{eh} - Q_{eh} \cdot (1 - P_{(eh,T)}) + Q'_{ehT} \cdot (1 - P_{(eh,D)}) \tag{3.27}$$

where,

Q_{ehT}: e-h charge trapped in the mesh region at time t

Q'_{ehT}: e-h auxiliary variable

Q_{eh}: e-h charge in excess of equilibrium in the mesh region at time t

$P_{(eh,T)}$: probability that an e-h charge gets trapped after time Δ_t

$P_{(eh,D)}$: probability that an e-h charge gets de-trapped after time Δ_t

Then, after calculating the balance between free and trapped carriers, free charge $Q_{eh}(x, z)$ moves to a new position $Q_{eh}(x + \Delta_{x,z} + \Delta_z)$ in Δ_t. The values of $\Delta_{x,z}$ were calculated considering the value of the net electric field, as described by Equations

3.28-3.29 and Figure 3.8,

$$\Delta_x = (E_x o + E_x e + E_x h + E_x eT + E_x hT1 + E_x hT2) \cdot \mu_e \delta_t \tag{3.28}$$

$$\Delta_z = (E_z o + E_z e + E_z h + E_z eT + E_z hT1 + E_z hT2) \cdot \mu_e \delta_t \tag{3.29}$$

where,

$E_{x,z}o$: operating electric field calculated at the center of the mesh in the x- and z-directions

$E_{x,z}e$: electric field due to electrons in excess of equilibrium calculated at the center of the mesh in the x- and z-directions

$E_{x,z}h$: electric field due to holes in excess of equilibrium calculated at the center of the mesh in the x- and z-directions

$E_{x,z}eT$: electric field due to trapped electrons calculated at the center of the mesh in the x- and z-directions

$E_{x,z}hT1$: electric field due to trapped holes at shallow defect levels calculated at the center of the mesh in the x- and z-directions

$E_{x,z}hT2$: electric field due to trapped holes at deep defect levels calculated at the center of the mesh in the x- and z-directions

The relative position of the center of the charge with respect to the center of the mesh containing most of the charge was calculated as described in Figure 3.13. Values and signs of dx and dz define four possible scenarios:

I) $0 \leq dx$, $0 \leq dz$: center of charge Q is somewhere in the 1^{st} quadrant

II) $dx < 0$, $0 \leq dz$: center of charge Q is somewhere in the 2^{nd} quadrant

III) $dx < 0$, $dz < 0$: center of charge Q is somewhere in the 3^{rd} quadrant

IV) $0 \leq dx$, $dz < 0$: center of charge Q is somewhere in the 4^{th} quadrant

Figure 3.13 shows these four possible scenarios, where dx is the distance in the X-direction from the center of the new mesh (point O) to the center of the charge Q (point C) and dz is the defined in the same way, but in the Z-direction.

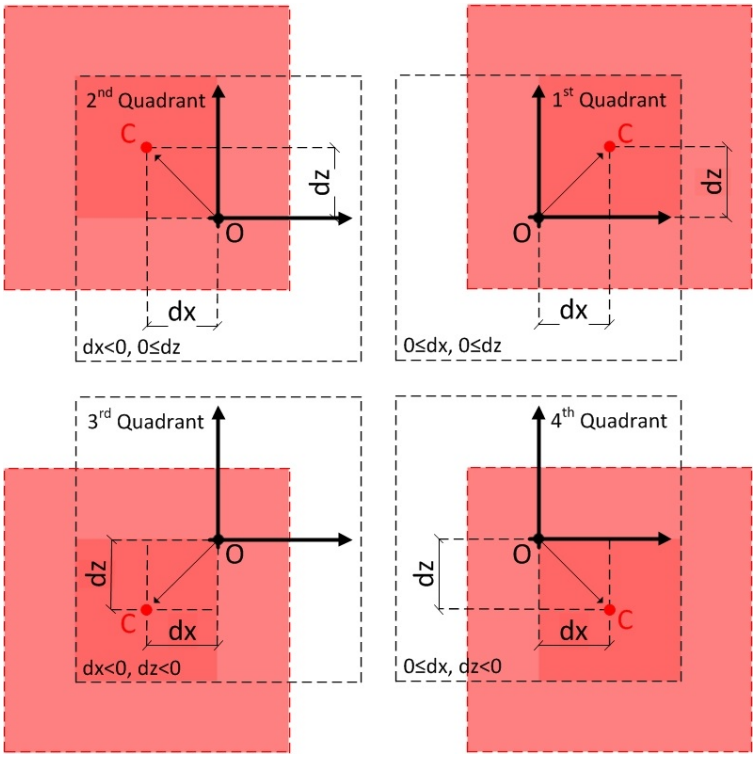

Figure 3.13: Four possible positions of the charge Q with respect to the center of the mesh.

Using these two values and knowing the indexes (i, k) of the mesh which contain the majority of the charge Q, the neighbor meshes sharing charge Q are determined. Charge Q was sub-divided into charges q_1, q_2, q_3 and q_4, which represented the charges in each of the four neighbor meshes, as described in Figure 3.14. These charges were calculated considering electron and hole predicted diffusion coefficients $D_e = 18.975$ cm^2/s and $D_h = 1.265$ cm^2/s, *Knoll* (2010). Notice that in this reference system, the indexes (i, k) were fixed while the indexes of the neighbor meshes where Q was re-distributed changed accordingly. The assumption was that charges q_1, q_2, q_3 and q_4 were uniformly re-distributed in their respective new meshes for each mesh position. Then, repeating the same procedure for all 14 400 mesh positions, a new map of

charges was re-defined after moving a small time step Δ_t. Induced signals in all electrodes considered, *pixel1*, *pixel2* and *cathode*, were calculated in every step for every charge, using the principle of superposition and applying the Shockley-Ramo Theorem,*Ramo* (1939) .

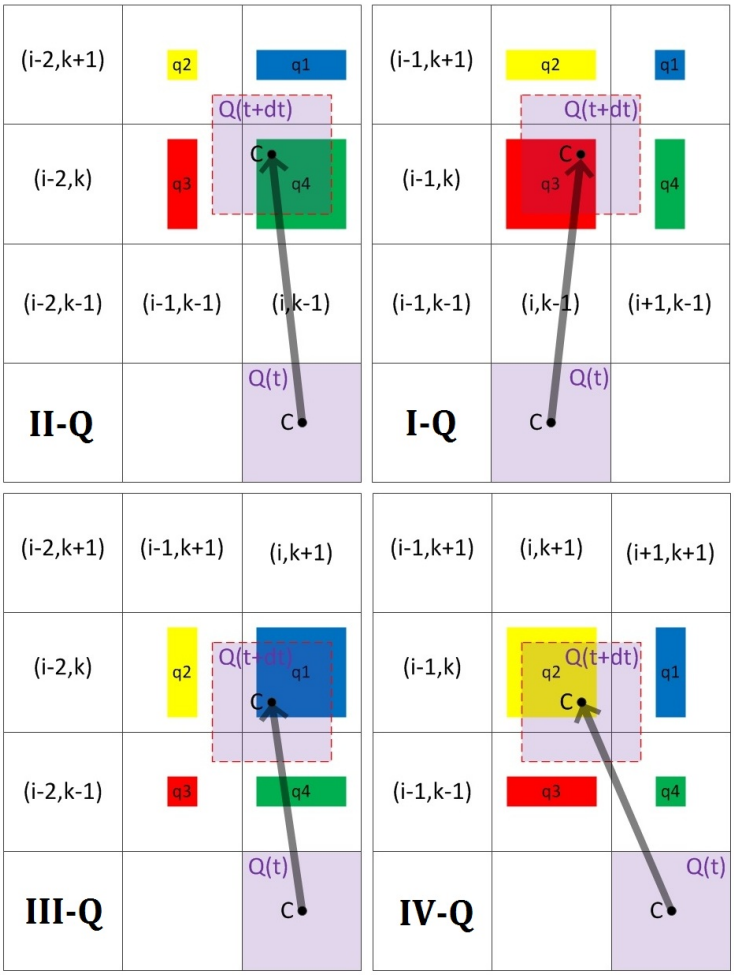

Figure 3.14: Relative positions of charges q_1, q_2, q_3 and q_4 for all four possible positions of the charge Q at $(t + dt)$ with respect to the center of the new mesh.

Figure 3.15 shows all 66 different positions for the charge Q with respect to the center of the new mesh and boundary condition, as described in Figure 3.9. Since, it would be repetitive to describe all 66 possible cases, only four cases highlighted in Fig.3.15 are explained in more detail here: cases 10, 35, 44 and 50. All other 62 cases can be easily explained by these four carefully chosen cases.

$X \rightarrow$	-98 → -82		-82 → -68		-68 → -32		-32 → -18		-18 → -0.5		-0.5 → 0		0 → 0.5		0.5 → 18		18 → 32		32 → 68		68 → 82		82 → 99.5		99.5 → 100	
Quadrants	II-Q	I-Q	II-Q	I-Q	II-Q	I-Q	II-Q	I-Q	II-Q	I-Q	II-Q	I-Q	II-Q	I-Q	II-Q	I-Q	II-Q	I-Q	II-Q	I-Q	II-Q	I-Q	II-Q	I-Q	II-Q	I-Q
	III-Q	IV-Q	III-Q	IV-Q	III-Q	IV-Q	III-Q	IV-Q	III-Q	IV-Q	III-Q	IV-Q	III-Q	IV-Q	III-Q	IV-Q	III-Q	IV-Q	III-Q	IV-Q	III-Q	IV-Q	III-Q	IV-Q	III-Q	IV-Q
144 → 144.5	-	-	-	-	-	-	-	-	-	-	-	-	-	-	-	-	-	-	-	-	-	-	-	-	-	-
	1	7	13	15	17	19	13	15	21	23	-	25	31	-	37	43	49	51	53	55	49	51	57	59	-	61
143.5 → 144	2	8	14	16	18	20	14	16	22	24	-	26	32	-	38	44	50	52	54	56	50	52	58	60	-	62
	-	-	-	-	-	-	-	-	-	-	-	-	-	-	-	-	-	-	-	-	-	-	-	-	-	-
0.5 → 143.5	3	9	3	9	3	9	3	9	3	9	-	27	33	-	39	45	39	45	39	45	39	45	39	45	-	63
	4	10	4	10	4	10	4	10	4	10	-	28	34	-	40	46	40	46	40	46	40	46	40	46	-	64
0 → 0.5	-	-	-	-	-	-	-	-	-	-	-	-	-	-	-	-	-	-	-	-	-	-	-	-	-	-
	5	11	5	11	5	11	5	11	5	11	-	29	35	-	41	47	41	47	41	47	41	47	41	47	-	65
-0.5 → 0	6	12	6	12	6	12	6	12	6	12	-	30	36	-	42	48	42	48	42	48	42	48	42	48	-	66
	-	-	-	-	-	-	-	-	-	-	-	-	-	-	-	-	-	-	-	-	-	-	-	-	-	-
$Z \rightarrow$	-98 → -82		-82 → -68		-68 → -32		-32 → -18		-18 → -0.5		-0.5 → 0		0 → 0.5		0.5 → 18		18 → 32		32 → 68		68 → 82		82 → 99.5		99.5 → 100	

Figure 3.15: Different positions for the charge Q in the simulated region in respect to the center of the new mesh.

Position 10:

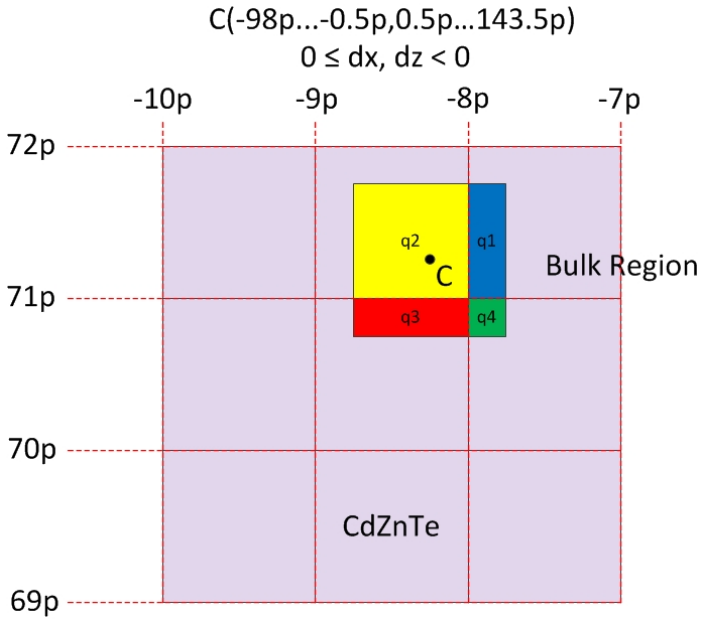

Figure 3.16: *Position 10*: In this position, the center of the charge Q is located in the 4^{th} quadrant of a mesh located in the bulk region of the detector, but having a negative index i.

In this case, the center of the charge Q was located in the 4^{th} quadrant of a mesh

located in the bulk region of the detector, but having a negative index i due to an arbitrary drift from any position inside the simulated region of 100×144 pixels, as described in Figure 3.16. First, the indexes of the mesh containing the center of the charge Q were calculated, (i, k). Then, charges q_1, q_2, q_3 and q_4 were transferred to their respective mirror positions, back into the region with positive index i. Then, the Shockley-Ramo Theorem was applied to calculate induced signals by each charge q_i, for $i = 1, 2, 3, 4$, by measuring the difference in the weighting potential between the original position of the charge Q and each final position of charges q_i.

Position 35:

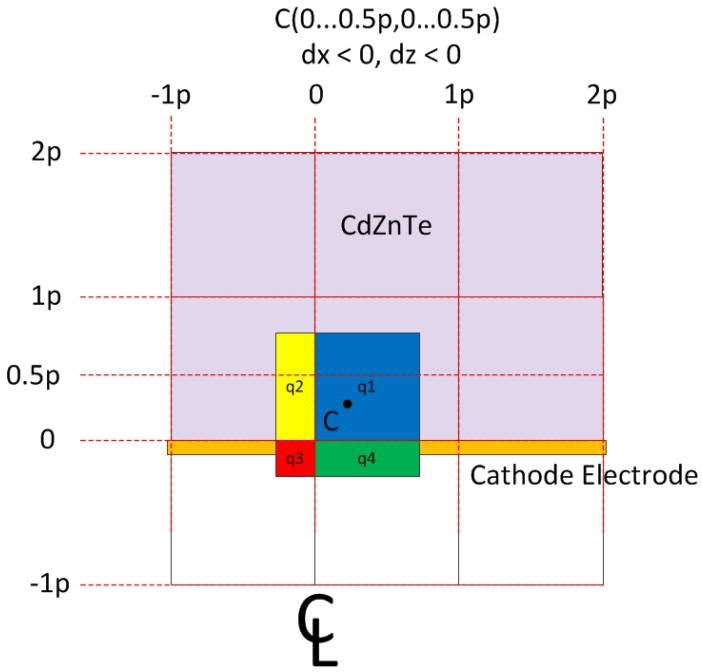

Figure 3.17: *Position 35*: In this position, the center of the charge Q is located in the 3^{rd} quadrant of a mesh located in the vicinity of the axis of symmetry, but having an index $i = 0$.

In this case, the center of the charge Q was located in the 3^{rd} quadrant of a mesh located in the vicinity of the axis of symmetry, but having an index $i = 0$ due to an arbitrary drift from any position inside the simulated region of 100×144 pixels, as described in Figure 3.17. First, the indexes of the mesh containing the

center of the charge Q were calculated, (i, k). Then, charge q_2 was transferred to its respective mirror position in the positive plane, back into the simulated region, while charges q_3 and q_4 were removed from the simulation, since they were collected by the cathode electrode. Note that this approach is generic and can be applied to either electrons or holes, although it would be wrong to consider that negative charges could be collected by the cathode. Then, the Shockley-Ramo Theorem was applied to calculate the induced signals by each charge q_i, for $i = 1, 2, 3, 4$, by measuring the difference in the weighting potential between the original position of the charge Q and each final position of charges q_i. For charges q_3 and q_4, the weighting potential at their final positions was considered to be equal to 1 for the cathode electrode and 0 for all other electrodes.

Position 44:

In this position, the center of the charge Q was located in the 1^{st} quadrant of a mesh located under the anode electrode, inside the simulated region of 100×144 pixels, as described in Figure 3.18.

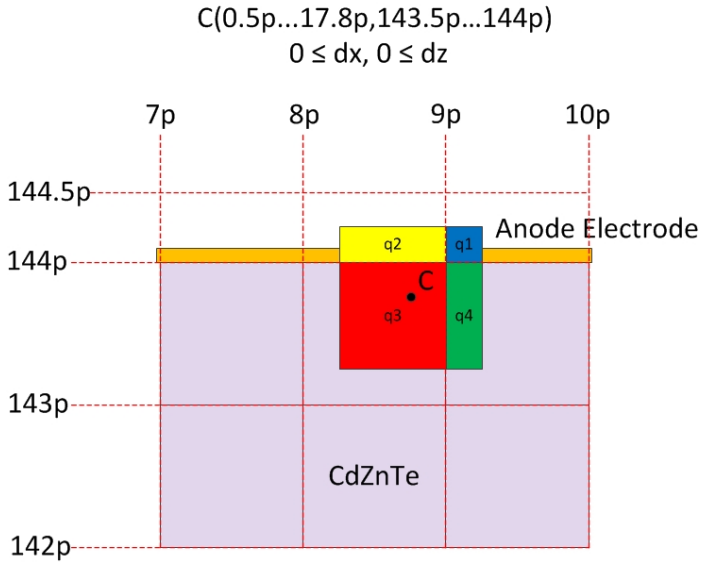

Figure 3.18: *Position 44*: In this position, the center of the charge Q is located in the 1^{st} quadrant of a mesh located under the anode electrode, inside the simulated region.

First, the indexes of the mesh containing the center of the charge Q were calculated, (i, k). Then, charges q_3 and q_4 were removed from the simulation, since they were collected by the anode electrode. Note that this approach was generic and could be applied to either electrons or holes, although it would be wrong to consider that positive charges could be collected by the anode. Then, the Shockley-Ramo Theorem was applied to calculate the induced signals by each charge q_i, for $i = 1, 2, 3, 4$, by measuring the difference in the weighting potential between the original position of the charge Q and each final position of charges q_i. For charges q_1 and q_2, the weighting potential at their final position was considered to be equal to 1 for the collecting anode electrode and 0 for all other electrodes.

Position 50:

In this position, the center of the charge Q was located in the 2^{nd} quadrant of a mesh located in the gap between two anode electrodes beneath the anode surface and inside the simulated region of 100×144 pixels, as described in Figure 3.19.

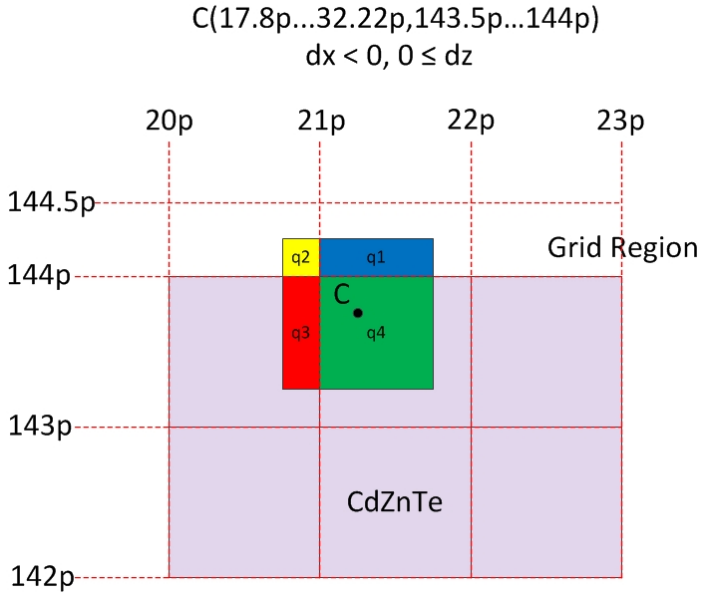

Figure 3.19: *Position 50*: In this position, the center of the charge Q is located in the 2^{nd} quadrant of a pixel located in the gap between two anode electrodes beneath the anode surface and inside the simulated region.

First, the indexes of the mesh containing the center of the charge Q were calculated, (i, k). Then, charges q_1 and q_2 were transferred to the mesh underneath then, since it was assumed that these charges could not be collected at this position, then q_1 was added to q_4 while q_2 was added to q_3. Then, the Shockley-Ramo Theorem was applied to calculate the induced signals by each charge q_i, $i = 1, 2, 3, 4$,by measuring the difference in the weighting potential between the original position of the charge Q and each final position of charges q_i. For charges q_1 and q_4, the same weighting potential was applied. The same idea worked for charges q_2 and q_3, measuring the difference in the weighting potential between the original position of the charge Q and each final position of charges q_3 and q_4.

3.4 Simulation Verification

Before using this tool in high-flux simulations, some preliminary results at low-flux were simulated, in order to verify that the results obtained in simulations at low flux agree with expected results. Table 3.3 summarizes some properties used in terms of simulated operating conditions as well as some material properties considered.

Property	Value
Detector Geometry	$20 \times 20 \times 5$ mm^3
Cathode Bias	-1000 V
Electron Mobility μ_e	750 cm^2/V/s
Hole Mobility μ_h	20 cm^2/V/s

Table 3.3: Properties used to simulate the detector and the operating conditions in the high-flux experiments.

The first simulated result considers a perfect material with no bulk defects, as shown in Figure 3.20. In this simulation only signals induced by the electrons were considered, injecting a 662 keV equivalent cloud of electrons at 354μm away from the axis of symmetry and very close to the cathode surface.

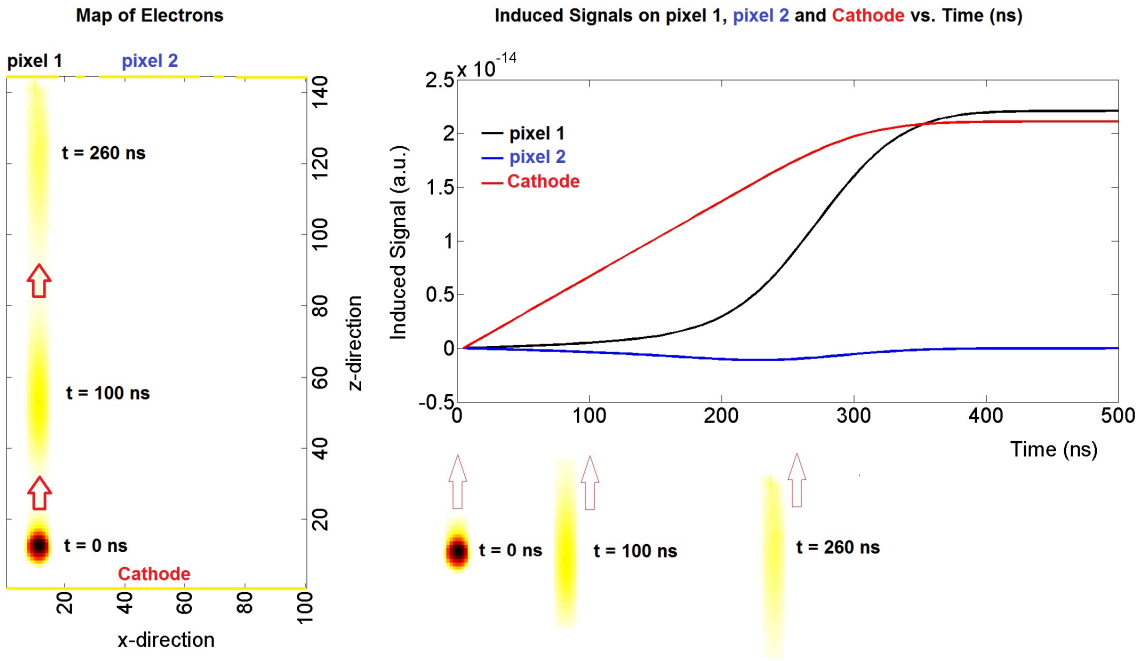

Figure 3.20: Electrons-only induced signals on pixel1, pixel2 and Cathode electrodes. On the left, map of free electrons in excess of equilibrium *mape* is shown superposing three different cloud positions: at the start position $t = 0$ and two other positions at $t = 100$ and 260 ns. On the right, the simulated induced signal is plotted for pixel1, -pixel2 and -cathode electrodes.

Using the properties listed in Table 3.3, it was predicted an electron drift time $d_{te} \approx 300$ ns, which was in good agreement with the simulated result shown in Figure 3.20.

The second simulated result considered the same perfect material simulated for electrons, but now holes-only induced signals were simulated by injecting a 662 keV equivalent cloud of holes at 354μm from the axis of symmetry and very close to the anode surface, as shown in Figure 3.21. Using the properties listed in Table 3.3, it was predicted a hole drift time $d_{th} \approx 12.5$ μs, which was in good agreement with the simulated result shown in Figure 3.21.

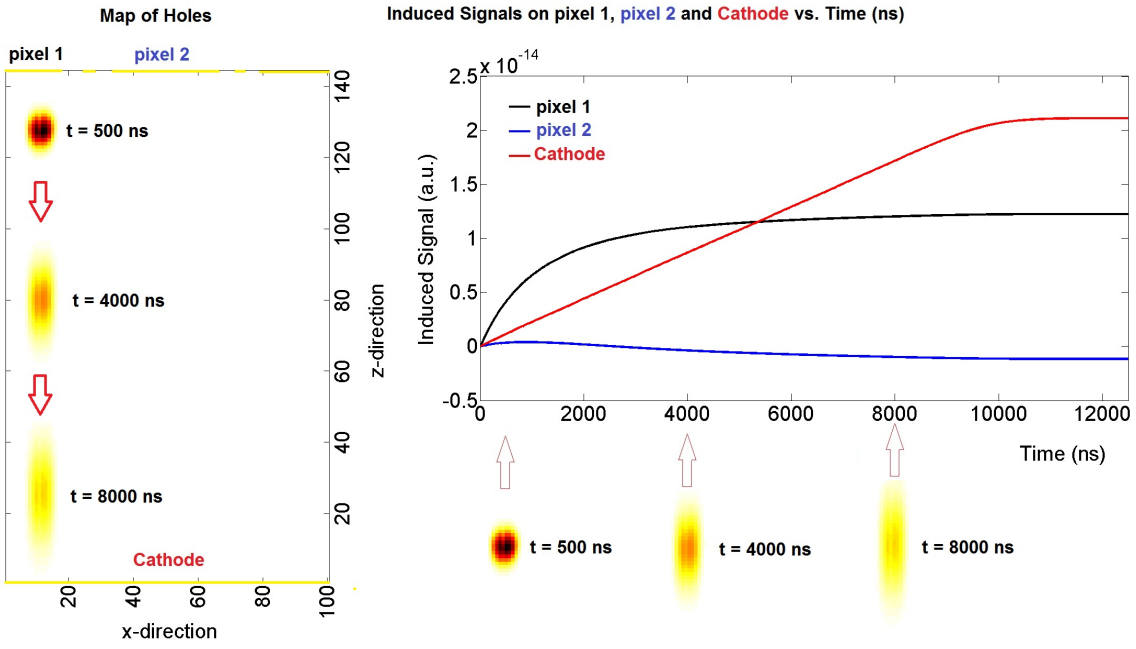

Figure 3.21: Holes-only induced signals on pixel1, pixel2 and Cathode electrodes. On the left, map of free holes in excess of equilibrium (*maph*) is shown superposing three different cloud positions: at $t = 0.5$, 4 and 8 μs. On the right, the simulated induced signal is plotted for pixel1, -pixel2 and -cathode electrodes.

Although signals shown in Figures 3.20 and 3.21 were in good agreement with expected results, they represented a perfect material. In reality, as already mentioned, the material has many defects. Then, it was also necessary to verify the agreement between signals simulated using the measured defects in the CdZnTe detectors used in our high-flux experiments. These measurements are shown in more detail in Chapter IV, where a better explanation is given for considering in the model one defect level for electrons and two defect levels for holes.

Average electron and hole trapping times $\tau_{e,h}$ were also important parameters required in the simulations. Figure 3.22 shows simulated holes-only induced signals, considering a fixed average hole trapping time $\tau_h = 250$ ns and variable average hole-detrapping times $\tau_{hD} = 10 \ldots 750$ μs.

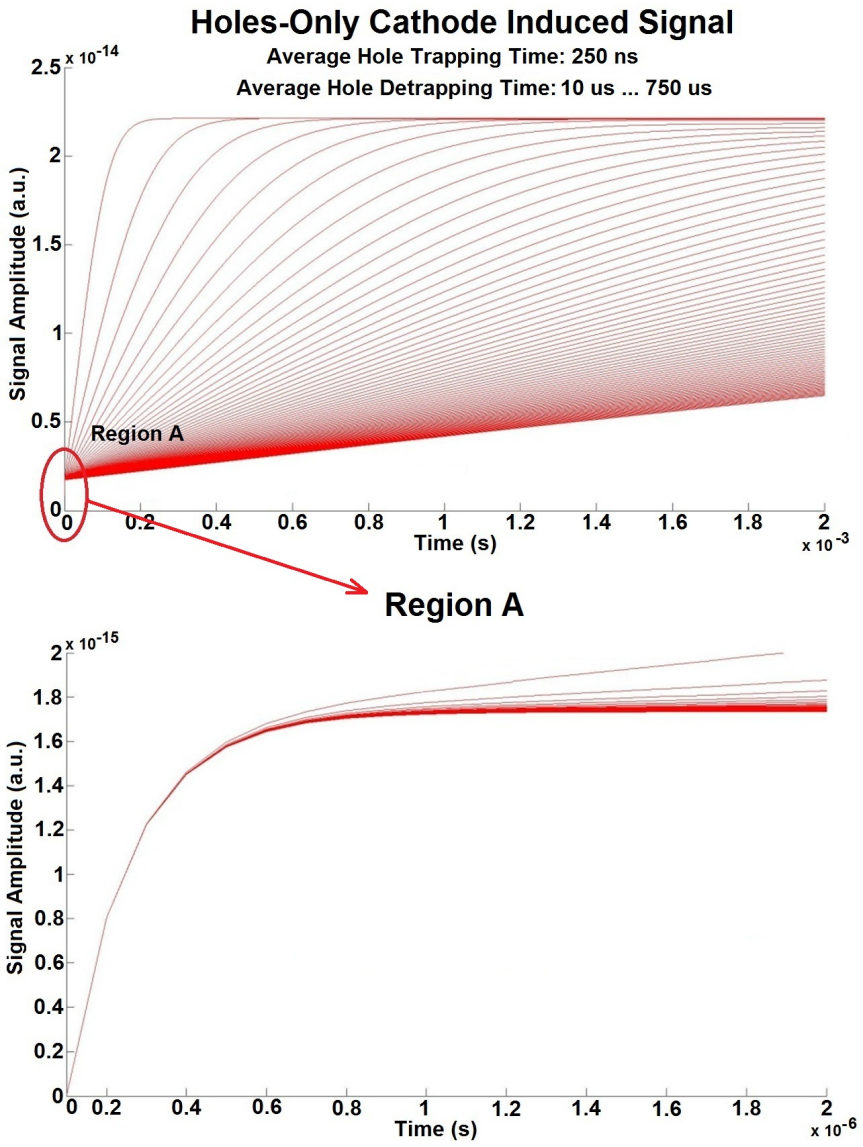

Figure 3.22: Simulated holes-only induced signals using average hole trapping time $\tau_h = 250$ ns and variable average hole-detrapping time $\tau_{hD} = 10 \ldots 750$ μs.

In these results, the detector was assumed to have a hole mobility $\mu_h = 80$ cm^2/V/s. The ratios between the amplitudes of these simulated signals considering the average trapping time $\tau_h = 250$ ns and average detrapping time varying from $\tau_{hD} = 10 \ldots 750$ μs were used to verify these simulated results. In extreme situations, where all charges trapped are not released, the amplitude of the induced signal is

determined by the average trapping time.

3.5 Analysis of Developed Simulation Tool

In Section 3.1, a simple model of the experimental apparatus was implemented. In this model, eight objects were considered, as described in Table 3.1. Monte-Carlo simulations of the experiment apparatus were combined with measured data at different fluxes to calculate the relationship between incident flux Φ at the surface of the detector and the average time between interactions $\bar{t}$. In future studies, a X-ray source needs to be implemented and modeled in simulations, *Sidky et al.* (2005a). Also, phantoms similar to the ones used in medical imaging, *Gach et al.* (2008), but using different material compositions specific for the application described in Chapter I are required in future studies. Results shown in Table 3.2 were used to calculate the constant of proportionality C used in Equation 3.1, considering fluxes $\Phi < 45\ 000$ photons/pixel/s.

Reasons for the non-proportionality found at higher fluxes, represented by deviations from calculated values of C at lower fluxes, are not well understood. These differences may be attributed to several approximation and errors during the process of measuring and estimating the value of C, such as:

a) Unknown/incorrect Cs-137 source distribution

b) Unknown/incorrect source shield materials and dimensions

c) Imprecise/incorrect alignment between source, collimator and detector

d) Effects of surrounding materials not correctly modeled in Monte-Carlo simulations

e) Pile-up of events in the data acquisition system

f) Detector energy response not modeled

In Section 3.2 the system described by Equations 3.2-3.9 solved the charge continuity equations in a homogeneous material having uniform distribution of defects.

The number of defects per unit volume was assumed to be larger than the number of charge carriers trapped per unit volume. Defect levels were treated as traps, being populated and depopulated by charge carriers according to statistical models predicted by Equations 3.2-3.6, where the amount of charges being trapped or de-trapped in any mesh was given by the average trapping and de-trapping times modeled. Recombination between electrons and holes at different energy levels play an important role in reducing the amount of positive space charge build up in the detector volume in high-flux irradiation as a function of time. This important effect was not included in this work and should be investigated in the future. The effect of having different contact materials and operating the detector at different temperatures should be studied in future work.

In Sec.3.2.1, reasons that motivated the change from the *Point-Cloud Model* to the *3D-Axisymmetric Model* were explained. In order to consider the effect of the electrodes, the mirror image method described in Section 3.2.2 was used to calculated the space charge electric field. The implementation of the *3D-Axisymmetric Model* described in Sec.3.3 considered a small region of the detector volume. In future studies, the simulated detector volume needs to be expanded, including more neighbor pixels. Future studies will require additional parallel processing capabilities, since it is expected that future models will have more trapping centers and other physical processes included in the modeling.

CHAPTER IV

Material Properties

In order to apply the simulation tool described in Chapter III, transport properties of electrons and holes needed in the simulations were carefully measured. It is well known that operating these detectors under high-flux irradiation ($\sim 1 \times 10^8$ photons/cm^2/s), positive space charge build up as a function of irradiation time, mainly due to poor hole transport properties, commonly known as the *polarization effect*, *Bale et al.* (2008), *Bale and Szeles* (2008) and *Rodrigues and He* (2011). Since holes limit the performance of these devices under high-flux irradiation, this chapter focuses on determining transport properties of holes rather than electrons. A systematic approach was used to measure the charge transport properties of CdZnTe detectors, such as electron and hole average trapping ($\tau_{e,h}$) and de-trapping ($\tau_{eD,hD}$) times. Although, it is well documented that CdZnTe has multiple electron and hole defect levels, *Hermon et al.* (2001), *Hermon et al.* (1999) and *Schieber et al.* (2001), in this work only one electron defect level and two hole defect levels were considered. In Section 4.3, a critical analysis of the measurements presented in this chapter suggests that adding a third trapping center could improve the matching between simulated and measured results in high-flux operating conditions.

Compensation techniques used to increase the resistivity of CdZnTe detectors, which are known to be plagued by shallow defect levels, introduce deep defect levels

in the material, *Dieguez* (2011). These defects act as trapping centers, trapping free charge carriers for longer times, degrading the performance of these devices when operated under high-flux scenarios, *Zanio et al.* (1968). Characterization of shallow and deep trapping centers in the detectors used in the high-flux experiments is required to correctly simulate and understand the causes of the polarization effect. This was accomplished by detailed analysis of measured induced signals irradiating the detectors with γ-rays, α-particles and K_α X-rays, on the cathode surface and on the sides, through the protective paint, *Rodrigues and He* (2011). Holes-only induced signals were obtained by removing the electron contribution in the measured signals and charge transport properties were calculated using simulated induced signals.

4.1 Theory and Models

In order to avoid confusion due to the fact that CdZnTe is considered to be an intrinsic semiconductor, the convention adopted in this work is to refer as *normal bias* when applying negative high-voltage to the *large* electrode, while *reverse bias* when applying a positive high-voltage to the same electrode. Normally, these detectors are manufactured to operate with the large electrode at negative bias voltage, applying a blocking contact to reduce the leakage current in this configuration.

At first, charge transport properties of CdZnTe were calculated by measuring cathode signals induced by electrons and holes irradiating the lateral surface of these detectors with Am-241 α-particles (E_α = 5.486 MeV (85.2%) and 5.443 MeV (12.8%), as described in Section 4.2.1, while operating the detectors at normal bias. Then, a different method measured directly holes-only induced signals by irradiating the cathode surface of the detectors with K_α X-rays produced by short pulsed lasers incident on a Molybdenum Mo target, *Hou et al.* (2008), *Seely et al.* (2007) and *Rousse et al.* (1994), while operating these detectors at reverse bias, as described in Section 4.2.2. Similar techniques were used in both methods, while the advantage

of using the second method, measuring the K_α X-rays produced by short pulsed lasers, was the reduction in the number of steps needed to measure holes-only induced signals and the absence of surface effects due to deeper penetration of K_α X-rays in comparison with α-particles.

4.1.1 Statistical Model of Charge Induction

The technique presented in this chapter consists of measuring the ratios between electrons-only and holes-only induced signals to calculate the average hole trapping time τ_h based on statistical models, i.e., the well known *Hecht equation*, *Hecht* (1932), *Shah et al.* (1990), *Nemirovsky et al.* (1996), *Nemirovsky* (1999) and *Ifraimov et al.* (2002). Direct comparison between measured and simulated holes-only induced signals were used to calculate average hole de-trapping times τ_{dh}, *Blakney and Grunwald* (1967), *Zanio et al.* (1968), *Juska et al.* (1969), *Jung et al.* (1999) and *Prokesch et al.* (2010). The method presented here can be extended to other semiconductor detectors. Results obtained using this method were used in our simulations to study the limits of operation of CdZnTe detectors under high-flux irradiation, presented in Chapter V.

Some properties of commercially available CdZnTe detectors used in this chapter are presented in Table 4.1. In order to reduce charge loss due to charge trapping

Property	Value
Band-gap (eV)	~ 1.6
Bulk resistivity Ω·cm	$\sim 10^{10}$
Electron mobility ($cm^2/V/s$)	~ 750
Hole mobility ($cm^2/V/s$)	~ 20
Electron lifetime (μs)	~ 6

Table 4.1: Electrical transport properties of considered in this work, representing results measured in laboratory for commercially available CdZnTe detectors.

and recombination, it is desirable to operate these detectors at the largest possible cathode bias voltage. However, the operating voltage is limited by leakage current

and other factors when high voltages are applied to the cathode electrode. In order to reduce bulk leakage current in good quality spectroscopic grade CdZnTe detectors, materials with high resistivity are required. Resistivity greater than 10^{10} Ω-cm is commonly found in commercially available CdZnTe detectors through the introduction of a relatively large concentration of deep trapping centers, which partially ionize and pin the Fermi level near the middle of the band gap, *Lee et al.* (1999), *Adamiak* (2003), *Babentsov et al.* (2007), *Prokesch and Szeles* (2006) and *Dieguez* (2011). This technique, known as *compensation*, is an effective method to increase the resistivity of large band-gap semiconductor detectors plagued by shallow defect levels, such as CdZnTe, *Dieguez* (2011).

However, the same deep trapping centers that increase the resistivity of these detectors introduce defects in the material, *Dieguez* (2011). This is more pronounced when operating under high-flux irradiation and using higher energy photon sources ($E > 100$ keV). In these operating conditions, photons interact deeper into the crystal, creating electron and hole e-h pairs. Then, due to poor hole transport properties, positive charges accumulate in these trapping centers as a function of irradiation time, limiting the performance of these devices under high-flux irradiation. In order to achieve higher fluxes, a fine balance between *compensation* and charge transport properties is required. Changing this balance can potentially improve the performance of these detectors under high-flux irradiation, however significant changes in signal induction are expected. Thus, current techniques used in 3D-position-sensitive CdZnTe detectors to improve their spectroscopic performance, such as cathode-to-anode ratio (CAR) and time-of-flight measurements, *Zhang et al.* (2004) and *Zhang et al.* (2005), are expected to be different when applied to future high-flux grade CdZnTe detectors.

The theory used to calculate charge transport properties in CdZnTe detectors is based on a statistical model of charge collection efficiency, *Ruzin and Nemirovsky*

(1997a) and *Ruzin and Nemirovsky* (1997b), combined with the model of combined signal induction from electrons and holes described here. Results presented here have been used to measure carrier mobilities μ_e and μ_h, average trapping times τ_e and τ_h and average detrapping times τ_{eD}, τ_{hD1} and τ_{hD2} in CdZnTe detectors.

Pixelated 3D-position-sensing CdZnTe detectors are normally considered as single-polarity charge sensing devices, *He* (2001), but in reality signals are induced by the drift of electrons and holes. As long as both charge carriers drift, currents are induced on electrodes and their values can be estimated applying the Shockley-Ramo Theorem, which states that the instantaneous current can be evaluated by Equation 4.1,

$$i(t) = q \cdot \vec{v} \cdot E_0 \tag{4.1}$$

where $\vec{v}$ is the velocity of the charge carrier q at (x_t, t) and E_0 is the weighting electric field. Considering only induced signals at the cathode electrode and irradiating the detector with α-particles on the side of the detector, through the protective paint existing on these devices, as described in Fig.4.1, the weighting electric field is given by $E_0 = -1/L$.

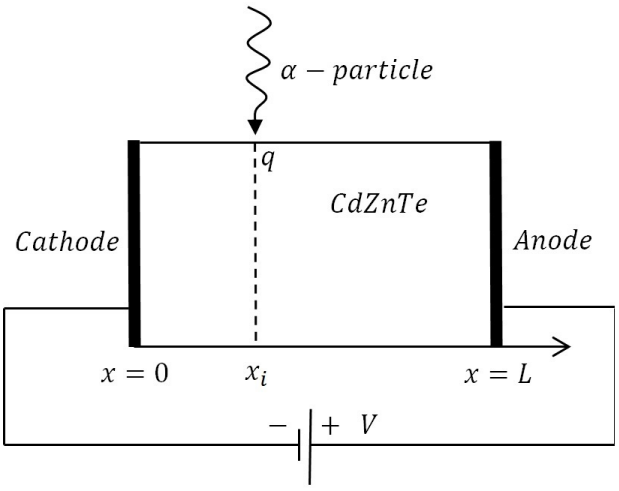

Figure 4.1: Diagram showing the 1D system of reference used when α-particles interact at position x_i.

Currents induced by the drift of electrons and holes were calculated using Equation 4.1. These signals were considered to be integrated in the external circuit. Electrons and holes generated by an α-particle at position (x_i,t) induce a signal with amplitude determined by the each carrier transport properties. The total charge induced by each carrier $Q_{e,h}$ was calculated integrating Equation 4.1, from the initial position x_i until complete charge collection at their respective collecting electrodes, as described in Equation 4.2,

$$Q_{e,h} = \int_0^{t_{e,h}} i_{e,h}(t)dt = -t_{e,h} \cdot q_{e,h} \cdot \mu_{e,h} \cdot \frac{E}{L} \tag{4.2}$$

where,

$t_{e,h}$: electron and hole collection time

$i_{e,h}$: current induced by the drift of electrons and holes

$q_{e,h}$: charge of each carrier at position x and time t

E: electric field

L: detector thickness

A statistical model considering electron and hole trapping, *Ruzin and Nemirovsky* (1997b), is shortly described here. This model considers the geometry of the detector with the reference system shown in Figure 4.1, and can be used to estimate individual amplitudes of electrons-only and holes-only induced signals when an α-particle interacts at position x_i. Free electron and hole lifetime probability density functions consider a finite detector geometry, as shown in Figure 4.2.

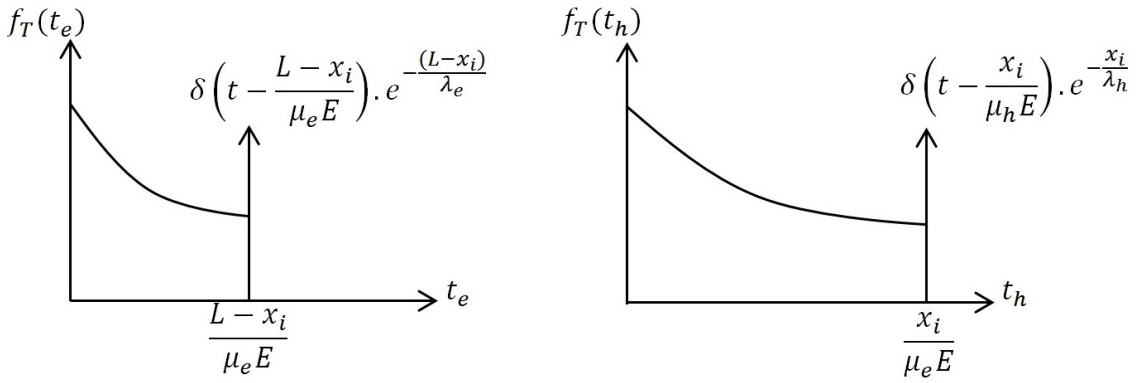

Figure 4.2: Electrons and holes probability density functions when α-particles interact at depth of interaction x_i.

These probability density functions are used to calculate the average electron and hole trapping times, as described in Equation 4.3.

$$\langle t_e \rangle = \tau_e[1 - e^{\frac{-(L-x_i)}{\lambda_e}}], \langle t_h \rangle = \tau_h(1 - e^{\frac{-x_i}{\lambda_h}}) \tag{4.3}$$

where,

$\lambda_e = \mu_e E \tau_e$: average electron drift length in an infinite semiconductor

$\lambda_h = \mu_h E \tau_h$: average hole drift length in an infinite semiconductor

Considering the result described by Equation 4.3, the expected amplitude of the signal measured by the external preamplifier circuit due to a single e-h pair generated at position x_i can be calculated, as described in Equation 4.4.

$$\langle Q_e(x_i) \rangle = \frac{q\lambda_e}{L}[1 - e^{\frac{-(L-x_i)}{\lambda_e}}], \langle Q_h(x_i) \rangle = \frac{q\lambda_h}{L}[1 - e^{\frac{-x_i}{\lambda_h}}] \tag{4.4}$$

The total signal amplitude measured by the external circuit, following the generation of N_0 e-h pairs at position x_i, is estimated using the principle of superposition,

as described in Equation 4.5.

$$\langle Q(x_i)\rangle = \frac{N_0 q}{L}[\lambda_e(1 - e^{\frac{-(L-x_i)}{\lambda_e}}) + \lambda_h(1 - e^{\frac{-x_i}{\lambda_h}})] \tag{4.5}$$

This is the well-known *Hecht equation*, which describes the average signal amplitude when an interaction occurs at coordinate x_i, considering only trapping effects for both charge carriers. Assuming that the average electron trapping time is known, one can estimate the average hole trapping time τ_h by comparing measured ratios between electrons-only and holes-only induced signals $Q_e(x_i)/Q_h(x_i)$ with values predicted by Equation 4.6.

$$\frac{\langle Q_e(x_i)\rangle}{\langle Q_h(x_i)\rangle} = \frac{\lambda_e(1 - e^{\frac{-(L-x_i)}{\lambda_e}})}{\lambda_h(1 - e^{\frac{-x_i}{\lambda_h}})} \tag{4.6}$$

Figure 4.3 shows results calculated using Equation 4.6 plotted in *a*) for different values of hole mobility $\mu_h = 80$, 40 and 20 cm^2/V/s and in *b*) for different values of interaction positions $x_i = 3$, 3.5 and 4 mm. Since the average electron trapping time τ_e is longer than the electron drift time, these plots are not sensitive to small changes in the value of τ_e. Then, considering known electric field E, these results can be used to determine the value of the average hole trapping time based on the ratio Q_e/Q_h.

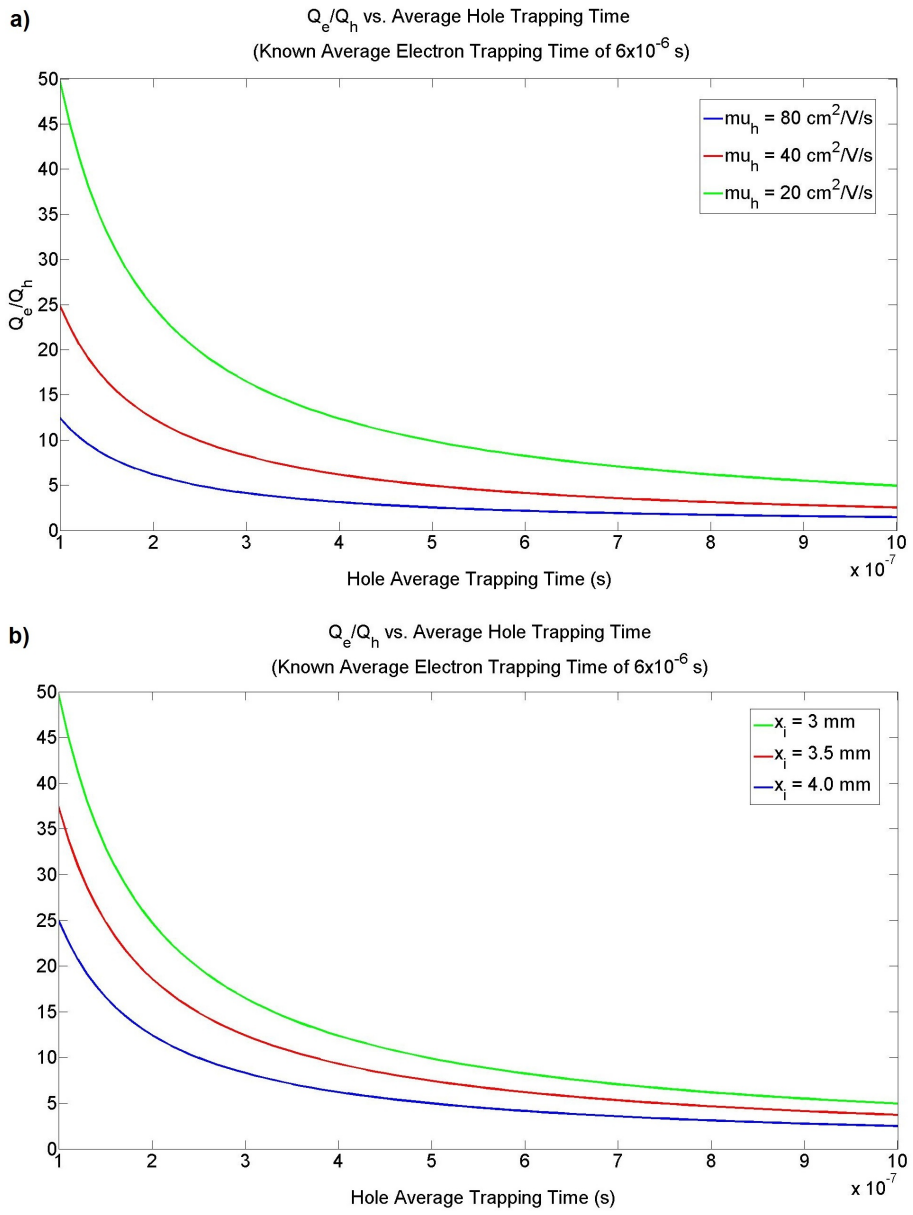

Figure 4.3: Q_e/Q_h plotted as a function of average hole trapping time τ_h, considering: *a*) different values of hole mobility μ_h = 80, 40 and 20 cm^2/V/s, and *b*) different values of interaction positions x_i = 3, 3.5 and 4 mm.

It can be observed in Figure 4.3 that uncertainties in μ_h and x_i introduce errors in the measurement of τ_h.

4.1.2 Modeling Electrons- and Holes-Only Induced Signals

In order to use the statistical model discussed in Section 4.1.1, it was necessary to measure for the same α-particle interaction the amplitudes of signals induced by electrons-only and holes-only for a known x_i depth of interaction. Although, it is relatively easy to measure electrons-only induced by α-particles incident on the cathode electrode while operating the detector at normal bias, the same does not apply for holes. Holes-only induced signals by α-particles incident on the anode surface can not be measured, since these detectors arrive with the printed circuit board pre-attached to the anode surface, obstructing the α-particles. It is only possible to measure holes-only induced signals by reversing the polarity of the high-voltage applied to the cathode electrode while irradiating the cathode surface with α-particles. Technically, the planar electrode becomes the anode of the device when applying positive rather than negative high-voltage to it, but in this work it is chosen to say that the *cathode* is reversed biased. This approach is not feasible in most of the detectors, since operating them at reverse bias increases the leakage current and the low-frequency noise disturbs the cathode baseline and hinders any α-particle measurement of holes-only induced signals. These low-frequency noise signals were highly correlated with the signals induced by holes in frequency and amplitude, being extremely difficult to distinguish them from real α-particle induced signals. One proposed solution is to irradiate the side of the detector with α-particles through the protective paint at a known interaction positions x_i, measured either by Cathode-to-Anode (CAR) ratio or time of flight techniques. Using this approach, induced signal on the anode electrode, mostly due to electrons drifting towards the anode, trigger the system while cathode induced signals are recorded for electrons and holes drifting. Electrons-only and holes-only induced signals are deconvolved from measured signals using the sequence of steps shown here.

First, we need to describe the model of signal induction and the assumptions

considered using this approach. In our measurements, an average electron trapping time $\tau_e = 6$ μs and an electron mobility $\mu_e = 750$ cm^2/V/s were measured. These values correspond to an electron drift-time (from cathode to anode) $\sim$ 400 ns at -1000 V cathode bias. Due to poor hole transport properties, corresponding to an average hole trapping time $\tau_h < \tau_e$, hole drift-time (from anode to cathode) $\sim$ 400 ns were expected. Also, few electrons were trapped before reaching the anode surface, due to their large mobility-lifetime product $\mu_e\tau_e$, while holes were completely trapped, most of the time before reaching the cathode surface, due to their low mobility-lifetime product $\mu_h\tau_h$. Then, using these assumptions, a combined model of signal induction for α-particles interacting on the side of the detector at position x_i is proposed, as described in Figure 4.4. In this model, individual contributions to the measured signal due to electrons and holes drifting is sub-divided into four regions:

a) Free electrons drifting from t_0 to t_1

b) Free holes drifting from t_0 to t_3

c) Trapping and de-trapping of electrons from t_1 to t_2

d) Trapping and de-trapping of holes from t_3 to t_4

Upper bounds for electrons-only and holes-only induced signals due to trapping and de-trapping mechanisms were estimated using Equation 4.7.

$$\langle Q_{ed}(x_i)\rangle_{max} = \frac{N_0 \cdot q}{L}\lambda_e e^{\frac{-(L-x_i)}{\lambda_e}}, \langle Q_{hd}(x_i)\rangle_{max} = \frac{N_0 \cdot q}{L}\lambda_h e^{\frac{-x_i}{\lambda_h}} \tag{4.7}$$

In Figure 4.4, considering the signal induced by electrons-only, the time interval $\overline{t_0 t_1} = (L - x_i)/\mu_e E$ was estimated considering known electron mobility μ_e, applied electric field E, detector geometry L and interaction position x_i. Since the average electron drift length λ_e is much larger than the thickness of the detector L ($\sim$10$\times$ larger), full charge collection of electrons is expected. The amplitude of electrons-only induced signals is estimated using results given by the charge collection efficiency

model $Q_e(x_i)$, described in the numerator of Equation 4.6. Considering holes-only induced signals, the time interval $\overline{t_0 t_3}$ as well as the amplitude of the signal are estimated using the same criteria, although caution is needed when using this model due to much smaller average hole drift length λ_h. It is expected that holes-only induced signals initially rise linearly due to drift of free holes in excess of equilibrium followed by a curvilinear portion due to trapping and de-trapping mechanisms, making it more challenging to distinguish them. Amplitude predictions given by Equation 4.7 are used to help measurements of holes-only induced signal amplitudes. The amplitude of the signal $Q_h(x_i)$ at t_3 is estimated using the charge collection efficiency model, as described by the denominator of Equation 4.6. Note that measuring the time interval $\overline{t_0 t_4}$ and the amplitude H_{t_4}, due to the slow rise of the signals and the

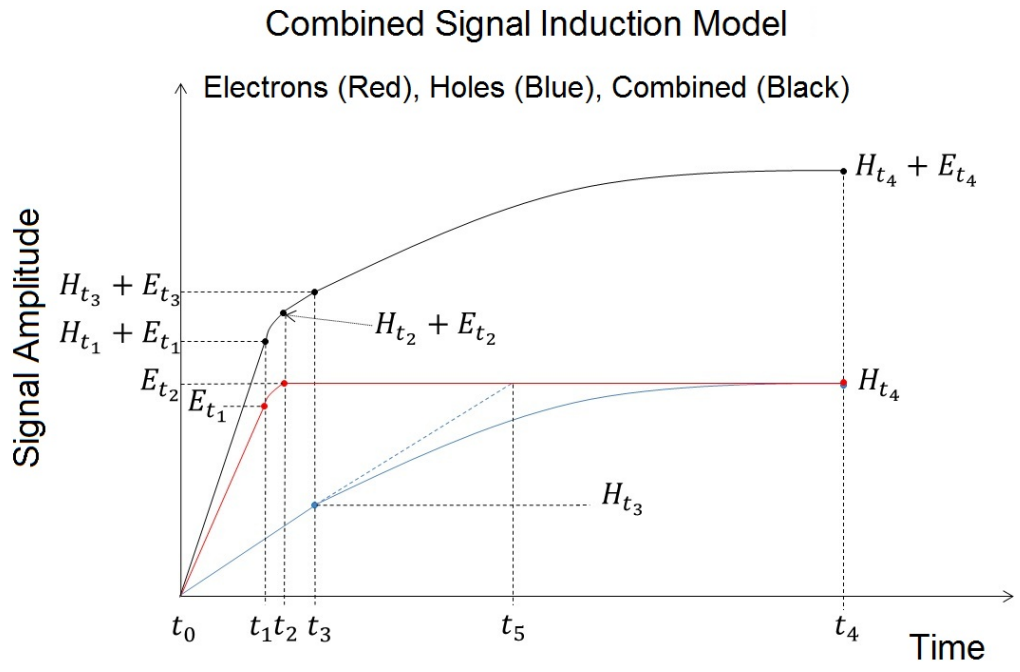

Figure 4.4: Model of combined signal induced by electrons and holes when an α-particle interacts at position x_i=L/2, where t_0 is the interaction time, t_1 is the time when all free electrons reach the anode, t_2 is the time when all electrons in excess of equilibrium are collected by the anode by trapping-detrapping mechanism, t_3 is the time when all free holes drift inside the material (they do not reach the cathode) and t_4 is the time when all holes in excess of equilibrium are collected by trapping-detrapping mechanism.

decay of the feedback circuit of the preamplifier as well as other sources of noise present in the system, is more challenging.

4.1.3 Measuring Electrons-Only and Holes-Only Induced Signals

Induced signals from electrons-only were measured by irradiating the cathode surface of these detector with α-particles. In this configuration, the contribution to the amplitude of these signals due to holes is negligible ($\sim$4/1000th of the total induced signal amplitude), since the average interaction length of α-particles in CdZnTe is only ~ 20 μm. These signals are used to calculate electron mobility μ_e, bulk electric field E and the total time it takes for electrons to drift from the cathode to the anode surface $t_{de} = L/\mu_e E$ of the detector. In principle, it is possible to measure holes-only induced signals by subtracting electrons-only induced signals from electrons-and-holes combined induced signals. Signals induced by electrons-and-holes combined are measured irradiating the side of the detectors through the protective paint, as shown in Figure 4.5.

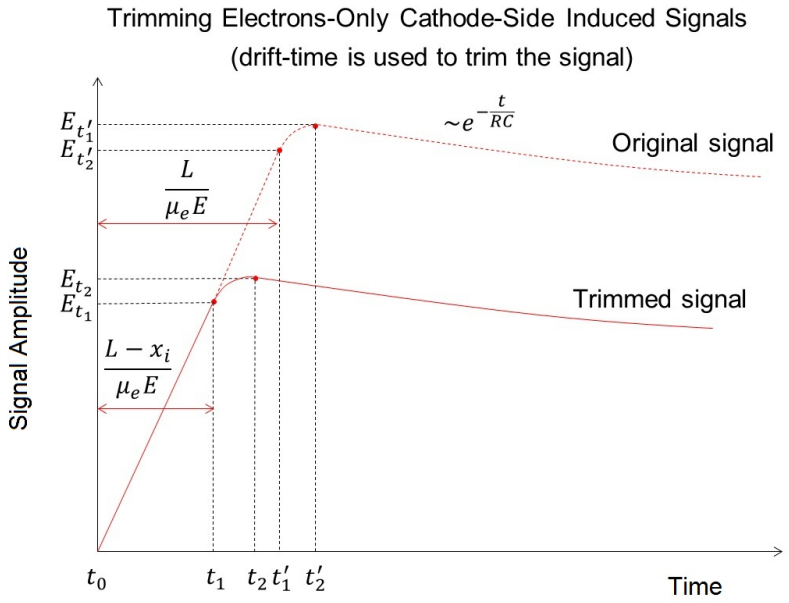

Figure 4.5: Original electrons-only induced signal measured when α-particles interact close to the cathode surface and trimmed electrons-only signal for an interaction position x_i.

The relative contribution of electrons and holes to these signals changes as a function of interaction depth. In order to calculate the equivalent electrons-only induced signal at position x_i, the measured induced signal with α-particles at the cathode surface needs to be trimmed accordingly. In this process, drift-time techniques are used to determine the depth of interaction. Then, irradiating the detectors with a collimated α-source positioned on the side, as described by Figure 4.6, induced signals due to the drift of electrons-and-holes are measured. Most of the electrons are collected by the common grid electrode while holes are collected by the cathode electrode.

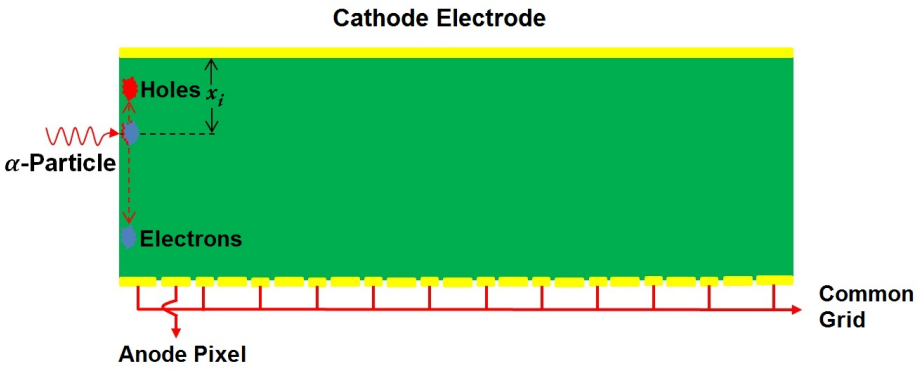

Figure 4.6: Schematic diagram of the experimental apparatus showing the initial position of the cloud x_i, the collecting electrode for electrons - the common grid electrode -, and the collecting electrode for holes - the cathode.

This entire process is realized in six steps, as described below:

a) First, align the measured induced signal by electrons-only with the signal induced by electrons-and-holes at the same starting time, as shown in Figure 4.7,

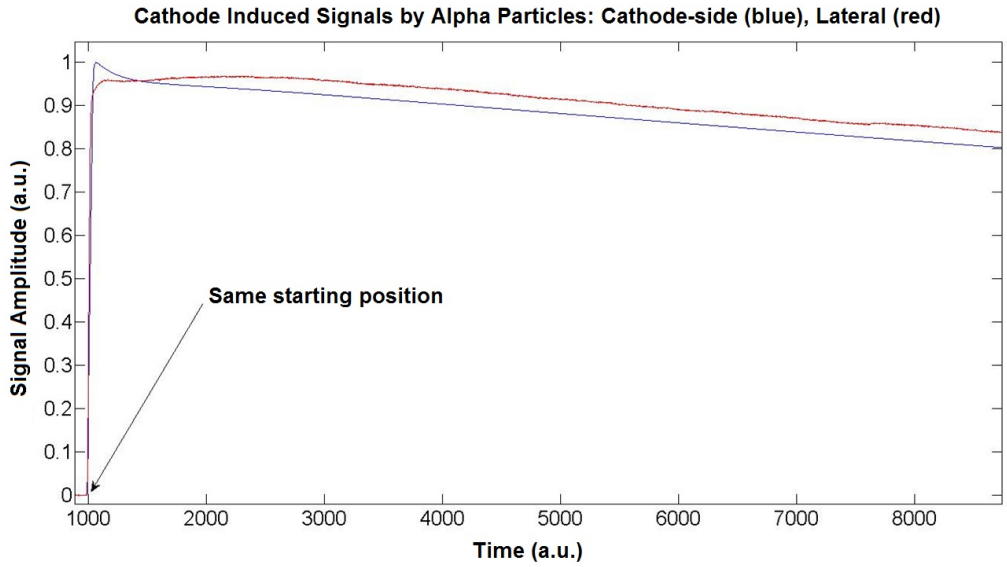

Figure 4.7: Normalized cathode-side induced signal by electrons-only (blue) and lateral side irradiation induced signal by electrons and holes (red) when interaction happens at position x_i.

b) Then, measure the drift time of the signal induced by electrons-and-holes (red signal) and use this calculated drift time to calculate the position where the electrons-only signal (blue signal) needs to be trimmed to have an equivalent electrons-only signal at depth of interaction x_i, as shown in Figure 4.8,

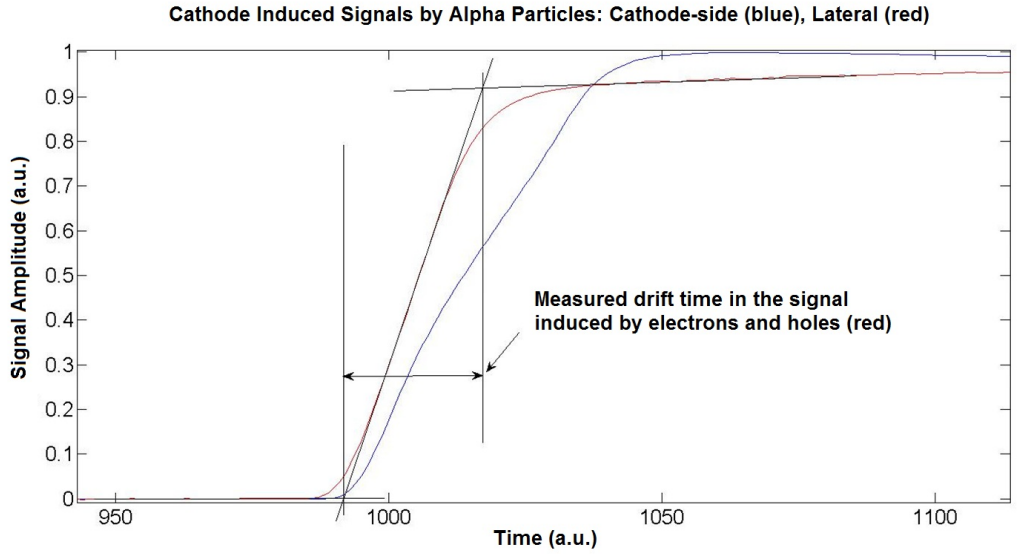

Figure 4.8: Measured drift time of side irradiated signal (red) induced by electrons and holes when an α-particle interacts at depth x_i.

c) Then, trim the electrons-only induced signal (blue signal) at the previous calculated drift-time, in order to have an equivalent electrons-only signal at depth of interaction x_i, as shown in Figure 4.9,

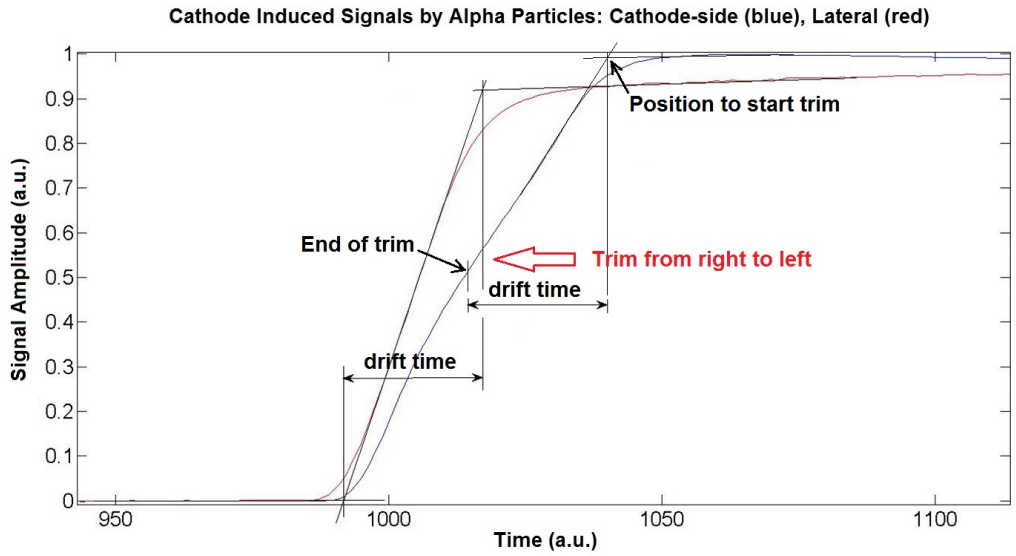

Figure 4.9: Measured drift time of side irradiated signal (red) induced by electrons and holes, and start and end positions of equivalent electrons-only induced signal (blue). Note that the new signal is trimmed from right to left, and the drift time is used to calculate the new starting position.

d) Then, adjust the new electrons-only induced signal (blue signal) to match the same amplitude of the electrons and holes induced signal (red signal), as shown in Figure 4.10,

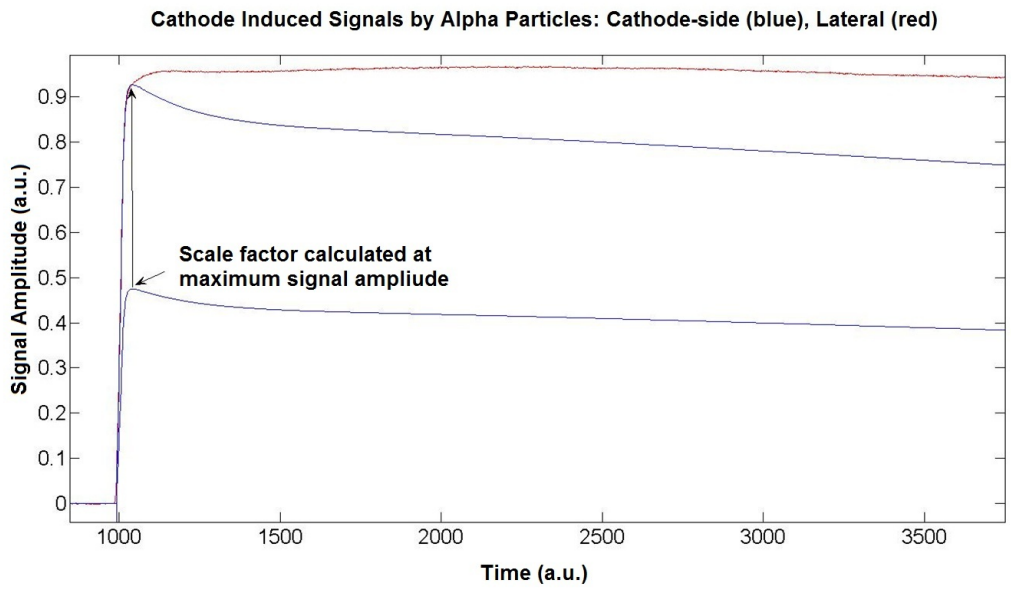

Figure 4.10: Scaled electrons-only induced signal (blue) matching the amplitude of the electrons and holes induced signal (red).

e) Then, subtract both signals to extract the holes-only induced signals, as shown in Figure 4.11. Note that the amplitude of the signal in the beginning needs to be corrected using the model described in Figure 4.4,

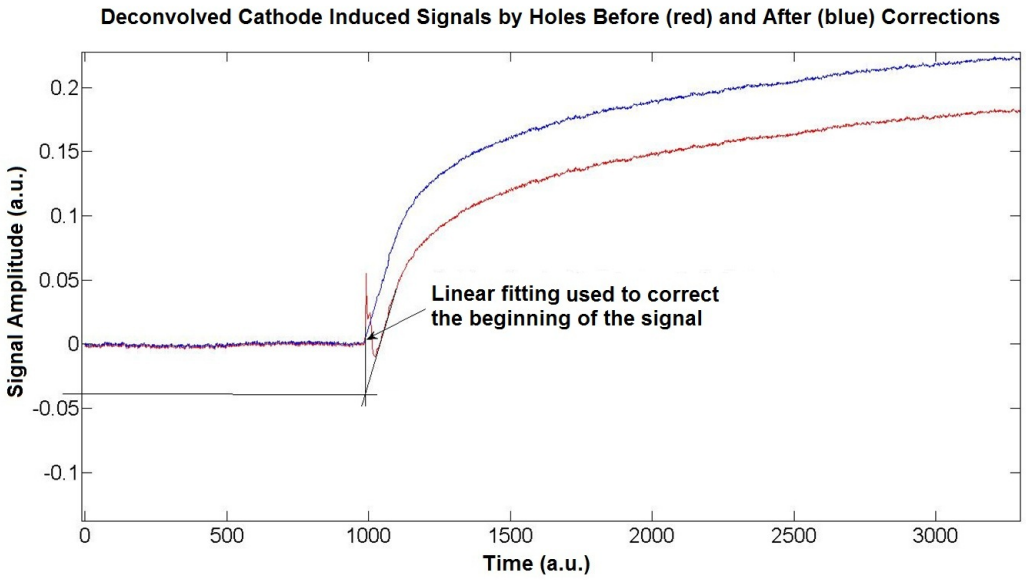

Figure 4.11: Deconvolved cathode induced signals by holes-only before (red) and after (blue) corrections. Linear fitting was used to correct the beginning of the signal, considering the model described in Fig.4.4.

f) The final step is to subtract the holes-only induced signal previously calculated from the original electrons-and-holes induced signal, as shown in Figure 4.12,

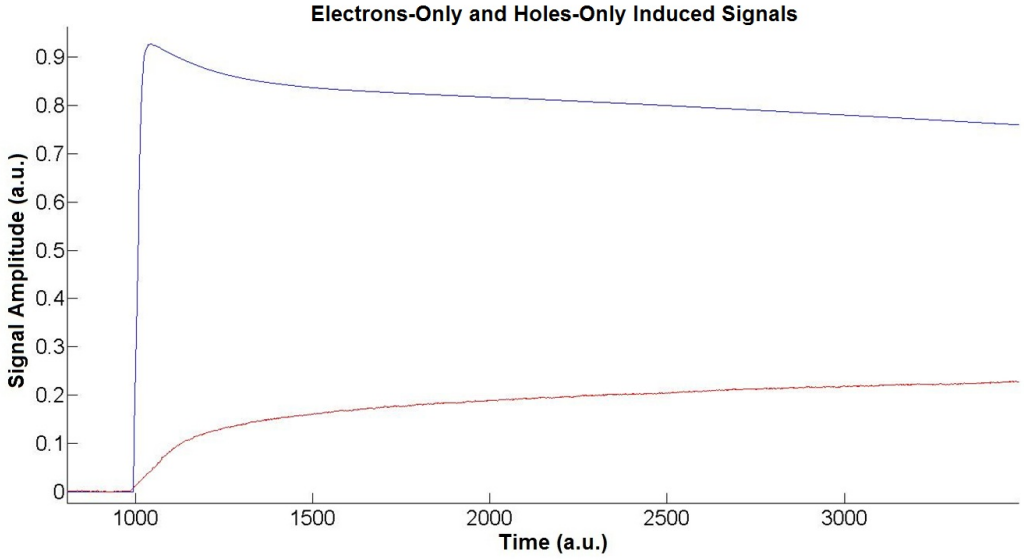

Figure 4.12: Electrons-only and holes-only induced signals deconvolved from measured signals.

Then, applying these steps to all measured signals, electrons-only and holes-only induced signals are calculated. Note that using this method, the decay due to the RC feedback circuit of the preamplifier is not removed, as shown in the electrons-only signal in Figure 4.12.

4.1.4 Compensating the RC Preamplifier Decay

The method described in Section 4.1.3 used to calculate holes-only signals did not need to remove the effect of the pre-amplifier decay, since this was kept in the deconvolved electrons-only induced signal. Holes-only induced signals were directly measured irradiating the cathode surface of these detectors with K_α X-rays produced by short pulsed lasers incident on a molybdenum target while operating these detectors at reverse bias. In order to remove the decay due to the preamplifier RC feedback circuit, it is required to measure the preamplifier response to a step function. In the

absence of a step function, the preamplifier response was approximated using the decay portion of the electrons-only induced signals measured when irradiating the cathode surface of the detector with α-particles, while operating the detectors at normal bias. Using a pulse generator would introduce systematic errors, since negative currents would be injected in the circuit during the fall of the pulse.

Holes-only induced signals are measured at fixed time intervals $s_1+s_2+s_3+\ldots+s_i$, for $i = 1 \ldots n$, where n was the total number of samples measured. Knowing the response function of the pre-amplifier $r_1 + r_2 + r_3 + \ldots + r_i$, the compensated signal $h_1 + h_2 + h_3 + \ldots + h_i$ is calculated according to Equation 4.8,

$$\begin{bmatrix} s_1 \\ s_2 \\ s_3 \\ s_4 \\ \vdots \\ s_i \end{bmatrix} = \begin{bmatrix} h_1 & 0 & 0 & 0 & \ldots & 0 \\ h_2 & h_1 & 0 & 0 & \ldots & 0 \\ h_3 & h_2 & h_1 & 0 & \ldots & 0 \\ h_4 & h_3 & h_2 & h_1 & \ldots & 0 \\ \vdots & \vdots & \vdots & \vdots & \ddots & \vdots \\ h_n & h_{n-1} & h_{n-2} & h_{n-3} & \ldots & h_1 \end{bmatrix} \times \begin{bmatrix} r_1 \\ r_2 \\ r_3 \\ r_4 \\ \vdots \\ r_i \end{bmatrix} \tag{4.8}$$

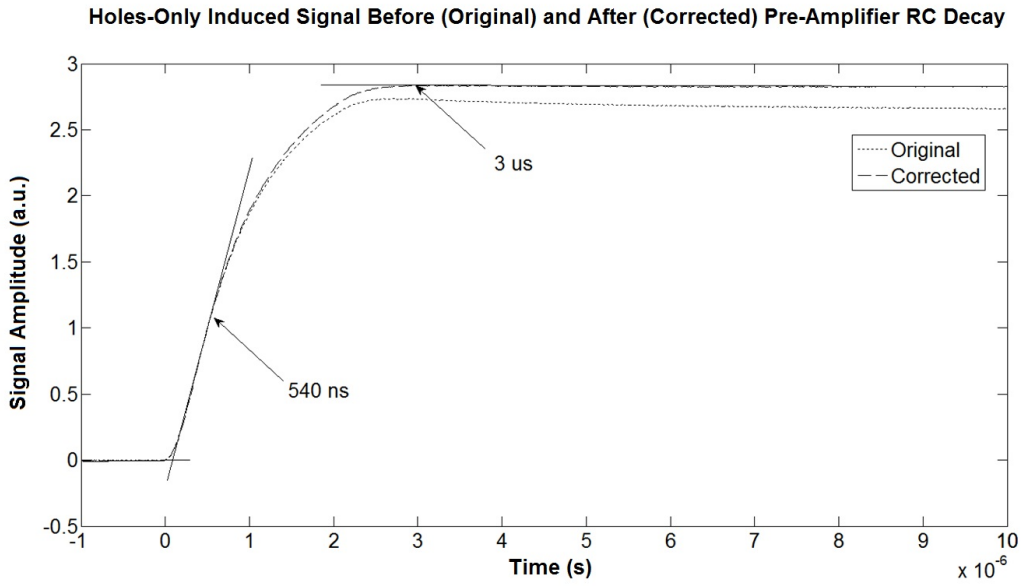

Figure 4.13: Holes-only measured by irradiating the cathode surface of these detectors with K_α X-rays produced by short laser pulses incident on a Molybdenum Mo target while operating these detectors at reverse bias, before and after pre-amplifier RC decay correction.

Figure 4.13 shows the original and corrected signals after the corrections given by Equation 4.8. Note that the system doesn't need to be inverted to find the values of $h_1 + h_2 + h_3 + \ldots + h_i$, since they can be easily determined in sequence.

4.2 Measurements

Holes-only induced signals were measured and hole transport properties of CdZnTe were calculated using two independent methods: using α-particles and K_α X-rays, according to the procedures described in Section 4.1. In these measurements, average hole trapping time τ_h and average hole detrapping times τ_{hD1} and τ_{hD2} were calculated.

4.2.1 Using Am-241 α-Particles

In these experiments, 5 mm thick CdZnTe detectors were irradiated using a 1 μCi Am-241 α-source (E_α = 5.486 MeV (85.2%) and 5.443 MeV (12.8%). The α-source was positioned close to the cathode surface and on the sides of the detectors, as described in Figure 4.14,

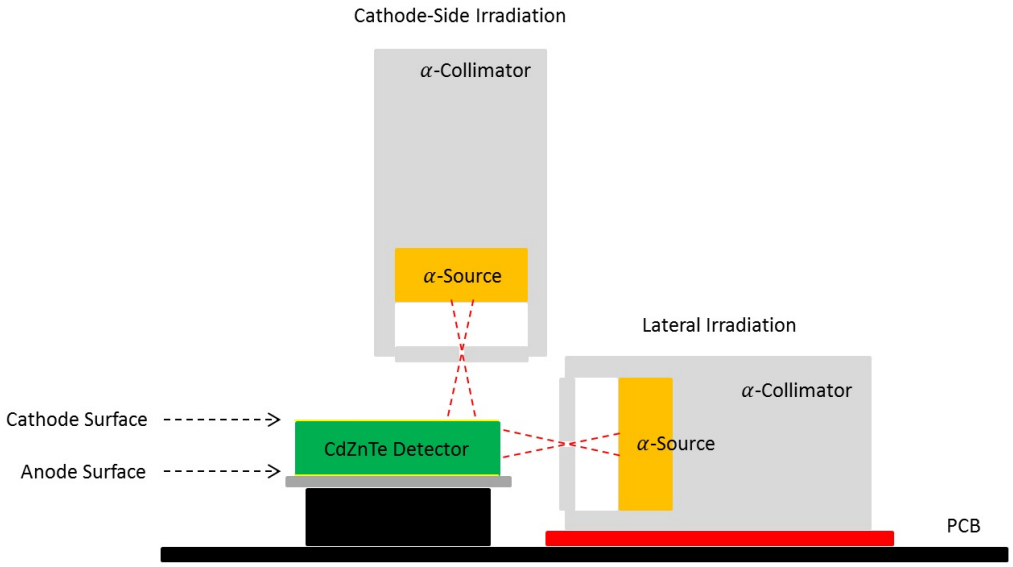

Figure 4.14: Schematic diagram of the experimental apparatus, showing the position of the semiconductor detector relative to the Am-241 α-source and collimator in both positions: Cathode-Side Irradiation and Lateral Irradiation.

Induced signals were measured using eV-509x preamplifiers connected to a GaGe Octopus 14-bit digitizer. Electrons-only induced signals were measured by placing the α-source close to the cathode surface. A collimator was used to measure these signals, as described in Figure 4.14.

Figure 4.15 shows an Am-241 α-spectrum, E_α = 5.486 MeV (85.2%), measured using this experimental setup. In these measurement, the data acquisition system was triggered by the anode (red) induced signals.

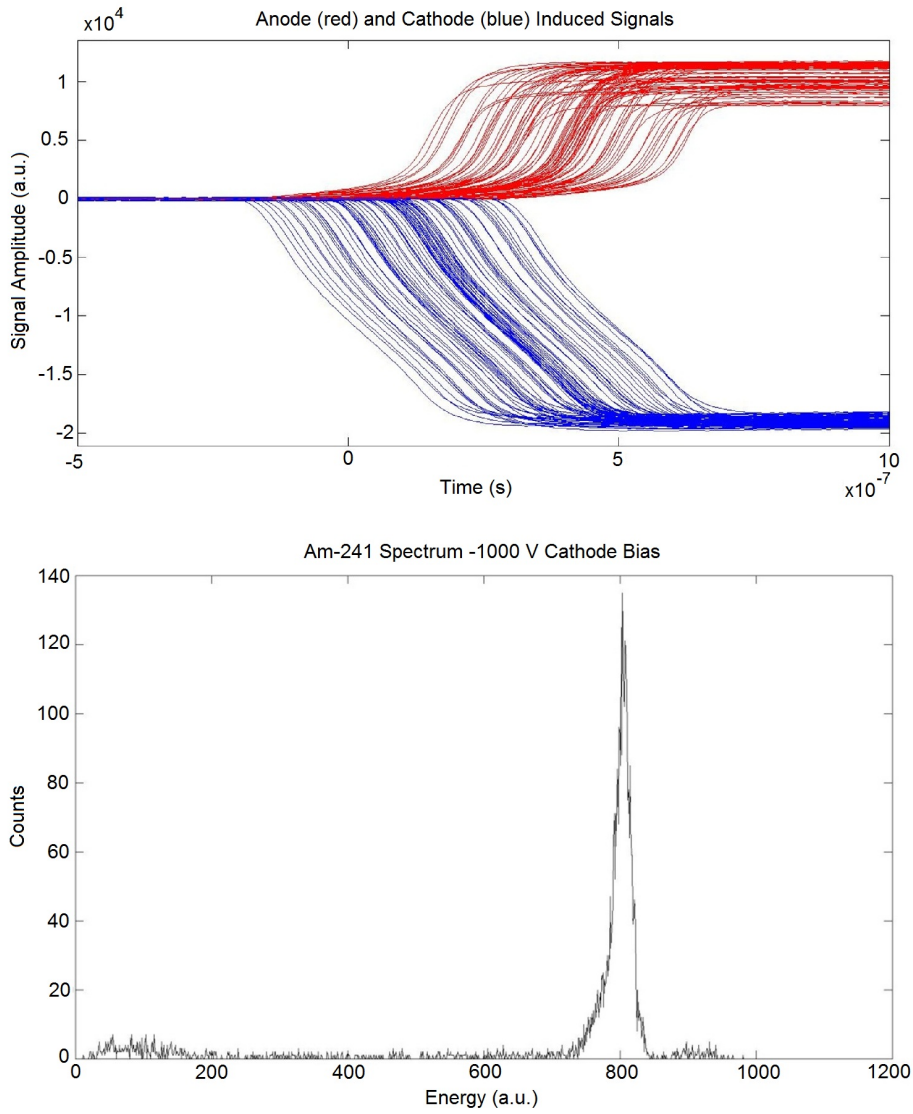

Figure 4.15: Anode pixel and cathode-induced signals when irradiating the cathode surface with Am-241 α-particles $E_\alpha = 5.486$ MeV (85.2%). The variation in amplitude for anode pixel induced signals is due to charge sharing events. Cathode-induced signals were used to calculate the α spectrum shown.

The spectrum was calculated considering cathode induced signals, while anode induced signals were used to trigger the digital acquisition system. The sampling frequency used was 125 MHz, which corresponds to sampling points every 8 ns. The larger amplitude variation of anode induced signals shown in Figure 4.15 is mostly due to charge sharing events Figure 4.16 shows the normalized averaged cathode induced

signals, i.e., the blue signals in Figure 4.15.

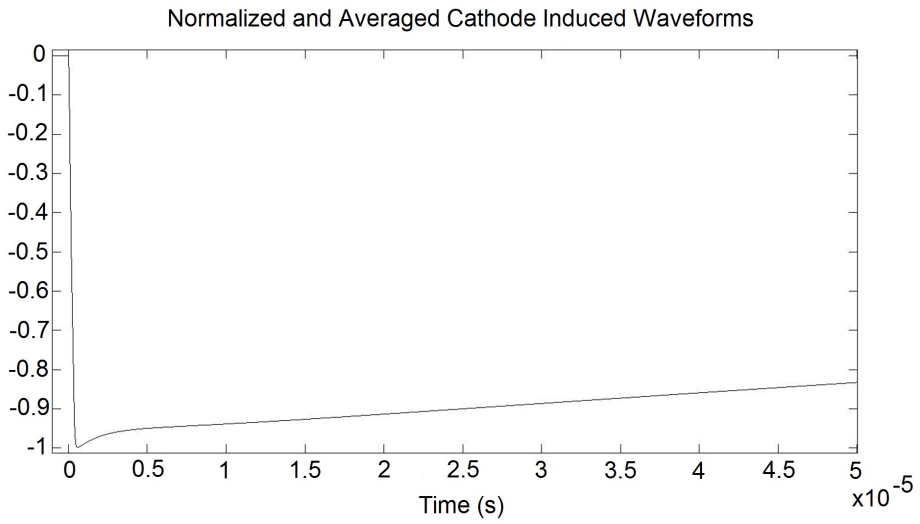

Figure 4.16: Averaged and normalized measured cathode-induced signal, irradiating the detector from the cathode-side.

The cathode induced signal shown in Figure 4.16 was used to determine electron transport properties, as shown in Figure 4.17. Figure 4.17 shows two distinct regions of electron drift velocity measured. The region close to the cathode surface with faster electron drift velocity is attributed to either a stronger electric field or less impurities. The region close to the anode surface with a slower drift velocity is attributed to either a weaker electric field or more defects in the material. Similar problems have been observed in other detectors manufactured by Redlen, indicating that this may be related with their fabrication process. Although it is assumed in this section that the field changes as a function of the position of the cloud, the presence of shallow trapping centers would also change the effective mobility of the charges. The values of the field in each region are calculated making the assumption that the field is uniform in each region and the electron mobility μ_e is constant, as described by Equation 4.9,

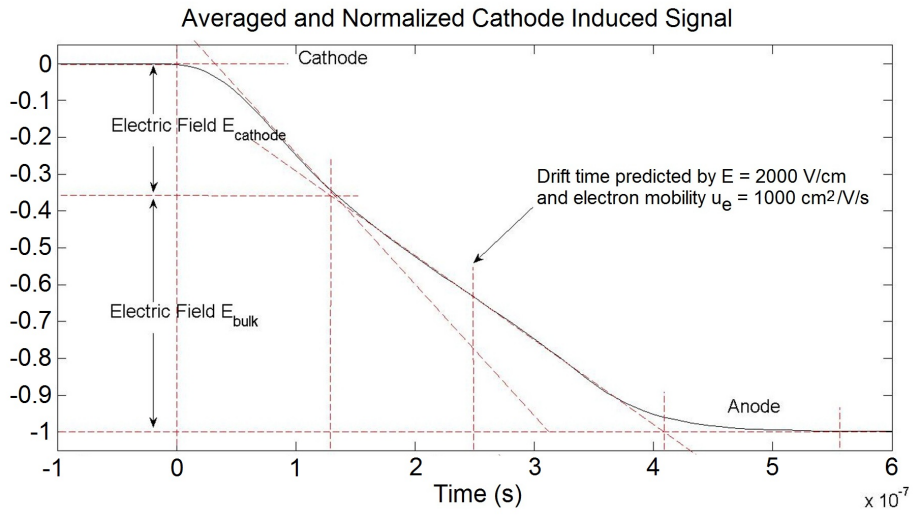

Figure 4.17: Normalized and averaged cathode-induced signal, showing two regions of electric field: stronger closer to the cathode surface ($E_{cathode}$) and weaker in the bulk region (E_{bulk}). The measured total electron drift time was 410 ns.

$$\begin{cases} 0.175 \times E_{cathode} + 0.325 \times E_{bulk} = 1000 \\ E_{cathode} = 1.16 \times E_{bulk} \end{cases} \tag{4.9}$$

where, the calculated values of $E_{cathode}$ and E_{bulk} were respectively 1894 and 2197 $\mathrm{V{\cdot}cm^{-1}}$. Thus, the calculated effective mobility of electrons was $\mu_e = 734\ \mathrm{cm^2{\cdot}V^{-1}{\cdot}s^{-1}}$. This calculated value was smaller than the expected electron mobility $\mu_e = 1000\ \mathrm{cm^2{\cdot}V^{-1}{\cdot}s^{-1}}$. This discrepancy is most likely to be caused by larger concentration of shallow defects close to the cathode surface. Another possible explanation for the non-uniform electric field observed in these detectors is the annealing treatment used by Redlen, which could introduce Te inclusions in the detector volume, creating shallow trapping centers in the material.

In order to acquire cathode induced signals from electrons-and-holes, signals were measured irradiating the sides of the detectors through the protective paint, as shown in Figure 4.14. The data acquisition system was triggered by signals induced by

electrons on the anode pixel. These α-particle interactions occurred close to the lateral surface of the detector, initially creating electron and hole pairs. Electrons drifted towards the anode and were mostly collected by the common-grid electrode, inducing a transient signal on the anode pixel electrode. Holes drifted towards the cathode and were collected by the cathode electrode, as shown in Figure 4.6.

The amplitude of the waveform induced on the anode pixel varied as a function of interaction depth x_i. This transient signal was also used to calculate the depth of interaction using time-of-flight measurements, as shown in Figure 4.18. The initial time is determined by either measuring the time when either A or A occurs, where A is measured post-processing the anode pixel induced signal and A' is measured post-processing the cathode induced signal. The time when the electrons are collected by the common grid electrode is determined by measuring when either C or C occurs, where C is measured post-processing the anode pixel induced signal and C' is measured post-processing the cathode induced signal. The best estimator for the drift time was chosen as the one that minimized the uncertainties in the measured parameters.

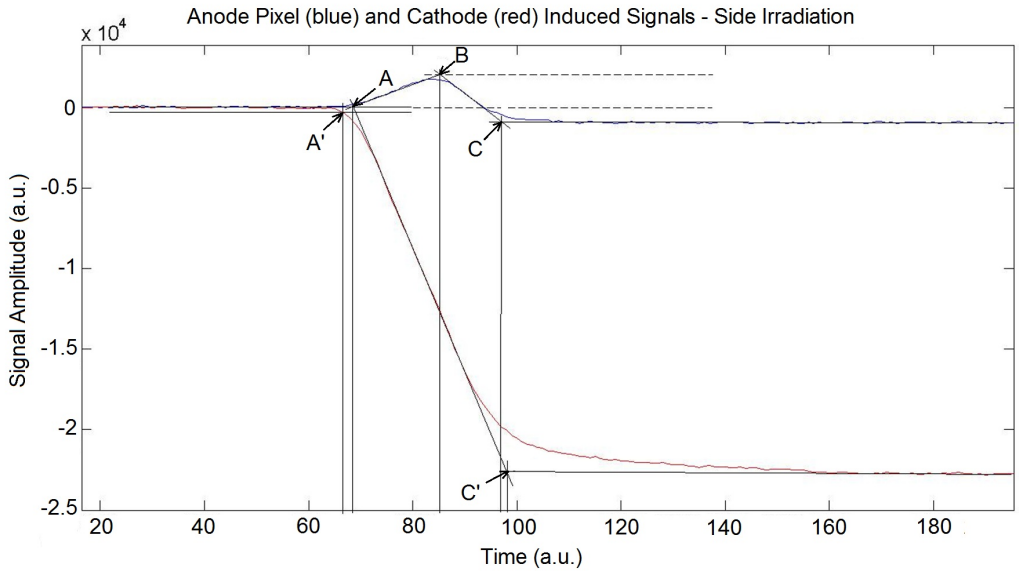

Figure 4.18: Anode transient signal induced on the anode pixel (blue signal) due to electrons being collected by the steering grid and cathode induced signal (red signal), showing the measured positions A, A', B, C and C'.

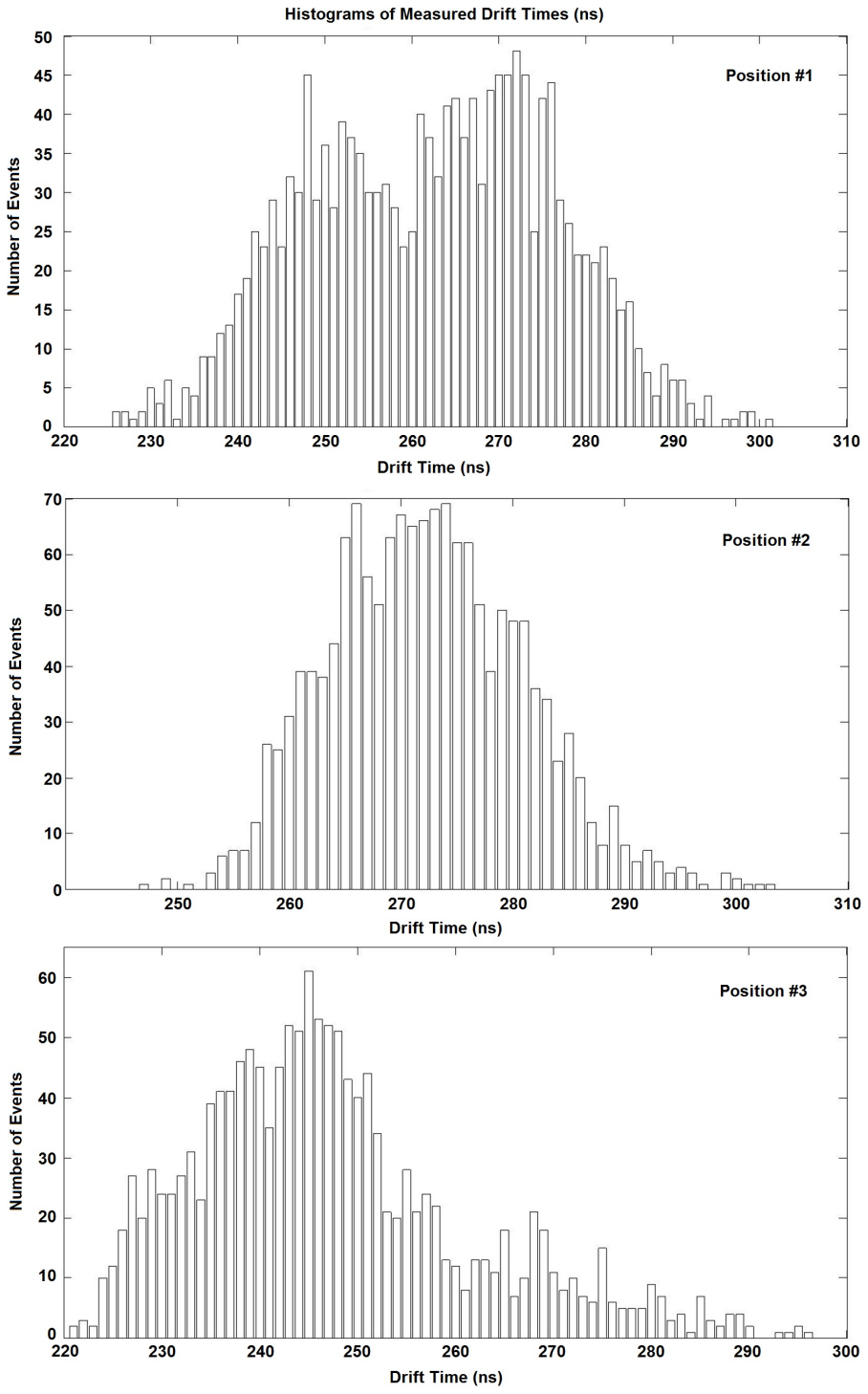

Figure 4.19: Histograms of measured drift time of electrons for three collimator positions x_i: positions 1, 2 and 3. Note that drift time close to 0 represent anode-side events, while drift times close to 410 ns represent cathode-side events.

The interaction time was estimated using the cathode induced signal A' while the collecting time was estimated using the anode pixel induced signal C. In these measurements, the α-source collimator was placed in three different positions and the calculated drift times were plotted in Figure 4.19.

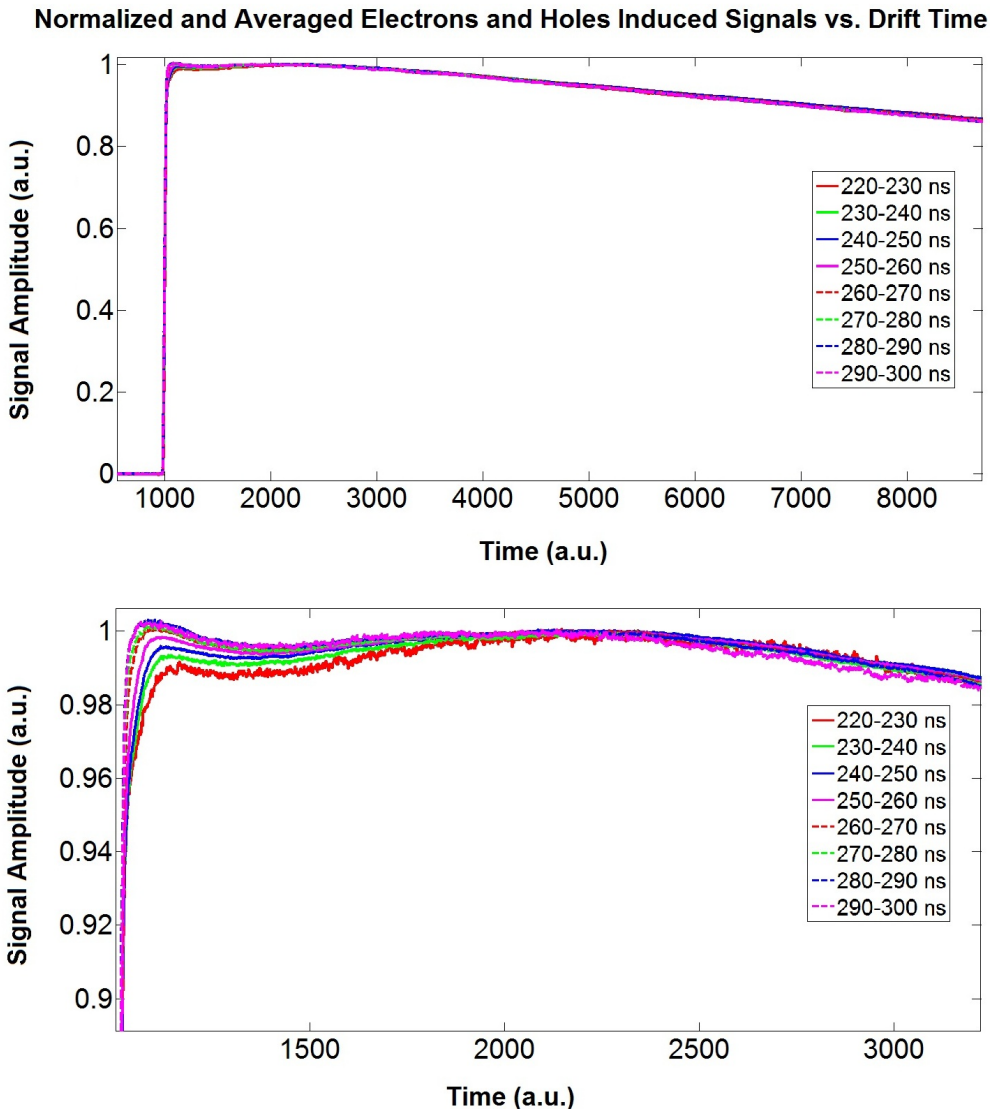

Figure 4.20: Averaged and normalized induced signals for position 1 as a function of calculated drift time.

Averaged and normalized induced signals for experiment position 1 were plotted in Figure 4.20 as a function of calculated drift time. Note that shorter drift times represent events closer to the anode. Plotted induced signals in Figure 4.20 were

normalized at peaking amplitudes measured between times $1500 < t < 4000$ units. It can be clearly seen the reduction in the relative amplitude of the electron component with respect to the hole component as a function of decreasing drift time. Also, the decay portion of these signals for time t> 3000 units did not change as a function of drift time. This was expected since for time t> 3000 units, only holes were expected to be inducing signals by trapping-detrapping mechanism.

The procedure described in Section 4.1.3 was used to deconvolve electrons-only and holes-only induced signals from measured signals. Results obtained are shown in Figure 4.21. Note that electrons-only induced signals maintain the preamplifier decay due to the feedback RC circuit. Adding electrons-only (blue signal) to holes-only (red signal) signals results in the combined signal (black signal) in Figure 4.21.

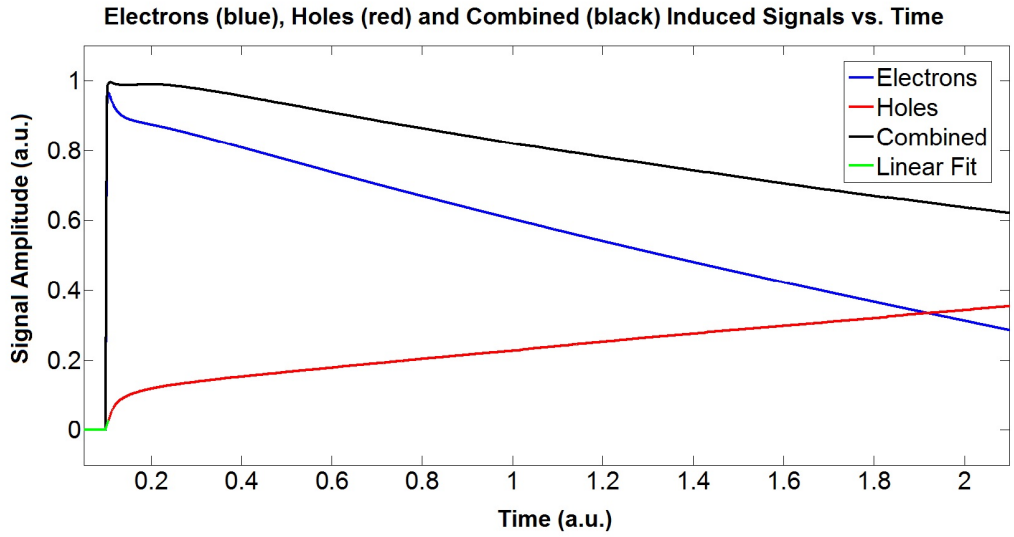

Figure 4.21: Deconvolved electrons-only and holes-only induced signals as a function of time when α-particles interact at the side of the detector.

Electrons-only and holes-only induced signal shown in Figure 4.22 were used to calculate electron and hole mobilities and average hole trapping time τ_h using the model described in Section 4.1.3. The amplitudes of the induced signals as described in Figure 4.22 were used to calculate hole trapping times τ_h based on results presented in Equation 4.6. The amplitudes were calculated at positions A and B, which

corresponded to the linear portion of the signals due to mostly by free carriers drifting.

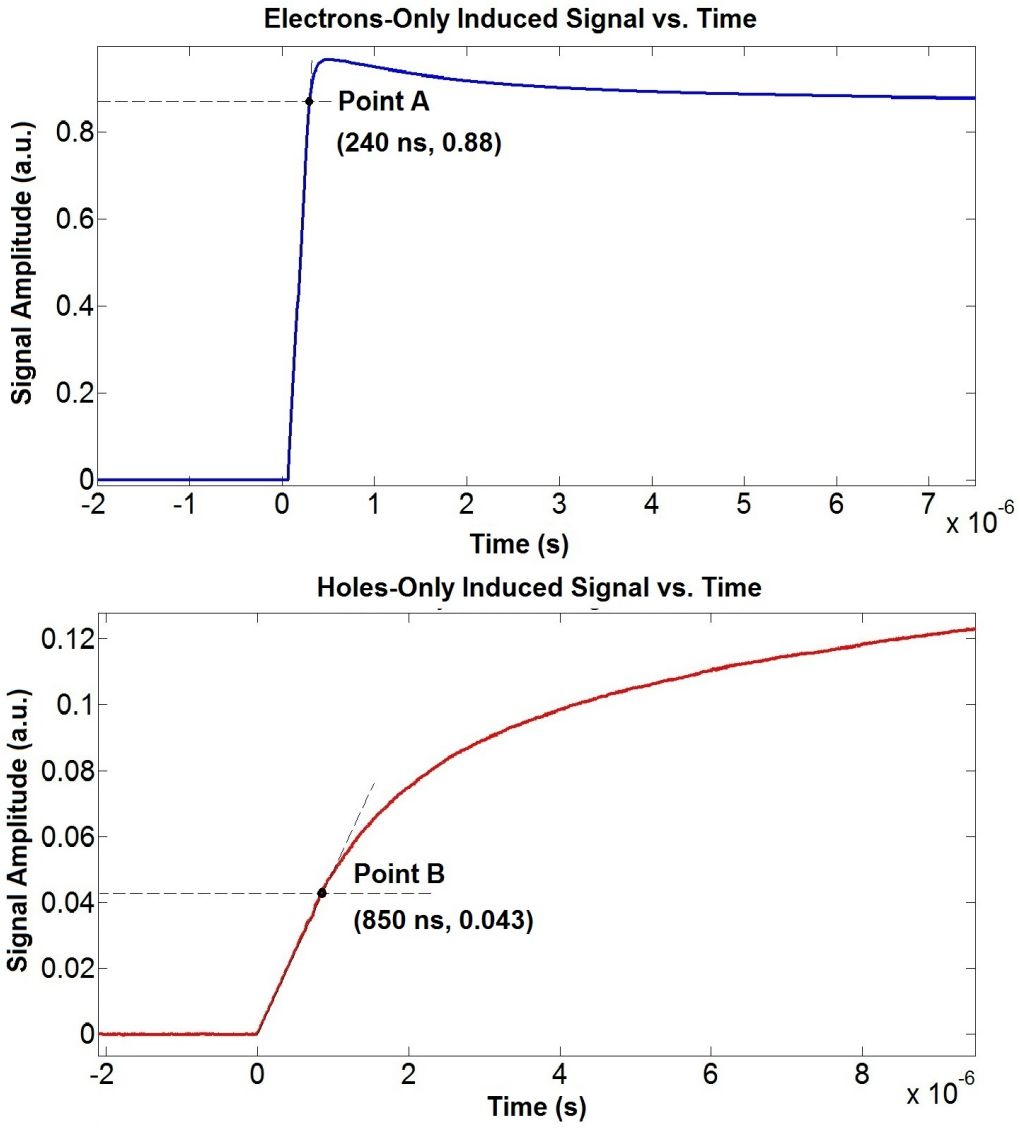

Figure 4.22: Deconvolved electrons-only and holes-only induced signals as a function of time when α-particles interact at the side of the detector.

According to results presented in Figure 4.22, assuming constant and uniform electric field $E = 2197$ V/cm, electron mobility $\mu_e = 830$ and hole mobility $\mu_h = 12$ cm^2/V/s were measured. In Figure 4.22, the average ratio between electrons-only and holes-only induced signal was ~ 20. Considering one electron and two holes trapping centers, Equation 4.6 can be re-written, but in the absence of better information on the density of trapping centers in the material, the calculated average hole trapping

times were assumed to be the same, $\tau_{h1} = \tau_{h2} = 430$ ns. Considering 10% error in measuring depth of interaction x_i and hole mobility μ_h results in ± 100 ns error in the calculated value for τ_h, using Equation 4.6, considering the worst case scenario. The other charge transport properties, average hole detrapping times τ_{hD1} and τ_{hD2}, were determined by direct comparison between measured and simulated holes-only induced signals. In Figure 4.23, simulated holes-only induced signals considered no, one and two hole trapping centers are shown.

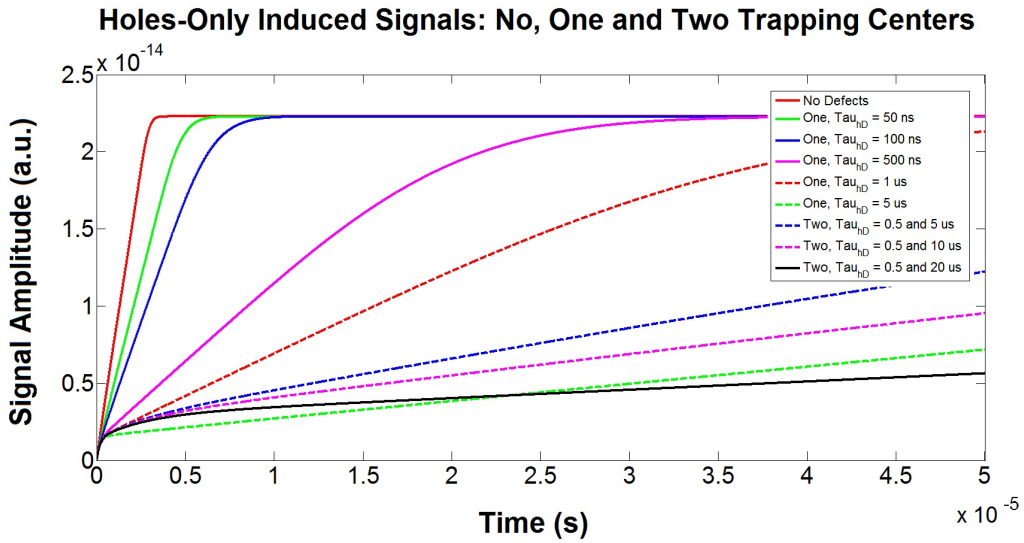

Figure 4.23: Simulated holes-only induced signals considering no, one- and two-hole trapping centers.

Modeling one hole trapping center is not sufficient to explain the measured induced signals. This can be observed by comparing measured holes-only induced signals shown in Figures 4.21 and 4.22 with simulated holes-only induced signals shown in Figure 4.23. In order to better match simulations with experiments, two hole trapping centers need to be modeled. Although it is known that CdZnTe can have more defect levels, only two hole trapping centers were considered in order to reproduce the measured induced signals with reasonable results. Also, the precision in our measurements using α-particles does not justify adding more trapping centers in the model. Then, two hole trapping centers were considered: one shallow and one deep

defect levels. Holes-only induced signals, black signal in Figure 4.23, are expected to have an initial linear rise due to free holes in excess of equilibrium followed by a non-linear induced signal from trapping and de-trapping mechanisms of shallow and deep trapping centers. These two trapping centers represent average values for shallow and deep defect levels in the material. Figure 4.24 shows the measured and simulated induced signals and the calculated average hole trapping and detrapping times using α-particles.

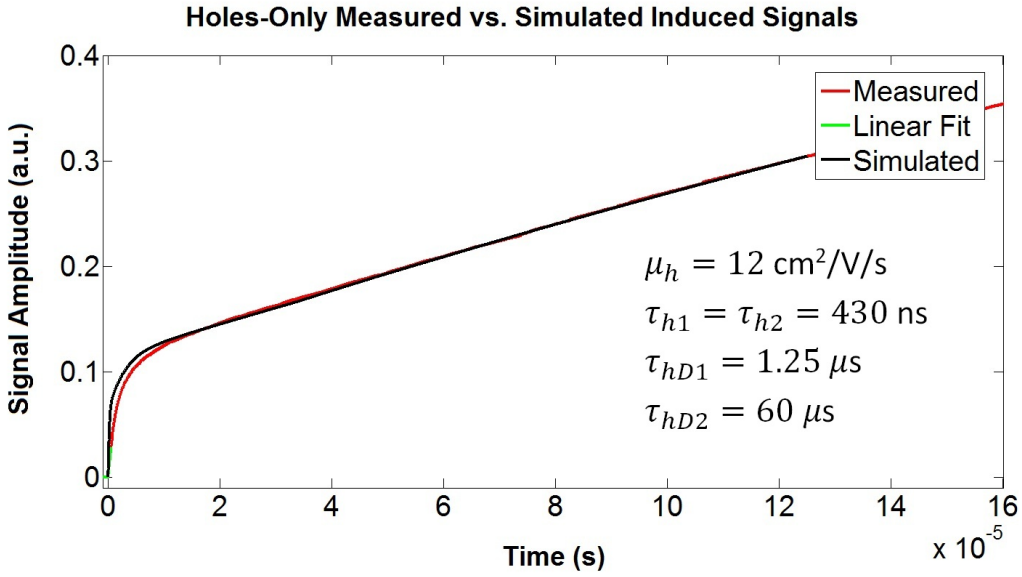

Figure 4.24: Measured and simulated holes-only induced signals and the calculated average hole trapping and detrapping times.

4.2.2 Measurements Using K_α X-Rays

In collaboration with the High Field Science group at the Center for Ultrafast Optical Science (CUOS), experiments were set up to measure directly holes-only induced signals. This was achieved by irradiating the large electrode with K_α X-rays produced by a picosecond high-power laser striking a molybdenum target while operating the detectors at reverse bias. In these experiments, the detector was operated at reverse bias, applying +1000 V to the cathode electrode while all other electrodes were kept grounded. Once these laser pulses struck the target, they produced almost

instantaneously K_α X-rays in 2π field of view, as described in Figure 4.25.

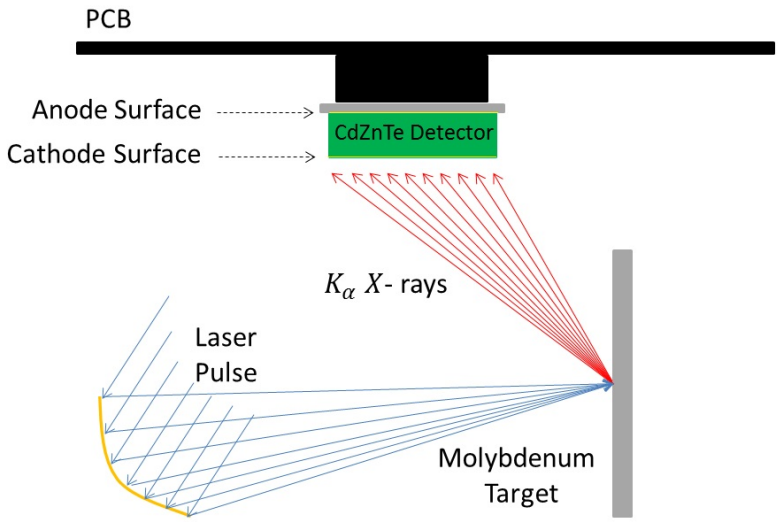

Figure 4.25: Diagram showing the experimental apparatus used to measure K_α X-rays. Since the Molybdenum target was kept at high vacuum, there was a Beryllium window between the target and the detector to minimize X-ray attenuation.

The detectors used to measure the K_α X-rays were the same used in the high-flux experiments. For the reasons described in Section 4.2.1, only hole transport properties were measured using this technique. Direct measurement of holes-only induced signals were achieved by measuring large signals produced by the K_α X-rays incident on the entire area of the large electrode. During these measurements, it was necessary to keep their amplitudes within the dynamic range of the data acquisition system and pre-amplifiers. This was achieved by adding different filters in the laser beam in order to reduce the power of the laser. The signals induced by K_α X-rays produced by laser were measured with amplitudes $\sim 10\times$ larger than the signals induced by α-particles, giving a better signal-to-noise ratio (SNR). Although the signals induced by the K_α X-rays had higher amplitude than the signals produced by the α-particles, the specific density of charge using the X-rays was much lower than using the α-particles. In these measurements, the entire cathode surface was irradiated by the X-rays while a very small region of the detector is irradiated by α-particles.

Results produced using X-rays were more reliable than results obtained with α-particles due to the following reasons:

a) X-rays interact deeper in the material, reducing surface defects

b) X-rays produce lower specific charge density, reducing undesirable charge cloud self-shielding effects

In these experiments, it was observed a large fluctuation in the amplitude of the signals induced by the K_α X-rays. Measured induced signals are plotted as a function of signal amplitude in order to check whether charge transport properties changes as a function of signal amplitude, as shown in Figure 4.26. Figure 4.27 shows results of induced signals measured from 500 to 14000 ADC units, where no significant difference between them is observed. Then, all induced signals were combined, normalizing the amplitudes, and hole trapping and detrapping properties were measured, as described in Figure 4.28.

Note that the compensation for the decay due to the preamplifier feedback circuit described in Section 4.1.4 is applied to correct these signals. This is an important step, because the duration of these measurements is on the order of ~ 400 μs, which is comparable to the measured preamplifier decay time constant $\sim RC = 320$ μs.

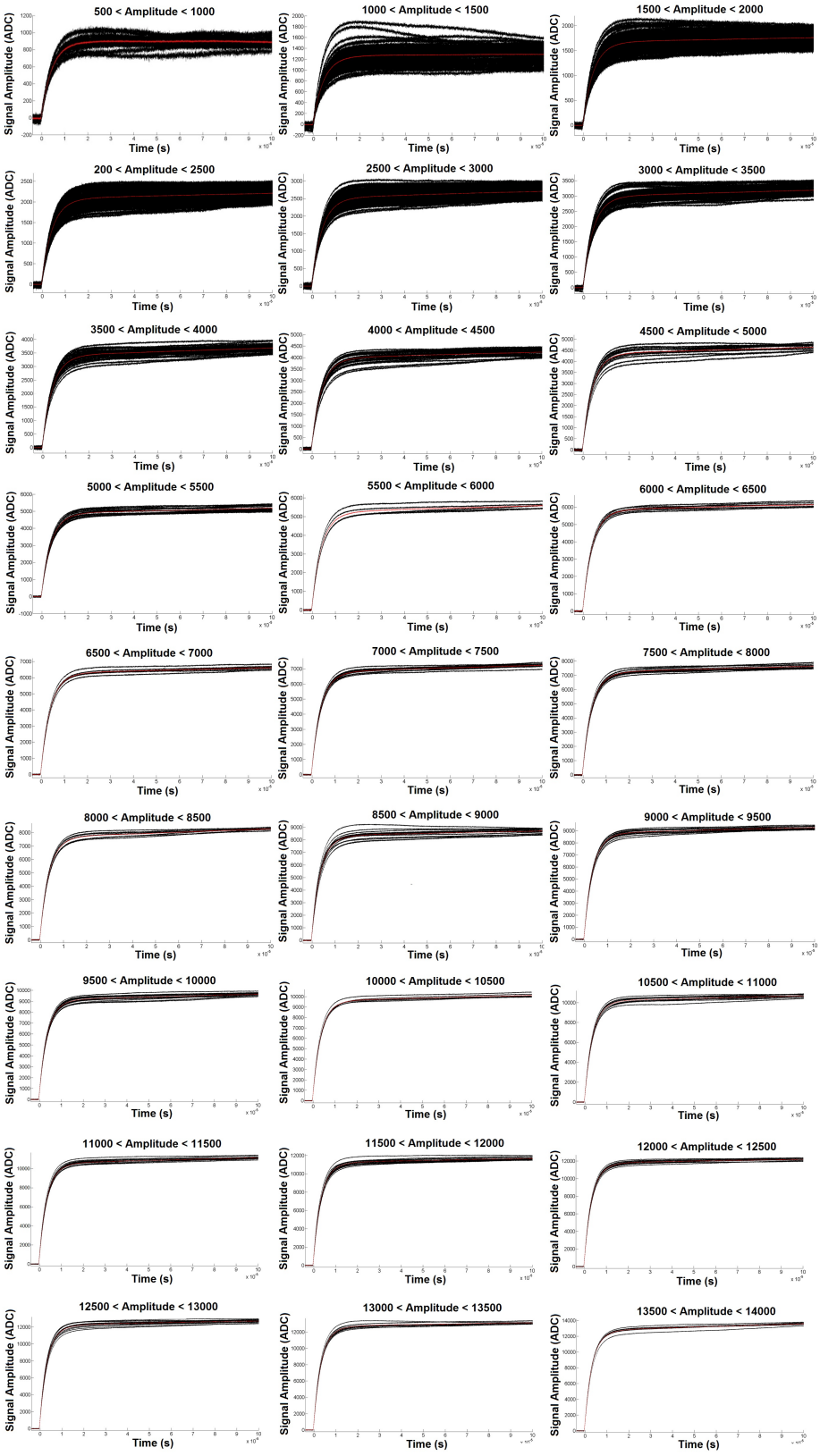

Figure 4.26: Measured holes-only induced signals by irradiating the cathode surface with K_α X-rays while operating the detector at reverse bias for signal amplitudes varying from 500 to 14 000 ADC units.

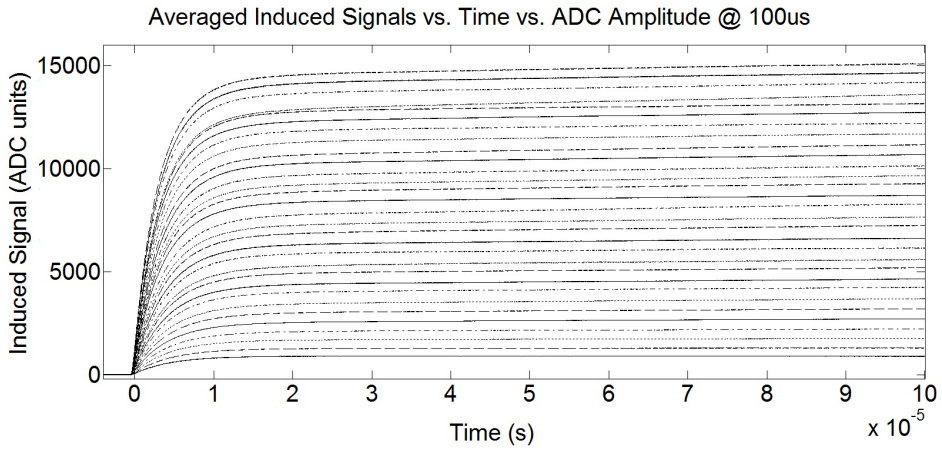

Figure 4.27: Measured averaged holes-only induced in every 500 ADC steps by irradiating the cathode surface with K_α X-rays while operating the detector at reverse bias.

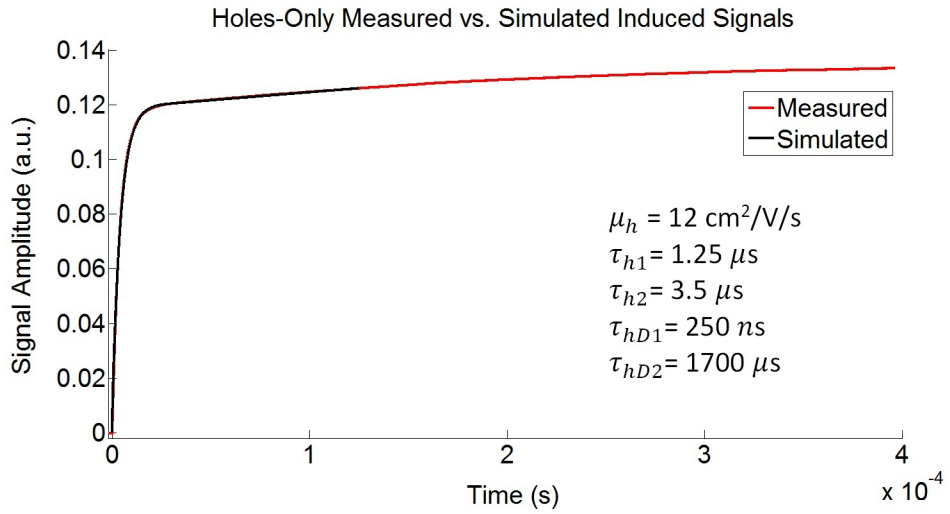

Figure 4.28: Measured and simulated holes-only induced signals and the calculated average hole trapping and detrapping times by irradiating the cathode surface with K_α X-rays while operating the detector at reverse bias.

4.3 Analysis of Results Using Proposed Technique

Statistical models described in Section 4.1.1 considered one electron and one hole trapping centers. In reality, CdZnTe is known to have multiple electron and hole trapping centers, *Hermon et al.* (2001), *Hermon et al.* (1999) and *Schieber et al.*

(2001). In Section 4.1.2, considering multiple hole trapping centers and assuming the same density of defects in all trapping centers, would produce the same result in terms of average hole trapping time. In future work, more detailed models considering multiple trapping centers with different densities of defects should be considered, which would change the ratios between electrons-only and holes-only induced signals.

Results described in Sections 4.2.1 and 4.2.2 are summarized in Table 4.2. In Figure 4.24, charge transport properties were calculated considering the same average hole trapping time for both defect levels considered. This was one reason why the matching between simulated and measured holes-only induced signals for time intervals less than $\sim$ 20 μs was not accurate. In Figure 4.28, the assumption of having the same density of defects for both defect levels was relaxed. These results produced better fitting, which indicates that the initial assumption considering the densities of different defect levels constant for all trapping centers may not be true. Also, measured signals using K_α X-rays while operating the detector at reverse bias showed better signal-to-noise ratio, which enabled the measurement of induced signals for longer periods of time $\sim$ 400 μs. In these measurements, there is a weak indication that considering a third hole defect level might be necessary to better represent the transport properties of holes in CdZnTe in future high-flux studies.

Property	α-Particles	K_α X-rays
Hole Mobility μ_h (cm^2/V/s)	12	12
Avg. Hole Trapping Time (shallow) (ns)	430	1250
Avg. Hole Trapping Time (deep) (ns)	430	3500
Avg. Hole Detrapping Time (shallow) (μs)	1.25	0.25
Avg. Hole Detrapping Time (deep) (μs)	60	1700

Table 4.2: Calculated average electrical transport properties of CdZnTe detectors used in high-flux experiments.

CHAPTER V

High-Flux Experiments

High-flux experiments using a JL Shepherd & Associates 3 Ci (09-20-2001) Cs-137 irradiator and a custom built experiment apparatus were conducted in the Ford Nuclear Reactor (FNR) building at the University of Michigan, as described in Section 5.1. The main objective of these experiments was to understand problems caused by positive space charge build up as a function of irradiation flux and time in CdZnTe detectors, the so-called *polarization effect*. The framework developed in this work used a Cs-137 γ-source rather than conventional X-ray tubes. In future work, the same methodology should be adapted to other sources, such as an X-ray tube, different detector materials, geometries, electrode configurations and different incident fluxes. The hardware used to acquire data in the high-flux experiments as well as details of the collimator and detectors used are described in Sections 5.1.2, 5.1.3 and 5.1.4. High photon fluxes Φ were produced in these experiments changing the distance between the source and detector.

In these experiments, signals induced on electrodes were digitized in continuous mode using commercial digitizers from GaGe Inc. These signals were post-processed using a 1D edge detection algorithm, as described in Section 5.2, *Mitiche and Davis* (1982) and *Davis and Mitiche* (1979). Initial experiments using the 3 Ci Cs-137 irradiator showed that detectors polarized before reaching the maximum achievable flux

which corresponded to the minimum possible distance between source and detector. Then, in order to understand this phenomenon, temporal evolution of the detector's response as a function of incident radiation flux was measured from $t = 0 \ldots 25.6$ s and $\Phi = 0 \ldots 219\ 000$ photons/pixel/s. Preliminary experiments showed photopeak shifts towards lower energy bins and spectral degradation as a function of increasing incident radiation flux, as described in Section 5.3.2.

A series of experiments were conducted, where the design of the experimental apparatus evolved over time in multiple interaction cycles. The main objective of these experiments was to gradually cause polarization in these detectors and study the causes of this phenomenon. Due to the non existence of fully pixelated electronic readout systems capable of acquiring simultaneous data from all pixels at high-flux irradiation, in this initial studies it was difficult to assess 3D space and time solutions of this problem.

5.1 Experimental Apparatus

Preliminary studies determined that a system capable of acquiring hundreds of thousands of photons/pixel/s was required in this work. Unfortunately, even until today, such system is not commercially available, and is under development by different research groups and ASIC manufactures. Limited time and resources narrowed down the choices of readout systems available to conduct this work. The alternative solution found was to use commercially available digitizers in *continuous mode*, such as the Octopus family of multi-channel digitizers developed by GaGe Inc., as seen in Figure 5.1.

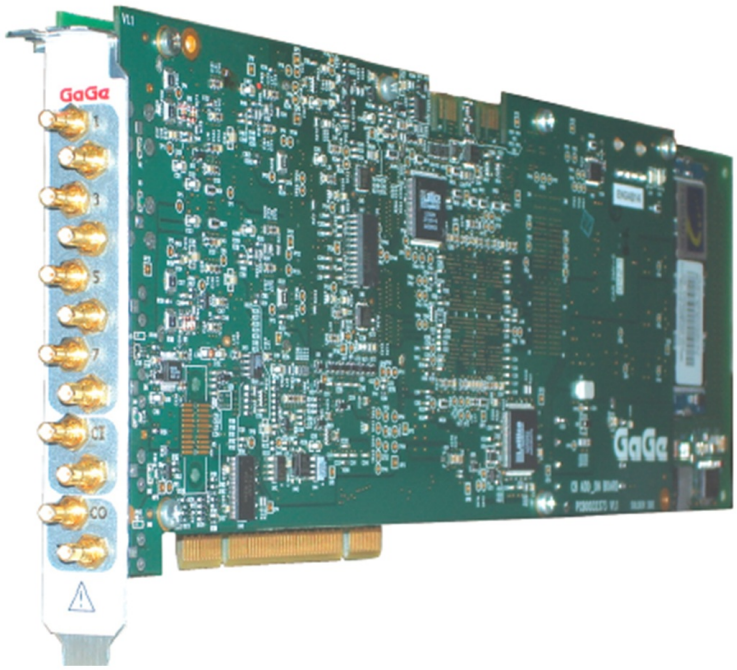

Figure 5.1: GaGe Octopus multi-channel digitizer, featuring 4 or 8 channels, from 128 MB up to 16 GB of on-board acquisition memory, and up to 125 MS/s sampling per channel on a single-slot PCI express card.

In continuous mode induced signals measured by eV-509 preamplifiers were continuously digitized for long periods of time, limited only by the amount of on-board memory available on the digitizer. The entire system was mounted on a mobile cart, as shown in Figure 5.2, consisting of: a) Instrument cart, b) Personal computer, c) GaGe Octopus digitizers, d) Digital oscilloscope, e) Test box containing the CdZnTe detector and eV-509 pre-amplifiers, f) XY translation stage, g) Custom built Pb-collimator w/ Am-241 α-source , h) MCA, i) GPIB interface, j) High voltage supply, k) DC power supply, l) NIM amplifiers, m) NIM pulse generator, cables, no-break, high-precision table and other smaller components. Gage Octopus multi-channel digitizers used in these experiments were equipped with large amount of on-board memory, capable of acquiring up to 128 MS in single channel operation.

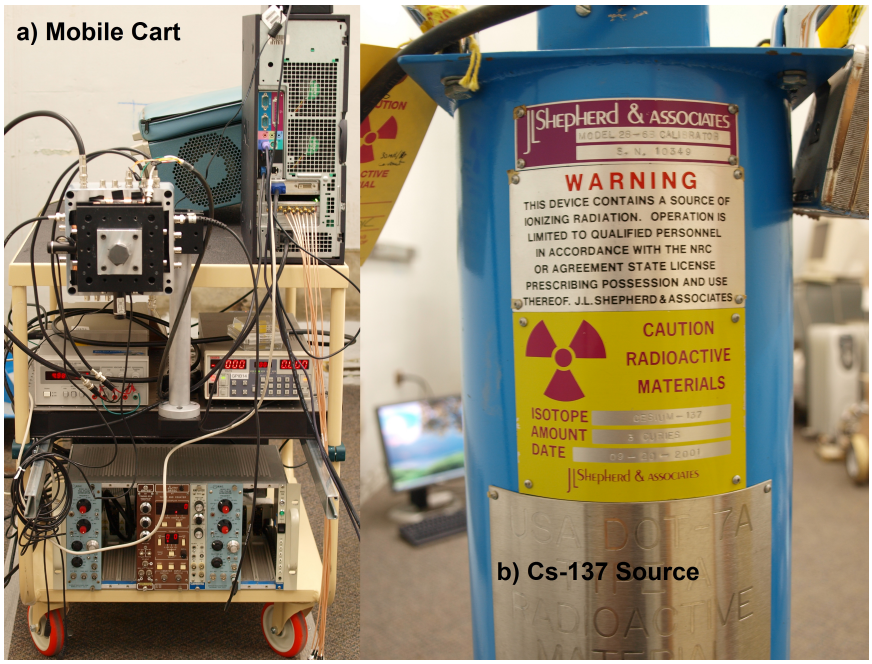

Figure 5.2: Experimental apparatus: a) mobile cart, containing the detector and data acquisition system, b) JL Shepherd & Associates 3 Ci (09-20-2001) Cs-137 irradiator.

5.1.1 High-Flux Sources

In order to receive authorization to operate the high activity Cs-137 irradiator in the Ford Nuclear Reactor (FNR) building, a safety protocol was written and submitted to the Occupational Safety & Environmental Health (OSEH) department at the University of Michigan. These experiments were conducted in room 2108 FNR.

The Cs-137 γ-source was chosen to study the so-called polarization effect for two main reasons: a) monoenergetic γ-ray source emission, b) commercial availability. These were ideal characteristics to conduct this study. Photopeak shifts and spectral degradation as a function of incident radiation flux and time were easily measured using the Cs-137 source. Also, due to its higher energy, Cs-137 γ-rays polarized the detectors at lower irradiation flux. Sources with energies, such as X-ray sources, would produce less charge carriers per average incident photon, *Knoll* (2010).

In order to monitor the internal electric field during these experiments, a 1 μCi

α-source was placed inside the collimator, positioned between the Cs-137 source and the detector, in close proximity to the cathode surface, as described in Figure 5.3.

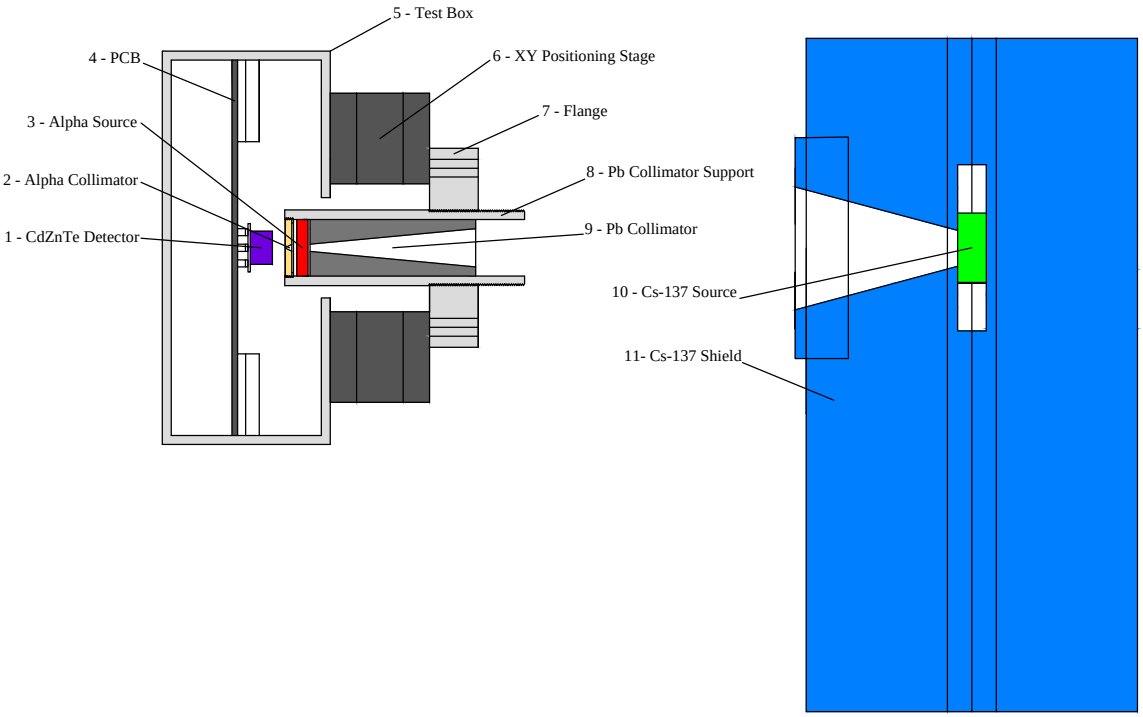

Figure 5.3: Diagram showing the relative position of the α and Cs-137 sources and collimators with respect to the CdZnTe detectors.

The XY translation stage shown was used to align the center of the collimator with the center of the anode pixel. The positioning system was also capable of changing the distance between the Am-241 α-source E_α=5.485 MeV (84.5%) and 5.443 MeV (13.0%) and the detector during the calibration of the system.

5.1.2 Data Acquisition Hardware

Modern multi-channel high-speed digitizers enabled acquisition and storage of waveforms induced on 3D position sensitive CdZnTe pixelated semiconductor detectors at high sampling rates. While analog systems use fast and slow shapers combined with peak-and-hold and timing pick-off circuits to obtain two data values, time and

energy, for each particle interaction, high-speed digitizers are able to store the entire signal, sampled at a constant time interval, providing more detailed information about the induced signal itself.

In more recent years, the operation of these devices under high irradiation flux ($\sim 1 \times 10^8$ photons/cm^2/s) has been pursued, *Bale and Szeles* (2008). In order to study the polarization effect and the behavior of these devices under high-flux irradiation, the commercial multi-channel high-speed digitizer used in this work acquired data in continuous mode. This system was tested at fluxes as high as $\sim$ 220k photons/pixel/s. The total time of acquisitions in each experiment varied as a function of selected sampling rate and number of active channels in the GaGe system, as described in Table 5.1. Sampling rates as high as 125 MS/s were used to acquired data. Additional post-processing steps were required to extract individual events from continuous acquired waveforms, as described in Section 5.2.1.

# of Active Channels	125 MS/s	100 MS/s	50 MS/s	25 MS/s	12.5 MS/s	10 MS/s
1	1.024	1.280	2.560	5.120	10.240	12.800
2	0.512	0.640	1.280	2.560	5.120	6.400
3	0.341	0.427	0.853	1.707	3.413	4.267
4	0.256	0.320	0.640	1.280	2.560	3.200

Table 5.1: Total acquisition time (s) as a function of sampling rate and number of active channels in the GaGe system, considering 128 MB on-board memory.

Results shown in this work were acquired at room-temperature using two active channels, one for the cathode and one for one anode pixel, using 25 MS/s sampling rate, as seen in Figure 5.4. Using this sampling rate enabled the acquisition of induced signals for 2.56 s in continuous mode in each experiment, as described in Section 5.2. Appendix A shows these measured signals at -750, -1000, -1250 and -1500 V applied cathode bias voltages and fluxes varying from $\Phi_1 = 39.3$k, ..., $\Phi_{11} = 219.3$k photons/pixel/s, while Fig.5.4 shows these results for -1000 V cathode applied voltage and flux $\Phi = 129.3$k, $\Phi = 147.3$k, $\Phi = 165.3$k, $\Phi = 183.3$k, $\Phi = 201.3$k and $\Phi =$

219.3k photons/pixel/s. In these figures, it is observed that anode induced signals completely vanish at fluxes higher than a critical flux. This is caused by the reduction of the internal electric field E due to positive space charge build up. It is also observed that although anode induced signals vanish, this effect is not caused by any preamplifier saturation as one would suspect. In contrary, this is solely caused by the internal electric field being reduced as a function of irradiation flux and time.

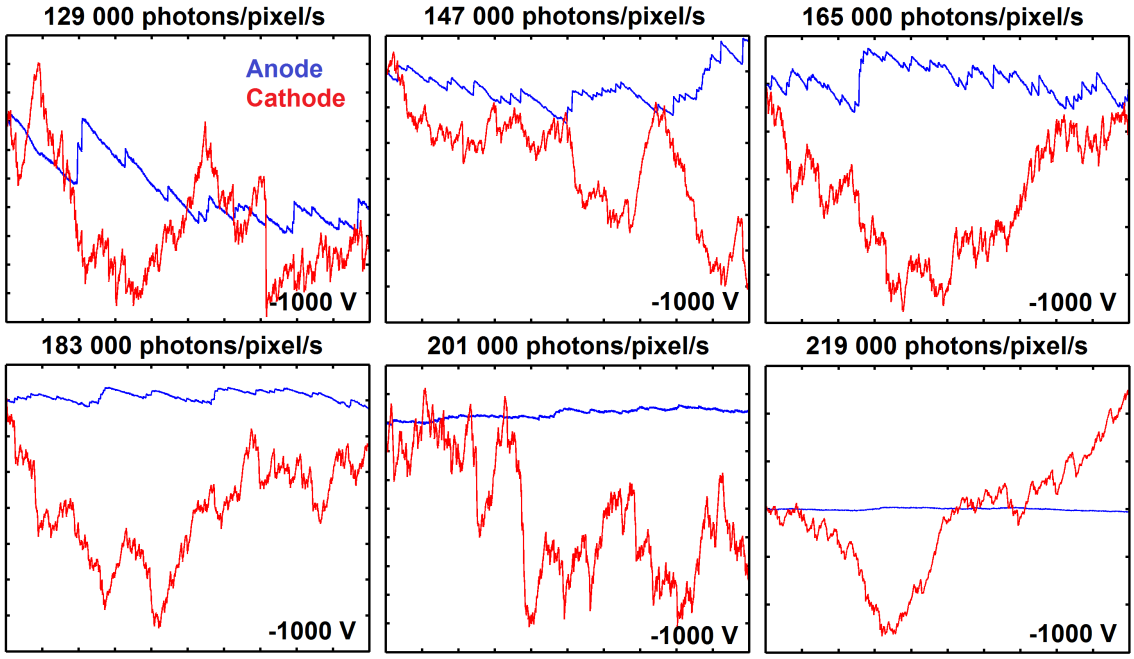

Figure 5.4: Anode and Cathode induced signals acquired in continuous mode at -1000 V cathode bias voltage and flux Φ = 129.3k, Φ = 147.3k, Φ = 165.3k, Φ = 183.3k, Φ = 201.3k and Φ = 219.3k photons/pixel/s.

5.1.3 The Lead Collimator Design

Initial experiments without collimators showed that the polarization occurred at lower fluxes compared with later results using collimators. The collimator was designed in order to minimize the number of events induced on the cathode electrode while measuring the polarization of the detectors with the 3 Ci Cs-137 irradiator, thus avoiding cathode pre-amplifier saturation. Also, without the collimator, cath-

ode induced signals measured at high-flux were piling-up due to γ-rays interacting in a large region of the detector volume. Relying on the cathode induced signal to measure depth of interaction during high-flux irradiation is not possible. Future techniques relying on induced signals on neighbor pixels need to be implemented to measure depth of interactions if 3D-position-sensitive information is desired.

The collimator was made of lead, drilling a conical hole in a cylindrical block of lead with $\sim 7^o$ internal angle as described in Figure 5.3. The final design has two compartments for placing small disk sources, one before and another after the collimator. The first compartment, closer to the detector, is intended for an α-source, positioned between the collimator and the detector, having a small α-collimator made of polytetrafluoroethylene (PTFE). The second compartment is on the opposite end of the collimator, for a small γ-source. The collimator was attached to the XY positioning stage, and a Co-57 disk source was used to align the system in the laboratory, avoiding unnecessary exposures to radiation in the high-flux irradiation room. Using this system, the center of the irradiation beam was aligned to be coincident with the center of the anode pixel. This was achieved by measuring Co-57 spectra in small X and Y increment steps in order to determine the geometric center of the pixel.

5.1.4 CdZnTe Detectors

Commercial $20 \times 20 \times 5$ mm^3 CdZnTe detectors manufactured by Redlen Inc. for medical applications were used in these experiments. These were common grid type detectors, where the *small pixel effect* enabled the operation in single charge sensing mode. Low-flux commercial spectroscopic grade CdZnTe detector materials suffer from poor hole electrical transport properties. Since these detectors were not manufactured for high-flux applications, these poor hole electrical transport properties limited their performance at high-flux irradiation. In future spectroscopic systems using CdZnTe detectors manufactured for high-flux applications, requiring good en-

ergy resolution relying on the small pixel effect, need to be manufactured with better hole transport properties.

In order to understand current limits of operation of CdZnTe detectors used in the high-flux experiments, more emphasis was given to hole electrical transport properties. The problem found on current CdZnTe detectors under high-flux scenarios is related with the large number of deep defect levels introduced in the material, which is known to be plagued by shallow defect levels, *Dieguez* (2011). These defects are introduced in the material during the fabrication and annealing processes in order to pin the Fermi level near the middle of the band-gap to reduce the leakage current and increase the operating field. Improved hole electrical transport properties should enable new CdZnTe detectors to reach higher flux limits. In future CdZnTe detectors for high-flux applications, new and optimized algorithms and methods need to be developed in order to take full advantage of all information available in 3D-position-sensitive devices, which can be useful in future imaging applications, such as spectroscopic CT and PET systems. Then, a fine balance between electrical hole transport properties, signal induction and electrode configuration should exist targeting specific applications. Results presented in this work were measured at different cathode bias voltages, having pixels either connected to pre-amplifiers or grounded and having the common grid electrode grounded during all measurements.

5.2 Data Acquisition

Since there are no known commercial systems capable of reading out either analog or digital signals from fully pixelated CdZnTe detectors under high-flux irradiation ($\sim 1 \times 10^8$ photons/cm^2/s), a continuous data acquisition system using a commercial digitizer manufactured by GaGe Inc. was used in this research. The total acquisition time is limited by the number of active channels read out simultaneously and the sampling rate, as described in Table 5.1. GaGe Octopus digitizers were chosen due

to their fast sampling rate (up to 125 MHz), large on-board memory (up to 16 GB), relative large number of channels (up to 8 in each card) and the capability of pairing multiple cards in a single system if more channels are needed to be read out simultaneously. These characteristics enable the acquisition of signals from multiple channels for relative long periods of time, as described in Section 5.3. Also, GaGe systems are flexible in respect to the acquisition of signals in multiple computer platforms and softwares, such as Labview, MATLAB and C++.

The GaGe cards used in this work had 256 MB of on-board memory installed, which enabled the acquisition of 128 MS using a single channel in continuous mode operation. At the highest sampling rate (125 MS/s), sampling in every 8 ns, the total acquisition time using a single channel was 1.024 s. Since the objective of this work was to study the polarization as a function of irradiation flux and time, longer acquisitions were required. During the high-flux experiments, no memory effect was observed seconds after each consecutive irradiation, even when these detectors were polarized in previous experiments. The solution found in order to acquired signals for longer periods of time was to combine several shorter experiments into a single long experiment. The sampling rate was reduced to 25 MS/s which enabled the acquisition of signals for 5.12 s in single mode and 2.56 s in dual mode, as described in Table 5.1. Using this setting, the system was able to acquire signals for 25.6 s of total acquisition time combining 10 experiments of 2.56 s each, collecting cathode and anode induce signals in continuous mode using two channels in the GaGe card, as described in Figure 5.5.

Since the Cs-137 irradiator was manually operated, the synchronization between the Cs-137 irradiator shutter opening and the start of data acquisition introduced timing uncertainties. Longer acquisition time in each small experiment $\sim$ 2.56 s was sufficient to acquire the data, since the uncertainty between them was estimated within $\pm$0.5 s.

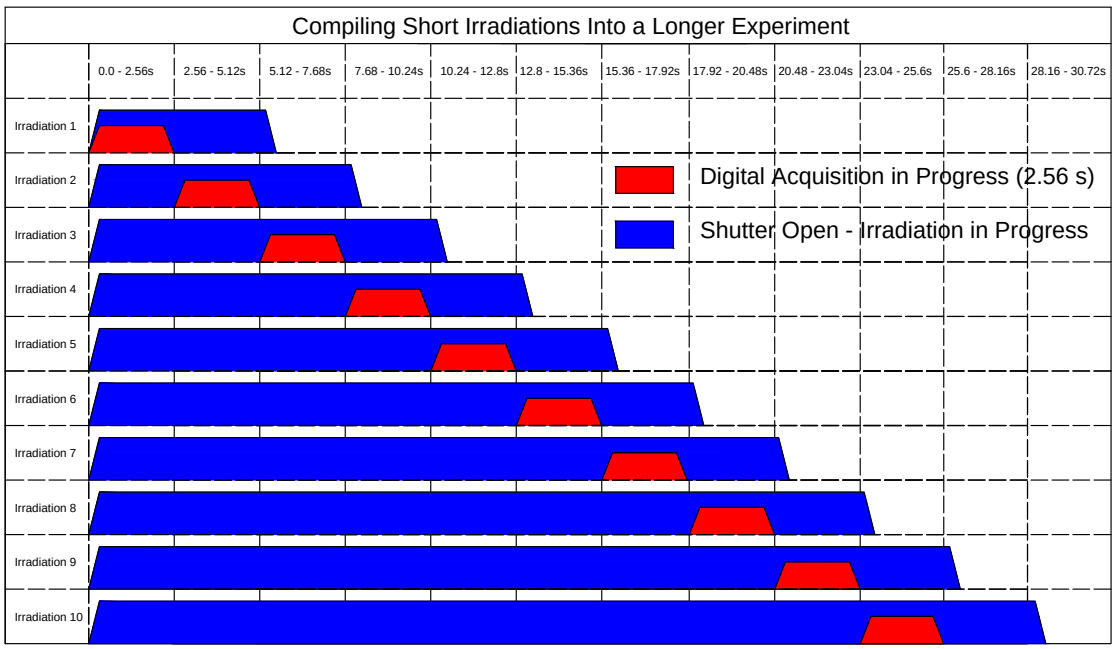

Figure 5.5: Diagram showing 10 short irradiation experiments, 2.56 s each, compiled to generated a single large irradiation experiment, 25.6 s long.

5.2.1 1D Edge Detection Algorithm

In continuous mode, signals induced on the preamplifiers due to charges drifting in the bulk of the detector were continuously sampled and stored in the GaGe digitizer on-board memory at sampling rates as high as 125 MS/s. In each acquisition cycle, these signals were stored in files after the digitizer memory was completely filled. Examples of signals are shown in Figure 5.4 and in Appendix A. A simple 1D edge detection algorithm was used to extract individual γ-ray and α-particle events from acquired signals in continuous mode, *Davis and Mitiche* (1979) and *Mitiche and Davis* (1982). This algorithm was implemented in three steps:

In the first step, a weighting factor $e_k(i)$ is calculated according to Equation 5.1 for every sampled point i in the collected waveform $wf(i)$, for $i = 1 \ldots n$, where n

represents the total number of points stored in the file or readout,

$$e_k(i) = \frac{1}{n}\sum_{j=1}^{k}[wf(i-j) - wf(i+j] = \frac{1}{n}[LS(i) - RS(i)] \tag{5.1}$$

where, k is an adjustable parameter that determines the number of points to the left $LS(i)$ and to the right $RS(i)$ of sampled point $wf(i)$ at position i. Figure 5.6 shows results after the first step was computed.

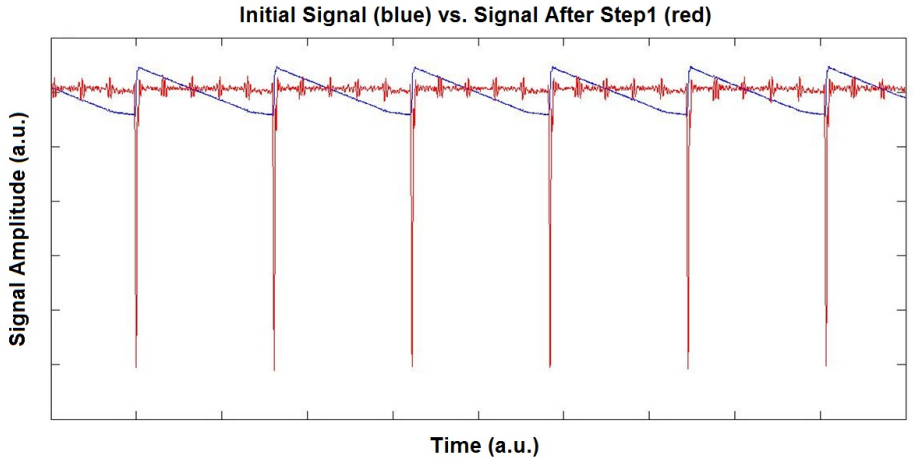

Figure 5.6: 1D edge detection algorithm applied to a test pulse showing the original signal $wf(i)$ (blue) and the post-processed signal $e_k(i)$ (red) after the first step.

In the second step, a threshold value t is set and values of $|e_k(i)| < t$ are discarded, discriminating between points that are edges of real waveforms and points which were between edges, but far from edges. Fig.5.7 shows results after this step was computed.

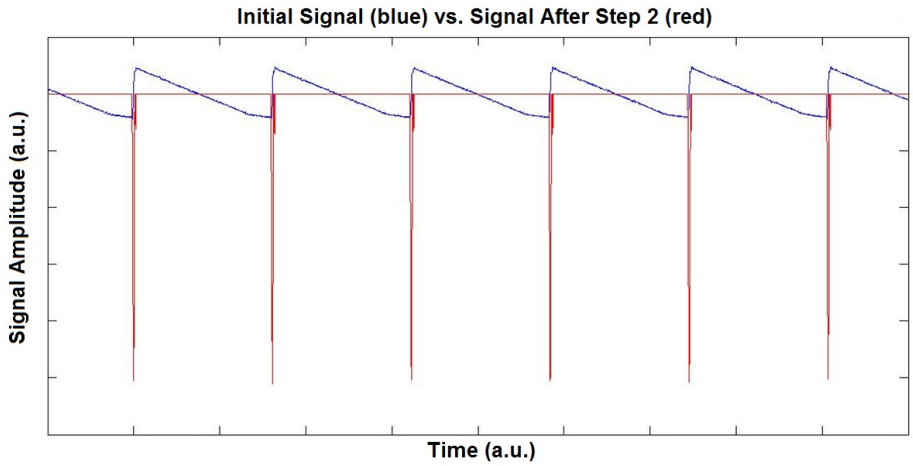

Figure 5.7: 1D edge detection algorithm applied to a test pulse showing the original signal $wf(i)$ (blue) and the post-processed signal $e_k(i)$ (red) after the second step.

In the third step, another parameter d is used to consider only values of $e_k(i)$ distant at least $\pm d$ time units away from position from i, which is used in the algorithm as a dead time parameter. Fig.5.8 shows results after this step was computed.

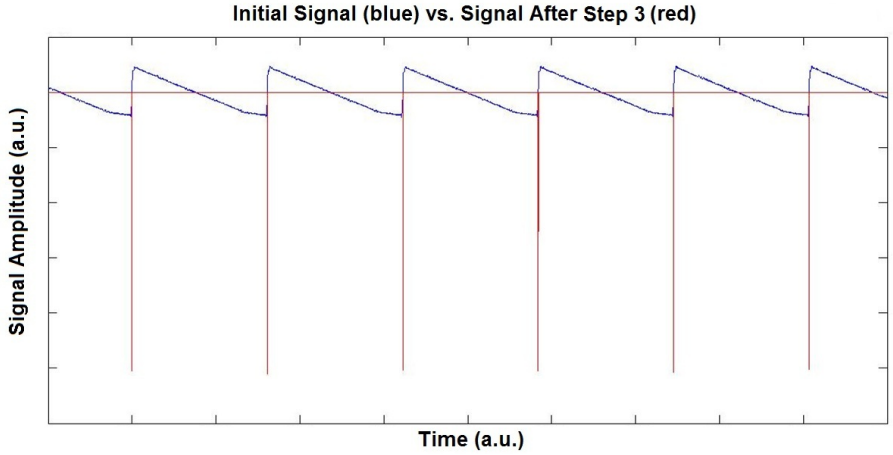

Figure 5.8: 1D edge detection algorithm applied to a test pulse showing the original signal $wf(i)$ (blue) and the post-processed signal $e_k(i)$ (red) after the third step.

Deconvolving radiation interaction events (energy deposited per event) in continuously acquired waveforms using commercial GaGe octopus systems was successfully accomplished using the algorithm shown in the previous three steps. Although results

shown in Figures 5.6, 5.7 and 5.8 were calculated for a test pulse, the algorithm was checked during all high-flux irradiation experiments by adding a test pulse during high-flux data acquisition. The algorithm used different calibration parameters k, d and t for anode and cathode induced signals. After finding these edges, deconvolved induced signals from measured signals in continuous mode were stored in files for digital post-processing (filtering, drift-time calculation, CAR, etc.)

5.3 High-Flux Experiments

Results for high-flux irradiation experiments presented here were measured at four cathode bias voltages: -750, -1000, -1250 and -1500 V and flux Φ varying from 39k ... 219k photons/pixel/s.

5.3.1 Pre-Irradiation: System Calibration

In order to minimize time spent in the irradiation room, aligning, calibrating and sometimes debugging the system, the entire system was assembled on a mobile cart. The system described in Figure 5.2 needed to be moved to the irradiation room only during the high-flux irradiation experiments. Before each set of high-flux irradiation experiments, the position of the collimator was checked using a Co-57 source. The system was also checked using a Cs-137 disk source. These tasks were conducted in the laboratory in a more controlled environment with known background.

5.3.2 High-Flux Irradiations

Since the objective of this work was to study the polarization effect, means of measuring distortions in the operating electric field caused by positive space charge build up were needed. The internal electric field was monitored during the high-flux experiments by placing a 1 μCi Am-241 α-source close to the cathode surface of the detector during high-flux irradiation. Since holes created by this source would

get immediately collected by the cathode electrode, no signal would be induced by holes generated by the α-source. These signals were used to understand how positive space charge builds up as a function of irradiation time and flux, reducing the operating electric field and causing spectral degradation. Comparison between high-flux experiments and simulations is described in Chapter VI, while in this chapter only experimental results are discussed.

Figures 5.9, 5.10, 5.11 and 5.12 show results for measured spectra at -750, -1000, -1250 and -1500 V applied cathode bias voltages from $0 \ldots 25.6$ s. In these plots, t_i represents the time interval of the smaller irradiations while Φ_j represents the calculated incident flux at the cathode surface of the detector, as described in Tables 5.2 and 5.3.

t_1	t_2	t_3	t_4	t_5	t_6	t_7	t_8	t_9	t_{10}
0	2.56	5.12	7.68	10.24	12.8	15.36	17.92	20.48	23.04
...	...	...	...	...	...	...	...	...	...
2.56 s	5.12 s	7.68 s	10.24 s	12.8 s	15.36 s	17.92 s	20.48 s	23.04 s	25.6 s

Table 5.2: Conversion between t_1, t_2, $\cdots$, t_{10} and irradiation time intervals in s.

In these results, the time required to polarize these detectors was consistently mea-

Φ_1	Φ_2	Φ_3	Φ_4	Φ_5	Φ_6	Φ_7	Φ_8	Φ_9	Φ_{10}	Φ_{11}
39.3	57.3	75.3	93.3	111.3	129.3	147.3	165.3	183.3	201.3	219.3

Table 5.3: Conversion between Φ_1, Φ_2, $\cdots$, Φ_{11} and irradiation flux in $\times 10^3$ *photons/pixel/s*.

sured to be less than 2.56 s, as seen in Figure 5.9 for $\Phi_9 - \Phi_{11}$, in Figure 5.10 for $\Phi_{10} - \Phi_{11}$, in Figure 5.11 for Φ_{11} and in Figure 5.12 for Φ_{12}.

These results show that increasing the applied electric field E, by increasing the magnitude of the applied voltage at the cathode electrode from -750 V to -1500 V, improves the performance of the detector, delaying the polarization effect. For

instance, at -750 V the detector polarized at an incident flux $\Phi_8 = 165.3 \times 10^3$ photons/pixel/s, while at -1500 V the same detector only polarized at $\Phi_1 0 = 201.3 \times 10^3$ photons/pixel/s.

The transition between normal operation and polarization is observed in more detail in results shown in Appendix B, where plots for each cathode bias voltage show measured spectra before and after polarization in 25.6 ms time intervals.

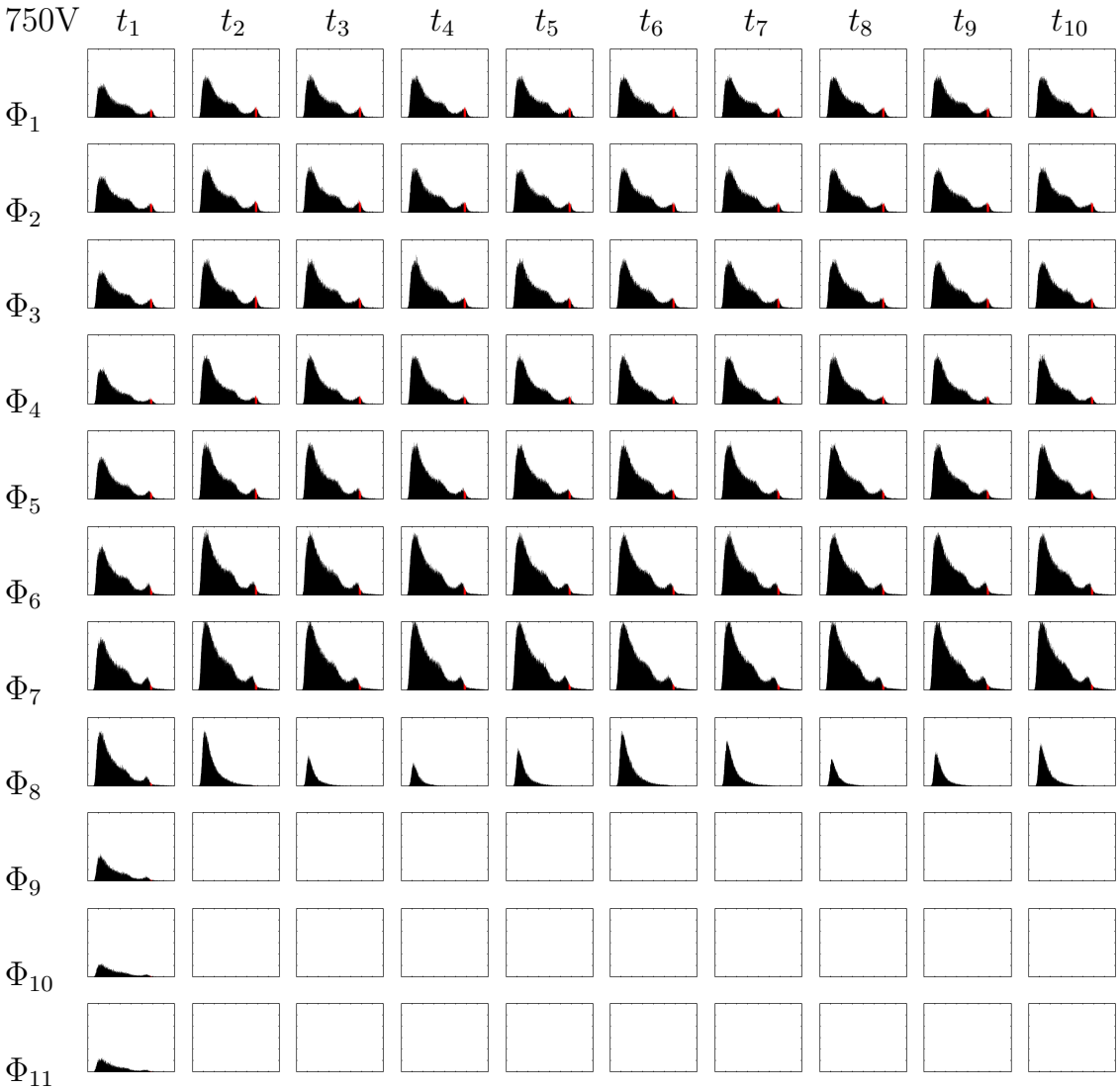

Figure 5.9: Measured spectra in every 2.56 s interval from 0 . . . 25.6 s, at -750 V and flux Φ=39.3. . .219.3$\times 10^3$ photons/cm^2/s.

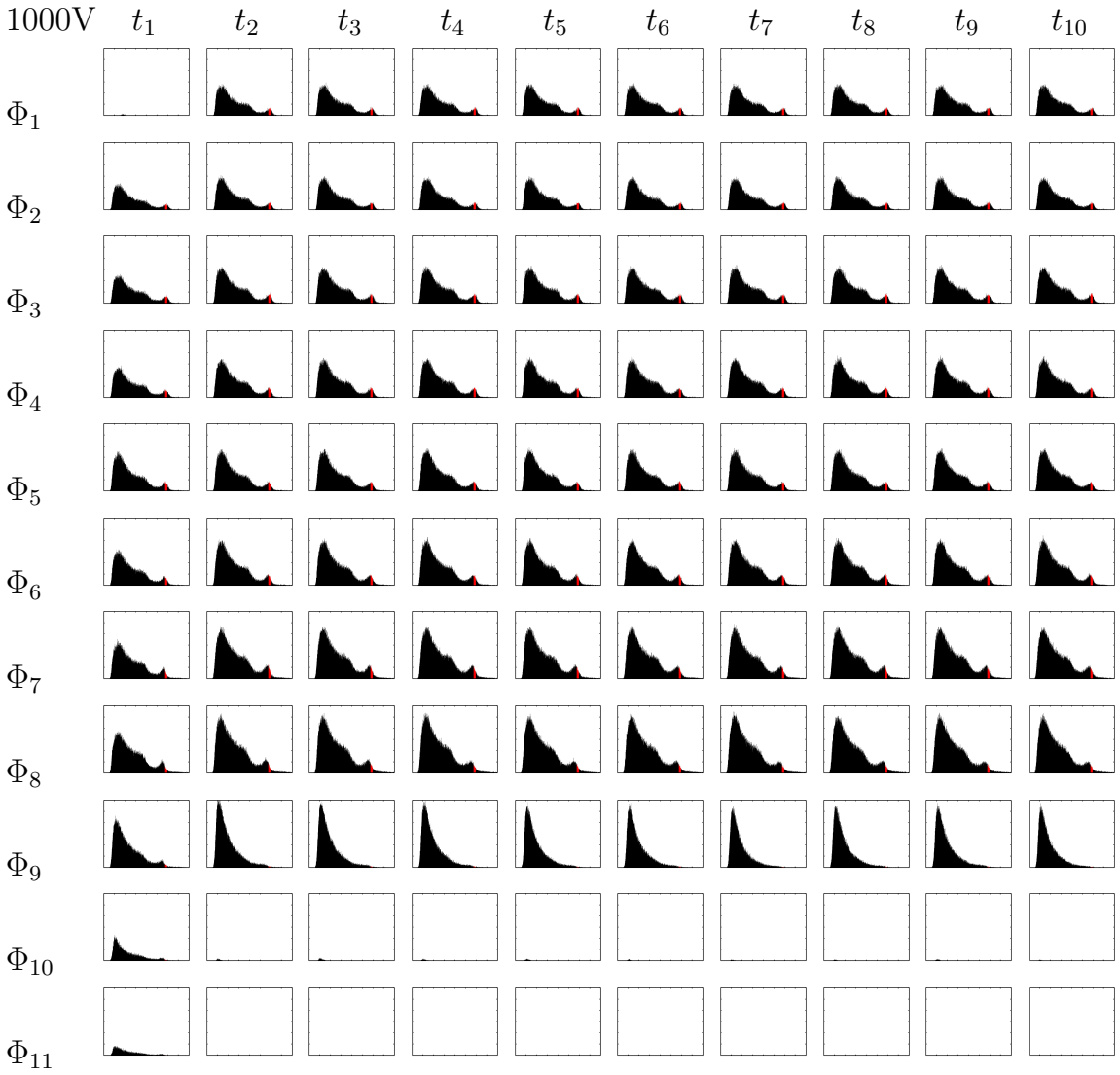

Figure 5.10: Measured spectra in every 2.56 s interval from $0 \ldots 25.6$ s, at -1000 V and flux Φ=39.3...219.3$\times 10^3$ photons/cm^2/s.

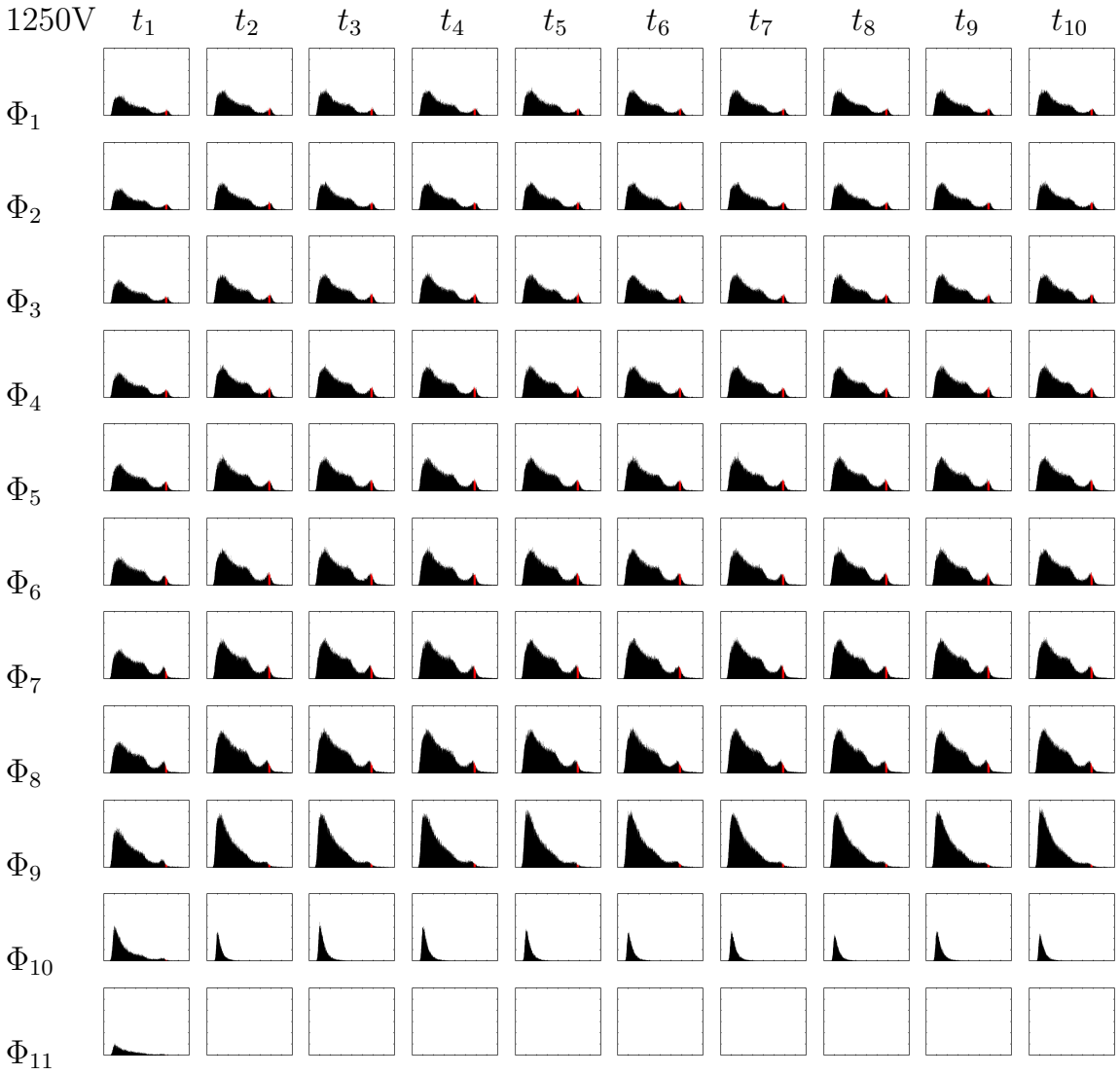

Figure 5.11: Measured spectra in every 2.56 s interval from $0 \ldots 25.6$ s, at -1250 V and flux Φ=39.3...219.3$\times 10^3$ photons/cm^2/s.

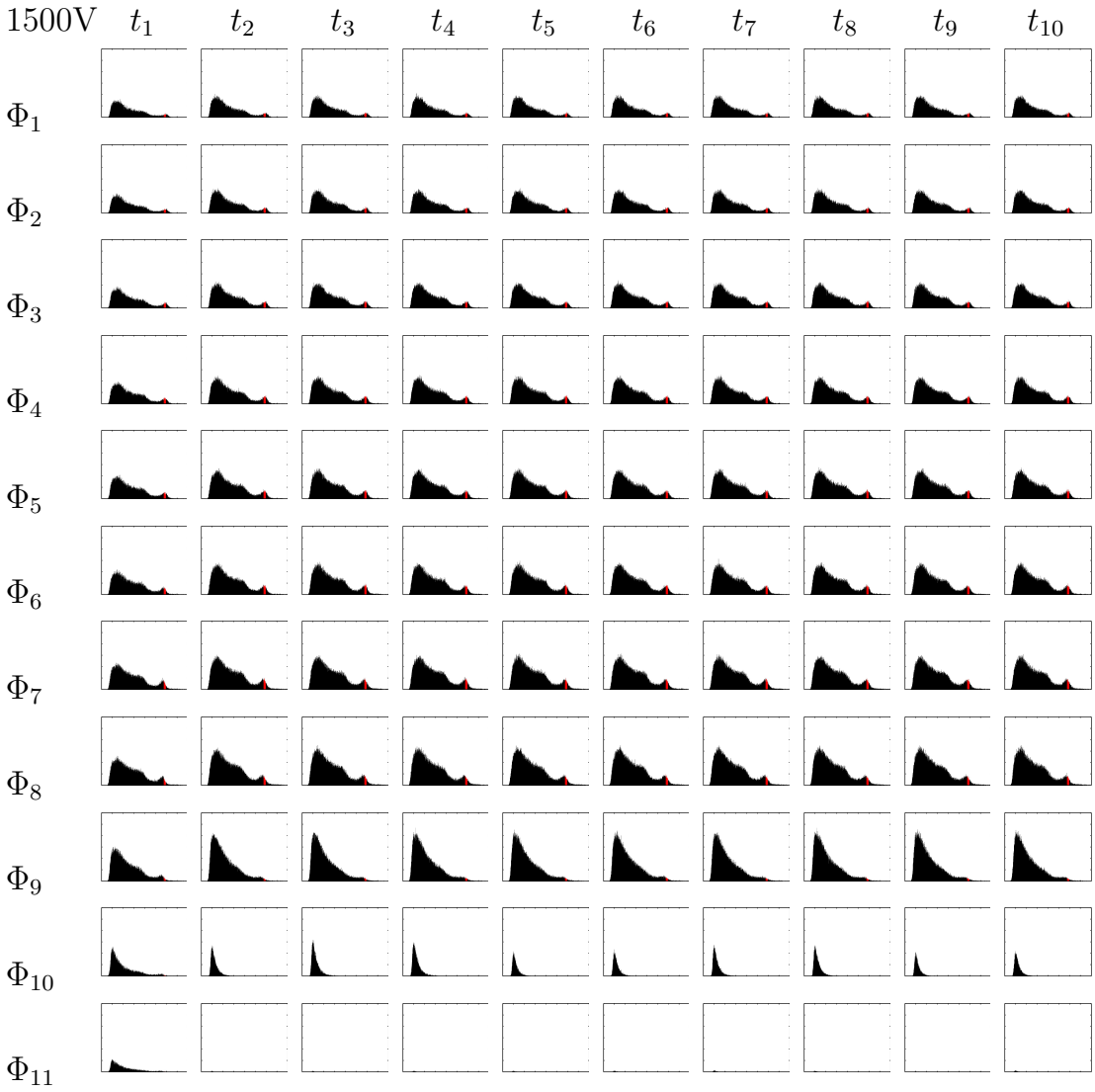

Figure 5.12: Measured spectra in every 2.56 s interval from 0 . . . 25.6 s, at -1500 V and flux Φ=39.3. . .219.3$\times 10^3$ photons/cm^2/s.

5.4 High-Flux Cs-137 γ-Spectra

Photopeak positions as a function of irradiation flux and time were calculated and are shown in Figures 5.13, 5.14, 5.15 and 5.16 for -750, -1000, -1250 and -1500 V cathode bias voltages.

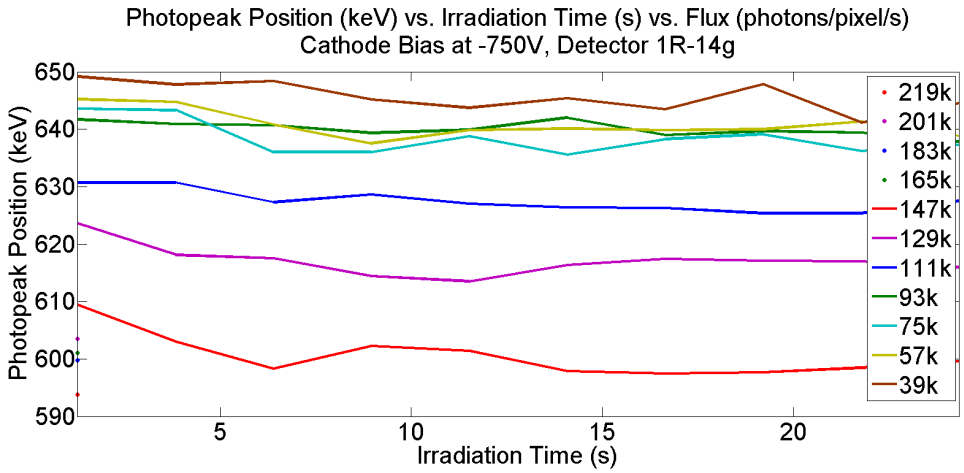

Figure 5.13: Photopeak position as a function of irradiation time and flux, for -750 V cathode bias voltage.

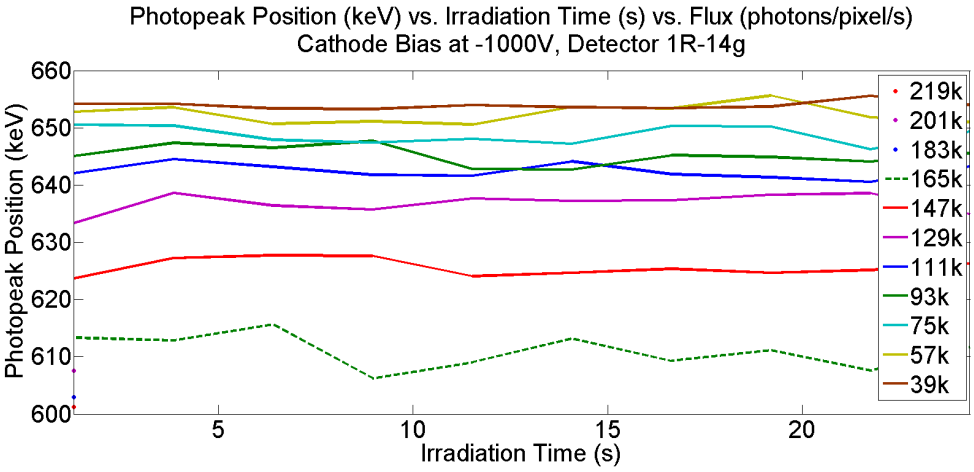

Figure 5.14: Photopeak position as a function of irradiation time and flux, for -1000 V cathode bias voltage.

Comparing results shown in Figures 5.13-5.16 with spectra shown in Figures 5.9-5.12, we observed that although the photopeak position was measured at lower energy bins as flux increased, detectors continued to work showing no photopeak with degraded performance when operated at higher irradiation flux.

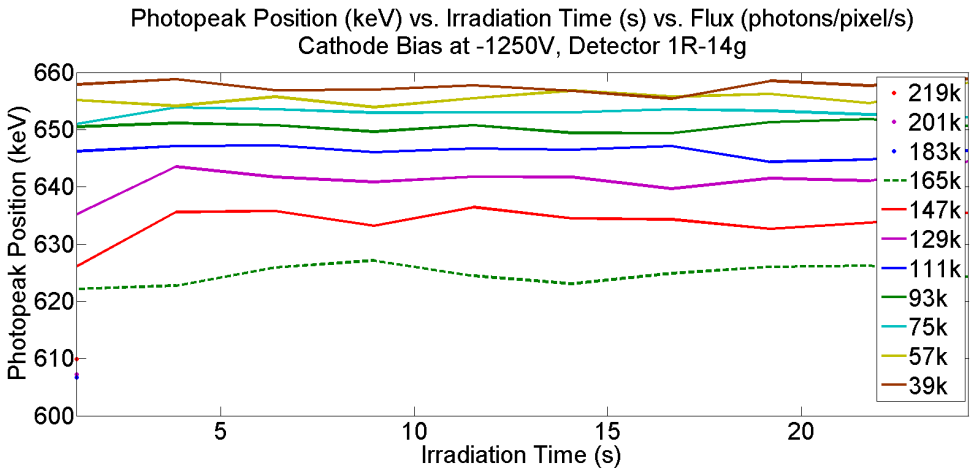

Figure 5.15: Photopeak position as a function of irradiation time and flux, for -1250 V cathode bias voltage.

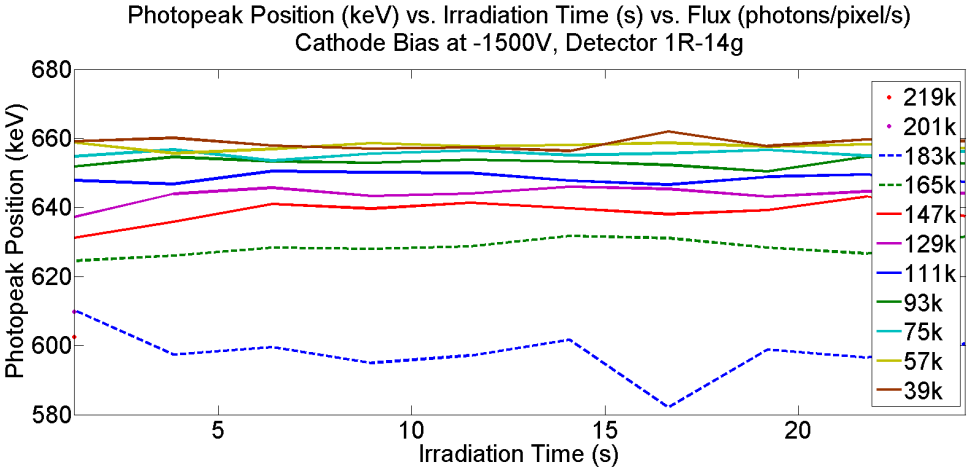

Figure 5.16: Photopeak position as a function of irradiation time and flux, for -1500 V cathode bias voltage.

These results suggest that at high irradiation flux, if the flux Φ is known, the shift in the photopeak positions measured can be compensated applying corrections. It was also observed that measured energy resolution degrades as a function of increasing flux. This effect is believed to be caused by irregular space charge build up in the detector volume, causing irregular signal induction.

Results presented in Figure 5.13 were measured while operating the detector at -750 V cathode bias voltage. These showed that increasing the incident flux from $\Phi_8 =$

165.3×10^3 to $\Phi_9 = 183.3 \times 10^3$ photons/pixel/s caused the photopeak to completely disappear. The detector continued working at flux Φ_8 with reduced performance, as seen in Figure 5.9. Results presented in Figure 5.14 were measured while operating the detector at -1000 V cathode bias voltage. These results showed that increasing the incident flux from $\Phi_9 = 183.3 \times 10^3$ to $\Phi_{10} = 201.3 \times 10^3$ photons/pixel/s caused the photopeak to completely disappear. The detector continued working at flux Φ_9 with reduced performance, as seen in Figure 5.10. Results presented in Figure 5.15 were measured while operating the detector at -1250 V cathode bias voltage. These showed that increasing the incident flux from $\Phi_9 = 183.3 \times 10^3$ to $\Phi_{10} = 201.3 \times 10^3$ photons/pixel/s caused the photopeak to completely disappear. The detector continued working at flux Φ_{10} with reduced performance, as seen in Figure 5.11. Results presented in Figure 5.16 were measured while operating the detector at -1500 V cathode bias voltage. These results showed that increasing the incident flux from $\Phi_9 = 183.3 \times 10^3$ to $\Phi_{10} = 201.3 \times 10^3$ photons/pixel/s caused the photopeak to completely disappear. The detector continued working at flux Φ_{10} with reduced performance, as seen in Figure 5.12.

Similar results were observed measuring raw energy resolution as a function of irradiation flux and time. These results are shown in Figures 5.17, 5.18, 5.19 and 5.20 for -750, -1000, -1250 and -1500 V cathode bias voltages.

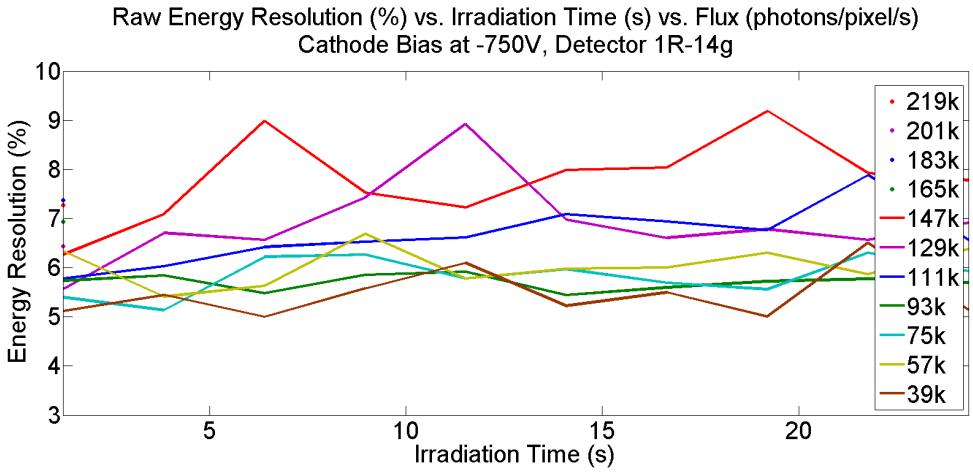

Figure 5.17: Raw energy resolution as a function of irradiation time and flux, for -750 V cathode bias voltage.

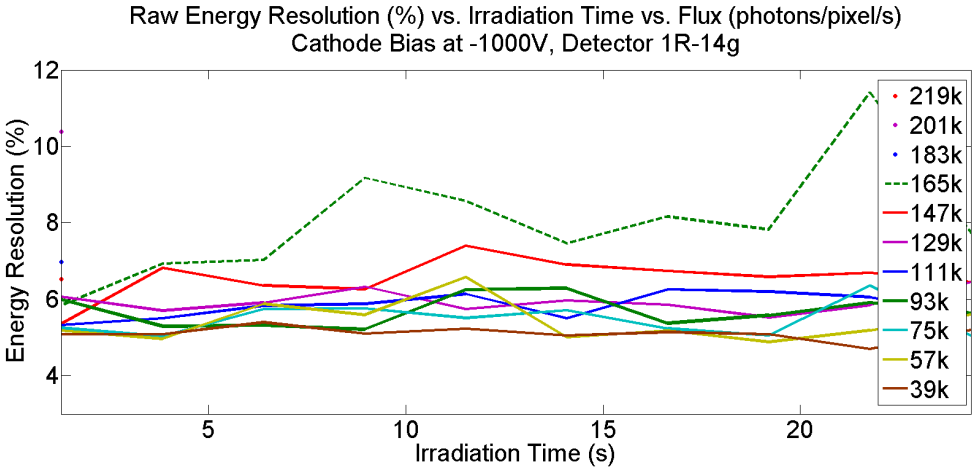

Figure 5.18: Raw energy resolution as a function of irradiation time and flux, for -1000 V cathode bias voltage.

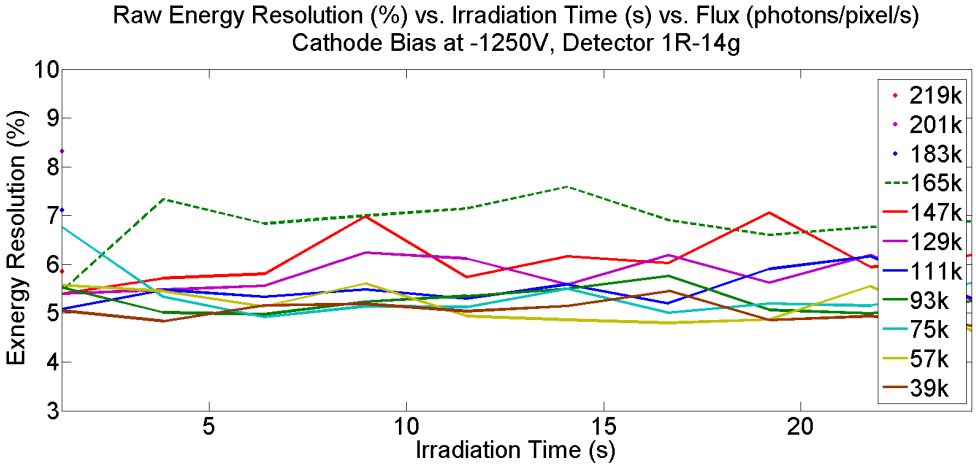

Figure 5.19: Raw energy resolution as a function of irradiation time and flux, for -1250 V cathode bias voltage.

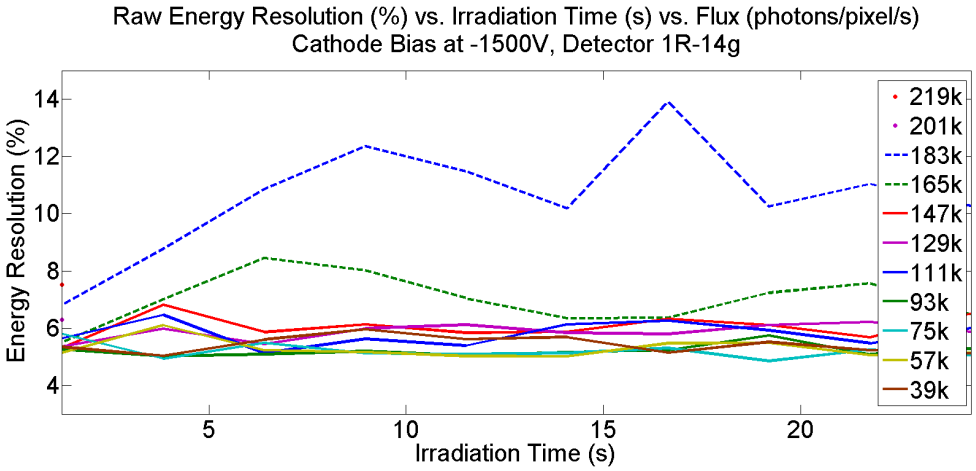

Figure 5.20: Raw energy resolution as a function of irradiation time and flux, for -1500 V cathode bias voltage.

Similar results were observed by measuring at room-temperature the total number of counts as a function of irradiation flux and time. These results are shown in Figures 5.21, 5.22, 5.23 and 5.24 for -750, -1000, -1250 and -1500 V cathode bias voltages. The non-linear increase in the total number of counts measured as a function of irradiation flux may be attributed to inaccurate source-detector alignment and other sources of error.

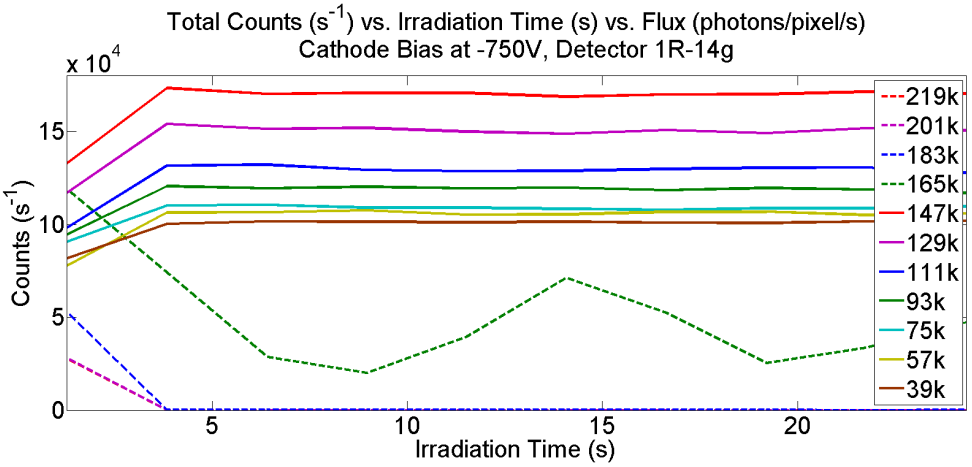

Figure 5.21: Total counts as a function of irradiation time and flux, for -750 V cathode bias voltage.

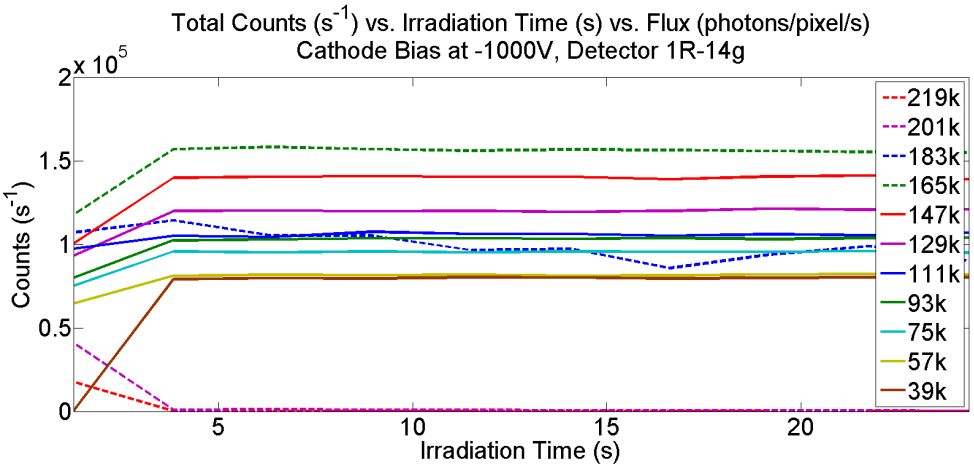

Figure 5.22: Total counts as a function of irradiation time and flux, for -1000 V cathode bias voltage.

Results shown in Figure 5.21, operating the detector at -750 V cathode bias voltage, showed that increasing the incident flux from $\Phi_7 = 147.3 \times 10^3$ to $\Phi_8 = 165.3 \times 10^3$ photons/pixel/s caused the total counts to be not proportional to the incident flux Φ. Measured data at -750 V showed that the detector continued working at flux Φ_8 with reduced performance, as seen in Figures 5.9 and 5.13.

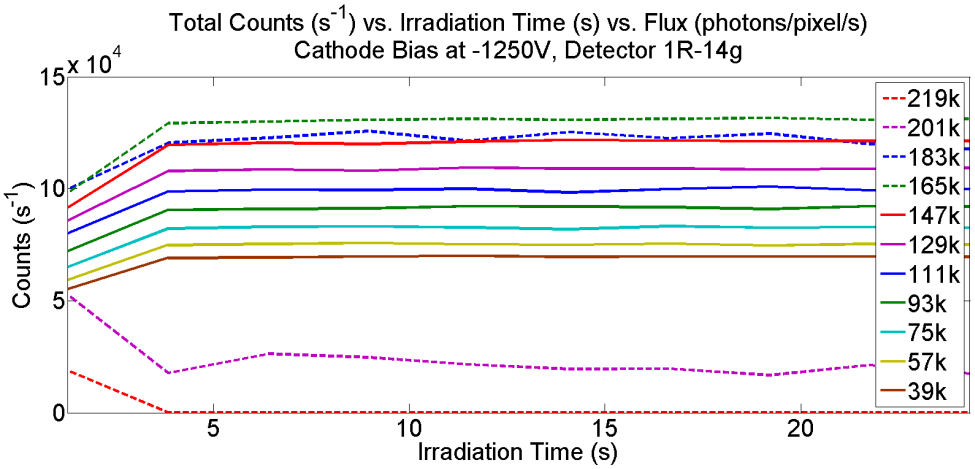

Figure 5.23: Total counts position as a function of irradiation time and flux, for -1250 V cathode bias voltage.

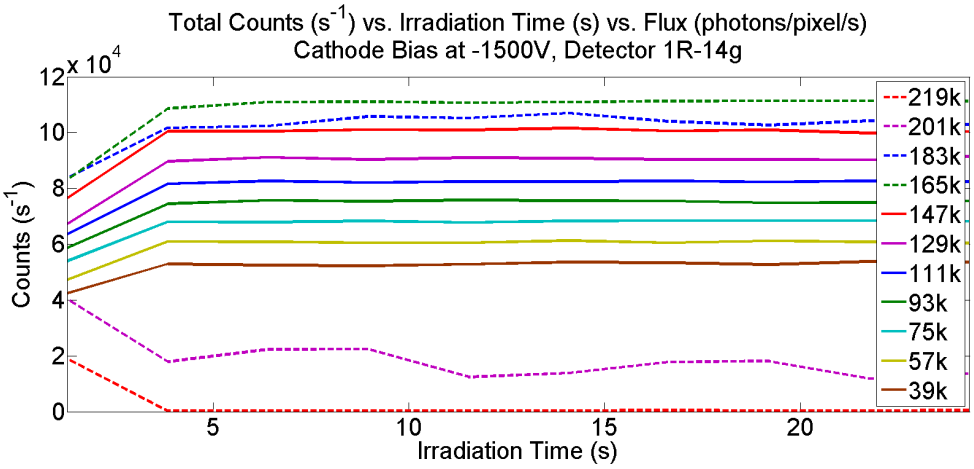

Figure 5.24: Total counts as a function of irradiation time and flux, for -1500 V cathode bias voltage.

Results shown in Figure 5.22, operating the detector at -1000 V cathode bias voltage, showed that increasing the incident flux from $\Phi_8 = 165.3 \times 10^3$ to $\Phi_9 = 183.3 \times 10^3$ photons/pixel/s caused the total counts to be non proportional to the incident flux Φ. Measured data at -1000 V showed that the detector continued working at Φ_9 with reduced performance, as seen in Figures 5.10 and 5.14. Results shown in Figure 5.23, operating the detector at -1250 V cathode bias voltage, showed that increasing the incident flux from $\Phi_8 = 165.3 \times 10^3$ to $\Phi_9 = 183.3 \times 10^3$ photons/pixel/s

caused the total counts to be non proportional to the incident flux Φ. Measured data at -1250 V showed that the detector continued working at Φ_{10} with reduced performance, as seen in Figures 5.11 and 5.15. Results shown in Figure 5.24, operating the detector at -1500 V cathode bias voltage, showed that increasing the incident flux from $\Phi_8 = 165.3 \times 10^3$ to $\Phi_9 = 183.3 \times 10^3$ photons/pixel/s caused the total counts to be non proportional to the incident flux Φ. Measured data at -1500 V showed that the detector continued working at Φ_{10} with reduced performance, as seen in Figures 5.12 and 5.16. In continuous data acquisition mode, the post-processing algorithm using the 1D-edge-operator discarded events that were triggered within 1.6 μs. Operating this detector at higher cathode bias voltages generated more false triggers due to noise caused by the increased leakage current. This is the reason why the total number of counts measured at lower voltages was greater than measured at higher voltages, i.e., comparing measurements at -750 V with -1500 V.

These results strongly suggest that the polarization effect cause the photopeak to shift towards lower energies and degraded spectrum resolution. The explanation for this phenomenon is given in Chapter VI, where it is shown that the build up of positive space charge perturbs the operating field E, limiting the performance of CdZnTe detectors operated at high-flux irradiation scenarios.

5.5 Electric Field $\vec{E}$ Monitored by α-Particles

During each high-flux irradiation, an Am-241 α-source, E_α=5.486 MeV (85.2%) and 5.443 MeV (12.8%), was kept close to the cathode surface irradiating the cathode with α-particles through a small α-source collimator. These α-particles deposit all energy within 20 μm from the cathode surface, amm (2001). Only electrons contribute to the induced signal, since holes are immediately collected by the cathode electrode. These Am-241 α-induced signals were easily discriminated from Cs-137 γ-induced signals using amplitude discrimination techniques. Due to the low activity of the

α-source (1 μCi) used, no α-spectra was measured during the high-flux experiments.

Figure 5.25 shows α-particle anode and cathode induced signals measured at different applied cathode bias voltages. In high-flux applications, it is desirable to operate the detectors at the maximum applied voltage, increasing the drift velocity of charges and at the same time reducing charge trapping. Unfortunately, increasing the applied cathode bias voltage causes signal degradation due to increased leakage current and detector breakdown, which prohibits the operation of these detectors at very high applied cathode voltages.

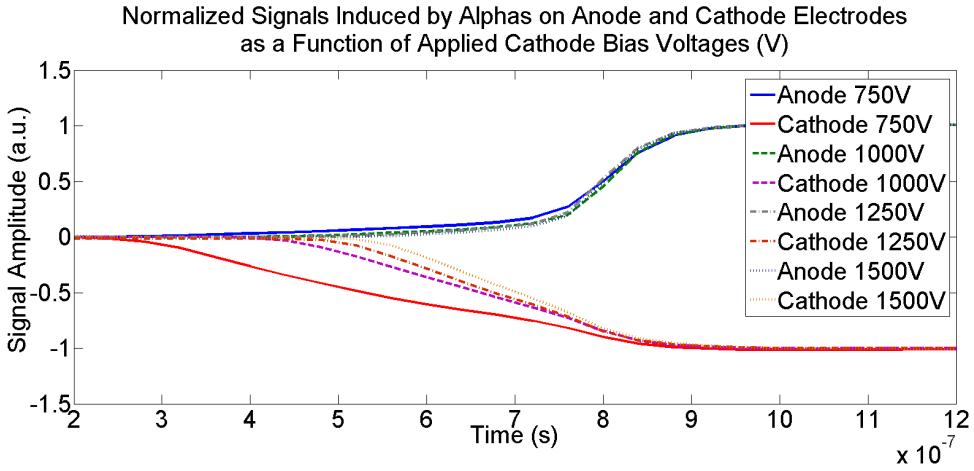

Figure 5.25: Normalized Signals Induced on the Anode and Cathode Electrodes by α Particles Incident on the Cathode Surface as a Function of Applied Cathode Bias Voltages: 750, 1000, 1250 and 1500 V.

Figure 5.26 shows α-particle anode and cathode induced signals measured at two fluxes: $\Phi = 39 \times 10^3$ and 183×10^3 photons/pixel/s. It was observed that increasing the flux distorted the operating field E, causing the charges to drift slower in the detector. Figure 5.27 showed the measured difference between the cathode signals shown in Figure5.26. Appendix C shows results for fluxes varying from $\Phi = 39 \times 10^3$, $\Phi = 57 \times 10^3$, ..., 183×10^3 photons/pixel/s and applied cathode bias voltages varying from -750, ..., -1500 V. At higher fluxes, the reduction of the internal electric field E also causes more charge trapping and recombination. For these two reasons, the measured spectra is expected to be shifted to lower energies. This effect is similar to

the known ballistic deficit effect caused by incomplete charge collection when using filters with fixed shaping time $\tau = RC$ smaller than the drift time of the signal, *Knoll* (2010). In Chapter VI, the ballistic deficit effect mentioned here is described in more detail, where it is found to be the main cause of spectral degradation at high-flux irradiation. In future studies, charge recombination and temperature effects need to be studied in more detail, *Hall* (1952), *Shockley and W. T. Read* (1952), *Hall* (1960), *Brown* (1955), *Baliga* (1978), *Lugakov and Shusha* (1984) and *Debuf et al.* (2002).

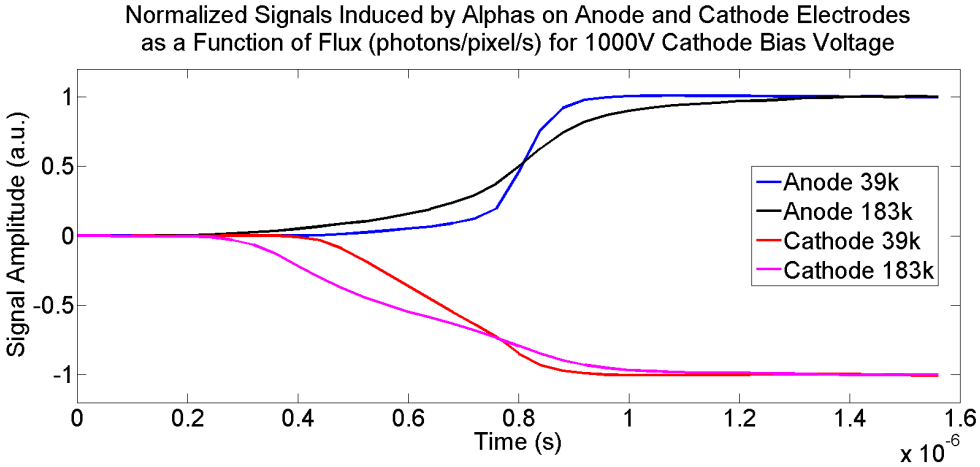

Figure 5.26: Normalized Signals Induced by α-particles on the Anode and Cathode Electrodes for Flux $\Phi = 39 \times 10^3$ and 183×10^3 photons/pixel/s.

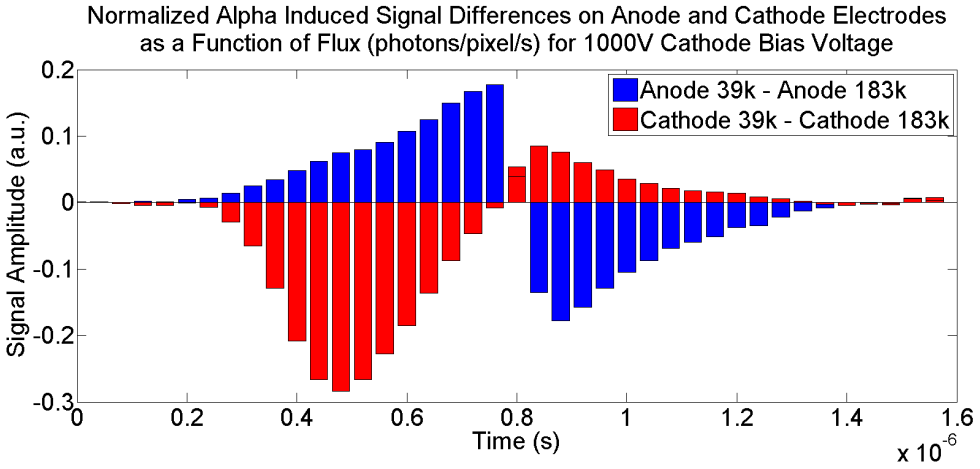

Figure 5.27: Difference Between Normalized Signals Induced by α-particles on the Anode and Cathode Electrodes for Flux $\Phi = 39 \times 10^3$ and 183×10^3 photons/pixel/s.

Electric field as a function of depth of interaction was calculated using α-particle cathode induced signals, as shown in Figure 5.28, for -1000 V applied cathode bias voltage. Appendix D shows results measured varying the applied cathode bias voltage from -500, ..., -2000 V.

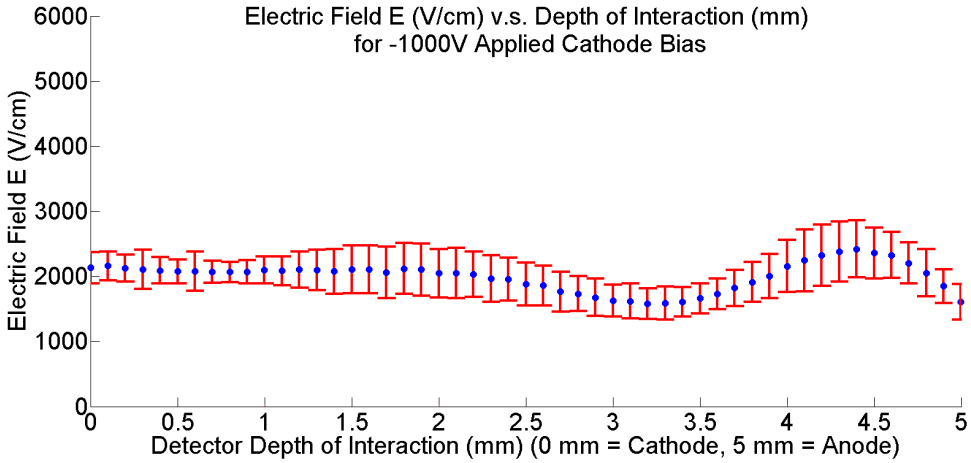

Figure 5.28: Calculated Electric field E as a function of depth of interaction for -1000 V applied cathode voltage bias.

Electric field E can be measured during high-flux experiments, starting from measured α-particle cathode induced signals, and assuming that the electron drift velocity is proportional to the product of the electric field E and electron mobility μ_e,

$$v_e = \mu_e E \tag{5.2}$$

The first step is to measure the initial time t_0 when the α-particle interact near the surface of the cathode electrode, as shown in Figure 5.29 a), where t_1 is the time when the electron cloud was collected. Then, assuming a linear cathode weighting potential, as described in Figure 5.29 b), depth of interaction Z is directly proportional to the amplitude of the measured signal. The derivative of the signal amplitude with respect to time is proportional to the electron drift velocity v_e, which if constant

electron mobility μ_e is assumed, is only proportional to the electric field E, since,

$$\frac{dV}{dt} = K \cdot E(t) \tag{5.3}$$

where, the value of the electric field is calculated applying a proportionality constant K based on the boundary conditions of the problem,

$$K = \frac{V_{cathode}}{\int_{t_0}^{t_1} E(t) \cdot dt} \tag{5.4}$$

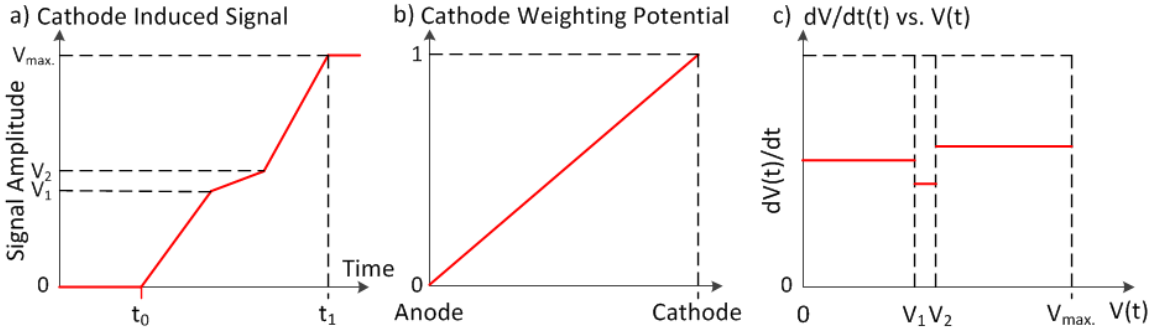

Figure 5.29: a) Cathode induced signals at low-flux; b) Cathode linear weighting potential; and c) $dV(t)/dt$ vs. $V(t)$, where $dV(t)/dt \propto E$ and $V(t) \propto Z$, where Z is the depth of interaction.

In future experiments, this technique is suggested to be used to measure the electric field E due to space charge only. This would enable to measure polarity and spatial distribution of space charge as a function of irradiation flux and time. A simple 1D model of charge distribution is not sufficient to calculate the distribution of space charge in this problem.

5.6 Analysis of High-Flux Experiment Results

The behavior of CdZnTe under high-flux irradiation when operated under higher temperatures is suggested in future studies, since the de-trapping of charges is highly correlated with temperature, *Zanio et al.* (1973). It is believed that under higher temperatures trapped charges will detrap faster, which will reduce the amount of positive space charge build up in the detector as a function of irradiation flux and time. Also, in future studies it is suggested to read out more channels simultaneously. This can be achieved easily by increasing the number of GaGe systems used and designing a system which better synchronizes the irradiator shutter with the data acquisition system. Also, it is suggested to test the system using an actual X-ray source rather than using a Cs-137 source. Since the current system was manually aligned and positioned in the irradiation room, it is suggested to use a better XYZ positioning system in future experiments.

CHAPTER VI

High-Flux Simulations

A series of high-flux simulations were conducted in order to explain the so-called *polarization effect*. These simulations considered properties listed in Table 4.2. Hole transport properties considered in simulations were obtained using Mo K_α X-rays ($E_{K\alpha}$=17.4 keV) rather than Am-241 α-particles (E_α=5.5 MeV). The main reason for choosing these results is related with surface preparation of the sides of the detectors, which may considerably change the results obtained with α-particles. Am-241 α-Particles interact close to the surface of the crystal (<20 μm), while Mo K_α X-rays interact deeper in the crystal (∼50 μm), thus α-particle measurements are more susceptible to surface imperfections. Results obtained in this chapter are not exact and need to be interpreted relative to each other rather than with respect to experimental results. In order to improve these results, it is believed that better experimental setup and improved simulation models are required to describe how CdZnTe material properties change under high-flux irradiation environments. For instance, models considered in current simulations did not take into account the effect of charge recombination and operating temperature, which are believed to be major sources of model mismatch. Also, a larger number of CdZnTe detectors manufactured for high-flux applications ($\sim 1 \times 10^8$ photons/cm^2/s) are required in future studies. Another important requirement in future studies is to have better and more controlled exper-

iments, reducing unnecessary uncertainties by minimizing known sources of errors.

In this chapter, a qualitative comparison between high-flux simulations using the simulation code described in Chapter III with experimental results described in Chapter V is presented. In order to explain some of the results in Chapter V, some of the simulated results presented in this chapter considered a hypothetical material having infinite average de-trapping time of trapped positive space-charge. A more detailed discussion of reasons why simulated results do not agree quantitatively with measured experimental results is presented in Section 6.5.

6.1 Introduction

It is well known that in order to simulate charge transport properties under high-flux irradiation scenarios, good measurements of charge transport properties as well as detailed models of physical processes are required. Electron and hole transport properties used in the simulations, measured in Chapter IV, are summarized in Table 6.1.

Property	Value
W-value (eV/e-h pair)	4.64
Time step for electronsΔ_{te} (s)	5×10^{-9}
Time step for holesΔ_{th} (s)	20×10^{-9}
Electron Mobility μ_e (cm^2/V/s)	750
Hole Mobility μ_h (cm^2/V/s)	12
Average Electron Lifetime τ_e (s)	6×10^{-6}
Average Hole Lifetime τ_{h1} - Shallow Defects (s)	1.25×10^{-6}
Average Hole Lifetime τ_{h2}- Deep Defects (s)	3.5×10^{-6}
Average Electron De-trapping Time τ_{de} (s)	2.5×10^{-7}
Average Hole De-trapping Time τ_{dh1} - Shallow Defects (s)	2.5×10^{-7}
Average Hole De-trapping Time τ_{dh2} - Deep Defects (s)	1.7×10^{-3}
Electron Diffusion FWHM$_e$ in 5 ns (μm)	10
Hole Diffusion FWHM$_h$ in 10 ns (μm)	6

Table 6.1: Calculated average electrical transport properties of CdZnTe detectors used in the high-flux experiments.

Using the properties shown in Table 6.1, the probabilities described by Equations

3.25-3.27 are calculated, as seen in Table 6.2, considering 5 ns electron time-step and 20 ns hole time-step.

Average Probability of	Value (%)
Electron Trapping (1-t_e) in 5 ns	0.083
Electron De-trapping (1-t_{eD}) in 5 ns	1.98
Hole Trapping (1-t_{h1}) in Shallow Defects in 20 ns	1.59
Hole Trapping (1-t_{h2}) in Deep Defects in 20 ns	0.57
Hole De-trapping (1-t_{hD1}) in Shallow Defects in 20 ns	7.69
Hole De-trapping (1-t_{hD2}) in Deep Defects in 20 ns	0.0012

Table 6.2: Probabilities of electrons and holes trapping and de-trapping. Electrons drifted every 5 ns while holes drifted every 20 ns time steps.

Results shown in Table 6.2 are used to calculate the balance between free and trapped carriers, using the model described by Equations 3.2-3.9. In these results, in every 5 ns time step, 0.083% of free electrons in excess of equilibrium in each mesh are trapped, while 1.98% of trapped electrons are de-trapped. In every 20 ns time step, 1.59% of free holes in excess of equilibrium in each mesh are trapped in shallow defect levels while 0.57% are trapped in deep defect levels. Also, 7.69% of trapped holes in shallow defect levels are de-trapped, while 0.0012% of trapped holes in deep defect levels are de-trapped. Charge conservation is preserved, since the total charge is kept constant unless an external source adds additional electrons and/or holes into the simulated region. It can be easily observed that positive space-charge trapped in deep defect levels causes the buildup of positive space-charge over time.

6.2 Operating Electric Field Considerations

In high-flux simulations, due to poor hole transport properties in CdZnTe, as shown in Tables 6.1 and 6.2, similar to experiments, positive space charge builds-up in simulations, reducing the operating electric field. The reduction in the operating field causes both charge carrier to drift slower in the semiconductor detector. It is believed that the slow down of both electrons and holes causes ballistic deficit in the

analog readout electronics and also increases the recombination of free carriers in the conduction and valence bands with opposite sign trapped charges. The recombination effect was not included in these simulations.

The drift time at various cathode applied voltages and during the high-flux experiments was measured injecting an α-particle near the cathode surface, as shown in Figures 5.25 and 5.26. In these experiments, an increase of $\sim 50\%$ in the drift time was measured comparing the α-particles cathode induced signals at low- and high-flux irradiation before complete spectrum degradation caused by the build up of positive space charge. In order to verify that the simulation code adequately simulates electrons and holes drifting at low operating fields, the drift time was measured for both carriers at various simulated applied cathode bias voltages. In theory, assuming constant mobility of both carriers μ_{eh}, no material detects, uniform operating electric field E and no space charge field, the drift time of both carriers $D_{t,eh}$ can be estimated according to Equation 6.1 using the properties listed in Table .6.1 and detector thickness $L = 5$ mm.

$$D_{t,eh} = L/\mu_{eh} \cdot E \tag{6.1}$$

Electrons and holes simulated drift times at various cathode applied voltages is compared with theoretical results given by Equation 6.1. These results verify that the simulation code can simulate low- and normal-operating electric field conditions, as shown in Tables 6.3 and Tables 6.4. Considering holes, the difference between predicted and simulated drift times is not significant.

Differences between drift time predicted by Equation 6.1 and simulated drift times at low- and normal-operating electric field are caused by the large mesh size used in simulations (34.6 μm) and discrete time steps considered when drifting electrons and holes, 5 ns and 20 ns respectively. Since after each time step charges are redistributed in neighbor meshes, as described in Figure 3.14, depending on the size of

Cathode Bias Voltage (V)	$D_{t,e}$ (ns), using Eq.6.1	$D_{ts,e}$ (ns), simulated
1000	317	340
950	334	390
900	353	444
850	373	504
800	397	583
750	423	661
700	453	747
650	488	845
600	529	957

Table 6.3: Comparison between predicted electron drift-time $D_{t,e}$ by Equation 6.1 with simulated drift time of electrons $D_{ts,e}$ calculated at various cathode bias voltages.

the mesh, more and more charges are artificially left behind, delaying the collection of both carriers. In future simulations, this problem can be minimized by reducing

Cathode Bias Voltage (V)	$D_{t,h}$ (μs), using Eq.6.1	$D_{ts,h}$ (μs), simulated
1000	11.9	12.3
950	12.5	13.0
900	13.2	13.8
850	14.0	14.7
800	14.9	15.7
750	15.9	16.9
700	17.0	18.2
650	18.3	19.6
600	19.8	21.3

Table 6.4: Comparison between predicted hole drift-time $D_{t,h}$ by Equation 6.1 with simulated drift time of holes $D_{ts,h}$ calculated at various cathode bias voltages.

the simulated mesh size. This requires more computer memory and more time to calculate space charge electric field used in simulations. Also, decreasing the mesh size increases the number of meshes needed to simulate the same region of the detector, which degrades the total simulation time. Then, future simulations using reduced mesh size will require reduced computational time.

6.3 Positive Space-Charge Buildup

Figure 6.1 shows the simulated buildup of positive space charge in a ~ 0.125 cm^3 region of the detector volume assuming that all positive space charge remains trapped and considering three different photon fluxes.

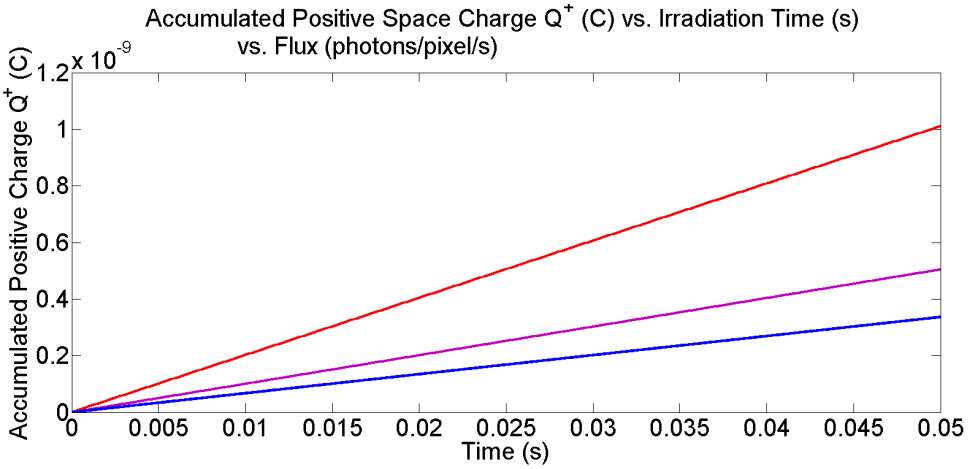

Figure 6.1: Accumulated positive space charge Q^+ as a function of irradiation time t, simulated for flux $\Phi = 60\times10^6$ (red), 30×10^6 (purple) and 20×10^6 (blue) photons/pixel/s considering no de-trapping of positive space charge.

Although, similar experiments were conducted at four different cathode bias voltages, as described in Chapter V, simulations considered a constant cathode bias voltage of -1000 V. These simulations also assumed the average time between interactions, $\bar{t} = 100$, 200 and 300 ns, to simulate the high irradiation fluxes $\Phi = 60\times10^6$, 30×10^6 and 20×10^6 photons/pixel/s, respectively, as described in Sec.3.1.2. These shorter average time between interactions compared with predicted in the high-flux experiments were necessary to accelerate the *polarization effect* in these detectors. This was required in order to accumulate positive space-charge in simulations, since using the parameters shown in Tables 6.1 and 6.2 was found to be a cost- or time-prohibitive endeavor.

These results show that positive space charge linearly builds up as a function of irradiation time if no de-trapping of space charge occurs in the material. In real-

ity, positive space charge must detrap after a finite time since, by observation, these detectors recover to their original operating condition a few seconds after the irradiator shutter is closed. If this type of polarization caused permanent damage to the crystal lattice, we would expect to measure gradual degradation in the spectral performance of these detectors, which was not observed in experiments. Although this might be true, and certainly should be studied in future work, irradiation levels to which these detectors were exposed were not sufficient to cause permanent damage to these detectors.

Using the same method, the accumulation of positive space charge Q^+ as a function of irradiation time was calculated considering the material properties listed in Table 6.1, as shown in Figure 6.2. Previous results with no detrap of positive space-charge are plotted in the background for comparison purposes.

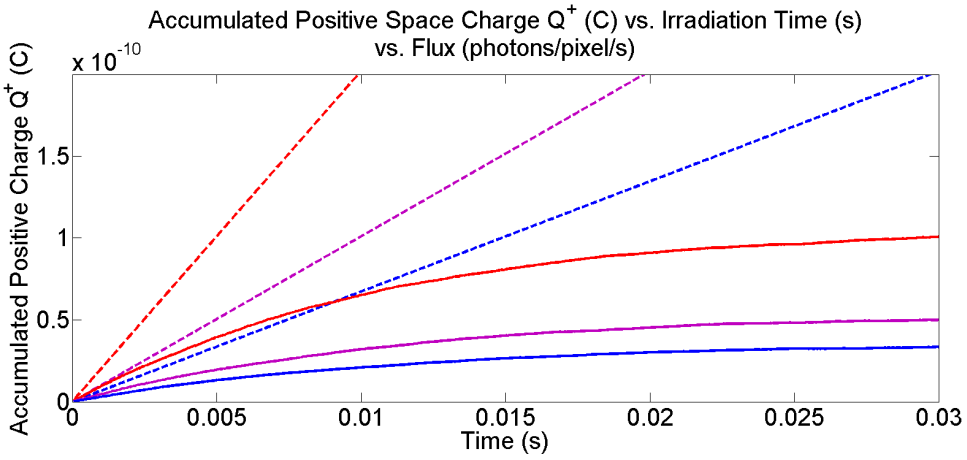

Figure 6.2: Accumulated positive space charge Q^+ as a function of irradiation time t, simulated for flux $\Phi = 60\times10^6$ (red), 30×10^6 (purple) and 20×10^6 (blue) photons/pixel/s, considering no de-trapping (dotted lines) and material properties listed in Table 6.1 (solid lines).

Considering material properties listed in Table 6.1, positive space charge slowly builds up until a plateau is reached. This plateau represents an equilibrium between positive space charge being injected into the detector and positive space charge being removed by the cathode electrode, described by the probabilities shown in Table

6.2. The equilibrium between positive space charge injection and charge collection, i.e. the value of the plateau, is a function of the applied flux Φ, charge transport properties, the concentration and distribution of material defects in the detector, charge recombination and other physical processes.

In simulations, only one defect level for electrons and two defect levels for holes were considered. It is suggested in future work to measure the concentration of defect levels in each trapping center using Deep Level Transient Spectroscopy (DLTS) techniques, since this information can be used to reduce the model mismatch found in the present work. For instance, the addition of a third and even deeper defect level for holes may be necessary in future models, but more experimental results are required to confirm this claim.

Figure 6.2 shows the predicted accumulated positive space charge Q^+ as a function of irradiation time, considering three different fluxes: $\Phi = 60 \times 10^6$ (red), 30×10^6 (purple) and 20×10^6 (blue). In high-flux experiments, described in Chapter V Figures 5.13-5.16, it was observed that these detectors operated with reduced internal electric field as Φ increased. This was concluded after measuring photopeak shifts towards lower energies as a function of increasing flux as well as α-particle induced signals during the high-flux experiments. It was also shown in Figures 5.9-5.12 that although the internal field was reduced by the buildup of positive space charge as a function of irradiation flux and time, these detectors continued to operate with reduced performance.

6.4 The Polarization Effect

In order to qualitatively explain the *polarization effect*, a critical flux Φ_c is defined in this work as the flux necessary to create sufficient positive space charge capable of reducing and distorting the internal electric field to levels that cause severe spectral degradation. In experiments, spectral degradation between different flux levels

can be observed in more detail in the results shown in Appendix B. In this simple analysis, there must be a critical amount of positive space charge Q_c^+. Then, operating these detectors above this critical level is not possible, but near this critical level of accumulated positive space-charge Q_c^+, these detectors can still work with degraded spectroscopic performance, showing no clear photopeak and reduced count rate, as described in Figures 5.9-5.12. Below this critical level of positive space-charge Q_c^+, these detectors can operate with reduced performance, showing photopeak shift towards lower energies as a function of increasing incident photon flux, which can be corrected. The simulated maximum level of accumulated positive space-charge is represented by the plateau level discussed in Section 6.3, which causes the operating electric field to be reduced in the detector volume if below the critical level.

High-flux simulations were conducted at different positive space-charge buildup levels A, B, C and D shown in Figure 6.3.

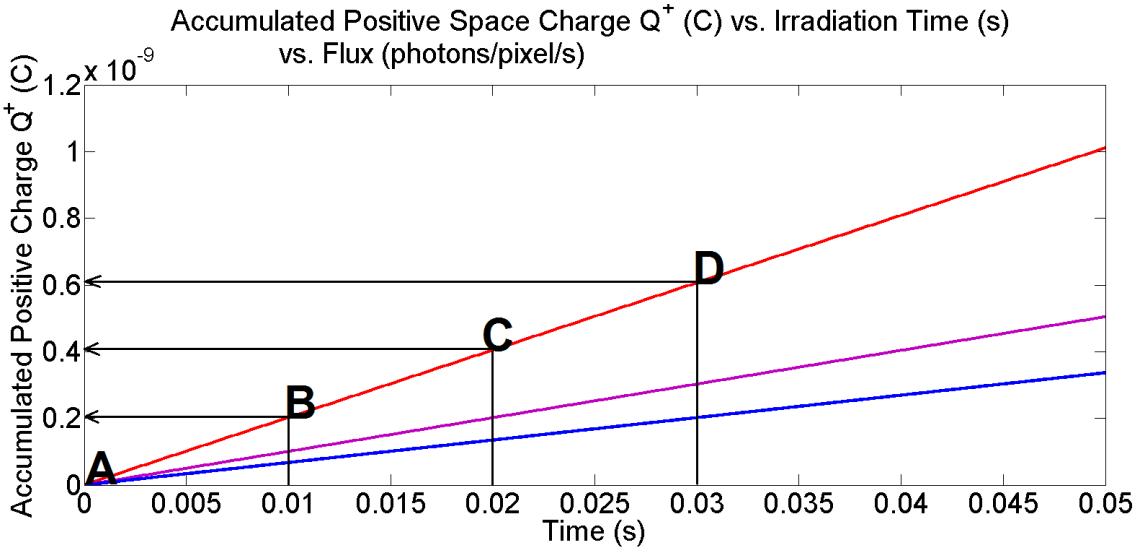

Figure 6.3: Initial positive space-charge distributions in the high-flux simulations, where A considered no positive space-charge buildup, B started with positive space-charge buildup after 10 ms, C started with positive space-charge buildup after 20 ms and D started with positive space-charge buildup after 30 ms.

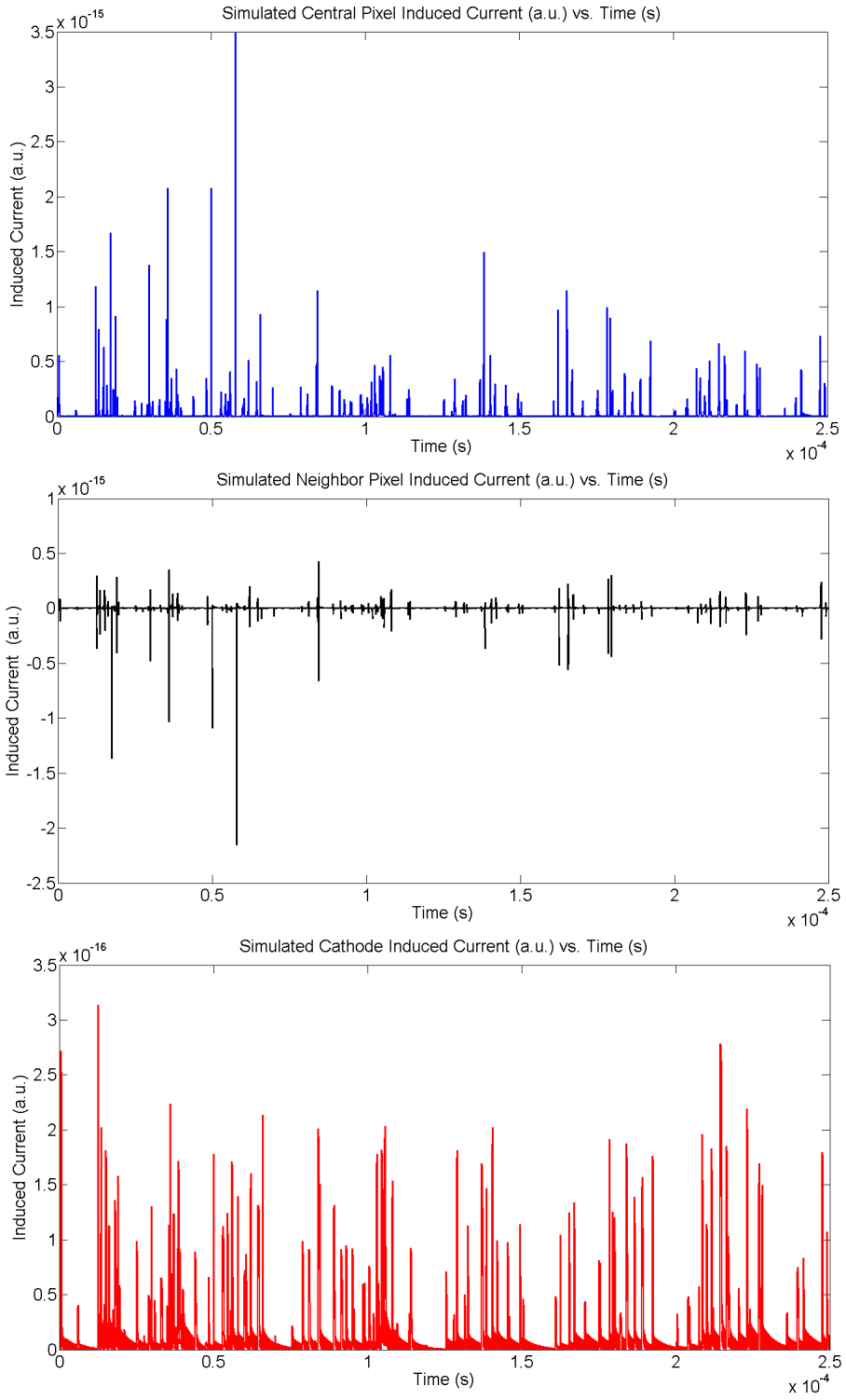

Figure 6.4: Simulated high-flux induced currents on collecting pixel (blue), neighbor pixel (black) and cathode (red) electrodes applying the Shockley-Ramo Theorem and considering an average time between interactions of 500 ns.

In each simulation, the initial distribution of positive space-charge was considered to be the accumulated space-charge at different simulated times, corresponding to t = 0 ms (position A), 10 ms (position B), 20 ms (position C) and 30 ms (position D). 3D interaction positions and energies were generated and stored in list-mode, as described in Section 3.1.1. These simulated events were injected into the simulation with an average time between interactions of 500 ns. Figure 6.4 shows the simulated induced currents on pixel1, pixel2 and cathode electrodes applying the Shockley-Ramo Theorem. Then, in order to measure the amplitude of induced signals using the same post-processing software used in the high-flux experiments, induced currents are converted into induced charge, integrating the current over time, as seen in Figure 6.5.

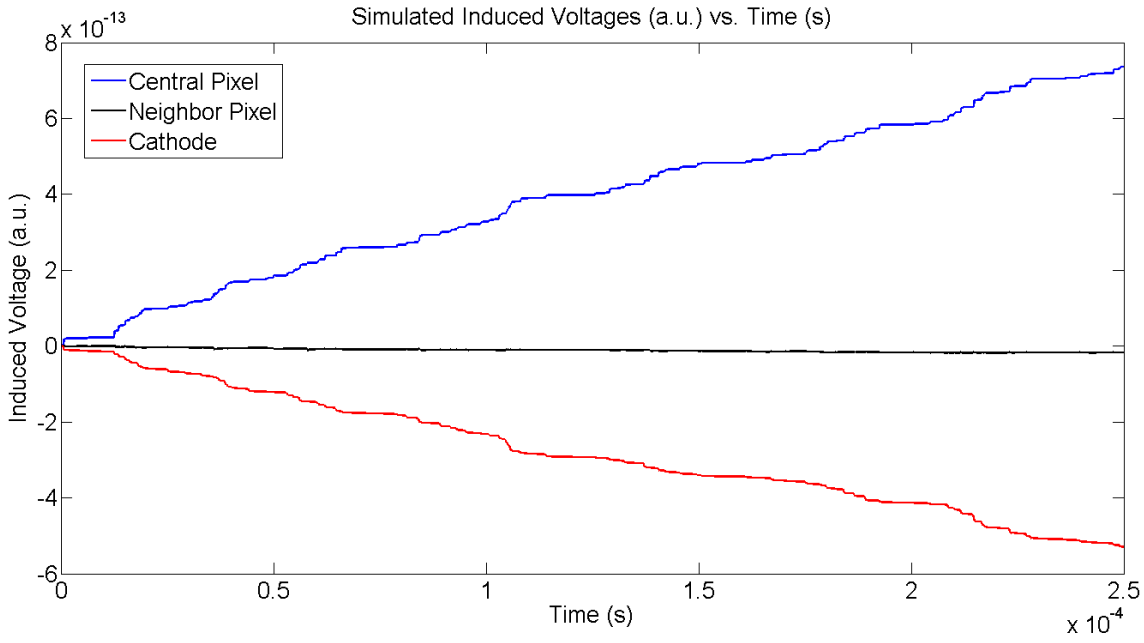

Figure 6.5: Simulated high-flux induced charge on collecting pixel (blue), neighbor pixel (black) and cathode (red) electrodes applying the Shockley-Ramo Theorem and considering an average time between interactions of 500 ns.

Individual signals induced on the collecting pixel, neighbor pixel and cathode electrodes are extracted from simulated induced signals in continuous mode, as shown

in Figure 6.5, similarly to measured induced signals in high-flux experiments described in Figure 5.4. The main difference is that in simulations the preamplifier RC feedback was not modeled. Figure 6.6 shows a typical event extracted from Figure 6.5, where electrons are collected in the collecting pixel (blue) while a transient signal is induced on the neighbor pixel (black) and a linear signal is induced on the cathode electrode (red).

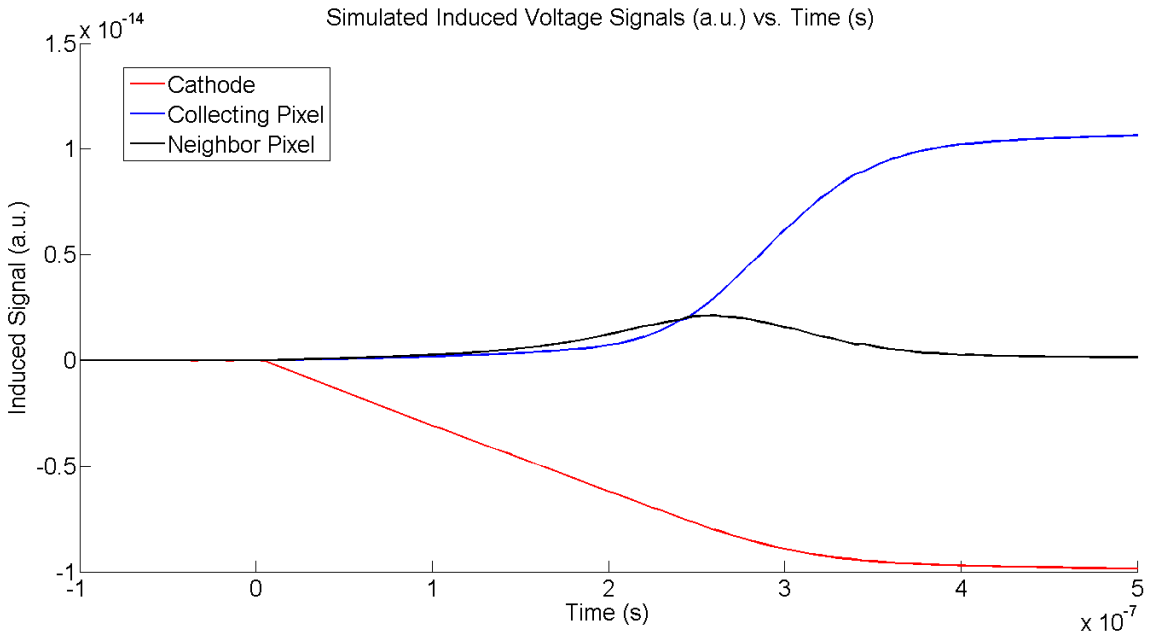

Figure 6.6: Simulated high-flux induced charge on collecting pixel (blue), neighbor pixel (black) and cathode (red) electrodes applying the Shockley-Ramo Theorem, extracted from Figure 6.5.

Then, starting at different levels of positive space-charge buildup, points A, B, C and D described in Figure 6.3, and using a 1 μs shaping time for pixel induced signals and 3 μs shaping time for cathode induced signals, simulated Cs-137 spectra is calculated. Figure 6.7 shows the simulated collecting pixel and cathode spectra when no positive space-charge buildup is considered in the beginning of the simulation, represented by position A in Figure 6.3.

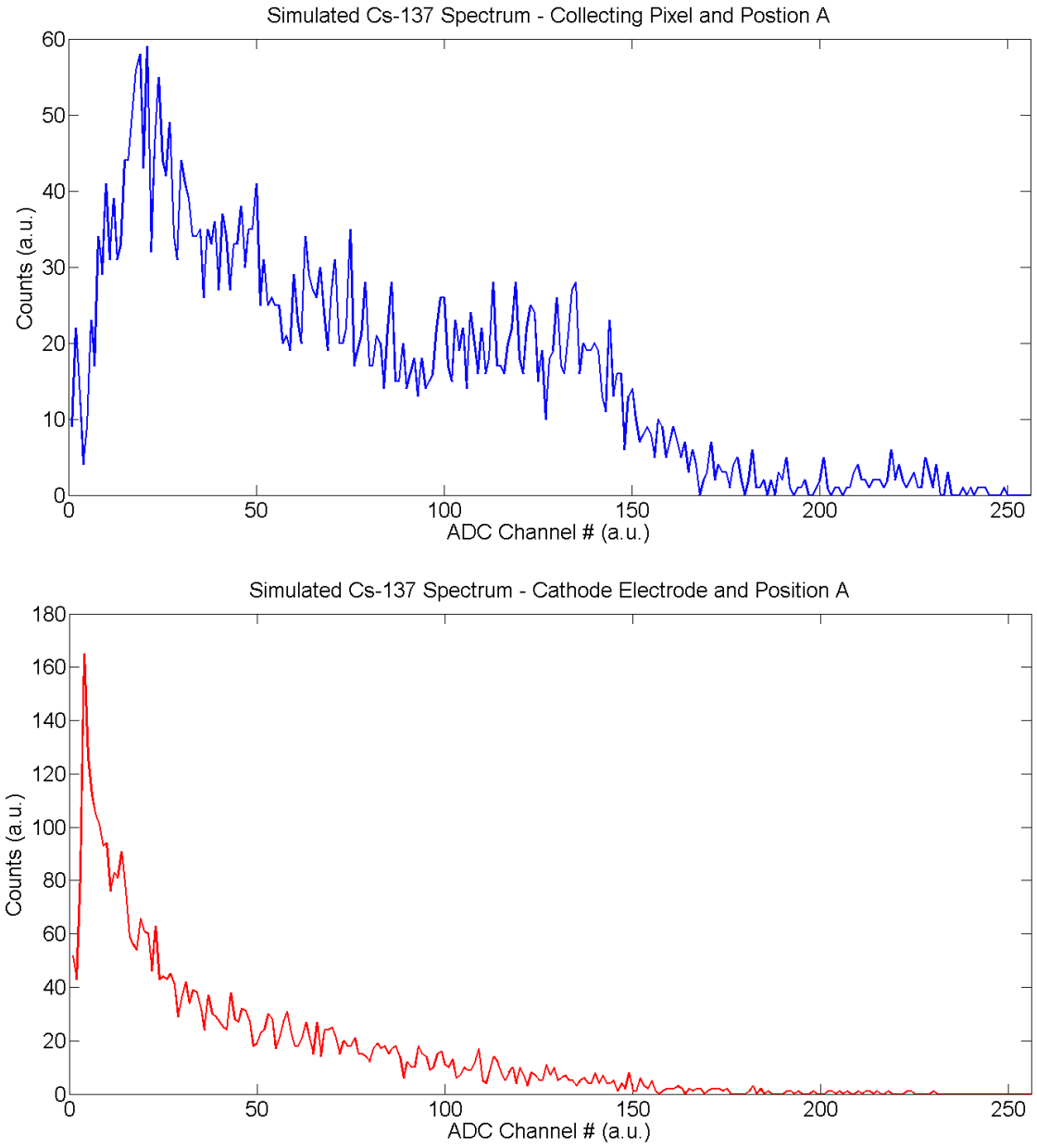

Figure 6.7: Simulated high-flux Cs-137 spectra for the collecting pixel (blue) and the cathode electrode (red) when no positive space-charge buildup is considered in the beginning of the simulation, represented by position A in Figure 6.3.

In experiments, an Am-241 α-source is used to monitor changes in the internal electric field E as a function of irradiation flux Φ and time. The same technique is used in simulations, injecting a simulated α-particle near the cathode surface at fixed

time intervals.

Figure 6.8 shows simulated α-particle induced signals on the collecting pixel and cathode electrode plotted as a function of irradiation time. These signals were simulated considering no de-trapping of positive space charge and the injection of simulated Monte-Carlo Cs-137 photons at every 100 ns and α-particles at every 50 μs, as described in Figure 6.1 (red curve). It can be observed in these plots that charges (electrons and holes) move slower inside the detector due to positive space-charge buildup. Signals induced on collecting pixel and cathode electrode, as a function of the amount of positive space-charge buildup, have longer charge collection times. Positive space-charge buildup causes an increase in drift time, which is consistent with the reduction of the internal electric field. In the beginning of the irradiation, $t = 0 \ldots 5$ ms, the measured drift time was $\sim$ 350 ns. After $\sim$ 10 ms, the drift time increased from $\sim$ 350 ns to $\sim$ 550 ns, an increase of $\sim$ 50% which is similar to the increase in drift time observed in measurements before detector polarization, as shown in Figure 5.26. These simulated α-particle induced signals are used to determine the critical amount of positive space charge Q_c^+ needed to degrade the spectral performance of these detectors when operated in high-flux conditions. Then, considering only the drift time criterion, polarization of the detector occurs at $\sim$ 10 ms when injecting charges at every 100 ns and assuming no de-trapping of positive space-charge, which is equivalent to position B in Figure 6.3. In experiments and simulations, collecting these signals at fixed time intervals causes ballistic deficit and incomplete charge collection when integrating these induced signals with a filter having a fixed shaping time. In experiments-only, since recombination models were not implemented in this work, more charge recombination is expected when there is more positive space-charge buildup due to the lower drift velocity of electrons and higher concentration of positive space-charge. The most important recombination process is between electrons in the conduction band with positive space-charge trapped in

deep-level trapping centers.

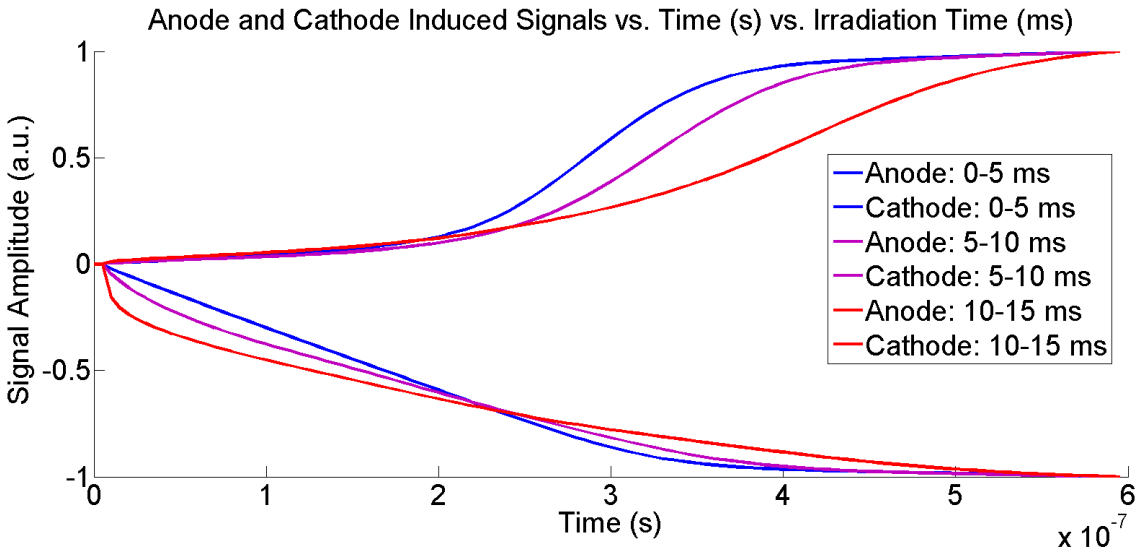

Figure 6.8: Simulated α induced signals as a function of irradiation time, considering the injection of Cs-137 simulated photons at every 100 ns while operating the detector at -1000 V cathode bias voltage and no de-trapping of positive space charge.

Figure 6.9 shows the total number of simulated events counted as a function of irradiation time, considering the injection of events at every 100 ns and no de-trapping of positive space charge, which is calculated assuming no de-trapping of positive space-charge and injection of simulated photons at an average time of 100 ns, represented by the red curve in Figure 6.1. Simulated Cs-137 spectra was calculated at different levels of positive space-charge buildup, represented by positions B, C and D in Figure 6.3. At first, collecting pixel and cathode electrode simulated spectra were calculated considering the level of positive space-charge buildup at position B, as shown in Figure 6.10. This level of space-charge buildup is equivalent to 10 ms after the beginning of the simulation. Comparing results in Figure 6.10 with results in Figure 6.7, it can be observed that the simulated spectra shown in Figure 6.10 are slightly shifted towards lower energy bins. Then, using the same post-processing criteria, collecting pixel and the cathode electrode simulated spectra were calculated

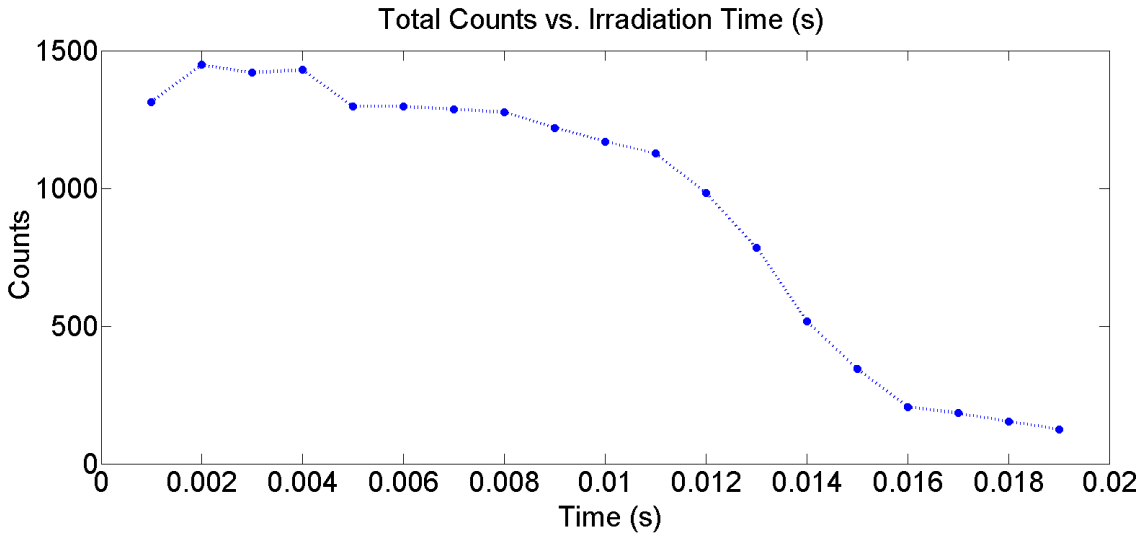

Figure 6.9: Simulated total number of events counted as a function of irradiation time, considering the injection of Cs-137 simulated photons at every 100 ns, while operating the detector at -1000 V cathode bias voltage and assuming no de-trapping of positive space charge.

considering the level of positive space-charge buildup at position C, as shown in Figure 6.11. This level of space-charge buildup is equivalent to 20 ms after the beginning of the simulation. Comparing results in Figure 6.11 with results in Figure 6.7, it can be observed that the simulated spectra shown in Figure 6.11 are significantly shifted towards lower energy bins and the overall shape of the collecting pixel spectra has changed significantly. Finally, using the same post-processing criteria, collecting pixel and the cathode electrode simulated spectra were calculated considering the level of positive space-charge buildup at position D, as shown in Figure 6.12. This level of space-charge buildup is equivalent to 30 ms after the beginning of the simulation. Comparing results in Figure 6.12 with results in Figure 6.7, it can be observed that the simulated spectra shown in Figure 6.12 are significantly shifted towards lower energy bins, more than observed in Figure 6.11, and the overall shape of the collecting pixel spectra has changed even more than previously observed at position C.

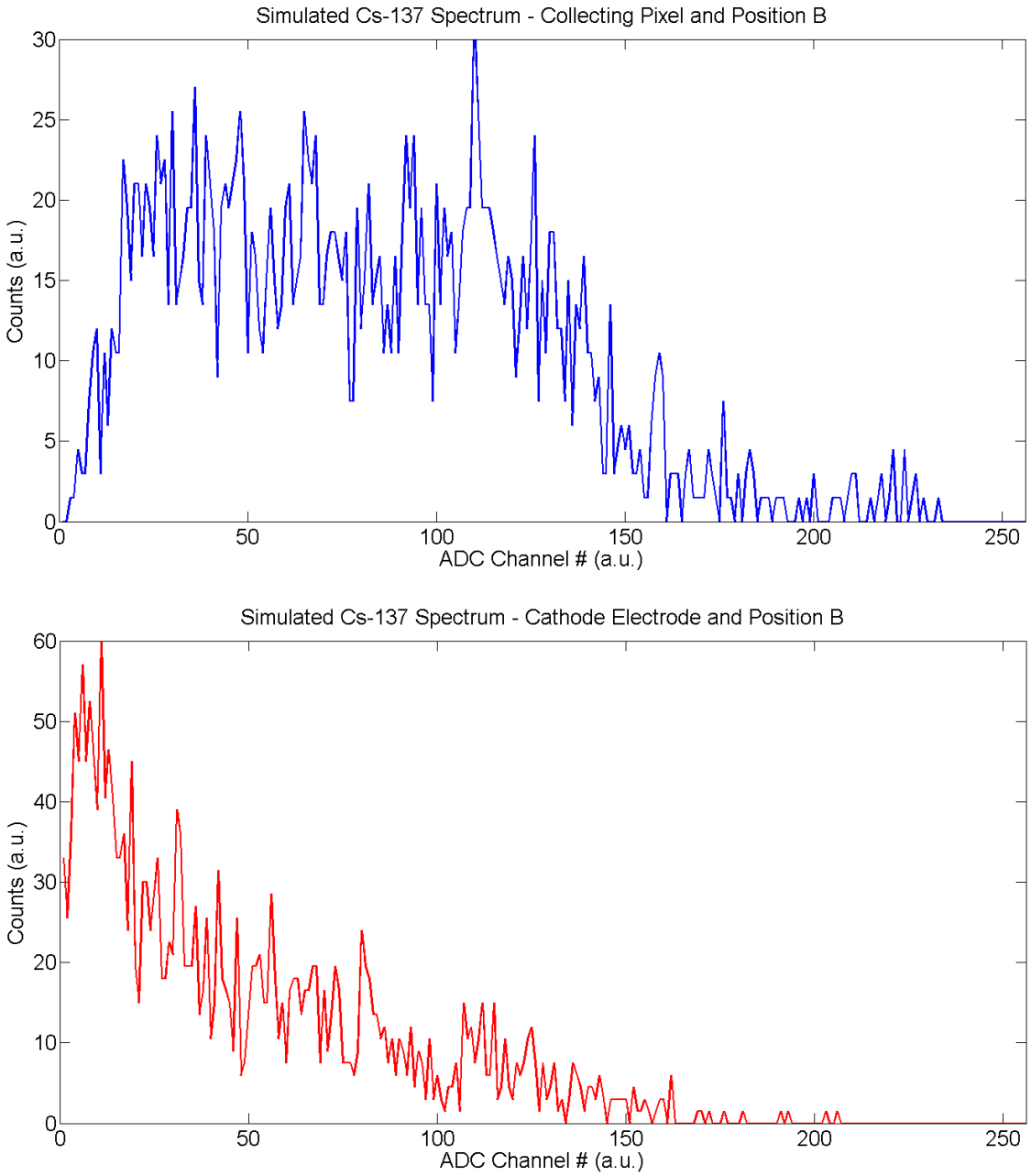

Figure 6.10: Simulated high-flux Cs-137 spectra for the collecting pixel (blue) and the cathode electrode (red) when 10 ms of simulated positive space-charge buildup is considered at the beginning of the simulation, represented by position B in Figure 6.3.

6.5 Analysis of High-Flux Simulation Results

In order to better understand and improve future simulation results, it is suggested to minimize unnecessary and known sources of errors in the current experimental

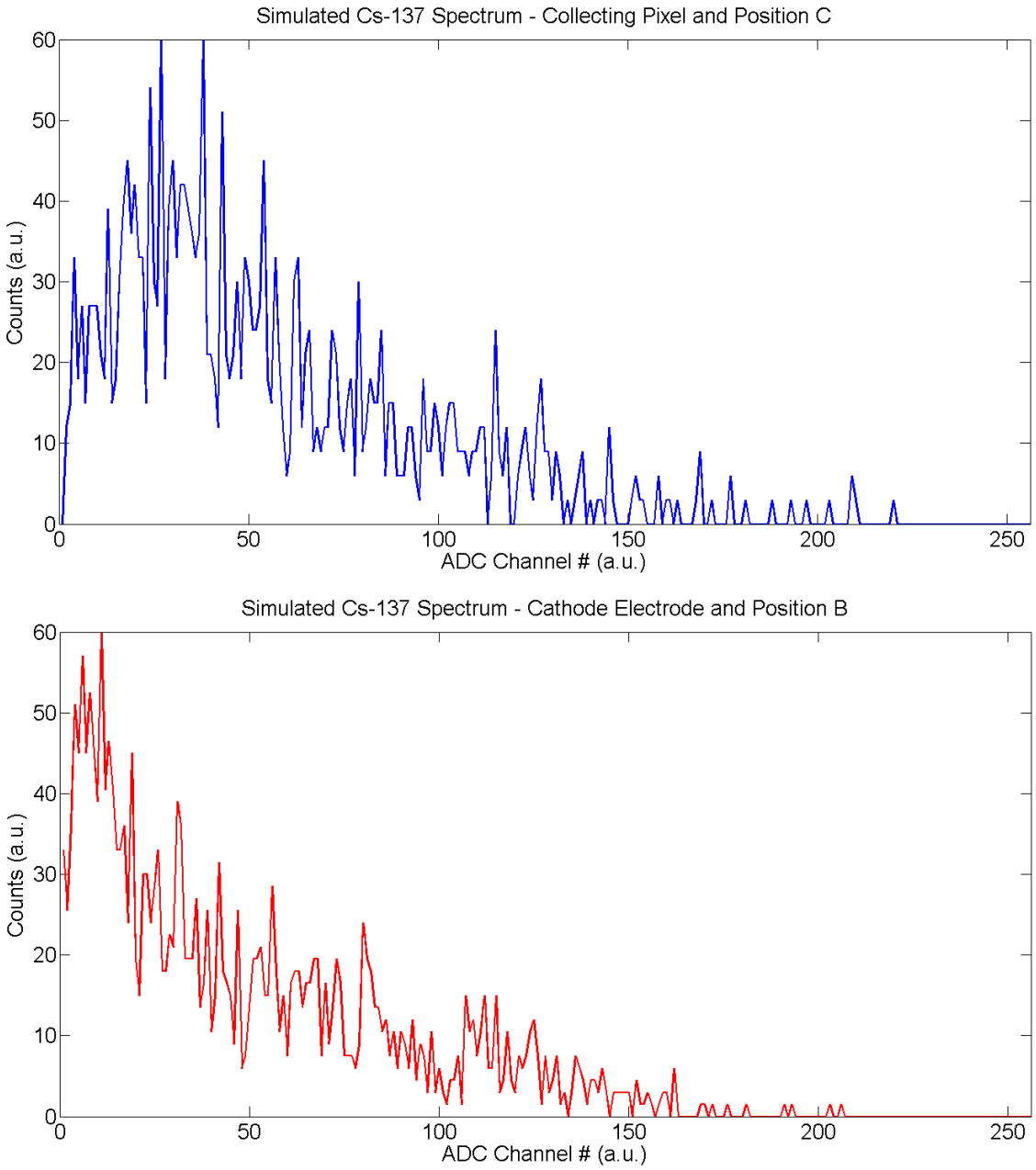

Figure 6.11: Simulated high-flux Cs-137 spectra for the collecting pixel (blue) and the cathode electrode (red) when 20 ms of simulated positive space-charge buildup is considered in the beginning of the simulation, represented by position C in Figure 6.3.

apparatus and simulation models. Including the effects of charge recombination and operating temperature can significantly improve current results, although increasing

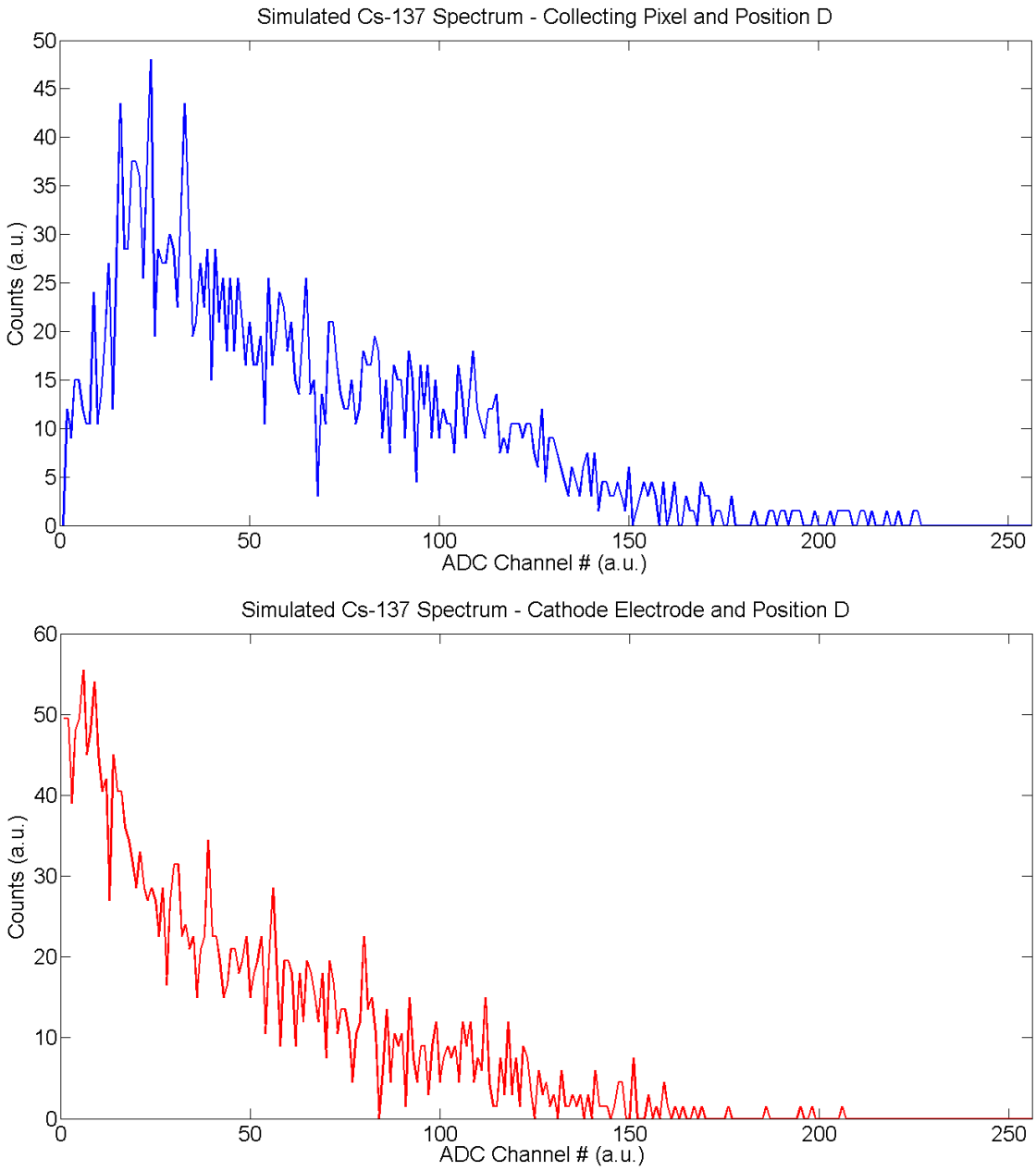

Figure 6.12: Simulated high-flux Cs-137 spectra for the collecting pixel (blue) and the cathode electrode (red) when 30 ms of simulated positive space-charge buildup is considered in the beginning of the simulation, represented by position D in Figure 6.3.

model complexity can slow down simulations. Also, improving the Monte-Carlo model of the experimental apparatus can reduce model mismatches in future simulations.

In Section 6.2, a 1D-approach was used to monitor changes in the electric field

in high-flux simulations, since a similar approach was considered in high-flux experiments using an Am-241 α-source. Although, 2D distributions of positive space-charge as a function of irradiation flux and time were calculated in current high-flux simulations, this feature was not fully explored in this work. The main reason is related with the current measurements, since in each experiment only two active channels were used in the GaGe Octopus digitizers - collecting pixel and cathode electrode. Then, future experiments having reduced total collection time in continuous mode, using more active channels (collecting pixel + neighbor pixels + cathode electrode), would provide the required spatial information.

It is shown in this work that the slow down of both electrons and holes causes ballistic deficit when using an analog readout circuit. Recombination is also increased at lower electric fields, thus recombination models of free electrons in the conduction and holes in the valence bands with opposite sign trapped charges need to be implemented in future simulations. Temperature effects are also needed in future models, since it is known that charge transport properties of room-temperature semiconductor detectors vary considerably as a function of temperature. Also, it is believed that average de-trapping time of positive space-charge trapped in deep defect levels can be reduced by increasing the operating temperature of CdZnTe detectors. These physical processes need to be understood and implemented in future simulations.

Differences between drift times predicted by Equation 6.1 and simulated drift times at low- and normal-operating electric field are caused by the large mesh size (34.6 μm) used in the current simulation. It was concluded that redistributing charges according to the method described in Figure 3.14 causes more and more charges to be artificially left behind, delaying the collection of both carriers. In order to reduce this artificially generated effect, larger time steps can be used, although this is not desired in these simulations. Alternatively, in future simulations this problem can be minimized by reducing the size of the mesh. In order to correctly simulate charge

diffusion, the size of the mesh needs to be smaller than the diffusion length of both carriers ($FWHM_{e,h}$) in each time step. The estimated electron and hole diffusion lengths after each time step, 5 ns and 20 ns respectively, are $FWHM_e = 10$ μm and $FWHM_h = 6$ μm. Then, in order to correctly simulate diffusion, the mesh size is required to be less than 6 μm in future simulations. More computer memory is required and longer simulation times are expected, thus improved computational performance is also required.

High-flux simulations considering no de-trapping of positive space-charge were necessary to accelerate the *polarization effect* in simulations, since using the parameters shown in Tables 6.1 and 6.2 was found to be a cost- or time-prohibitive endeavor. These results show that positive space charge linearly builds up as a function of irradiation time if no de-trapping of space charge occurs in the material. In experiments, positive space charge must detrap after a finite time since, by observation, these detectors recovered to their original operating condition a few seconds after the irradiator shutter is closed. If this type of polarization caused permanent damage to the crystal lattice, we would expect to measure gradual degradation in the spectral performance of these detectors, which was not observed in experiments. This *memory effect* should be studied in future work, exposing CdZnTe detectors to higher irradiation photon fluxes.

In experiments and simulations, collecting these signals at fixed time intervals causes ballistic deficit and incomplete charge collection when integrating these induced signals with a filter having a fixed shaping time. In experiments-only, since recombination models were not implemented in this work, more charge recombination is expected when there is more positive space-charge buildup due to the lower drift velocity of electrons and higher concentration of positive space-charge. The most important recombination process is between electrons in the conduction band with positive space-charge trapped in deep-level trapping centers. In future work,

recombination models combined with temperature models are required.

The so-called *polarization effect* was studied by comparing results in Figures 6.10, 6.11 and 6.12 with results in Figure 6.7. It is observed that the simulated spectra shown in Figures 6.10, 6.11 and 6.12 are progressively shifted towards lower energy bins as higher positive space-charge buildup is considered in the beginning of each simulation. The simulated spectral change is similar to changes in measured spectra observed in experiments just before the *polarization* effect. More simulations considering the inclusion of temperature and recombination effects in the modeling are needed to quantitatively predict the polarization time in future work.

CHAPTER VII

Conclusions

In the beginning of this research, as represented in Figure 1.1, very little information was known. This Ph.D. research investigated all seven topics addressed in Figure 1.1, although some of them were more explored than others. This preliminary work was concerned with building foundations, rather than exploring in detail all of the seven topics addressed. More attention was given to the high-flux experiments and simulations, data analysis and measuring the electrical transport properties of CdZnTe. In future work, more effort is needed in ASIC development for high-flux applications focusing specific project requirements, since these were not clearly defined in the beginning of this study and there was no clear definition of the meaning of the term *high-flux*. Initial studies published by other researchers concluded that the incident flux Φ was the only factor limiting the operation of CdZnTe detectors in high-flux scenarios. Clearly, in this work, important parameters such as the energy of the source, the operating conditions (i.e. temperature T and applied voltage V) and the dimension of the detector as well as electrode configuration are important factors that need to be addressed in more depth in future work. The reason why CdZnTe has not yet been fully implemented in high-flux applications is believed to be related to its material properties and limited performance of fast readout electronics. Current ASIC developed by different manufacturers are becoming more feasible. In

the future, it should be possible to use 3D-position-sensitive detectors in pulse mode at reasonably high count rates ($>\sim$ 100 kHz per channel). CdZnTe crystal growth technology is more mature and crystal quality has improved. There has been little agreement between researchers on the fundamental issues related to the properties of materials needed for this specific application, and the tools developed in this work can be used in the future to help CdZnTe manufactures to make better detectors for high-flux applications. In order to completely understand this problem, we have been building over the past years a full 3D simulation tool kit of pulse waveforms induced on pixelated CdZnTe detectors under high irradiation fluxes.

7.1 Simulation Modeling

In Section 3.1, a simple model of the experimental apparatus was implemented. In this model, eight objects were considered, as described in Table 3.1. Monte-Carlo simulations of the experiment apparatus were combined with measured data at different fluxes to calculate the relationship between incident flux Φ at the surface of the detector and the average time between interactions $\bar{t}$ used in simulations. In future studies, a X-ray source needs to be implemented and modeled in simulations, *Sidky et al.* (2005a). Also, phantoms similar to the ones used in medical imaging, *Gach et al.* (2008), but using different material compositions, specific for each application, are required in future studies. Results shown in Table 3.2 were used to calculate the constant of proportionality C used in Equation 3.1, considering fluxes $\Phi < 45$ 000 photons/pixel/s. Reasons for the non-proportionality found at higher fluxes, represented by deviations from calculated values of C at lower fluxes, are not well understood and need to be investigated in future work. These differences may be attributed to several approximation and errors during the process of measuring and estimating the value of C, such as:

a) Unknown/incorrect Cs-137 source distribution

b) Unknown/incorrect source shield materials and dimensions

c) Imprecise/incorrect alignment between source, collimator and detector

d) Effects of surrounding materials not correctly modeled in Monte-Carlo simulations

e) Pile-up of events in the data acquisition system

f) Detector energy response not modeled

In Section 3.2 the system described by Equations 3.2-3.9 solved the charge continuity equations in a homogeneous material having uniform distribution of defects. The number of defects per unit volume was assumed to be larger than the number of charge carriers trapped per unit volume. Defect levels were treated as traps, being populated and depopulated by charge carriers according to statistical models predicted by Equations 3.2-3.6, where the amount of charges being trapped or de-trapped in any mesh was given by the average trapping and de-trapping times modeled. Recombination between electrons and holes at different energy levels play an important role in reducing the amount of positive space charge buildup in the detector volume at high photon flux irradiation. Also, recombination plays an important role reducing the amplitude of measured signals - which is seen as a shift of photopeak to lower energy bins -, especially at low electric fields. This important effect was not included in this work and should be investigated in the future.

The implementation of the *3D-Axisymmetric Model* described in Sec.3.3 considered a small region of the detector volume. In future studies, the simulated detector volume needs to be expanded, including more neighbor pixels. Future studies will require additional parallel processing capabilities, since it is expected that future models will have more trapping centers and other physical processes included in the modeling.

7.2 Material Properties

Statistical models described in Section 4.1.1 considered one electron and one hole trapping centers. In future work, more detailed models considering multiple trapping centers with different densities of defects should be considered, which would change the ratios between electrons-only and holes-only induced signals. In Chapter IV, charge transport properties were calculated considering the same average hole trapping time for both defect levels in the α-particle measurements and different concentrations in the K_α X-ray measurements. This was one reason why the matching between simulated and measured holes-only induced signals for the α-particle measurements was not as accurate as the K_α X-ray measurements. These results produced better fitting, which indicates that the initial assumption considering the densities of different defect levels constant for all trapping centers may not be true. Also, measured signals using K_α X-rays while operating the detector at reverse bias showed better signal-to-noise ratio, which enabled the measurement of induced signals for longer periods of time ~ 400 μs with higher confidence level. In these measurements, there is a weak indication that considering a third hole defect level might be necessary to better represent the transport properties of holes in CdZnTe in future high-flux studies.

7.3 High-Flux Experiments

The behavior of CdZnTe under high-flux irradiation when operated under higher temperatures is suggested in future studies, since the de-trapping of charges is highly correlated with temperature, *Zanio et al.* (1973). It is believed that under higher temperatures trapped charges will detrap faster, which will reduce the amount of positive space charge buildup in the detector as a function of irradiation flux and time. Also, in future studies it is suggested to read out more channels simultaneously. This

can be achieved easily by increasing the number of GaGe systems used and designing a system which better synchronizes the irradiator shutter with the data acquisition system. Also, it is suggested to test the system using an actual X-ray source rather than using a Cs-137 source. Since the current system was manually aligned and positioned in the irradiation room, it is suggested to use a better XYZ-positioning system in future experiments.

7.4 High-Flux Simulations

In order to better understand and improve future simulation results, it is suggested to minimize unnecessary and known sources of errors in the current experimental apparatus and simulation models. Including the effects of charge recombination and operating temperature can significantly improve current results, although increasing model complexity can slow down simulations. Also, improving the Monte-Carlo model of the experimental apparatus can reduce model mismatches in future simulations. It is suggested to explore spatial changes in the distribution of positive space-charge as a function of irradiation flux and time in future work, since this feature was not fully explored in this work due to reduced number of channels active in the high-flux experiments. Then, future experiments having reduced total collection time in continuous mode, using more active channels (collecting pixel + neighbor pixels + cathode electrode), would provide the required spatial information.

It is shown in this work that the slow down of both electrons and holes causes ballistic deficit when using an analog readout circuit. Recombination increases at lower electric fields, thus recombination models of free electrons in the conduction and holes in the valence bands with opposite sign trapped charges need to be implemented in future simulations. Temperature effects are also needed in future models, since it is known that charge transport properties of room-temperature semiconductor detectors vary considerably as a function of temperature. Also, it is believed that average de-

trapping time of positive space-charge trapped in deep defect levels can be reduced by increasing the operating temperature of CdZnTe detectors. These physical processes need to be understood and implemented in future simulations.

Differences between drift times predicted by Equation 6.1 and simulated drift times at low- and normal-operating electric field were found to be caused by the large mesh size (34.6 μm) used in the current simulation. It was concluded that redistributing charges according to the method described in Figure 3.14 causes more and more charges to be artificially left behind, delaying the collection of both carriers. In future simulations this problem can be minimized by reducing the size of the mesh. Then, in order to correctly simulate diffusion and minimize this problem, the mesh size is required to be less than 6 μm in future simulations. More computer memory is required and longer simulation times are expected, thus improved computational performance is also required.

High-flux simulations considering no de-trapping of positive space-charge were necessary to accelerate the *polarization effect* in simulations, since using the parameters shown in Tables 6.1 and 6.2 was found to be a cost- or time-prohibitive endeavor. In experiments, positive space charge must detrap after a finite time since, by observation, these detectors recovered to their original operating condition a few seconds after the irradiator shutter is closed. It is suggested in future work to measure the leakage current during the high-flux experiments to indirectly monitor the buildup of positive space-charge. Also, in order to investigate if this type of polarization causes permanent damage to the crystal lattice, it is suggested in future work to monitor the decay of the leakage current after the irradiator shutter is closed. This requires a faster and more elaborate control of the *turn-on* and *turn-off* of the irradiation source, which can not be achieved with current mechanical shutters. A X-ray source can be used instead, and this *memory effect* should be studied in future work, exposing CdZnTe detectors to higher irradiation photon fluxes.

In future work, recombination models combined with temperature models are required in simulations, since more charge recombination is expected when there is more positive space-charge buildup due to the lower drift velocity of electrons and higher concentration of positive space-charge. The most important recombination process is between electrons in the conduction band with positive space-charge trapped in deep-level trapping centers.

The so-called *polarization effect* was studied by comparing results in Figures 6.10, 6.11 and 6.12 with results in Figure 6.7. It is observed that the simulated spectra shown in Figures 6.10, 6.11 and 6.12 are progressively shifted towards lower energy bins as higher positive space-charge buildup is considered in the beginning of each simulation. The simulated spectral change is similar to changes in measured spectra observed in experiments just before the *polarization* effect, as seen in Appendix B. More simulations considering the inclusion of temperature and recombination effects in the modeling are needed to quantitatively predict the polarization time in future work.

7.5 Final Comments and Suggestions

In our models, we assumed only two defect levels for holes, one representing an average shallow defect level and another representing an average deep defect level. Clearly, this is not the case, but deep defects are difficult to measure with our current technique. Using more advanced techniques, such as Deep Level Transient Spectroscopy (DLTS), would improve these results. Studying these properties at different temperatures is also suggested for future work, since average de-trapping times are strongly correlated with temperature. Although simulations qualitatively agree with experiments, discrepancies between simulated and measured results exist. These discrepancies were attributed to possible model mismatches. In future work, more detailed studies of each of the problems listed in this work is suggested in order to

improve the agreement between simulations and experiments. This will enable more precise predictions of the detector performance when operating under high-flux scenarios. One fundamental problem found in this research was the difficulty found in measuring the transport properties of holes in CdZnTe detectors. In future work, better source and detector characterization is also needed to improve current results, including:

a) Source distribution and source shield materials and dimensions

b) Alignment between source, collimator, and detector

c) Effects of surrounding materials in the irradiation room

d) Detector response

The implementation of the *3D-Axisymmetric Model* described in Sec.3.3 considered a small region of the detector volume. Due to increasing memory capacity available in computers, a larger region of the detector volume should be modeled in future work. Additionally, increasing the number of threads enables the inclusion of additional physical processes without degrading the performance of the code, which is needed in future work. In fact, a true parallel code can substantially improve computational time. Also, more detailed models considering multiple trapping centers with different densities of defects should be analyzed, which would change the ratios between electrons and holes induced signals.

In future work, it is suggested to investigate the behavior of CdZnTe under high-flux irradiation when operated under higher temperatures. It is believed that under higher temperatures, trapped charges will detrap faster, which will reduce the amount of positive space charge build up in the detector as a function of irradiation flux and time. Also, in future studies it is suggested to read out more channels simultaneously while irradiating the system using a X-ray source rather than using a Cs-137 source. The current system was manually aligned and positioned in the irradiation room, which introduced errors in the measurements. It is suggested to use a better XYZ-

positioning system in future experiments. More importantly, this work has shown a complete 3D framework that can be used to study and predict the performance of any semiconductor detector when operated under high-flux scenarios.

APPENDICES

APPENDIX A

Cs-137 Induced Signals at $\Phi_1 = 39 \times 10^3$, $\Phi_2 = 57 \times 10^3$, ..., $\Phi_{11} = 219 \times 10^3$ photons/pixel/s as a Function of Irradiation Time t_1, t_2, ..., t_{10} at -750, -1000, -1250 and -1500 Cathode Bias Voltages.

Figs.A.1 and A.2 show measured anode and cathode induced signals in continuous mode at -750, -1000, -1250 and-1500 cathode bias voltages and flux Φ_1 = 39.3k, ..., Φ_{11} = 219.3k photons/pixel/s. Only part of the data is shown in these plots, equivalent to 1000 samples, which is $\sim 400\mu$s of total acquisition time.

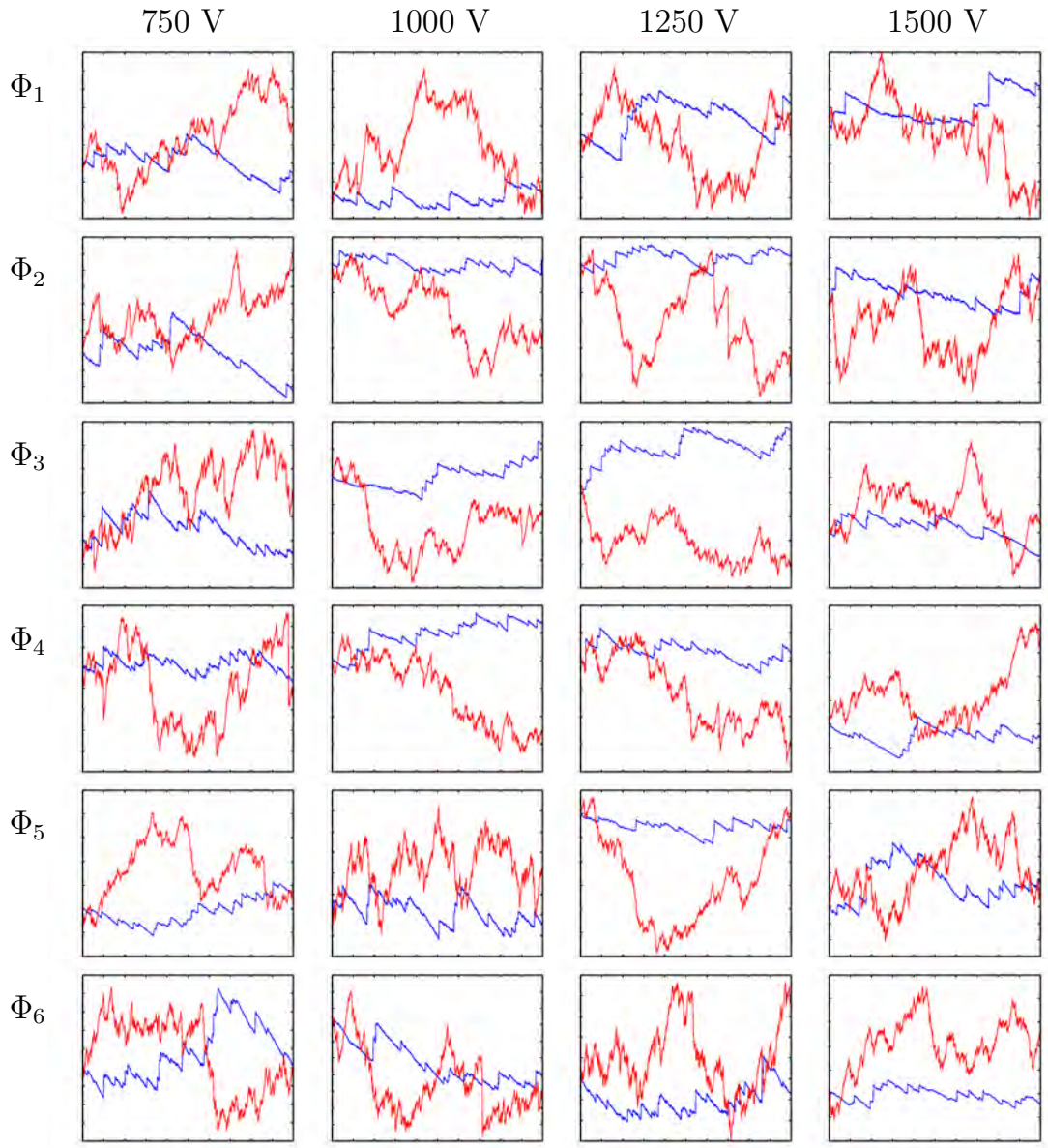

Figure A.1: Measured anode and cathode induced signals at -750, ..., -1500 V and flux $\Phi_1 = 39.3$k, ..., $\Phi_6 = 129.3$k photons/pixel/s.

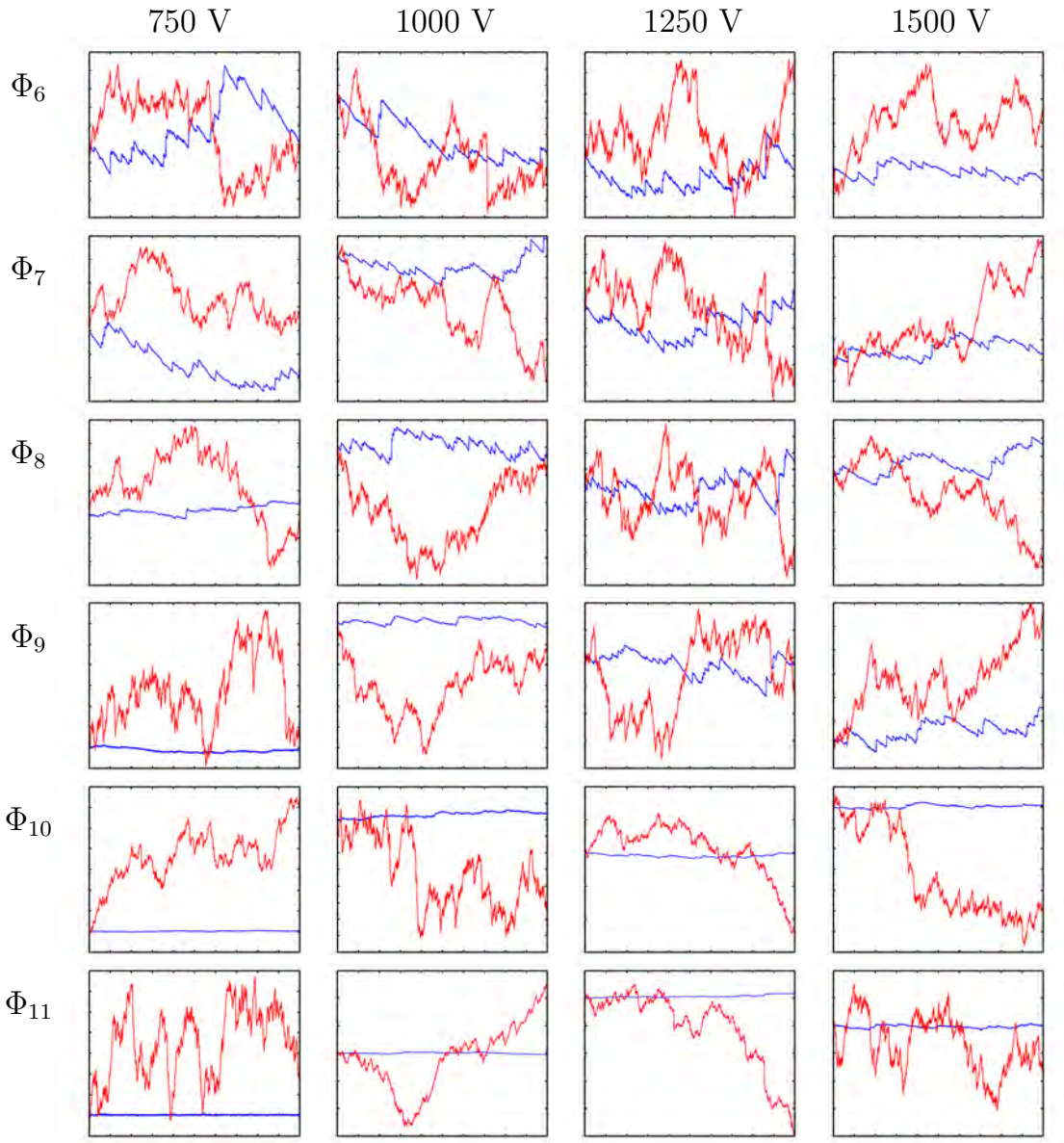

Figure A.2: Measured anode and cathode induced signals at -750, ..., -1500 V and flux $\Phi_6 = 129.3$k, ..., $\Phi_{11} = 219.3$k photons/pixel/s.

APPENDIX B

Cs-137 Spectra Measured at $\Phi_1 = 39 \times 10^3$, ..., $\Phi_{11} = 219 \times 10^3$ photons/pixel/s as a Function of Irradiation Time t_1, ..., t_{10} at -750, -1000, -1250 and -1500 Cathode Bias Voltages.

Figs.B.1...B.14 show measured Cs-137 spectra at high-flux experiments at -750, -1000, -1250 and-1500 cathode bias voltages. Although in these plots data was measured by changing the source-to-detector distance from 50 cm to 30 cm in all experiments, only the critical data is presented here, before and after polarization.

In order to read the graphs, the numbers varying from $1 \ldots 10$ in horizontal and vertical directions represent indexes, where the total irradiation time in each graph is 25.6 s, and position $(1, 1)$ represent the initial 25.6 ms and $(10, 10)$ the last 25.6 ms, increasing in time row-by-row in 25.6 ms steps.

-750 V, $\Phi_7 = 147.3 \times 10^3$ photons/pixel/s:

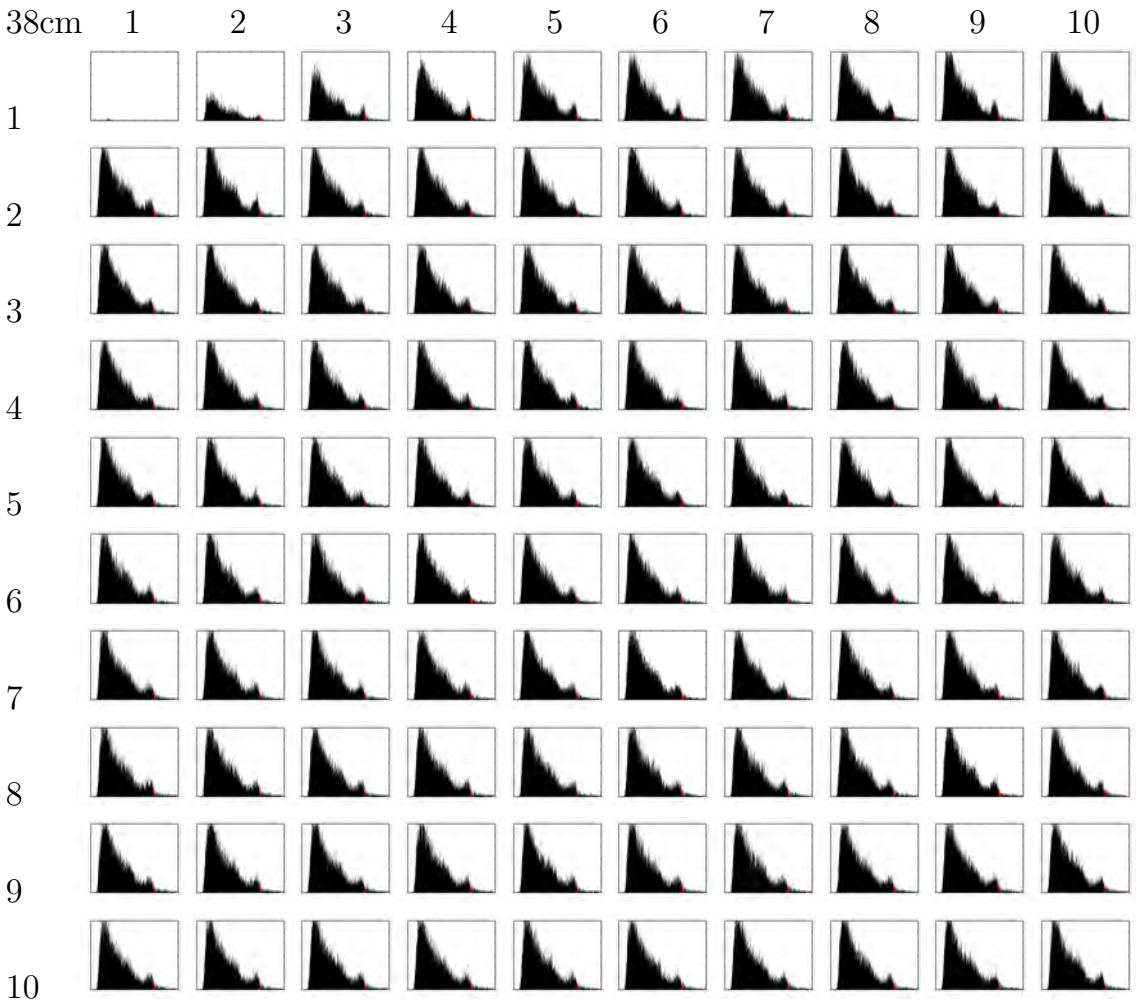

Figure B.1: Measured spectra in every 25.6 ms interval, starting at position $(1, 1)$, from $0.0 \ldots 25.6$ s, at -750 V and 38 cm source-detector distance, $\Phi_7 = 147.3 \times 10^3$ photons/pixel/s

-750 V, $\Phi_8 = 165.3 \times 10^3$ photons/pixel/s:

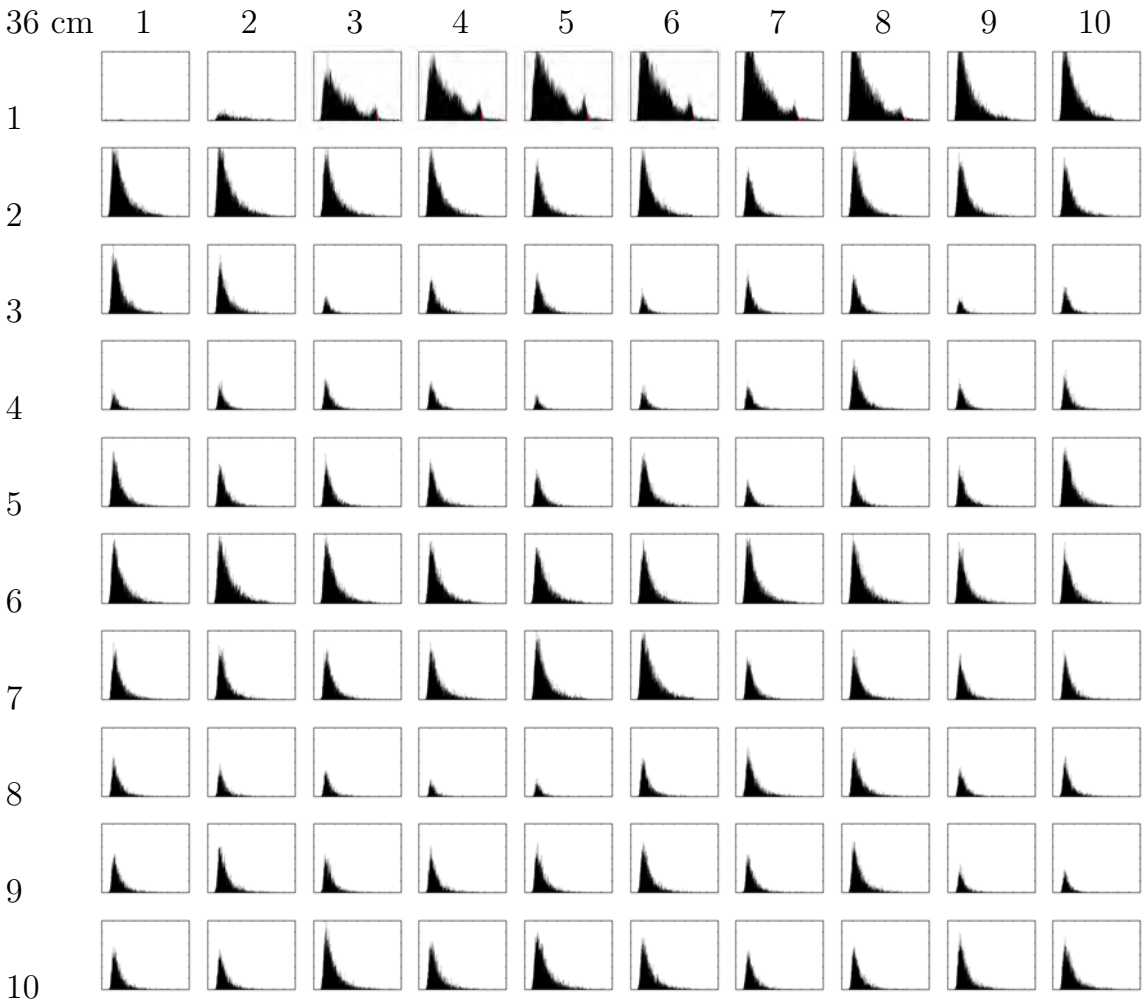

Figure B.2: Measured spectra in every 25.6 ms interval, starting at position $(1, 1)$, from $0.0 \ldots 25.6$ s, at -750 V and 36 cm source-detector distance, $\Phi_8 = 165.3 \times 10^3$ photons/pixel/s

-750 V, $\Phi_9 = 183.3 \times 10^3$ photons/pixel/s:

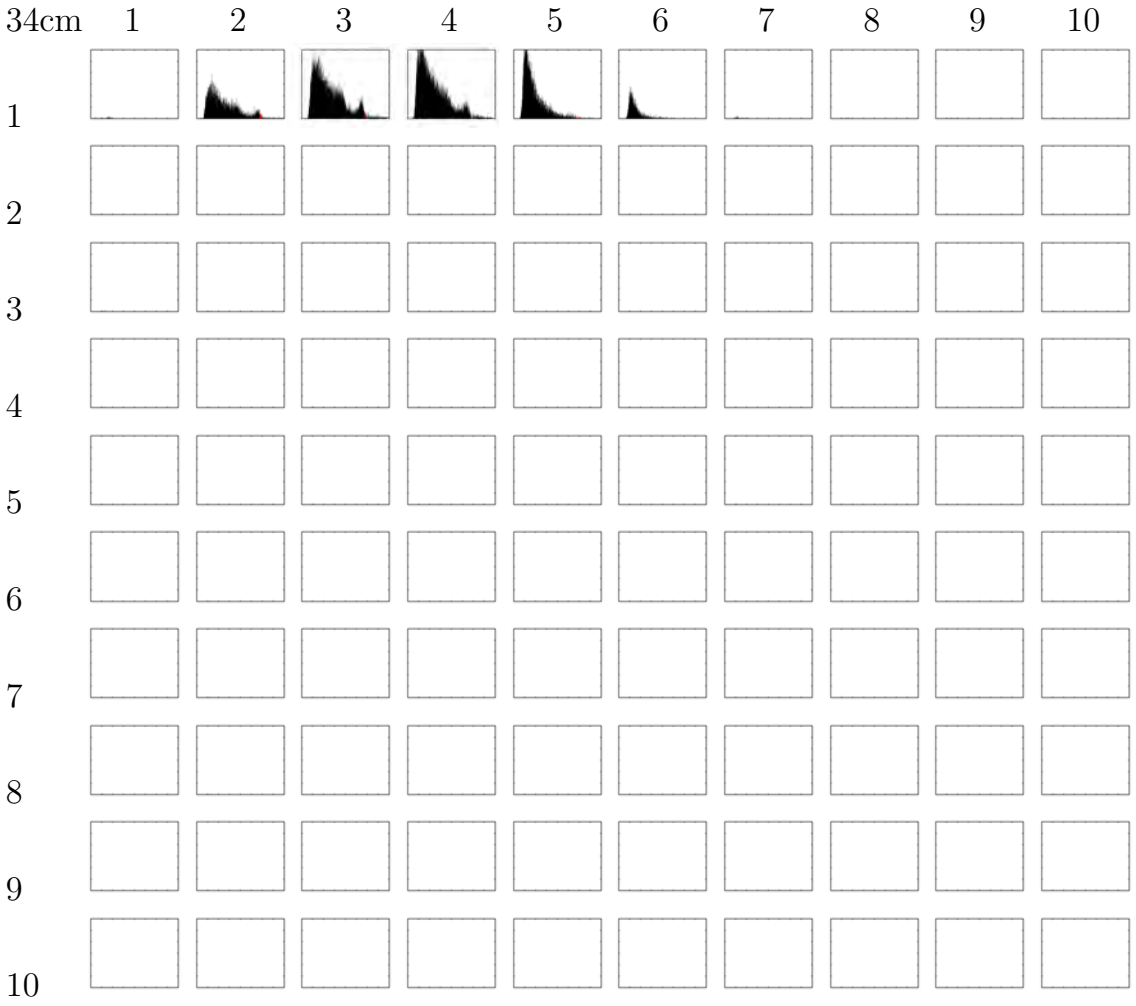

Figure B.3: Measured spectra in every 25.6 ms interval, starting at position $(1, 1)$, from $0.0 \ldots 25.6$ s, at -750 V and 34 cm source-detector distance, $\Phi_9 = 183.3 \times 10^3$ photons/pixel/s.

-1000 V, $\Phi_8 = 165.3 \times 10^3$ photons/pixel/s:

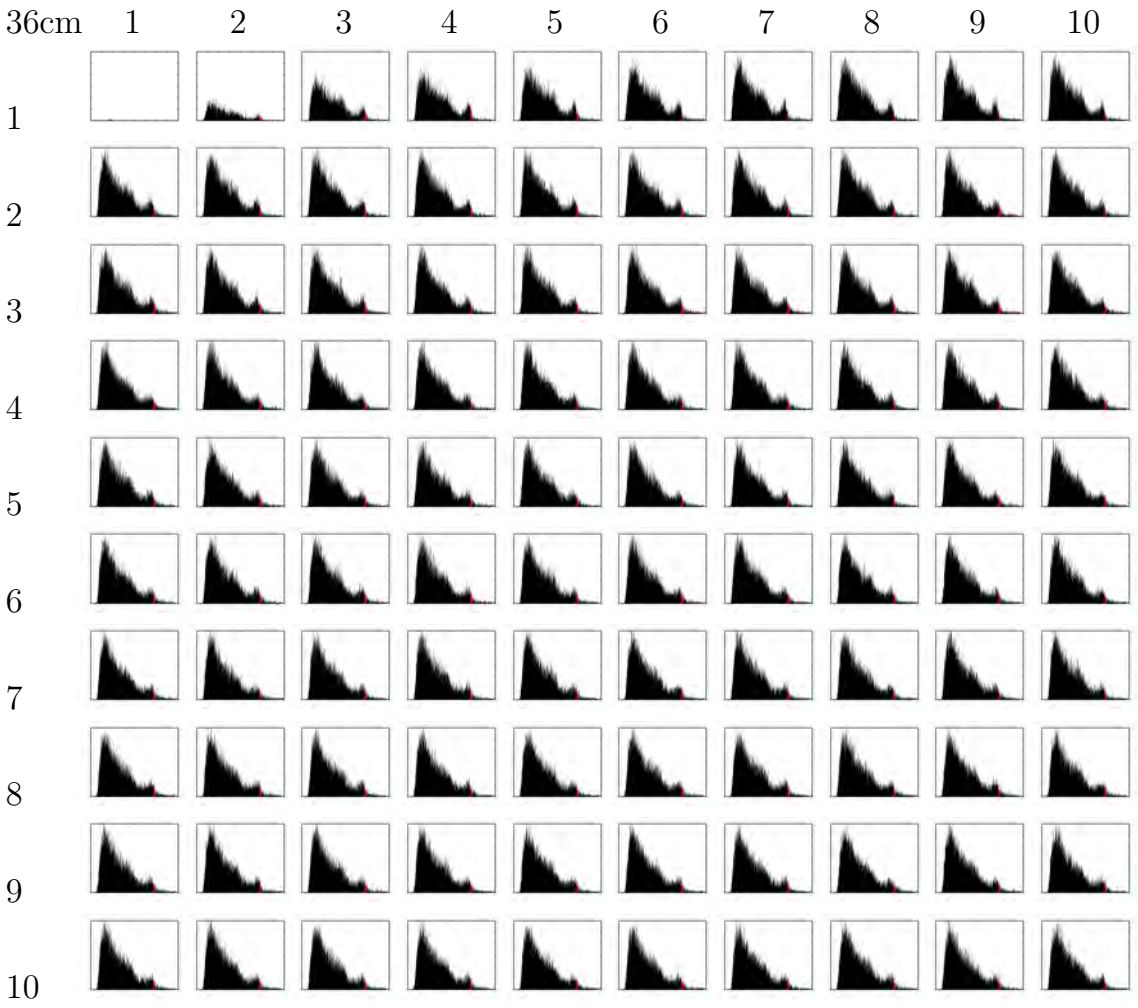

Figure B.4: Measured spectra in every 25.6 ms interval, starting at position $(1, 1)$, from $0.0 \ldots 25.6$ s, at -1000 V and 36 cm source-detector distance, $\Phi_8 = 165.3 \times 10^3$ photons/pixel/s

-1000 V, $\Phi_9 = 183.3 \times 10^3$ photons/pixel/s:

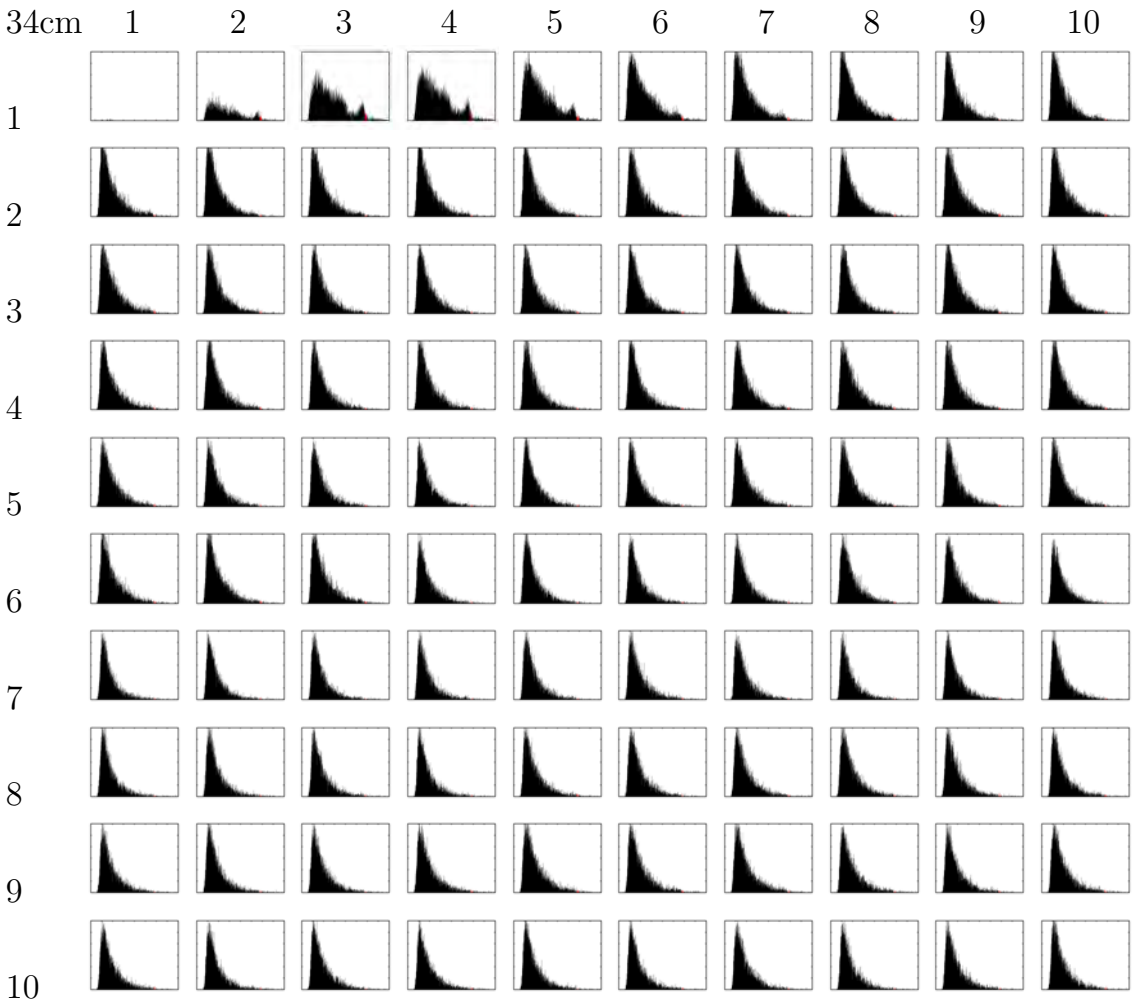

Figure B.5: Measured spectra in every 25.6 ms interval, starting at position $(1, 1)$, from $0.0 \ldots 25.6$ s, at -1000 V and 34 cm source-detector distance, $\Phi_9 = 183.3 \times 10^3$ photons/pixel/s.

-1000 V, $\Phi_{10} = 201.3 \times 10^3$ photons/pixel/s:

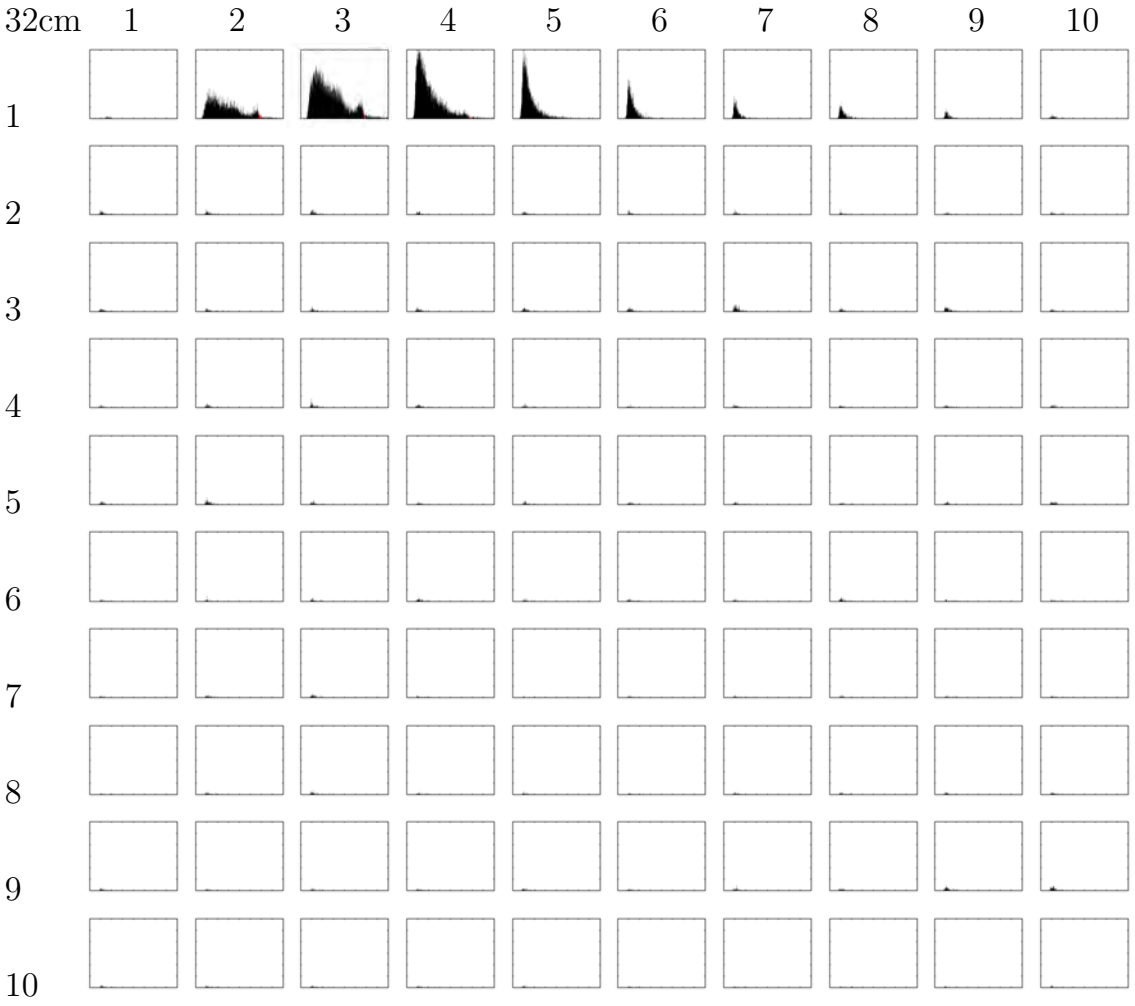

Figure B.6: Measured spectra in every 25.6 ms interval, starting at position $(1, 1)$, from $0.0 \ldots 25.6$ s, at -1000 V and 32 cm source-detector distance, $\Phi_{10} = 201.3 \times 10^3$ photons/pixel/s.

-1250 V, $\Phi_8 = 165.3 \times 10^3$ photons/pixel/s:

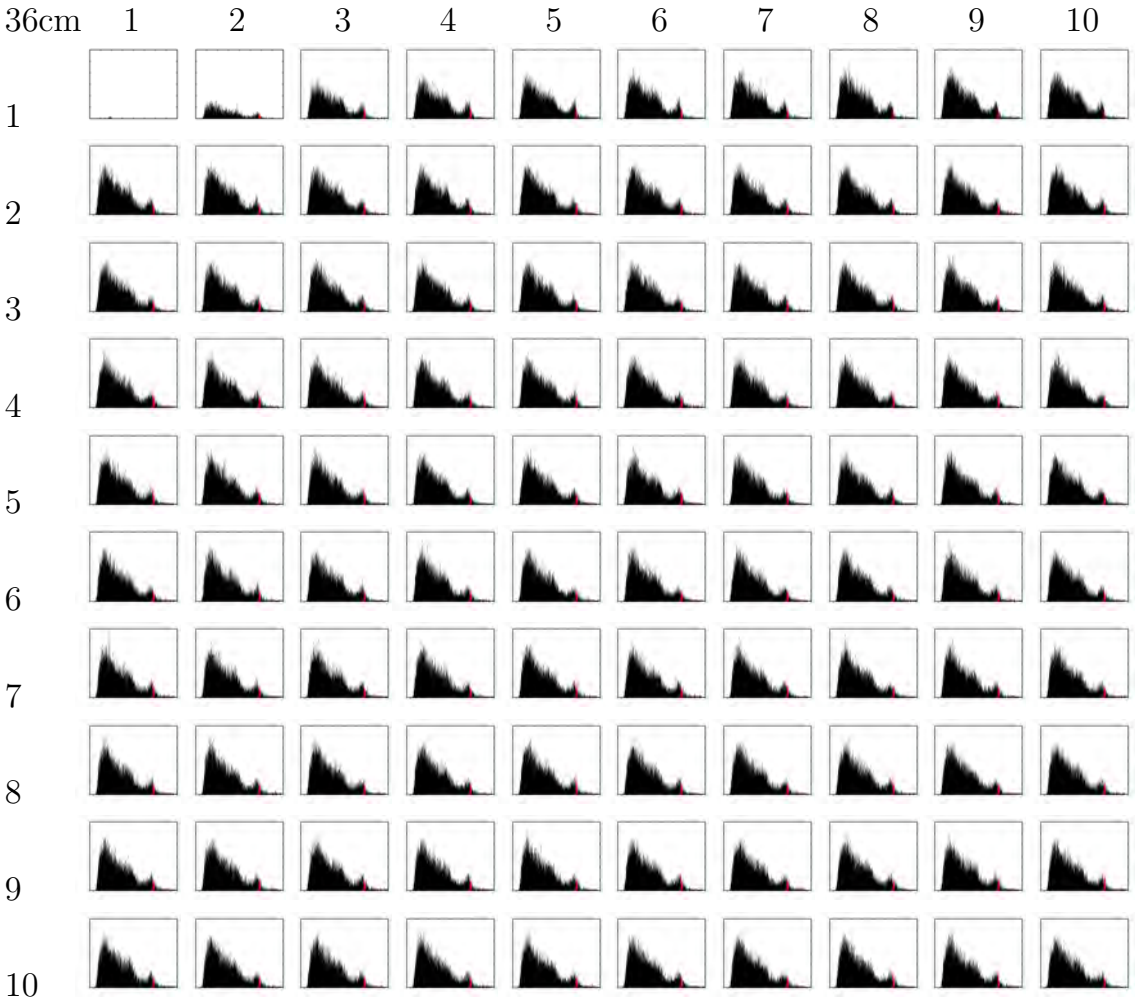

Figure B.7: Measured spectra in every 25.6 ms interval, starting at position $(1, 1)$, from $0.0 \ldots 25.6$ s, at -1250 V and 36 cm source-detector distance, $\Phi_8 = 165.3 \times 10^3$ photons/pixel/s

-1250 V, $\Phi_9 = 183.3 \times 10^3$ photons/pixel/s:

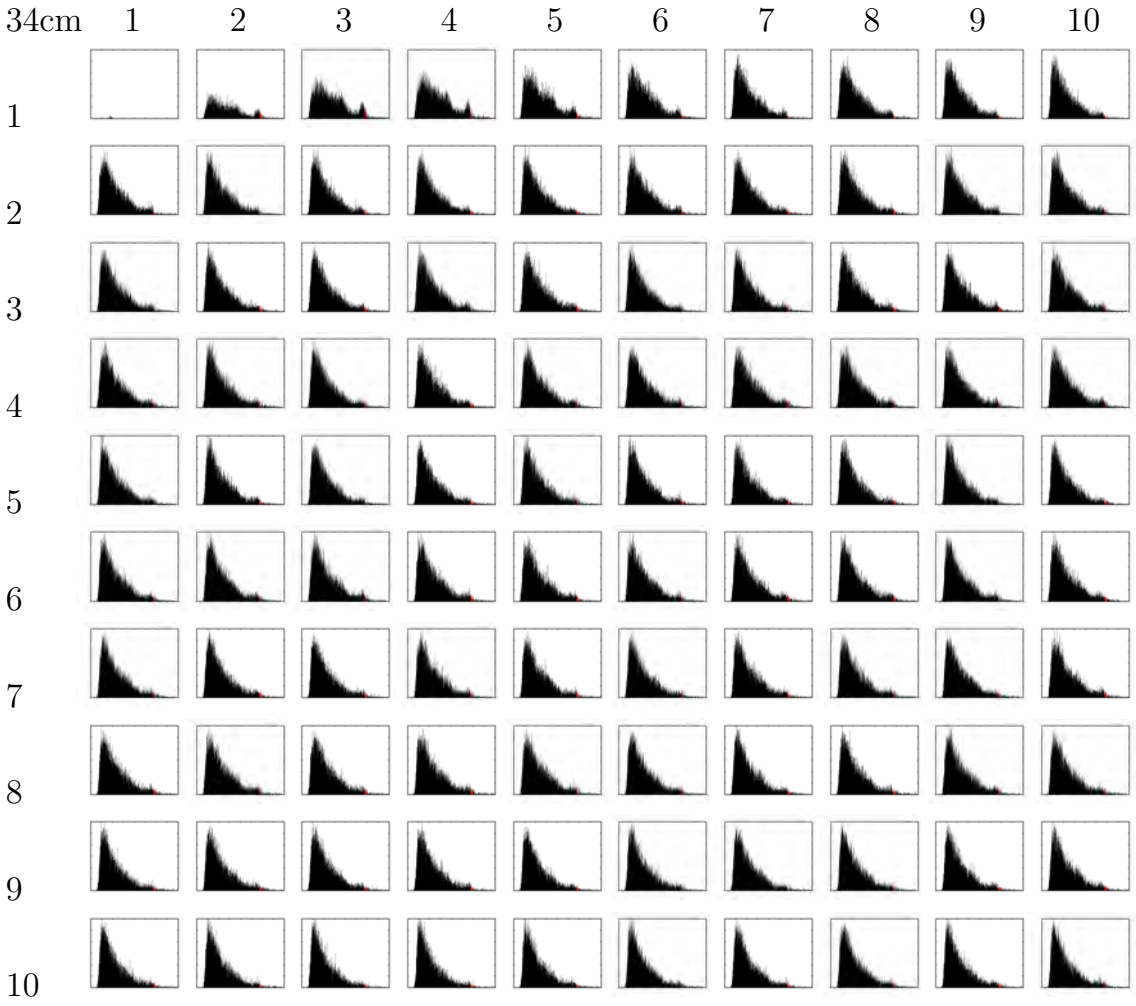

Figure B.8: Measured spectra in every 25.6 ms interval, starting at position $(1, 1)$, from $0.0 \ldots 25.6$ s, at -1250 V and 34 cm source-detector distance, $\Phi_9 = 183.3 \times 10^3$ photons/pixel/s.

-1250 V, $\Phi_{10} = 201.3 \times 10^3$ photons/pixel/s:

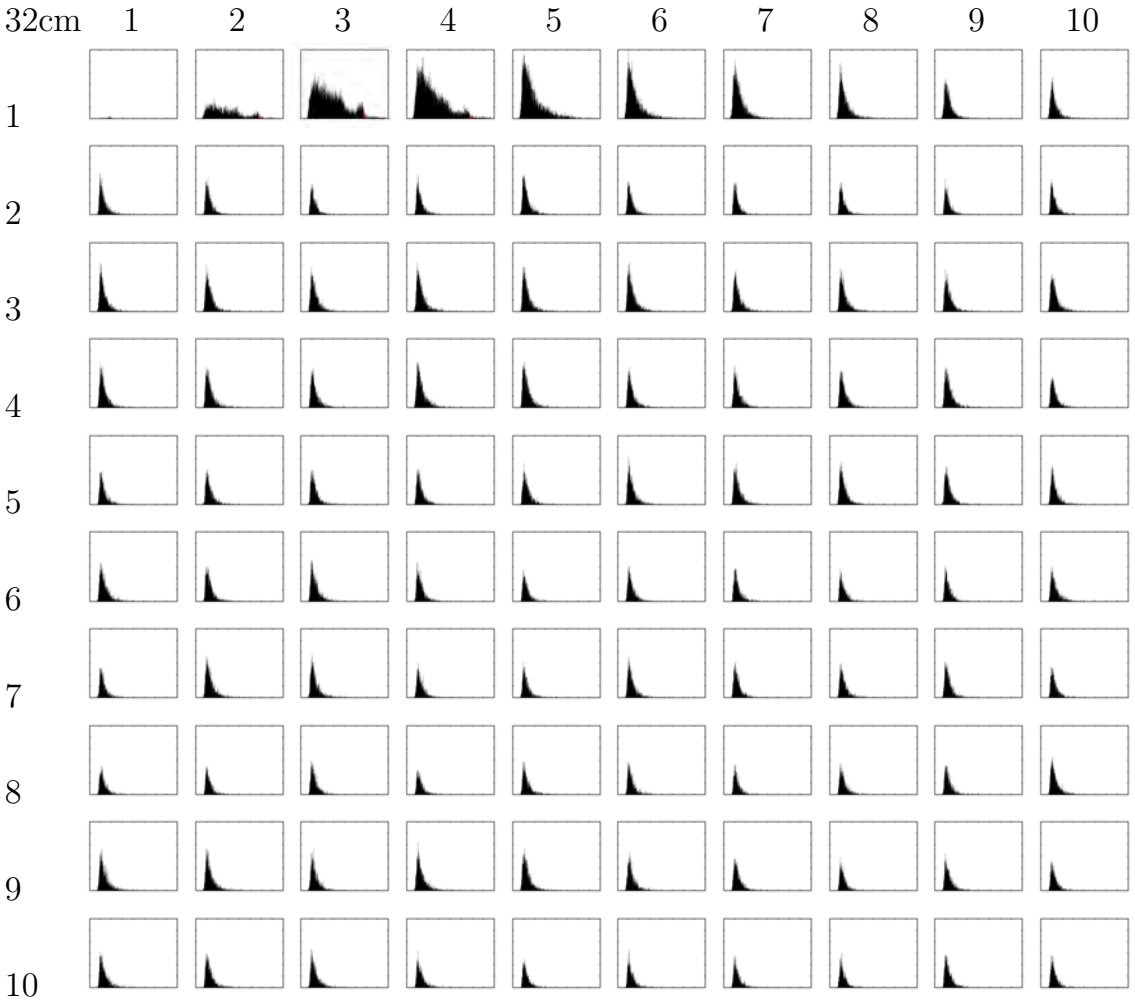

Figure B.9: Measured spectra in every 25.6 ms interval, starting at position $(1, 1)$, from $0.0 \ldots 25.6$ s, at -1250 V and 32 cm source-detector distance, $\Phi_{10} = 201.3 \times 10^3$ photons/pixel/s.

-1250 V, $\Phi_{10} = 219.3 \times 10^3$ photons/pixel/s:

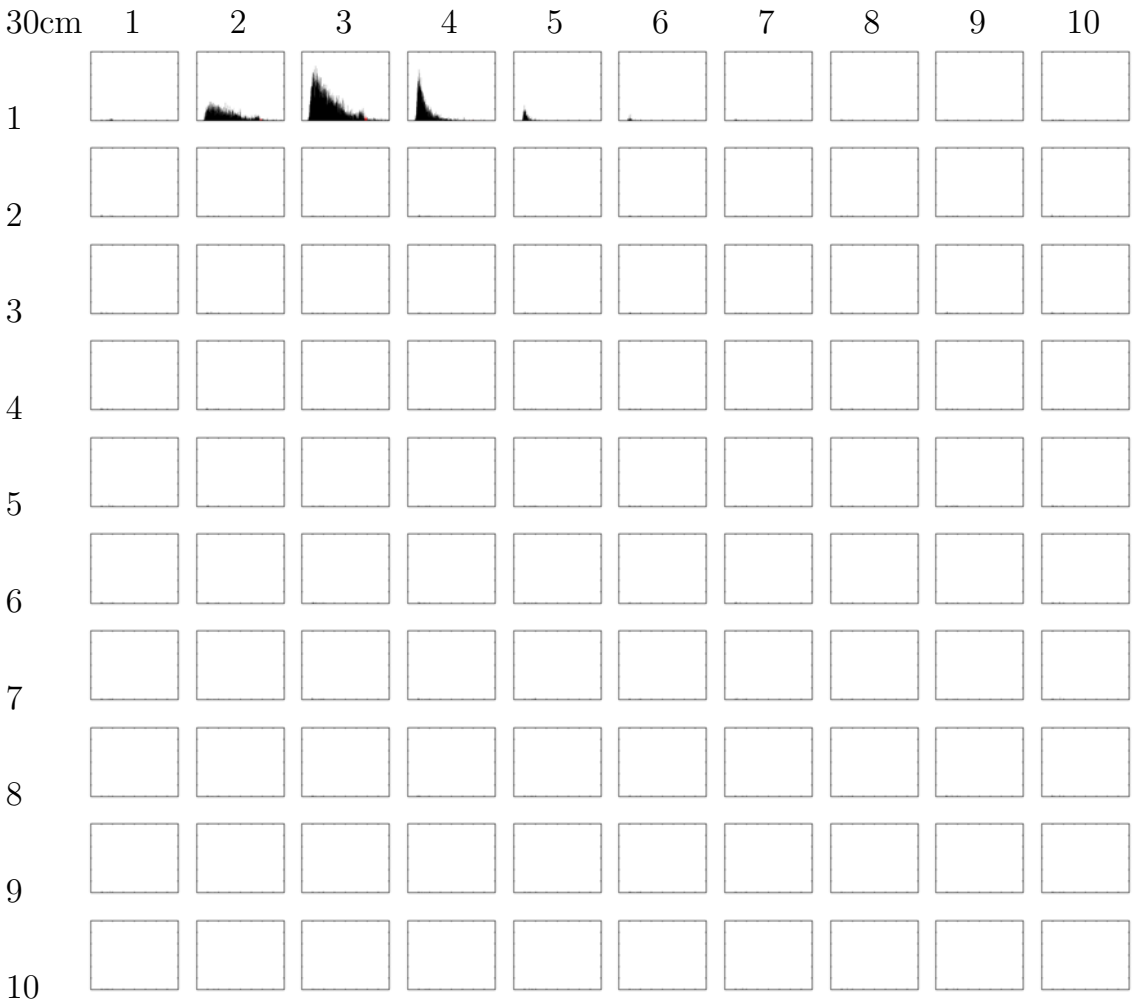

Figure B.10: Measured spectra in every 25.6 ms interval, starting at position $(1, 1)$, from $0.0 \ldots 25.6$ s, at -1250 V and 30 cm source-detector distance, $\Phi_{11} = 219.3 \times 10^3$ photons/pixel/s.

-1500 V, $\Phi_8 = 165.3 \times 10^3$ photons/pixel/s:

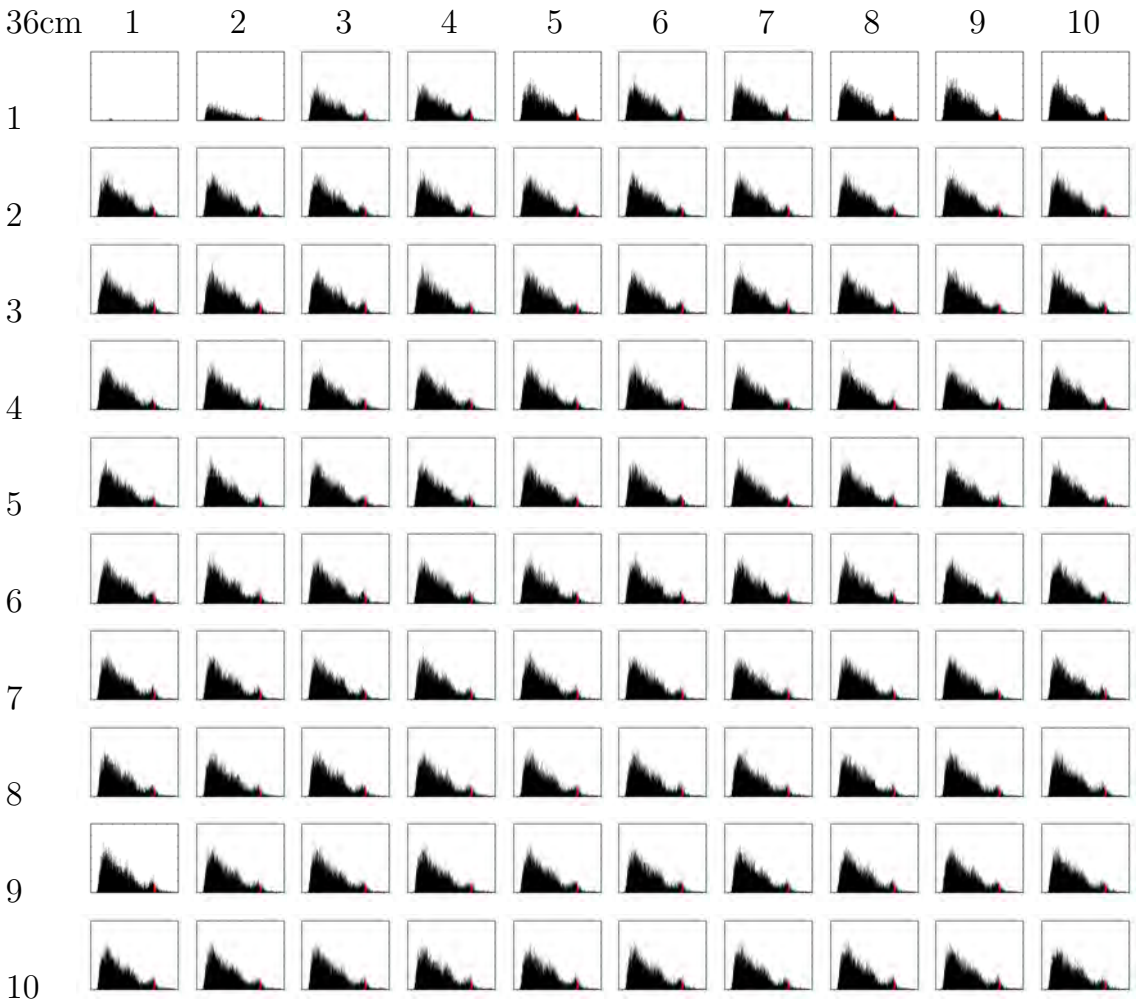

Figure B.11: Measured spectra in every 25.6 ms interval, starting at position $(1, 1)$, from $0.0 \ldots 25.6$ s, at -1500 V and 36 cm source-detector distance, $\Phi_8 = 165.3 \times 10^3$ photons/pixel/s.

-1500 V, $\Phi_9 = 183.3 \times 10^3$ photons/pixel/s:

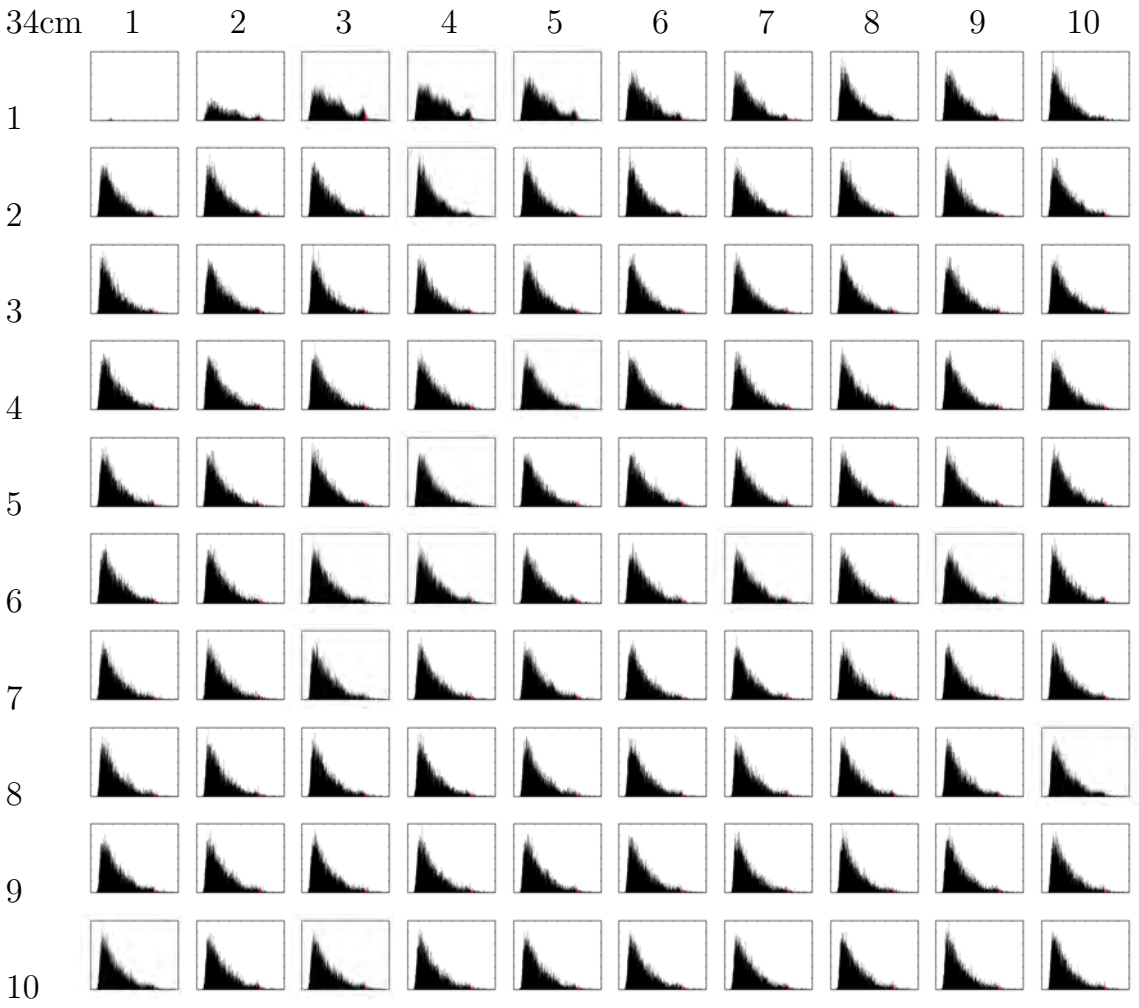

Figure B.12: Measured spectra in every 25.6 ms interval, starting at position $(1, 1)$, from $0.0 \ldots 25.6$ s, at -1500 V and 34 cm source-detector distance, $\Phi_9 = 183.3 \times 10^3$ photons/pixel/s.

-1500 V, $\Phi_{10} = 201.3 \times 10^3$ photons/pixel/s:

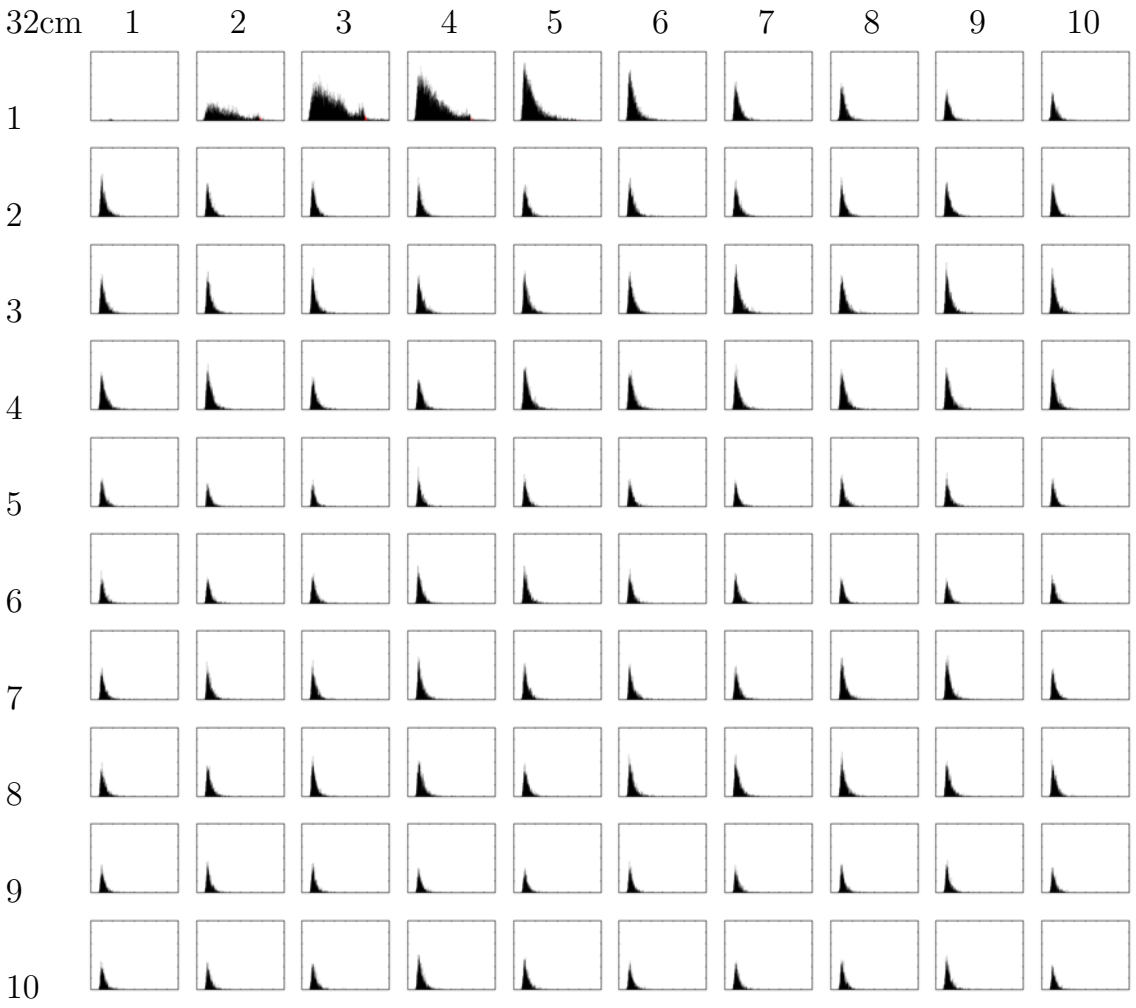

Figure B.13: Measured spectra in every 25.6 ms interval, starting at position $(1, 1)$, from $0.0 \ldots 25.6$ s, at -1500 V and 32 cm source-detector distance, $\Phi_{10} = 201.3 \times 10^3$ photons/pixel/s.

-1500 V, $\Phi_{10} = 219.3 \times 10^3$ photons/pixel/s:

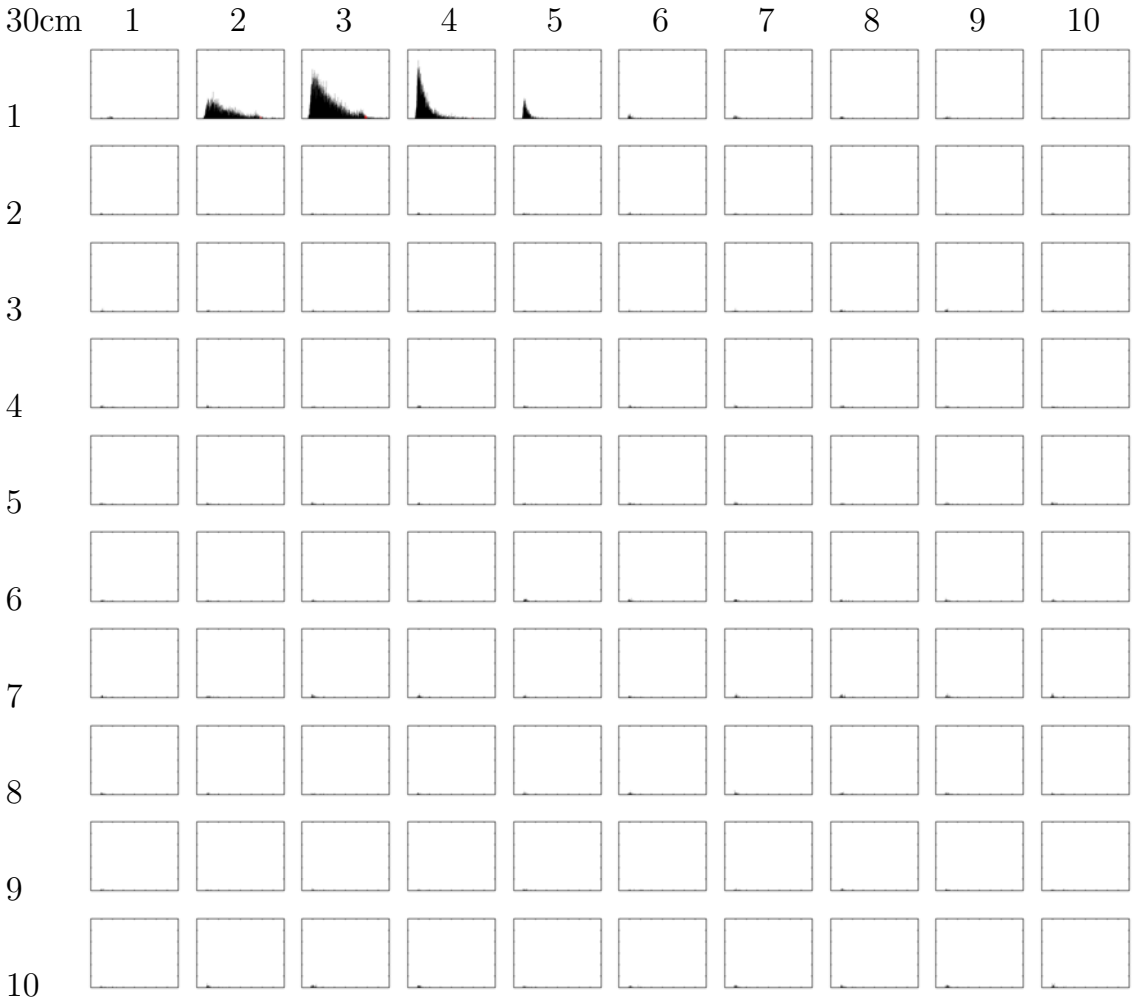

Figure B.14: Measured spectra in every 25.6 ms interval, starting at position $(1, 1)$, from $0.0 \ldots 25.6$ s, at -1500 V and 30 cm source-detector distance, $\Phi_{11} = 219.3 \times 10^3$ photons/pixel/s.

APPENDIX C

Comparison Between α-Induced Waveforms at the beginning of the irradiation at $\Phi_1 = 39 \times 10^3$ with waveforms measured at higher fluxes, $\Phi_1 = 39 \times 10^3$, ..., $\Phi_{11} = 219 \times 10^3$ photons/pixel/s, as a Function of Irradiation Time t_1, t_2, ..., t_{10} and -750, -1000, -1250 and -1500 Cathode Bias Voltages.

Figs.C.1...C.4 show measured α Induced Waveforms at $\Phi = 39 \times 10^3$ and $\Phi = 39 \times 10^3$, 57×10^3, ..., 219×10^3 photons/pixel/s as a Function of Irradiation Time t_1, t_2, ..., t_{10} at -750, -1000, -1250 and -1500 Cathode Bias Voltages. In order to read these graphs, the values corresponding to the time intervals t_i are given in Table D.1, while the values of flux Φ_i are given in Table D.2.

t_1	t_2	t_3	t_4	t_5	t_6	t_7	t_8	t_9	t_{10}
0	2.56	5.12	7.68	10.24	12.8	15.36	17.92	20.48	23.04
...	...	...	...	...	...	...	...	...	...
2.56 s	5.12 s	7.68 s	10.24 s	12.8 s	15.36 s	17.92 s	20.48 s	23.04 s	25.6 s

Table C.1: Conversion between t_1, t_2, $\cdots$, t_10 and irradiation time intervals in s.

Φ_1	Φ_2	Φ_3	Φ_4	Φ_5	Φ_6	Φ_7	Φ_8	Φ_9	Φ_{10}	Φ_{11}
39.3	57.3	75.3	93.3	111.3	129.3	147.3	165.3	183.3	201.3	209.2

Table C.2: Conversion between Φ_1, Φ_2, $\cdots$, Φ_{11} and irradiation flux in $\times 10^3$ *photons/pixel/s*.

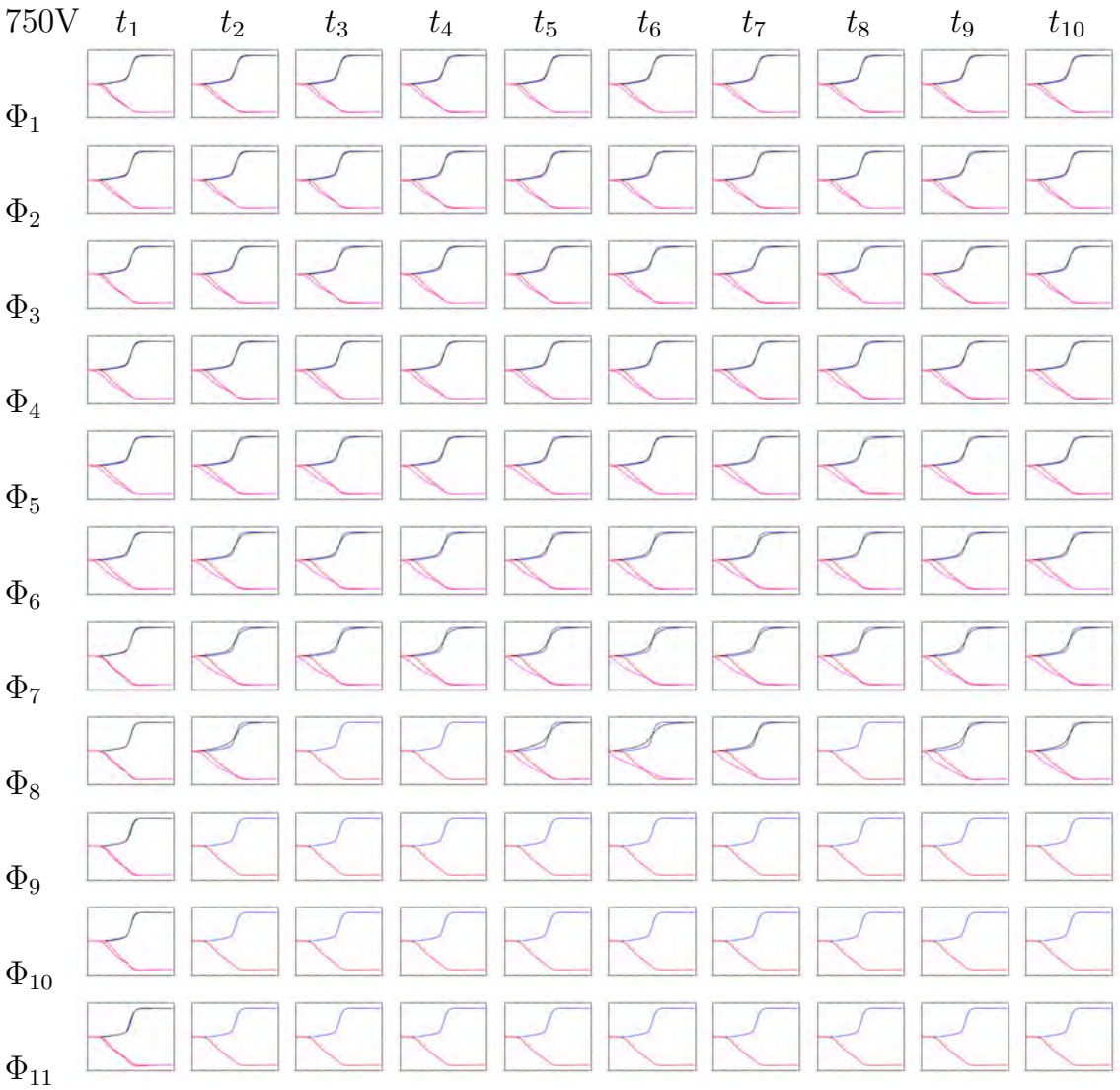

Figure C.1: Measured α-Induced Waveforms at $\Phi = 39 \times 10^3$ and $\Phi = 39 \times 10^3$, 57×10^3, ..., 219×10^3 photons/pixel/s as a Function of Irradiation Time t_1, t_2, ..., t_{10} at -750 V Cathode Bias Voltage.

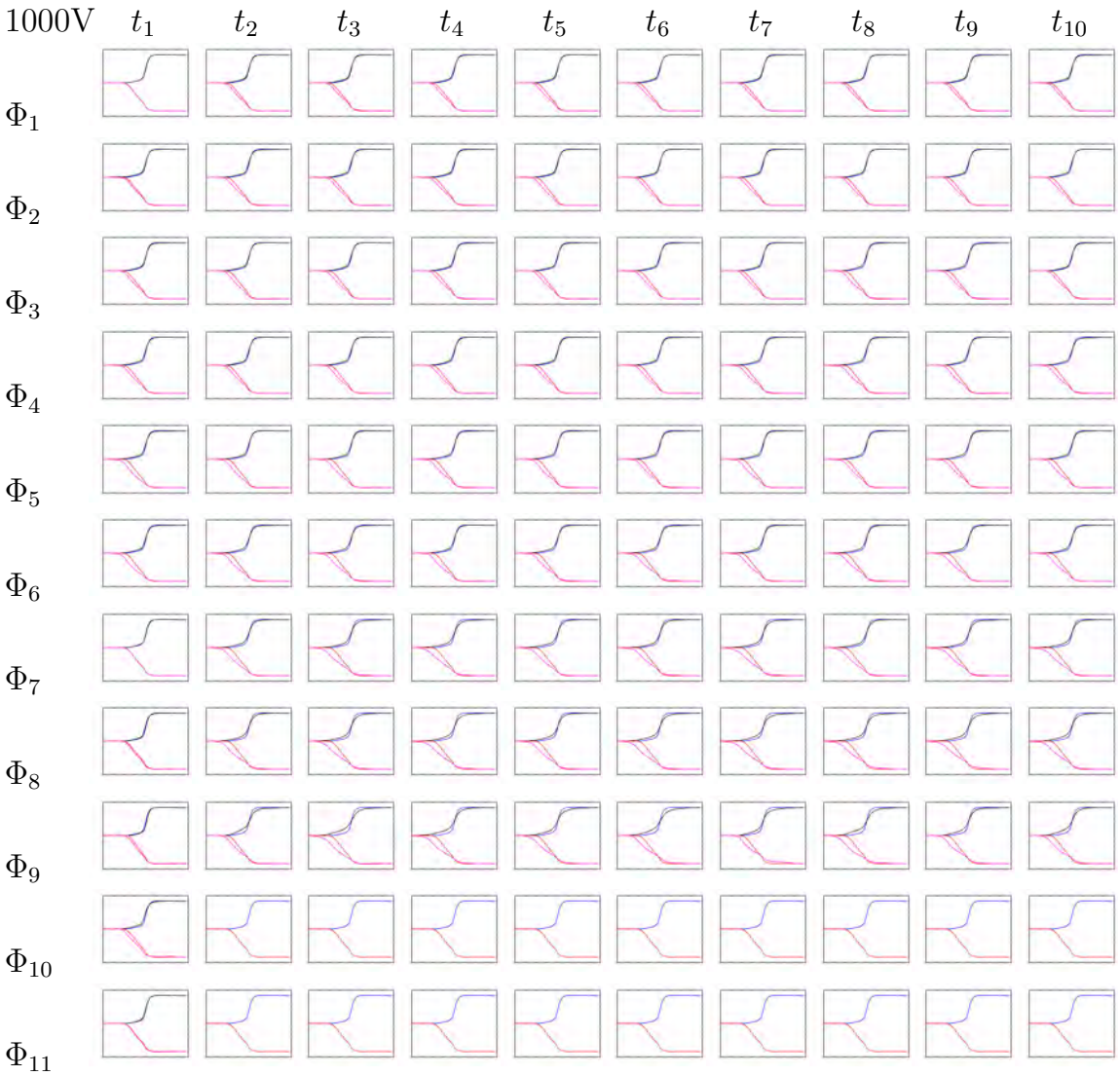

Figure C.2: Measured α-Induced Waveforms at $\Phi = 39 \times 10^3$ and $\Phi = 39 \times 10^3$, 57×10^3, ..., 219×10^3 photons/pixel/s as a Function of Irradiation Time t_1, t_2, ..., t_{10} at -1000 V Cathode Bias Voltage.

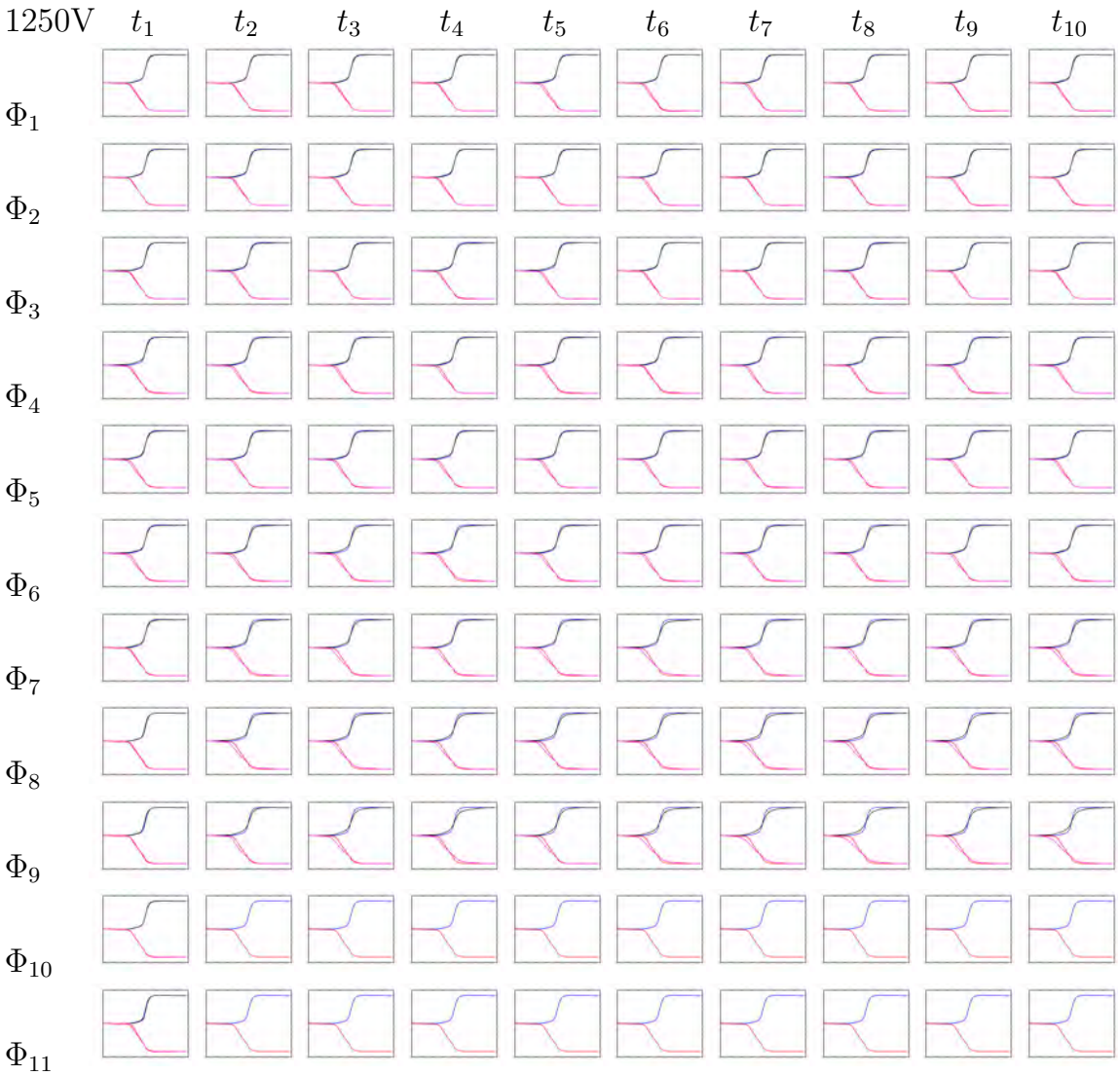

Figure C.3: Measured α-Induced Waveforms at $\Phi = 39 \times 10^3$ and $\Phi = 39 \times 10^3$, 57×10^3, ..., 219×10^3 photons/pixel/s as a Function of Irradiation Time t_1, t_2, ..., t_{10} at -1250 V Cathode Bias Voltage.

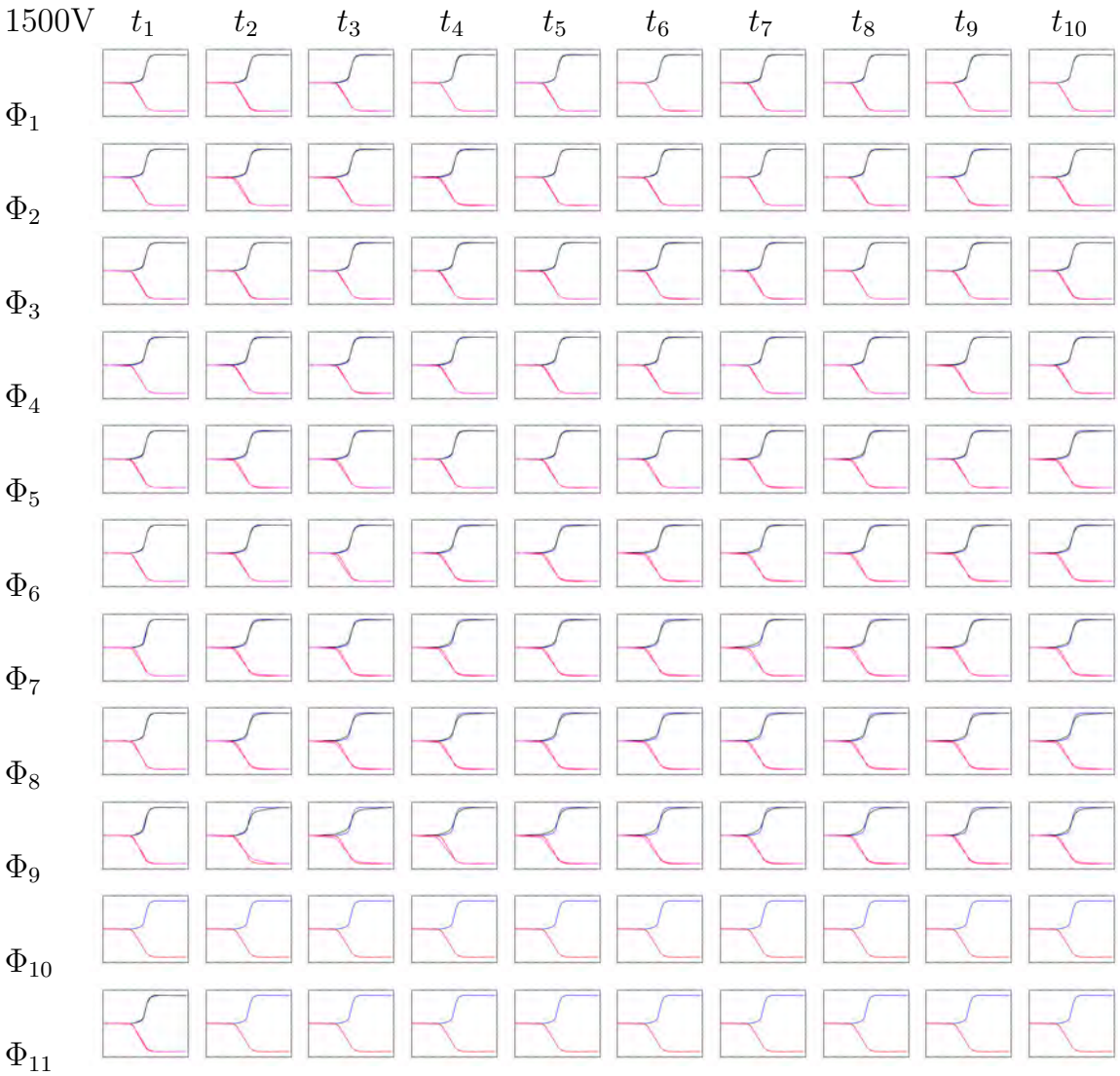

Figure C.4: Measured α-Induced Waveforms at $\Phi = 39 \times 10^3$ and $\Phi = 39 \times 10^3$, 57×10^3, ..., 219×10^3 photons/pixel/s as a Function of Irradiation Time t_1, t_2, ..., t_{10} at -1500 V Cathode Bias Voltage.

APPENDIX D

Difference Between α-Induced Waveforms at the beginning of the irradiation at $\Phi_1 = 39 \times 10^3$ with differences measured at higher fluxes, $\Phi_1 = 39 \times 10^3$, ..., $\Phi_{11} = 219 \times 10^3$ photons/pixel/s, as a Function of Irradiation Time t_1, t_2, ..., t_{10} ans -750, -1000, -1250 and -1500 Cathode Bias Voltages.

Figs.D.1...D.4 show difference between measured α Induced Waveforms at $\Phi = 39 \times 10^3$ and $\Phi = 39 \times 10^3$, 57×10^3, ..., 219×10^3 photons/pixel/s as a Function of Irradiation Time t_1, t_2, ..., t_{10} at -750, -1000, -1250 and -1500 Cathode Bias Voltages. In order to read these graphs, the values corresponding to the time intervals t_i are given in Table D.1, while the values of flux Φ_i are given in Table D.2.

t_1	t_2	t_3	t_4	t_5	t_6	t_7	t_8	t_9	t_{10}
0	2.56	5.12	7.68	10.24	12.8	15.36	17.92	20.48	23.04
...	...	...	...	...	...	...	...	...	...
2.56 s	5.12 s	7.68 s	10.24 s	12.8 s	15.36 s	17.92 s	20.48 s	23.04 s	25.6 s

Table D.1: Conversion between t_1, t_2, $\cdots$, t_10 and irradiation time intervals in s.

Φ_1	Φ_2	Φ_3	Φ_4	Φ_5	Φ_6	Φ_7	Φ_8	Φ_9	Φ_{10}	Φ_{11}
39.3	57.3	75.3	93.3	111.3	129.3	147.3	165.3	183.3	201.3	209.2

Table D.2: Conversion between Φ_1, Φ_2, $\cdots$, Φ_{11} and irradiation flux in $\times 10^3$ *photons/pixel/s*.

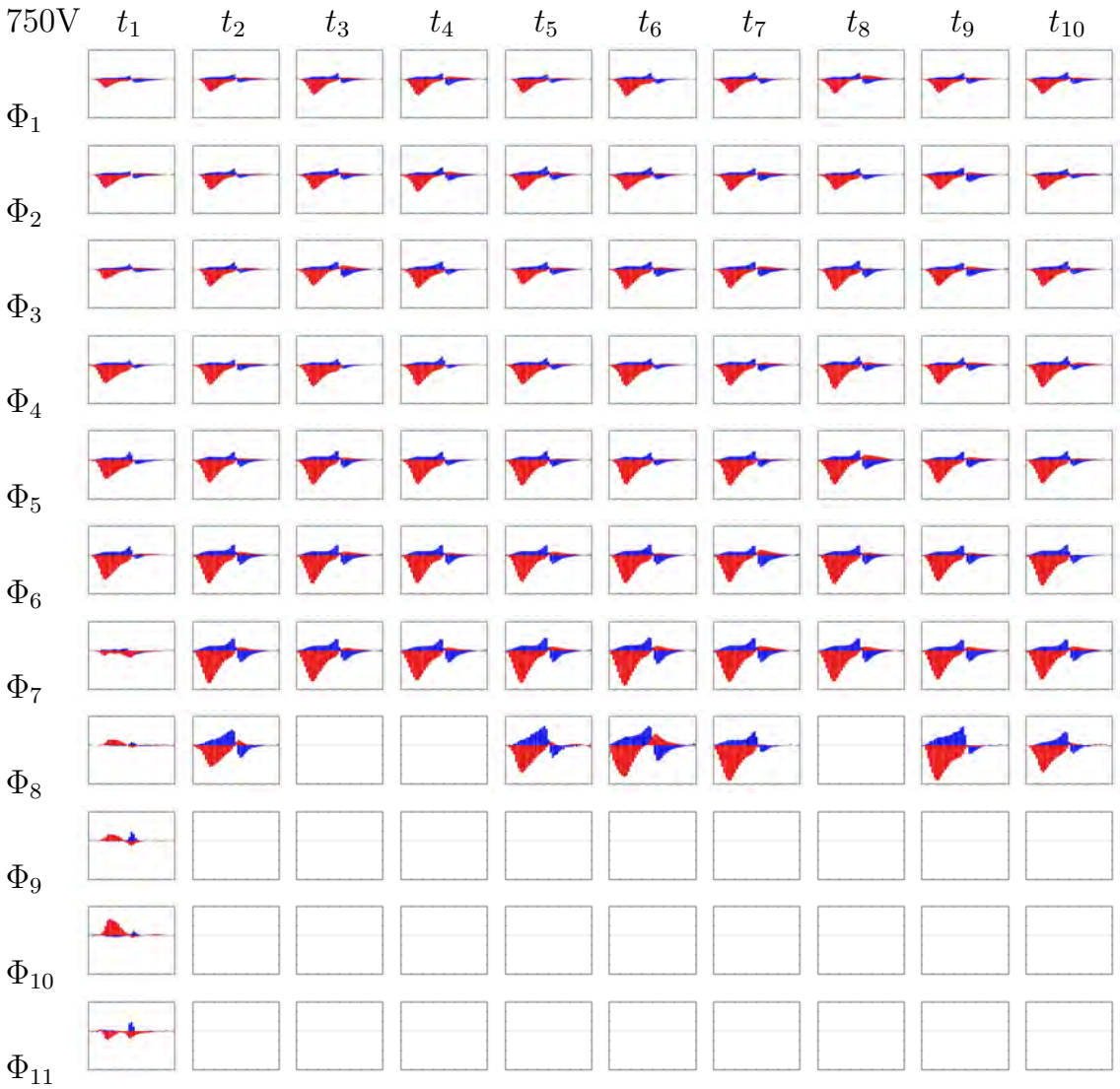

Figure D.1: Difference Between Measured α-Induced Waveforms at $\Phi = 39 \times 10^3$ and $\Phi = 39 \times 10^3$, 57×10^3, ..., 219×10^3 photons/pixel/s as a Function of Irradiation Time t_1, t_2, ..., t_{10} at -750 V Cathode Bias Voltage.

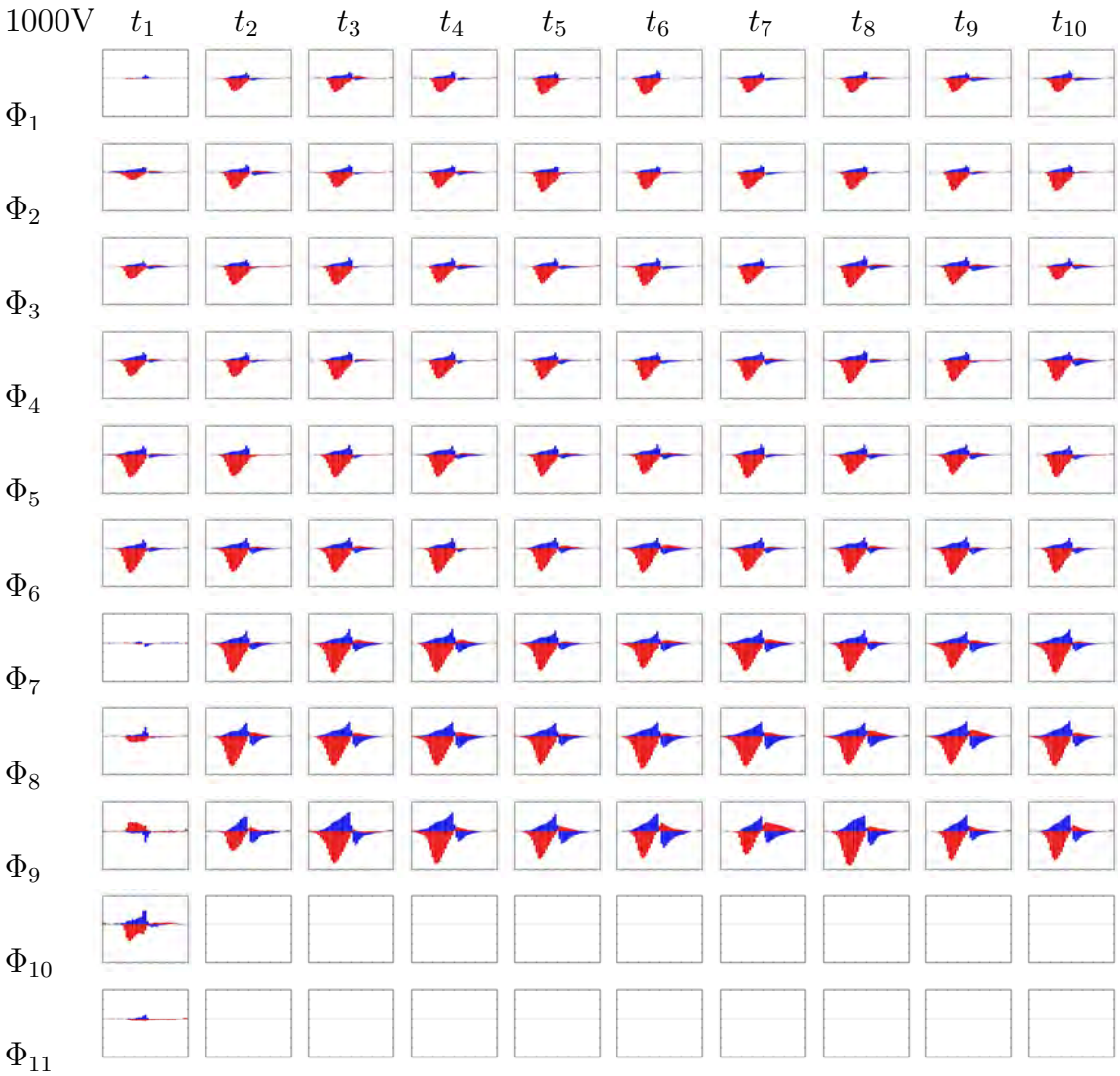

Figure D.2: Difference Between Measured α-Induced Waveforms at $\Phi = 39 \times 10^3$ and $\Phi = 39 \times 10^3$, 57×10^3, ..., 219×10^3 photons/pixel/s as a Function of Irradiation Time t_1, t_2, ..., t_{10} at -1000 V Cathode Bias Voltage.

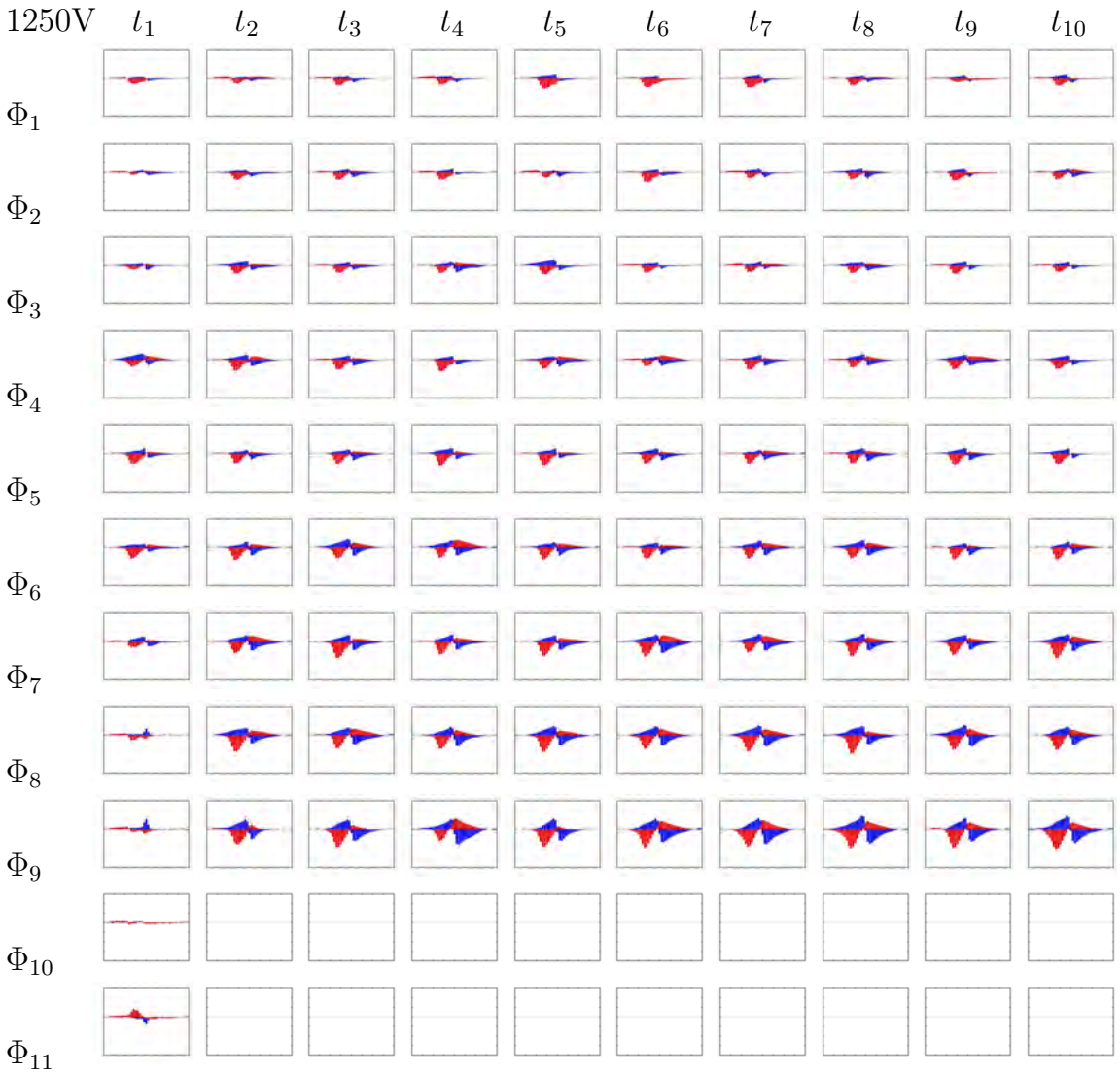

Figure D.3: Difference Between Measured α-Induced Waveforms at $\Phi = 39 \times 10^3$ and $\Phi = 39 \times 10^3$, 57×10^3, ..., 219×10^3 photons/pixel/s as a Function of Irradiation Time t_1, t_2, ..., t_{10} at -1250 V Cathode Bias Voltage.

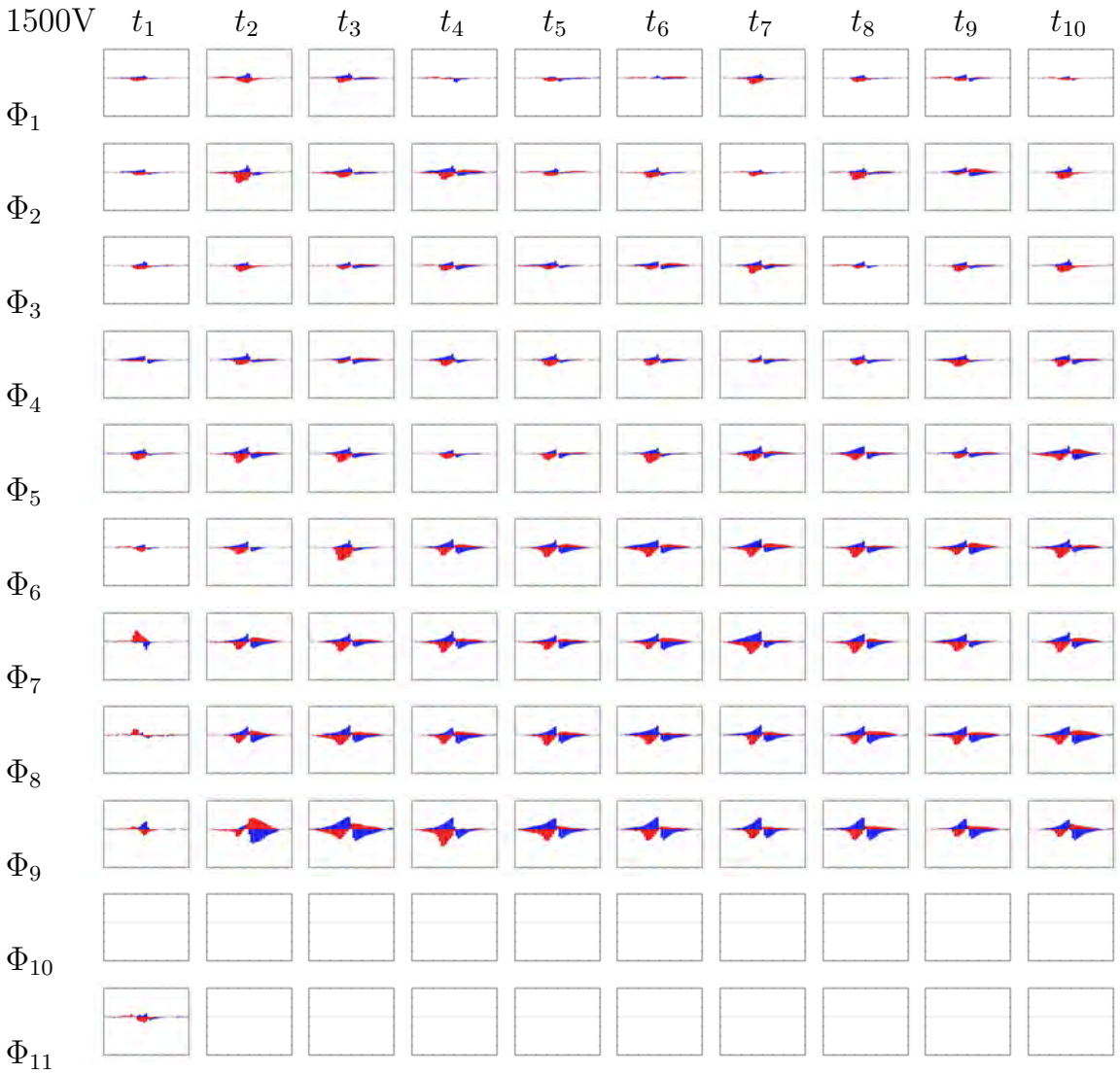

Figure D.4: Difference Between Measured α-Induced Waveforms at $\Phi = 39 \times 10^3$ and $\Phi = 39 \times 10^3$, 57×10^3, ..., 219×10^3 photons/pixel/s as a Function of Irradiation Time t_1, t_2, ..., t_{10} at -1500 V Cathode Bias Voltage.

APPENDIX E

Calculated Electric Field E (V/cm) as a Function of Depth of Interaction (mm) for Applied Cathode Voltages Varying from $500 \ldots 2000$ V.

Figs.E.1 and E.2 show calculated internal electric varying applied cathode bias voltages from $500 \ldots 2000$ V.

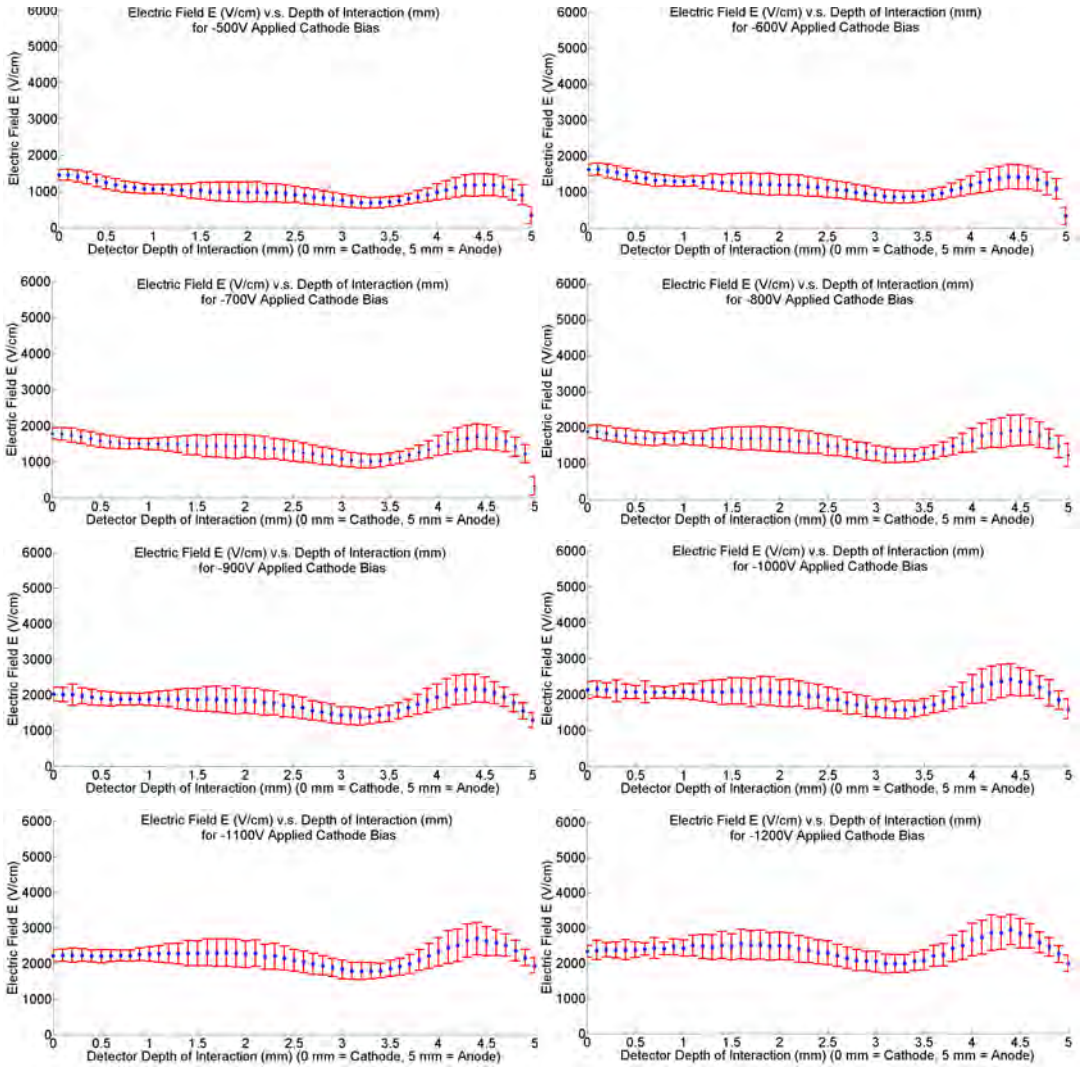

Figure E.1: Calculated Electric Field E (V/cm) as a Function of Depth of Interaction (mm) for Applied Cathode Voltages Varying from 500 to 1200 V.

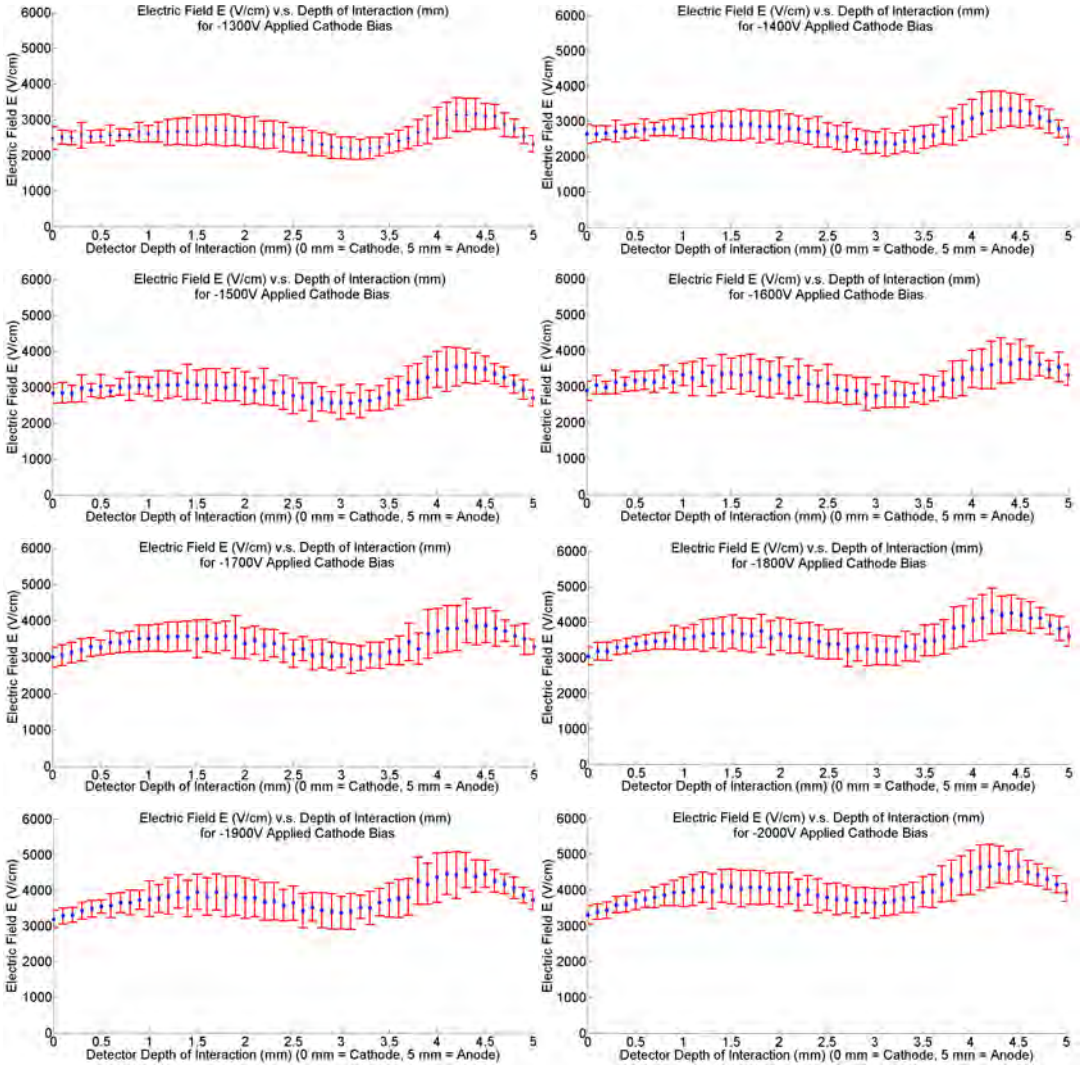

Figure E.2: Calculated Electric Field E (V/cm) as a Function of Depth of Interaction (mm) for Applied Cathode Voltages Varying from 1300 to 2000 V.

BIBLIOGRAPHY

BIBLIOGRAPHY

(2001), Alpha particle response characterization of CdZnTe., Lawrence Berkeley National Laboratory.

(2010), Al Qaeda still pursuing WMD, FBI Chief says, Global Security Newswire.

Adamiak, K. (2003), Analysis of charge transport in high resistivity conductors under different conduction models, *Journal of Electrostatics*, *57*, 325–335.

Agostinelli, S., J. Allison, K. Amako, and J. Apostolakis (2003), Geant4 - A simulation toolkit, *Nuclear Instruments and Methods in Physics Research A*, *506*, 250–303.

Alirol, O., F. Glasser, E. G. d'Aillon, and J. Tabary (2009), Simulation and mesurements of the internal electric field of a CZT (or CdTe) detector under high X-ray flux for medical imaging, *IEEE Nuclear Science Symposium Conference Record*, *2009*, 2460–2464.

Alvarez, R. E., and A. Macovski (1976), Energy-selective reconstructions in X-ray computerized tomography, *Physics in Medicine and Biology*, *21*, 733–744.

Aslund, M., E. Fredenberg, M. Telman, and M. Danielsson (2010), Detectors for the future of X-ray imaging, *Radiation Protection Dosimetry*, *139*, 327–333.

Babentsov, V., J. Franc, H. Elhadidy, A. Fauler, M. Fiederle, and R. B. James (2007), Dependence of the $Sn^{0/2+}$ charge state on the Fermi level in semi-insulating CdTe, *Journal of Materials Research*, *22*, 3249–3254.

Bale, D. S., and C. Szeles (2008), Nature of polarization in wide-bandgap semiconductor detectors under high-flux irradiation: Application to semi-insulating $Cd_{1-x}zn_xte$, *Physical Review B*, *77*, 035,205.

Bale, D. S., and C. Szeles (2009), Multiple-scale analysis of charge transport in semiconductor radiation detectors: Application to semi-insulating CdZnTe, *Journal of Electronic Materials*, *38*, 126–144.

Bale, D. S., and C. Szeles (2010), Electron transport and charge induction in CdZnTe detectors with space charge build up under X-ray irradiation, *Journal of Applied Physics*, *107*, 114,512.

Bale, D. S., R. J. Leveque, S. Mitran, and J. A. Rossmanith (2002), A wave propagation method for conservation laws and balance law with spatially varying flux functions, *SIAM J. Sci. Comput*, *24*, 2002.

Bale, D. S., S. A. Soldner, and C. Szeles (2008), A mechanism for dynamic lateral polarization in CdZnTe under high flux X-ray irradiation, *Applied Physics Letters*, *92*, 082,101.

Baliga, B. J. (1978), Recombination level selection criteria for lifetime reduction in integrated circuits, *Solid-State Electronics*, *21*, 1033–1038.

Barber, H. B., F. L. Augustine, L. R. Furenlid, C. M. Ingram, and G. P. Grim (2005), Prototype AEGIS: A pixel-array readout circuit for gamma-ray imaging, *Proceedings of SPIE*, *5923*, 59,230H–59,230H–10.

Barber, W. C., K. Iwata, B. H. Hasegawa, P. R. Bennett, L. J. Cirignano, and K. S. Shah (2003), A single CdZnTe detector for simultaneous CT/SPECT imaging, *Nuclear Instruments and Methods in Physics Research Section A*, *505*, 595–598.

Barrett, H. H., J. D. Eskin, and H. B. Barber (1995), Charge transport in arrays of semiconductor gamma-ray detectors, *Physical Review Letters*, *75*, 156–159.

Basolo, S., et al. (2008), A 20 kpixels CdTe photon-counting imager using XPAD chip, *Nuclear Instruments and Methods in Physics Research A*, *589*, 268–274.

Benoit, M., and L. A. Hamel (2009), Simulation of charge collection process in semiconductor CdZnTe γ-ray detectors, *Nuclear Instruments and Methods in Physics Research Section A*, *606*, 508–516.

Blair, D. B. (2010), Annual threat assessment of the US Intelligence Community for the Senate Select Committee on Intelligence, *Tech. rep.*, Director of National Intelligence.

Blakney, R. M., and H. P. Grunwald (1967), Small-signal current transients in insulators with traps, *Physical Review*, *159*, 658–671.

Blanquart, L., I. Valin, C. Trouilleau, S. Meillere, and L. Crest (2000), XPAD, a new read-out pixel chip for X-ray counting, *IEEE Nuclear Science Symposium Conference Record*, *2*, 92–97.

Bohnel, M., P. Bartl, T. Michel, and G. Anton (2007), Correlated counting and energy resolving properties of photon counting X-ray detectors like the Medipix detectors, *IEEE Nuclear Science Symposium Conference Record*, *2007*, 2732–2735.

Brown, F. C. (1955), Temperature dependence of electron mobility in AgCl, *Physical Review*, *97*, 355–362.

Butler, A. P. H., N. G. Anderson, R. Tipples, N. Cook, R. Watts, J. Meyer, A. J. Bell, T. R. Melzer, and P. H. Butler (2008), Bio-medical X-ray imaging with spectroscopic pixel detectors, *Nuclear Instruments and Methods in Physics Research A*, *591*, 141–146.

Castoldi, A., and E. Gatti (1996), Fast tools for 3-D design problems in semiconductor detectors, *Nuclear Instruments and Methods in Physics Research A*, *377*, 381–386.

Castoldi, A., E. Gatti, and P. Rehak (1996), Three-dimensional analytical solution of the Laplace equation suitable for semiconductor detector design, *IEEE Transactions on Nuclear Science*, *43*, 256–265.

Davis, L. S., and A. Mitiche (1979), Edge detection in textures, *Tech. rep.*, The University of Texas at Austin.

Debuf, D., Y. Shrivastava, and A. Dunn (2002), General analytic solution to the Shockley-Read-Hall rate equation with a single-level defect, *Physical Review B*, *65*, 245,211.

deCasteele, E. V., D. V. Dyck, J. Sijbers, and E. Raman (2002), An energy-based beam hardening model in tomography, *Physics in Medicine and Biology*, *47*, 4181–4190.

Dieguez, E. (2011), Growth of Cd0.9Zn0.1Te bulk crystals, *Comprehensive semiconductor science and technology*, *3*, 170–201.

Dougan, A., et al. (2004), Screening of maritime containers to intercept weapons of mass destruction, *Tech. rep.*, Lawrence Livermore National Laboratory.

Du, Y., J. LeBlanc, G. E. Possin, B. D. Yanoff, and S. Bogdanovich (2003), Temporal response of CZT detectors under intense irradiation, *IEEE Transactions on Nuclear Science*, *50*, 1031–1035.

Durst, J., P. Bartl, B. Kreisler, T. Michel, and G. Anton (2008), Monte Carlo simulation of pixelated photon counting X-ray detectors like the Medipix2 and the Medipix3 using high-Z sensor materials, *IEEE Nuclear Science Symposium Conference Record*, *2008*, 4990–4994.

Endicott (2011), Semiconductor detector material properties.

Eskin, J. D., H. H. Barrett, and H. B. Barber (1999), Signals induced in semiconductor gamma-ray imaging detectors, *Journal of Applied Physics*, *85*, 647–659.

Ettenauer, S. (2008), Considerations of the application of Ramo's theorem for segmented HPGe detector pulse-shape calculations, *Nuclear Instruments and Methods in Physics Research A*, *588*, 380–383.

Faridani, A. (2003), Introduction to the mathematics of computed tomography, *Inside Out: Inverse Problems and Applications*, *47*, 1–46.

Feuerlein, S., et al. (2008), Multienergy photon-counting K-edge imaging: Potential for improved luminal depiction in vascular imaging, *Radiology*, *249*, 1010–1016.

Firsching, M., J. Giersch, D. Niederlohner, and G. Anton (2004), A method for stoichiometric material reconstruction with spectroscopic X-ray pixel detectors, *IEEE Nuclear Science Symposium Conference Record*, *2004*, 4116–4119.

Firsching, M., D. Niederlohner, T. Michel, and G. Anton (2006), Quantitative material reconstruction in CT with spectroscopic X-ray pixel detectors - a simulation study, *IEEE Nuclear Science Symposium Conference Record*, *2006*, 2257–2259.

Firsching, M., T. Michel, and G. Anton (2007), First measurements of material reconstruction in X-ray imaging with the Medipix2 detector, *IEEE Nuclear Science Symposium Conference Record*, *2007*, 2736–2740.

Franchi, R., F. Glasser, A. Gasse, and J.-C. Clemens (2006), Photon counting X-ray imaging with CdTe pixel detectors based on XPAD2 circuit, *Nuclear Instruments and Methods in Physics Research A*, *563*, 249–253.

Gach, H. M., C. Tanase, and F. Boada (2008), 2D & 3D Shepp-Logan phantom standars for MRI, in *19th International Conference on Systems Engineering*.

Gatti, E., A. Longoni, P. Rehak, and M. Sampietro (1987), Dynamics of electrons in drift detectors, *Nuclear Instruments and Methods in Physics Research A*, *253*, 393–399.

Gustafson, K. (1991), Semiconductor device simulation, *Computer Physics Communications*, *65*, 133–136.

Hall, R. N. (1952), Electron-hole recombination in germanium, *Physical Review*, *87*, 387–387.

Hall, R. N. N. (1960), Recombination processes in semiconductors, *The Institution of Electrical Engineers*, *106*, 923–931.

Halpern, E. J., D. J. Halpern, J. H. Yanof, S. Amin-Spector, D. Fischman, G. Aviram, and J. Sosna (2009), Is coronary stent assessment improved with spectral analysis of dual energy CT?, *Academic Radiology*, *16*, 1241–50.

Hamel, L.-A., and M. Julien (2008), Generalized demonstration of Ramo's theorem with space charge and polarization effects, *Nuclear Instruments and Methods in Physics Research A*, *597*, 207–211.

He, Z. (1995), Potential distributions within semiconductor detectors using coplanar electrodes, *Nuclear Instruments and Methods in Physics Research A*, *365*, 572–575.

He, Z. (2001), Review of the Shockley-Ramo theorem and its application in semiconductor gamma-ray detectors, *Nuclear Instruments and Methods in Physics Research A*, *463*, 250–267.

Heanue, J. A., J. K. Brown, and B. H. Hasegawa (1996), The use of CdTe or CdZnTe for pulse-counting and current-mode medical imaging applications, *Nuclear Instruments and Methods in Physics Research Section A*, *380*, 392–396.

Hecht, K. (1932), Zum mechanismus des lichtelektrischen Primarstromes in. Isolierenden Kristallen, *Z. Physik*, *77*, 235–245.

Hermon, H., M. Schieber, R. B. James, E. Lee, E. Cross, M. Goorsky, T. Lam, T. E. Schlesinger, and M. Greaves (1999), Correlation between nuclear response and defects in CZT, *Proc. SPIE*, *3768*, 138–146.

Hermon, H., M. Schieber, M. Factor, T. E. Schlesinger, R. B. James, H. Yoon, and M. Goorsky (2001), Detector performance crystallinity and impurity study of cadmium zinc telluride crystals grown from the melt, *Proc. SPIE*, *4507*, 186–202.

Hou, B., J. Easter, A. Mordovanakis, K. Krushelnick, and J. A. Nees (2008), Vacuum-free x-ray source based on ultrashort laser irradiation of solids, *Optics Express*, *16*, 17,695–17,705.

Ifraimov, M., A. Ludwig, and Y. Nemirovsky (2002), Statistical modeling of the spectral performance of a two-dimensional array of gamma-ray spectrometers, *Journal of Applied Physics*, *91*, 3384–3397.

Iwata, K., B. H. Hasegawa, J. A. Heanue, P. R. Bennett, K. S. Shah, C. D. Boles, and B. E. Boser (1999), CdZnTe detector for combined X-ray CT and SPECT, *Nuclear Instruments and Methods in Physics Research A*, *422*, 740–744.

Jung, M., J. Morel, P. Fougeres, M. Hage-Ali, and P. Siffert (1999), A new method for evaluation of transport properties in CdTe and CZT detectors, *Nuclear Instruments and Methods in Physics Research A*, *428*, 45–57.

Juska, G., A. Matulionis, and J. Viscakas (1969), Measurement of thermal release and transit time in case of multiple trapping, *Physica Status Solidi*, *33*, 533–539.

Kalender, W. A., S. Buchenau, P. Deak, M. Kellermeier, O. Langner, M. van Straten, S. Vollmar, and S. Wilharm (2008), Technical approaches to the optimisation of CT, *Physica Medica*, *24*, 71–79.

Kang, M.-J., C. M. Park, C.-H. Lee, J. M. Goo, and H. J. Lee (2010), Dual-energy CT: Clinical applications in various pulmonary diseases, *RadioGraphics*, *30*, 685–698.

Kavadias, S., K. Misiakos, and D. Loukas (1994), Calculation of pixel detector capacitances through three dimensional numerical solution of the Laplace equation, *IEEE Transactions on Nuclear Science*, *41*, 397–401.

Kim, H., et al. (2006), SemiSPECT: a small-animal SPECT imager based on eight CZT detector arrays, *Med. Phys.*, *33*, 465–474.

Knoll, G. F. (2010), *Radiation detection and measurement*, third edition ed., John Wiley & Sons, Inc.

Kolobov, V. I. (2003), Fokker-Planck modeling of electron kinetics in plasmas and semiconductors, *Computational Materials Science*, *28*, 302–320.

Kozorezov, A. G., J. K. Wigmore, A. Owens, R. den Hartog, and A. Peacock (2005), Analytic model for the spatial and spectral resolution of pixellated semiconducting detectors of high-energy photons, *Journal of Applied Physics*, *97*, 074,502.

Kreisler, B., J. Durst, T. Michel, and G. Anton (2008), Generalised adjoint simulation of induced signals in semiconductor X-ray pixel detectors, *Journal of Instrumentation*, *3*, P11,002.

Kurokawa, M., S. Shimoura, H. Iwasaki, H. Baba, S. Michimasa, S. Ota, H. Murakami, and H. Sakai (2003), Pulse shape simulation and analysis of segmented Ge detectors for position extraction, *IEEE Transactions on Nuclear Science*, *50*, 1309 – 1316.

Lanza, R. C. (2009), Homeland Security and contraband detection, *Neutron Scattering Applications and Techniques*, *3*, 319–338.

Lee, E. Y., R. B. James, R. W. Olsen, and H. Hermon (1999), Compensation and trapping in CdZnTe radiation detectors studied by thermoelectric emission spectroscopy, thermally stimulated conductivity, and current-voltage measurements, *Journal of Electronic Materials*, *28*, 766–773.

Li, W., Z. He, G. F. Knoll, D. K. Wehe, and J. E. Berry (1999a), A data acquisition and processing system for 3D position sensitive CZT gamma-ray spectrometers, *IEEE Transactions on Nuclear Science*, *46*, 1989 – 1994.

Li, W., Z. He, G. F. Knoll, D. K. Wehe, and Y. F. Du (1999b), A modeling method to calibrate the interaction depth in 3-D position sensitive CdZnTe gamma-ray spectrometers, *IEEE Nuclear Science Symposium Conference Record*, *1*, 478 – 482.

Li, W., Z. He, G. F. Knoll, D. K. Wehe, and C. M. Stahle (1999c), Spatial variation of energy resolution in 3-D position sensitive CZT gamma-ray spectrometers, *IEEE Transactions on Nuclear Science*, *46*, 187 – 192.

Llopart, X., M. Campbell, R. Dinapoli, D. S. Segundo, and E. Pernigotti (2002), Medipix2: a 64-k pixel readout chip with 55-μm square elements working in single photon counting mode, *IEEE Transactions on Nuclear Science*, *49*, 2279–2283.

Lugakov, P. F., and V. V. Shusha (1984), A model of nonequilibrium charge-carrier recombination in semiconductors containing nonuniformities, *Physica Status Solidi (a)*, *86*, 309–312.

Masetti, S., M. Fiaschetti, A. Turco, L. Roma, P. L. Rossi, M. Mariselli, N. Lanconelli, and G. Baldazzi (2009a), Development of a multi-energy CT for small animals: characterization of the quasi-monochromatic X-ray source, *IEEE Transactions on Nuclear Science*, *56*, 29–35.

Masetti, S., L. Roma, P. L. Rossi, N. Lanconelli, and G. Baldazzi (2009b), Preliminary results of a multi-energy CT system for small animals, *Journal of Instrumentation*, *4*, P06,011.

McConnell, J. M. (2008), Annual threat assessment of the Intelligence Community for the House Permanent Select Committee on Intelligence, *Tech. rep.*, Director of National Intelligence.

Medalia, J. (2010), Detection of nuclear weapons and materials: science, technologies, observations, *Tech. rep.*, Congressional Research Service.

Michel, T., et al. (2006), Investigating the DQE of the Medipix detector using the multiplicity concept, *IEEE Nuclear Science Symposium Conference Record*, *2006*, 1955–1959.

Mikkelsen, S., A. Helland, D. Meier, G. Maehlum, N. Ostaard, Y. Skogseide, B. Sundal, J. Talebi, and K. Ullaland (2008a), A low power and low noise multi-channel ASIC for X-ray and gamma-ray spectroscopy in space, in *Congrex*.

Mikkelsen, S., D. Meier, G. Maehlum, P. Oya, B. Sundal, and J. Talebi (2008b), An ASIC for multi-energy X-ray counting, *IEEE Nuclear Science Symposium Conference Record*, *2008*, 1996–2001.

Mitiche, A., and L. S. Davis (1982), Finding edges in natural textures, *Signal Processing*, *4*(2-3), 181–192.

Montgomery, E. B. (2009), Nuclear terrorism: Assessing the threat, developing a response, *Tech. rep.*, Center for Strategic and Budgetary Assessments.

Moon, J. Y., J. H. Lee, and C. S. Lee (2004), Pulse shape analysis of a segmented planar germanium detector by using the Green's function method and rise-time correlations for depth information, *The Physical Society of Japan*, *73*, 3312–3318.

Nachtrab, F., T. Hofmann, M. Firsching, N. Uhlmann, and R. Hanke (2009), Simple solutions for spectroscopic, photon counting X-ray imaging detectors, *IEEE Nuclear Science Symposium Conference Record*, *2009*, 1636–1639.

Nemirovsky, Y. (1999), Statistical modeling of charge collection in semiconductor gamma-ray spectrometers, *Journal of Applied Physics*, *85*, 8–15.

Nemirovsky, Y., A. Ruzin, G. Asa, and J. Gorelik (1996), Study of the charge collection efficiency of CdZnTe radiation detectors, *Journal of Electronic Materials*, *25*, 1221–1231.

Pangaud, P., P. Delpierre, and J.-F. Berar (2010), *Semiconductor radiation detection systems*, CRC Press.

Pangaud, P., et al. (2007), XPAD3: A new photon counting chip for X-ray CT-scanner, *Nuclear Instruments and Methods in Physics Research A*, *571*, 321.

Persson, A., and B. Cederwall (2011), Development of a multimodality sensor for spectral photon counting CT, standard CT and PET, *Nuclear Instruments and Methods in Physics Research A*, *648*, S72–S74.

Picone, M., A. Gliere, and P. Masse (2003), A three-dimensional model of CdZnTe gamma-ray spectrometer, *Nuclear Instruments and Methods in Physics Research A*, *504*, 313–316.

Prettyman, T. H. (1998), Method for mapping charge pulses in semiconductor radiation detectors, *Nuclear Instruments and Methods in Physics Research Section A*, *422*, 232–237.

Prokesch, M., and C. Szeles (2006), Accurate measurement of electrical bulk resistivity and surface leakage of CdZnTe radiation detector crystals, *Journal of Applied Physics*, *100*, 014,503.

Prokesch, M., D. S. Bale, and C. Szeles (2010), Fast high-flux response of CdZnTe X-ray detectors by optical manipulation of deep level defect occupations, *IEEE Transactions on Nuclear Science*, *57*, 2397–2399.

Pumplin, J. (1969), Application of Sommerfeld-Watson transformation to an electrostatics problem, *American Journal of Physics*, *37*, 737–739.

Ramo, S. (1939), Currents induced by electron motion, *Proceedings of the IRE*, *9*, 584–585.

Ricq, S., F. Glasser, and M. Garcin (2001), Study of CdTe and CdZnTe detectors for X-ray computed tomography, *Nuclear Instruments and Methods in Physics Research A*, *458*, 534–543.

Rodrigues, M. L., and Z. He (2010), 3D Monte Carlo simulations of pixelated CdZnTe detectors under high photon fluxes, *IEEE Nuclear Science Symposium Conference Record*, *1*, 3836 – 3838.

Rodrigues, M. L., and Z. He (2011), Properties and spectroscopic performance of semiconductor detectors under high-flux irradiation, *Proc. SPIE*, *8143*, 81,430A.

Rodrigues, M. L., Z. He, and A. S. Serra (2009), Maximizing signal-to-noise ratio (SNR) in 3-D large bandgap semiconductor pixelated detectors in optimum and non-optimal filtering conditions, in *International Nuclear Atlantic Conference - INAC*.

Roessl, E., and R. Proksa (2007), K-edge imaging in X-ray computed tomography using multi-bin photon counting detectors, *Physics in Medicine and Biology*, *52*, 4679–96.

Rousse, A., P. Audebert, J. P. Geindre, F. Fallies, J. C. Gauthier, A. Mysyrowicz, G. Grillon, and A. Antonetti (1994), Efficient K α X-ray source from femtosecond laser-produced plasmas, *Physical Review E*, *50*, 2200–2207.

Ruat, M., E. G. D'Aillon, J. Tabary, and L. Verger (2007), 3D semiconductor radiation detectors for medical imaging, in *Proceedings of the COMSOL Users Conference*.

Ruzin, A., and Y. Nemirovsky (1997a), Methodology for evaluation of mobility-lifetime product by spectroscopy measurements in CdZnTe spectrometers, *Journal of Applied Physics*, *82*, 4166–4171.

Ruzin, A., and Y. Nemirovsky (1997b), Statistical models for charge collection efficiency and variance in semiconductor spectrometers, *Journal of Applied Physics*, *82*, 2754–2758.

Samedov, V. V. (2007), Charge induction in semiconductor detectors with pixellated structure, *X-Ray Spectrometry*, *36*, 158–161.

Scheiber, C. (1996), New developments in clinical applications of CdTe and CdZnTe detectors, *Nuclear Instruments and Methods in Physics Research Section A*, *380*, 385–391.

Schieber, M., et al. (2001), Comparison of cadmium zinc telluride crystals grown by horizontal and vertical Bridgman and from the vapor phase, *Journal of Crystal Growth*, *231*, 235–241.

Schlomka, J. P., et al. (2008), Experimental feasibility of multi-energy photon-counting K-edge imaging in pre-clinical computed tomography, *Physics in Medicine and Biology*, *53*, 4031–4047.

Seely, J. F., G. E. Holland, L. T. Hudson, C. I. Szabo, A. Henins, H.-S. Park, P. K. Patel, R. Tommasini, and J. M. Laming (2007), K-shell spectra from Ag, Sn, Sm, Ta, and Au generated by intense femtosecond laser pulses, *High Energy Density Physics*, *3*, 263–271.

Sempau, J., E. Acosta, J. Baro, J. M. Fernandez-Varea, and F. Salvat (1997), An algorithm for Monte Carlo simulation of coupled electron-photon transport, *Nuclear Instruments and Methods in Physics Research B*, *132*, 377–390.

Shah, K. S., J. C. Lund, and F. Olschner (1990), Charge collection efficiency in a semiconductor radiation detector with a non-constant electric field, *IEEE Transactions on Nuclear Science*, *37*, 183–186.

Shanker, T., and E. Scmitt (2009), U.S. to make stopping terror key aim, *Tech. rep.*, New York Times.

Shikhaliev, P. M., and S. G. Fritz (2011), Photon counting spectral CT versus conventional CT: comparative evaluation for breast imaging application, *Physics in Medicine and Biology*, *56*, 1905–1930.

Shockley, W., and J. W. T. Read (1952), Statistics of the recombination of holes and electrons, *Physical Review*, *87*, 835.

Sidky, E. Y., L. Yu, X. Pan, Y. Zou, and M. Vannier (2005a), A robust method of X-ray source spectrum estimation from transmission measurements: Demonstrated on computer simulated, scatter-free transmission data, *Journal of Applied Physics*, *97*, 124,701.

Sidky, E. Y., Y. Zou, and X. Pan (2005b), Volume image reconstruction from a straight-line source trajectory, *IEEE Nuclear Science Symposium Conference Record*, *2005*, 2441–2444.

Slaughter, D., et al. (2003), Detection of special nuclear material in cargo containers using neutron interrogarion, *Tech. rep.*, Lawrence Livermore National Laboratory.

Soldner, S. A., D. S. Bale, and C. Szeles (2007), Dynamic lateral polarization in CdZnTe under high flux X-ray irradiation, *IEEE Transactions on Nuclear Science*, *54*, 1723–1727.

Steadman, R., C. Herrmann, O. Mulhens, and D. G. Maeding (2011), ChromAIX: Fast photon-counting ASIC for spectral computed tomography, *Nuclear Instruments and Methods in Physics Research A*, *648*, S211–S215.

Sze, S. M. (1981), *Physics of semiconductor devices*, John Wiley & Sons, Inc.

Szeles, C., S. A. Soldner, S. Vydrin, J. GRaves, and D. S. Bale (2007), Ultra high flux 2-D CdZnTe monolithic detector arrays for X-ray imaging applications, *IEEE Transactions on Nuclear Science*, *54*, 1350–1358.

Takekida, H., and K. Nanbu (2004), Weighting factor for particle modeling of axisymmetrical low temperature plasmas, *Journal of the Physical Society of Japan*, *73*, 756–757.

Talla, P. T., M. Firsching, T. Michel, J. Durst, and G. Anton (2008), Reconstruction of incident X-ray spectra using the Medipix2 detector, *IEEE Nuclear Science Symposium Conference Record*, *2008*, 2459–2461.

Tlustos, L. (2010), Spectroscopic X-ray imaging with photon counting pixel detectors, *Nuclear Instruments and Methods in Physics Research A*, *623*, 823–828.

Valero, S., P. Lapostolle, A. M. Lombardi, N. Pichoff, and E. Tanke (1999), An analytical approach to the Poisson equation in 3-dimensional space charge problems, in *Particle Accelerator Conference*.

Veigele, W. J. (1973), Photon cross sections from 0.1 KeV to 1 MeV for elements Z = 1 to Z = 94, *Atomic Data*, *5*, 51.

Xing, Y., L. Zhang, X. Duan, J. Cheng, and Z. Chen (2011), A reconstruction method for dual high-energy CT with MeV X-rays, *IEEE Transactions on Nuclear Science*, *58*, 537–546.

Yang, H. (2009), Active interrogation methods for detection of special nuclear material, Ph.D. thesis, The University of Michigan.

Ying, Z., R. Naidu, and C. R. Crawford (2006), Dual energy computed tomography for explosive detection, *Journal of X-Ray Science and Technology*, *14*, 235–256.

Zanio, K., G. Ottaviani, C. Jacoboni, and A. A. Quaranta (1973), Hole mobility and Poole-Frenkel effect in CdTe, *Journal of Applied Physics*, *44*, 360.

Zanio, K. R., W. M. Akutagawa, and R. Kikuchi (1968), Transient currents in semi-insulating CdTe characteristic of deep traps, *Journal of Applied Physics*, *39*, 2818–2828.

Zhang, F. (2005), Events reconstruction in 3-D position sensitive CdZnTe gamma-ray spectrometers, Ph.D. thesis, The University of Michigan.

Zhang, F., Z. He, and D. Xu (2004), Improved resolution for 3-D position sensitive CdZnTe spectrometers, *IEEE Transactions on Nuclear Science*, *51*, 2427–2431.

Zhang, F., Z. He, D. Xu, and L. J. Meng (2005), Feasibility study of using two 3-D position sensitive CZT detectors for small animal PET, *IEEE Nuclear Science Symposium Conference Record*, *3*, 4 pp.